SINGLE-PARTICLE STRUCTURE OF NEUTRON-RICH SILICON ISOTOPES AND THE BREAKDOWN OF THE N=28 SHELL CLOSURE

By

Steven Ragnar Stroberg

A DISSERTATION

Submitted to
Michigan State University
in partial fulfillment of the requirements
for the degree of

Physics - Doctor of Philosophy

2014

ABSTRACT

SINGLE-PARTICLE STRUCTURE OF NEUTRON-RICH SILICON ISOTOPES AND THE BREAKDOWN OF THE N=28 SHELL CLOSURE

By

Steven Ragnar Stroberg

The well-known shell structure of stable atomic nuclei has been observed to change in systems with extreme proton-neutron ratios. Understanding this changing structure can provide insight into the underlying forces between nucleons, and how they can lead to shell structure. The $N = 28$ shell gap, which disappears in the region of the nuclear chart centered on ^{42}Si, is an interesting case because this gap is the first gap which requires the assumption of a strong spin-orbit splitting in the shell-model framework.

Previous experimental work on the breakdown of the $N = 28$ shell gap has generally utilized collective observables which have then been interpreted though theoretical calculations in terms of changing shell structure. In this work, one-proton and one-neutron knockout reactions are used to obtain a complimentary, single-particle picture of this region, focusing on the neutron-rich silicon isotopes ^{36}Si, ^{38}Si, and ^{40}Si. This isotopic chain connects the closed-shell nucleus ^{34}Si to ^{42}Si, which does not reflect a good shell closure. Level schemes of knockout residues ^{35,37,39}Si and ^{35,37,39}Al are constructed, with new levels identified for each nuclide. These results, in conjunction with large-scale shell model and eikonal reaction model calculations, generally support the interpretation developed to explain the collective observables. They further emphasize and illuminate the importance of excitations across both the $N = 20$ and $N = 28$ shell gaps for describing nuclides in this region, and provide additional guidance for shell model effective interactions in describing this region.

In addition, an empirical method is introduced to model the asymmetry observed in the

momentum distributions by utilizing inelastic scattering reactions to approximate the dissipative effects of target breakup, producing good agreement with the measured distributions.

To my dad, for encouraging my critical thinking and mistrust of authority (although this can at times cause some trouble), and for toughing it out through two (now three) bouts with cancer to see me graduate for the third time. And to my mom, for sharing her boundless energy (often in the form of care packages sent regularly for nearly a decade throughout my undergraduate and graduate school careers), and for keeping dad going though the darkest times. You are the best people I know.

ACKNOWLEDGMENTS

The list of those who have helped me along the way to this thesis is long, and while this section is correspondingly long, I am sure I have omitted many people, and for this I apologize.

I would like to thank my teachers, especially my high school teacher Ken Umholtz who gave me my first real taste of physics, and Professor Rick Norman, who took me into his group at Berkeley and gave me the opportunity to go to my first conference and write my first paper.

I thank the members of my committee, all of whom have done far more for me than show up to meetings and sign my paper work. My advisor, Professor Alexandra Gade, gave me freedom to explore my interests without letting me founder, and spoke to me as an equal, despite her overwhelmingly superior knowledge of nuclear physics. She has been an adamant promoter of my career throughout my five years here, encouraging me to seek out opportunities and writing outstanding letters of recommendation. The idea for this project, like many other ideas within this thesis, was originally hers. Professor Vladimir Zelevinsky taught me both physics and humility in the many classes I took with him, as well as during the summer after my first year, in which he was willing to provide a project for a young experimentalist who was curious about theory. Professor Remco Zegers sat on shift with me during my first experiment, shortly after I arrived in grad school, and patiently explained much of the equipment that I would eventually use for my own thesis experiment. He also spent countless hours teaching and developing a course on electronics that served me well during my time here. Professor Sean Liddick generously gave his time, equipment, and expertise to help me with the project that makes up the first appendix of this thesis. Professor Phil Duxbury introduced me to computational physics (and to Fortran, although

I'm unsure if I should thank him for that part) and took me to the Netherlands to learn about it.

Although he was not on my committee, Professor Alex Brown certainly received more than his fair share of visits from me, asking all manner of questions about nuclear structure. I am always amazed by his ability to catch up in thirty seconds to an idea that I had mulled for weeks. Likewise, Professor Jeff Tostevin has proved an invaluable resource for reaction theory, and devoted a substantial amount of time, thought, and energy to the ideas and language contained in this thesis and the resulting publication. Professors Dick Furnstahl and Achim Schwenk, who taught the 2013 TALENT school on nuclear forces, taught me a semester's worth of material in a month (some of which made it into the pages of this thesis), and inspired me to pursue a post-doc in nuclear theory.

I am also indebted to the members of the Gamma Group. Dr. Dirk Weisshaar seems to know absolutely everything about detecting γ rays, and is often happy to share his knowledge. My favorite time in any Gamma Group meeting is always when Dirk starts out with "Ya, well you see..." because I know that, without fail, I'm about to learn something. Without Dirk working round the clock, the entire GRETINA campaign, including my thesis experiment, would have been impossible. Dr. Andrew Ratkiewicz sat down in my office and talked to me the week I arrived, and quickly became my first friend at the lab, introducing me to the DALMAC and to Crunchy's. He also taught me most of what I know about the SeGA filling system, which is still far less than he knows. Dr. Travis Baugher became one of my closest friends, and was always happy to pull my out-of-shape butt through the painful last miles of a long bike ride, even when, for example, a blizzard appeared out of nowhere. Dr. Vinny Bader helped me learn things I should have already known by asking questions that I wouldn't have thought of, or that I had been too embarrassed to ask. Professor Kathrin

Wimmer and Eric Lunderberg developed the GrROOT analysis framework that I used to analyze the experimental data for this thesis. Having previously analyzed an experiment without this framework, I can confidently say that their work made my life much easier than it otherwise would have been. I'm also thankful for the members of the Lifetime Group, Chris Morse, Kenneth Whitmore, and Charles Loelius, who gamely took their turns with the filling system pager and helped to lighten that oppressive burden.

Jon Bonofiglio, Renan Fontus, Dr. Thomas Baumann, Dr. Mathias Steiner, and the rest of the cycling group made me feel like I was a part of the lab, rather than just a grad student passing through. The Tuesday morning basketball crew helped to break up the hours upon hours of sitting that is graduate school. My friends Samantha Keeney, Dr. Abigail Lynch, Damien Sheppard, and James Vatter became my family in Lansing, and kept me aware that there was a world outside the lab. Older grad students, especially Dr. Rhiannon Meharchand, Dr. Andrew Ratkiewicz, Dr. Angelo Signoracci, Dr. Phil Voss, and Dr. Josh Vredevoogd quickly made me feel like I belonged here and provided guidance, either verbal or by example. Rachel Showalter has been a terrific friend and office-mate for five years, especially in those not-so-infrequent cases in which she corrected my algebra on the whiteboard.

I thank the Oak Ridge Associated Universities for giving me the opportunity to go to the meeting of Nobel Laureates in Lindau, Germany, where I got to meet not only famous old physicists but also brilliant young physicists.

Finally, I of course must thank my friend, partner, confidant, counselor, and inspiration, Dr. Jenna Smith. Few people would have the patience to work on physics all day, only to come home to me rattling on about even more physics, but she generally manages to take it all with a smile and then point out where I'm wrong. Who could ask for more?

TABLE OF CONTENTS

LIST OF TABLES

LIST OF FIGURES

Chapter 1

Introduction

All my life through, the new sights of Nature made me rejoice like a child.
(M. Curie)

1.1 Nuclear structure and the "magic numbers"

The atomic nucleus was proposed in 1911 by Rutherford [14], based on the experiments of Geiger and Marsden [15], and a century later it remains the subject of vigorous experimental and theoretical research. This is a testament to the depth and complexity of the problem of understanding the nucleus.

At first consideration, one might think that attempting to describe the nucleus with high precision would be a hopeless endeavor. The protons and neutrons (collectively called *nucleons*) which make up the nucleus interact via all four known forces of nature [1], and are confined to a region of a few fermi (1 fm = 10^{-15} m) by the strong nuclear force. These nucleons are bound by roughly 5-10 MeV, which, by the uncertainty principle, implies that the spatial extent of their wave functions should be $(2mE)^{-1/2} \sim 1.5$ fm, indicating that this is very much a quantum system. Furthermore, because nucleons carry spin 1/2, they obey Fermi-Dirac statistics. This requires that the wave functions of the individual nucleons should be correlated with each other, in order to avoid having two nucleons simultaneously

[1] Gravity is, of course, irrelevant to the considerations of nuclear structure.

in the same state. Finally, there exists no simple analytic form for the strong interaction between nucleons, in contrast to the Coulomb potential of atomic physics.

Nonetheless, some simple properties do emerge in the structure of nuclei, one of the most notable being the appearance of the so-called *magic numbers*. As a simple first approximation, we may model a nucleus as a drop of nuclear liquid, and calculate the binding energy [16]. We take a term which is attractive in the bulk – proportional to the volume, which for a liquid should be proportional to the number of nucleons A – and add terms for surface tension (proportional to $A^{2/3}$) and the Coulomb repulsion of the charged protons. Further, since there are two kinds of nucleon, which each obey the Pauli exclusion principle, we would expect that for a given A, nuclei with an equal number of protons Z and neutrons N, should have a lower energy than asymmetric nuclei. Finally, since there is a noted staggering of binding energies between even and odd numbers of protons or neutrons, we add a pairing term which is attractive for even N and even Z and repulsive for odd N and odd Z.

$$\delta(N,Z) = \begin{cases} a_P A^{-1/2} & N \text{ odd and } Z \text{ odd} \\ -a_P A^{-1/2} & N \text{ even and } Z \text{ even} \\ 0 & N+Z \text{ odd} \end{cases} \tag{1.1}$$

This results in the *semi-empirical mass formula* [16]:

$$BE = a_V A - a_S A^{2/3} - a_C \frac{Z^2}{A^{1/3}} - a_A \frac{(N-Z)^2}{A} + \delta. \tag{1.2}$$

The parameters of this model can be fit to experimental data, and give a quite good reproduction of the binding energies across most of the chart. Figure 1.1 shows the difference between the experimental binding energies [1] and those calculated with (1.2) using the

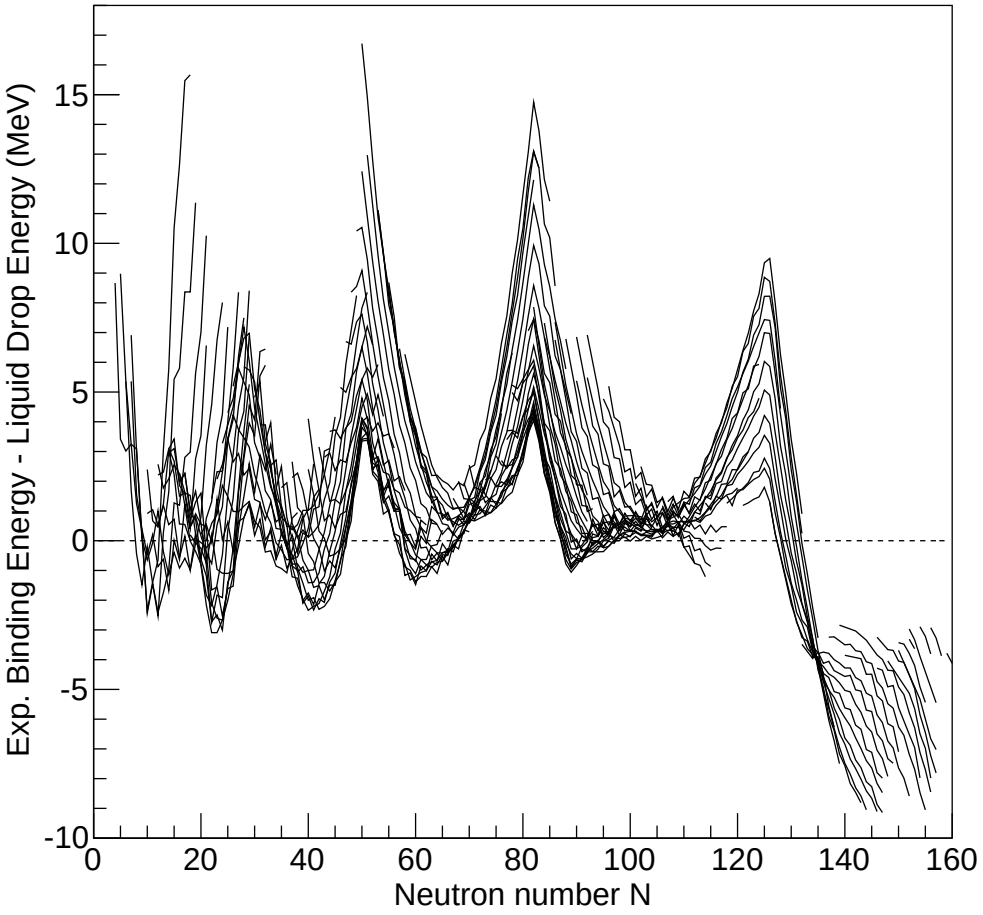

Figure 1.1: The difference between experimental binding energies and binding energies calculated within the liquid drop model, as a function of neutron number N. Nuclides with $Z \geq 8$ are shown. An excess of binding energy can be clearly seen for neutron numbers 28, 50, 82, and 126. Binding energy data taken from [1].

parameters (in MeV) $a_V = 15.54, a_S = 17.23, a_C = 0.697, a_A = 22.6, a_P = 12.0$ (*cf.* [17]). The first feature we note is that the binding energies are reproduced to within 10 MeV for almost all nuclei, while nuclear binding energies are of the order of 10 MeV per nucleon. Second, it is clear that there is some additional structure to the binding energies. Nuclei with 28, 50, 82, and 126 neutrons (as well as 2, 8 and 20, although these are more difficult to see here) are particularly well-bound with respect to their neighbors. They also exhibit high neutron separation energies, and high first excited states. The same effect is observed for nuclei with the equivalent number of protons. These numbers, called *magic numbers* (a term likely coined by Wigner [18]), suggest that some additional structure beyond the liquid drop picture makes these nuclei particularly stable.

By the 1930's the presence of these magic numbers had been remarked upon [19], and some properties of nuclei had been interpreted in terms of a shell model [20], but a microscopic picture which robustly predicted these numbers remained elusive. As an illustration, consider a nucleon moving in a mean field potential, generated by all the other nucleons in the nucleus. It is known that the force between nucleons is short-ranged, so the shape of the potential should be similar to the shape of the density. A simple parameterization is given by the Woods-Saxon form:

$$V(r) = -V_0 f_{\mathrm{ws}}(r) \tag{1.3}$$

$$f_{\mathrm{ws}}(r) = \frac{1}{1 + e^{(r-R_0)/a_0}}. \tag{1.4}$$

Typical values for the parameters are $V_0 = 50$ MeV, $R_0 = 1.25A^{1/3}$ fm, and $a_0 = 0.7$ fm [21]. Solving the Schrödinger equation for this potential, we obtain allowed energies which are shown on the left side of Figure 1.2. This reproduces the magic numbers 2, 8, and 20, but fails for numbers beyond.

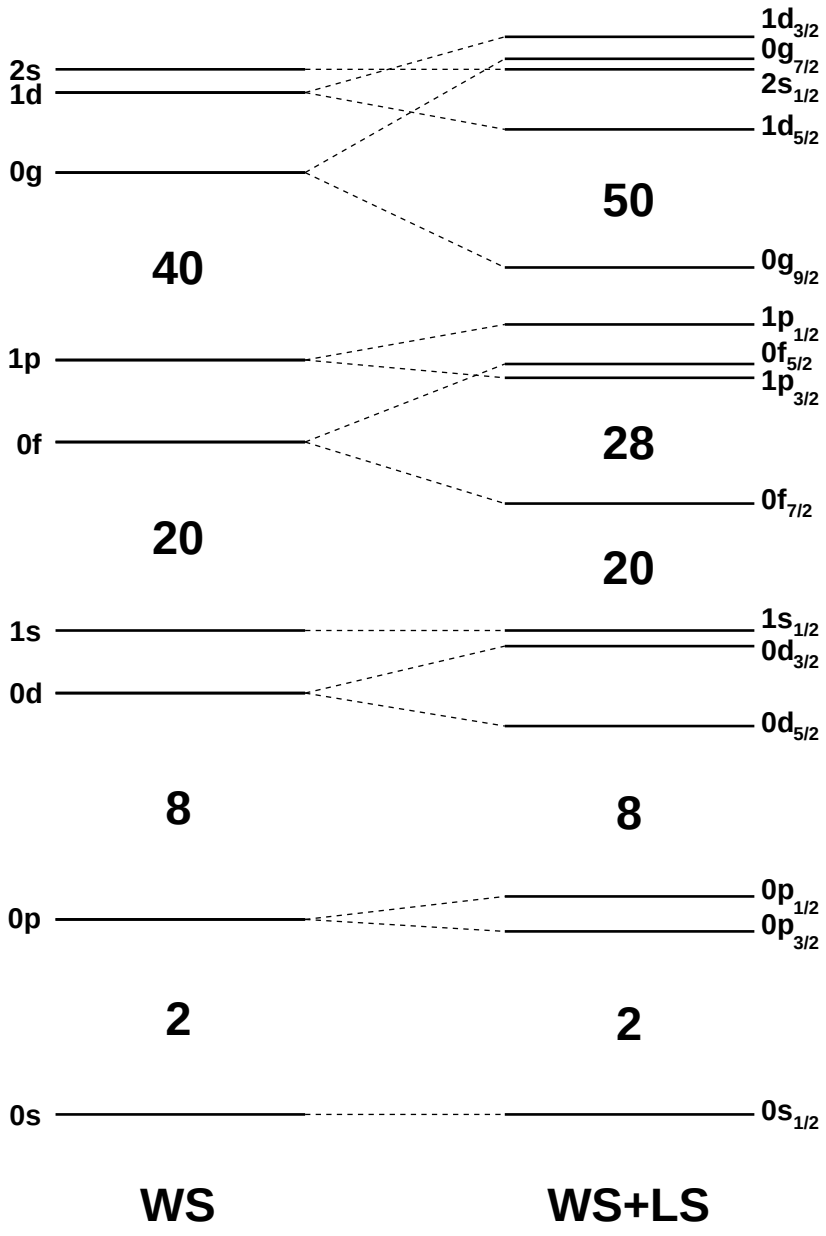

Figure 1.2: Eigenvalues for the Schrödinger equation for neutron orbits in ^{100}Sn. In the spectrum labeled WS, the mean field potential is modeled as a Woods-Saxon with parameters $V_0 = 50$ MeV, $r_0 = 1.25$ fm, and $a_0 = 0.7$ fm. The spectrum labeled WS+LS includes a spin orbit term with strength $V_{LS} = 20$ MeV. Note the (unlabeled) sub-shell gap at 14.

In 1949, it was suggested independently by Mayer [22], and Haxel, Jensen, and Suess [23] that one should make a further refinement and assume a strong, attractive, one-body spin-orbit potential, given by

$$V_{LS}(r) = (\ell \cdot s)\ V_{LS} \frac{d}{dr} f_{\rm ws}(r). \tag{1.5}$$

The radial form of the potential is chosen to make it surface-peaked. This is because in the interior of the nucleus we would expect the spin-orbit forces from all directions to cancel out, while at the surface there is no such cancellation. The addition of this term, with $V_{LS} = 20$ MeV, gives levels which are shown on the right side of Figure 1.2. With this adjustment, all observed magic numbers (at stability) are reproduced. However, as observed by Goeppert-Mayer:

> There is no adequate theoretical reason for the large observed value of the spin orbit coupling. The Thomas splitting has the right sign, but is utterly inadequate in magnitude to account for the observed values. A proper type of meson potential can be made to predict splitting qualitatively similar to the Thomas splitting and therefore qualitatively similar to the observed, but greater in magnitude than the Thomas splitting although usually somewhat less than the observed value.
>
> (M. G. Mayer [24])

(The Thomas term to which she refers is a relativistic effect acting on a vector, in this case the spin, in non-uniform motion, which contributes to the spin-orbit term in atomic fine structure splitting [25].)

Relativistic mean field (RMF) theories, initiated in the 1950s [26, 27] and developed further in the 1970s [28], do in fact predict a strong spin-orbit splitting, relying on the combination of strong scalar and vector potentials which add destructively for the central potential, and constructively for the spin-orbit potential (see [29] for an overview). These

RMF theories are phenomenological (they often omit explicit pion fields) and so the magnitude of these potentials is fit to data. However, if the potentials are constrained by the requirement of saturation, the empirical spin-orbit splitting is then reproduced without further adjustments (see, for example [30] and references therein).

In a non-relativistic framework, spin-orbit splitting arises from various sources, including a two-body spin-orbit force between nucleons [9], tensor forces [31], and three-body forces [32]. The exact degree to which each of these sources contributes, and the correspondence between the sources in the relativistic and non-relativistic frameworks, remains an open question. It has even been suggested that there may be cancellations between the various sources of spin-orbit splitting [33], and that these cancellations may change for different situations. It is therefore interesting to investigate how the observed spin-orbit splitting evolves with different parameters, such as proton-neutron asymmetry, in order to help elucidate the various contributions.

1.2 The breakdown of the N=28 shell gap

Recent developments in the study of exotic nuclei have shown that far away from stability, magic numbers can disappear, and new ones can emerge [34]. This changing shell structure can provide insight into how the various components of the nuclear interaction – for example the spin-isospin [35] or tensor [31] components – contribute to the observed structure.

I concentrate here on the magic number $N = 28$, as it is the first magic number that arises in the mean field picture due to the empirical strong spin-orbit potential. It is hoped that an understanding of how this shell gap changes will provide complimentary information to that obtained by investigating the $N = 8$ and $N = 20$ gaps, which arise due to the mean

field alone.

Early suggestions of the disappearance of the $N = 28$ shell gap came from measurements of the energy of the first $J^\pi = 2^+$ state and reduced quadrupole transition probability $B(E2; 2_1^+ \rightarrow 0_1^+)$ in the neutron-rich nucleus ^{44}S [36]. I will briefly outline, in a qualitative way, why these quantities are indicators of the presence of a shell gap.

In a simple collective model along the lines of the liquid drop picture, we can consider a vibrational excitation of a spherical nucleus (see for example [37]). The lowest-energy excitation should be a single quadrupole phonon excitation (a monopole corresponds to the compression of the nuclear fluid, and a dipole corresponds to the translation of the center of mass, which is not an intrinsic excitation). A quadrupole phonon has $J^\pi = 2^+$ and energy $\hbar\omega$, where ω is the vibrational frequency. If the drop is tightly bound, it will be more "rigid" and vibrate at a higher frequency, and thus the 2^+ one-phonon excitation will lie at a higher energy.

If we now consider an electromagnetic transition from the excited 2^+ state to the 0^+ ground state, we see that this transition must be an electric quadrupole ($E2$) transition. If the 2^+ state is well described by a quadrupole phonon, i.e. it is a collective state, then this oscillating charge distribution will readily emit an electric quadrupole photon [2], and this transition will proceed rapidly, with a large corresponding transition probability $B(E2; 2^+ \rightarrow 0^+)$. These collective states consist of many particles being coherently excited out of the closed core, and so they are unfavored if there is a large energy gap between the core and the next available state. For a good shell closure, the excited 2_1^+ state is not well-described by a collective vibration and so the decay to the 0^+ ground state proceeds more slowly.

[2] A photon has spin $S = 1$, so an electric quadrupole photon with $J^\pi = 2^+$ must additionally carry what is often interpreted as orbital angular momentum $L = 1$ or 3.

The result is that good shell closures should be associated with high 2_1^+ energies and low $B(E2)$ strengths. ^{44}S, which has 28 neutrons and 16 protons, exhibits a relatively low 2^+ and high $B(E2)$, indicating that the $N = 28$ shell gap is not so large. However, it was unclear whether this collectivity is mainly due to the protons, which do not have a good shell closure. This prompted the investigation of ^{42}Si, which has a proton sub-shell[3] gap at $Z = 14$ [38]. A measurement of a very small two-proton knockout cross section for $^{44}\text{S} \rightarrow {}^{42}\text{Si}$ [39, 40] was interpreted as evidence that the $Z = 14$ gap remained good at ^{42}Si and that ^{42}Si might be doubly magic. The observation of a very low lying 2^+ energy in ^{42}Si in a subsequent measurement [41] provided convincing evidence that ^{42}Si is in fact not a good doubly magic nucleus, suggesting that in this extreme region of the nuclear landscape, the $N = 28$ shell gap vanishes. Figure 1.3 shows the experimental 2^+ energies for the calcium, argon, sulfur, and silicon isotopes. Large 2^+ energies can be clearly seen in doubly-magic calcium ($Z = 20$) isotopes at $N = 20$ and $N = 28$, indicating good shell closures. At $N = 20$ silicon also displays closed-shell behavior, enhanced by its $Z = 14$ sub-shell closure. However, at $N = 28$ the 2^+ energy of ^{42}Si is even lower than its open-shell neighbor ^{40}Si.

More recently, the (tentative) measurements of the first excited 4^+ state in these silicon isotopes [3] reinforced the notion that $N = 28$ is no longer a good closure, and that ^{42}Si is in fact well-deformed. In the simple phonon model described above, the next excited state should be a two-phonon state, where the two phonons can couple to $J^\pi = 0^+, 2^+, 4^+$, with energy $2\hbar\omega$. Thus for a vibrational nucleus, we would expect a triplet of states with an excitation energy equal to twice that of the first excited 2^+ state. On the other hand, if the nucleus is not spherical but deformed, then there is the possibility of a rotational excitation

[3]The distinction between a sub-shell gap and a proper shell gap is not well defined. In fact, many older works (e.g. [23, 37]) list 14 as a magic number.

with energy $\hbar^2 J(J+1)/2\mathcal{I}$, where $\mathcal{I}$ is the moment of inertia. For the ground-state band of an even-even nucleus, J takes on only even values (see appendix B), and so the first excited state has $J^\pi = 2^+$ and the second excited state is 4^+. Assuming a constant $\mathcal{I}$, the ratio of the 4^+ energy to the 2^+ energy is $4(4+1)/2(2+1) = 20/6 = 3.333$. Figure 1.4 shows the experimental ratio $E(4^+)/E(2^+)$ for a range of silicon isotopes as a function of neutron number N. The upward trend in the ratio with increasing N indicates the onset of deformation, with the greatest deformation found at $N = 28$, in clear defiance of the expected shell gap.

It is therefore established that ^{42}Si does not behave as a traditional doubly-magic nucleus. The next step is then to understand the mechanisms which lead to the disappearance of the $N = 28$ shell gap. The most promising proposed explanation [41, 42] is that the action of the tensor force (discussed in §2.1.3) leads to the simultaneous reduction of the $N = 28$ and $Z = 14$ shell gaps at large proton-neutron asymmetry, enhancing quadrupole deformation and collective behavior. This explanation is framed in a single-particle picture of nuclear structure, while the experimental data so far are of a collective nature. In this work, we use single-nucleon knockout reaction cross sections (very much a single-particle picture observable) to shed more light on the underlying mechanism behind the evolving shell structure in the vicinity of ^{42}Si.

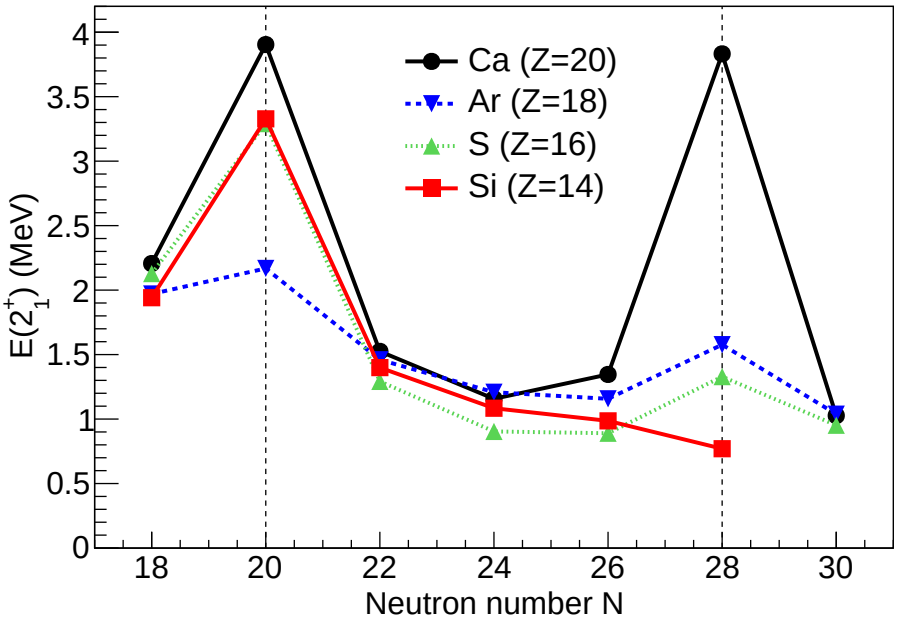

Figure 1.3: Experimental energies of the first 2^+ states as a function of neutron number for the Ca, Ar, S, and Si isotopic chains. Data taken from [2]. For the interpretation of the references to color in this and all other figures, the reader is referred to the electronic version of this thesis.

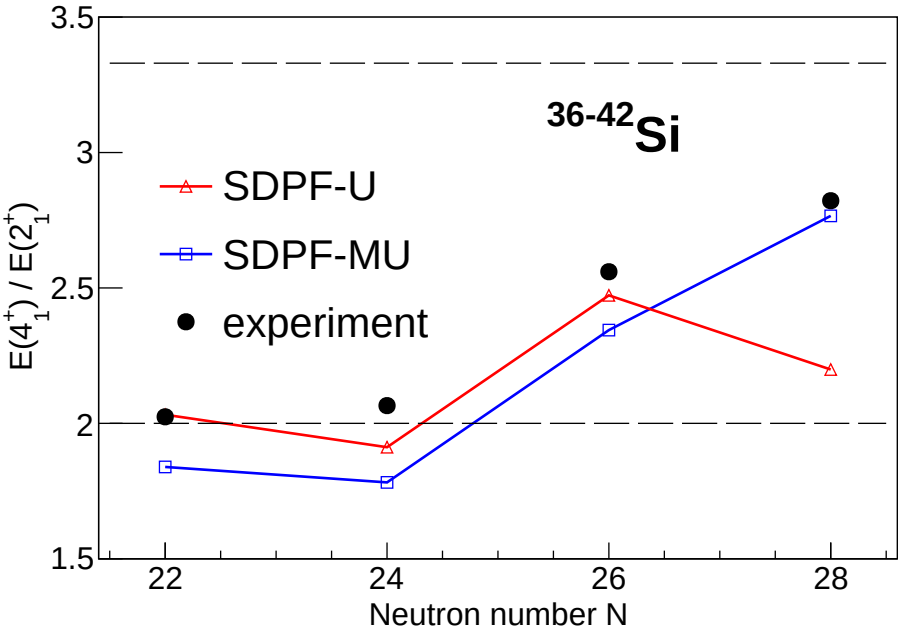

Figure 1.4: Ratio of the energy of the first 4^+ state to the energy of the first 2^+ state in silicon isotopes with $22 \leq N \leq 28$. Experimental points from Takeuchi *et al.* [3] are indicated with black dots, while shell model calculations with two different effective interactions are indicated with sold lines. The dashed lines indicate the simple vibrational (2.0) and rotational (3.33) model predictions (see text).

Chapter 2

Theoretical background

The miracle of the appropriateness of the language of mathematics for the formulation of the laws of physics is a wonderful gift which we neither understand nor deserve. (E. Wigner)

In this chapter, I discuss the connection between nuclear structure and the underlying nuclear forces, with an emphasis on the role of the tensor force. I then outline the theoretical techniques used in the analysis and interpretation of this work.

2.1 Nuclear forces and their impact on structure

The fundamental theory describing the nuclear force is quantum chromodynamics (QCD) which describes the interaction between quarks and gluons. Thus far, no deviations from the predictions of QCD have been observed and so, in principle, the whole of nuclear physics should be derived from QCD. Unfortunately, unlike in quantum electrodynamics (QED) – where the coupling $\alpha \approx 1/137$ is small and varies only weakly with momentum [43], thus admitting a good perturbative expansion – the strong coupling α_s *increases* with decreasing momentum [44, 45] and becomes much greater than 1 for momenta near the QCD momentum scale $\Lambda_{QCD} \approx 250$ MeV/c [43]. This means that at the energies of interest for nuclear physics (the Fermi energy in a nucleus is ~ 30 MeV [17]), QCD is highly non-perturbative, which is to say that any calculation in perturbation theory requires an infinite number of infinitely

complicated Feynman diagrams. Non-perturbative QCD calculations can be performed with lattice gauge theory [46] (called Lattice QCD), and while such calculations have had success in predicting the properties of hadrons (2 and 3 quark systems), the calculations of multi-hadron systems are more difficult. Some progress has been made on systems of up to a few nucleons [47], but the calculation of heavier nuclei using these methods will not likely be achieved in the near future (see [48] for a summary of the status of this work). For quantitative predictions about nuclear systems, we must rely on *effective theories* of the nuclear force.

Fortunately, the interaction between nucleons is not quite so unwieldy as that of quarks and gluons. This is because hadrons are color-neutral and at large distances (more than a few fermi) the interaction between nucleons goes to zero, analogous to the interaction between neutral atoms. At smaller distances, the interaction is due to fluctuations in color-charge density, analogous to the van der Waals force, while at the smallest distances, there is a strong repulsion due to the Pauli exclusion principle between the constituent quarks. At distances greater than about 1 fm, the interaction may be modeled as due to the exchange of pions.

2.1.1 One-pion exchange

Pions are pseudoscalar ($J^\pi = 0^-$) isovector ($T = 1$) particles, and the potential between two nucleons due to pion exchange is given by [49]

$$V_\pi(r) = \frac{f_\pi^2}{4\pi m_\pi}(\tau_1 \cdot \tau_2)(\sigma_1 \cdot \nabla_1)(\sigma_2 \cdot \nabla_2)\frac{e^{-m_\pi r}}{r}, \tag{2.1}$$

where 1 and 2 label the two nucleons, $r = |\vec{r}_1 - \vec{r}_2|$, σ and τ are the spin and isospin Pauli matrices, ∇ is the spatial derivative, $m_\pi \approx 140$ MeV is the pion mass, and f_π is the pion coupling.

This may be decomposed into scalar and tensor parts:

$$V_\pi(r) = \frac{f_\pi^2}{12\pi}(\tau_1 \cdot \tau_2)\left[(\sigma_1 \cdot \sigma_2)\left(\frac{e^{-m_\pi r}}{r} - \frac{4\pi}{3}\delta^3(r)\right) + \mathbf{S}_{12}\left(\frac{1}{r} + \frac{3}{m_\pi r} + \frac{3}{(m_\pi r)^2}\right)\frac{e^{-m_\pi r}}{r}\right] \tag{2.2}$$

with the tensor operator $\mathbf{S}_{12}$ defined as (see appendix B)

$$\mathbf{S}_{12} \equiv (\vec{\sigma}_1 \cdot \hat{r})(\vec{\sigma}_2 \cdot \hat{r}) - \frac{1}{3}\vec{\sigma}_1 \cdot \vec{\sigma}_2 \tag{2.3}$$

$$= \sqrt{\frac{8\pi}{15}}\,[\sigma_1, \sigma_2]^{(2)} \cdot Y^{(2)}, \tag{2.4}$$

where σ_1 and σ_2 have been coupled to form a rank-2 tensor, $Y^{(2)}$ is the rank-2 spherical harmonic for the relative coordinate, and the dot indicates a scalar product. At finite distance, the one-pion exchange potential has a central term that depends on the magnitude of the distance r between the nucleons, and a tensor term that depends on a combination of the relative positions and the orientation of the spins. This tensor part has a subtle but important impact on nuclear structure which will be discussed in §2.1.3.

2.1.2 Other contributions

There are, of course, other mesons aside from the pion, and they will also contribute to the interaction between nucleons. These heavier mesons, such as the ρ and ω, also produce a potential proportional to $\frac{e^{-mr}}{r}$ and their range is correspondingly shorter than that of the one-pion exchange potential. Additionally, because nucleons are composite particles, the

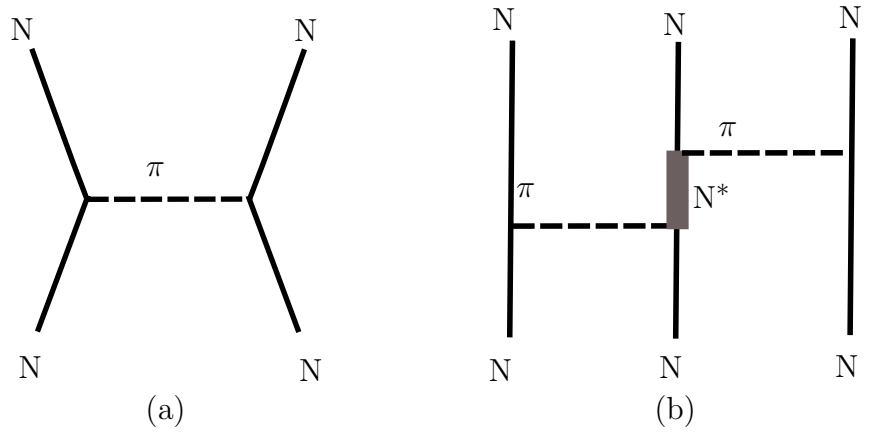

Figure 2.1: Diagrams for (a) a two-body interaction mediated by pion exchange, and (b) a three-body interaction in which the middle nucleon is excited into a resonance – for example, the $\Delta(1232)$ resonance.

presence of a third nucleon will modify the internal structure of nucleons 1 and 2 – shown schematically in Figure 2.1b – and thus modify their interaction in a way that cannot be described by a sum of pairwise interactions [50]. This gives rise to 3-body and higher-body parts of the potential which – while weaker than the pairwise interactions – have a significant impact on structure.

2.1.3 The role of the tensor force

In this section, I describe the effect of the tensor force on the evolution of nuclear structure along the lines laid out in [31]. The term *tensor force* is commonly used in the literature to refer to the component of the two-body interaction in which the spins of each nucleon combine into a rank-2 tensor. This is in contrast to the central (scalar, rank-0) component, which is proportional to $\vec{\sigma}_1 \cdot \vec{\sigma}_2$, and the spin-orbit (vector, rank-1) component which is proportional to $\vec{\sigma}_1 + \vec{\sigma}_2$. The tensor component is written as:

$$V_T = (\vec{\tau}_1 \cdot \vec{\tau}_2)\, \mathbf{S}_{12} f_T(r). \tag{2.5}$$

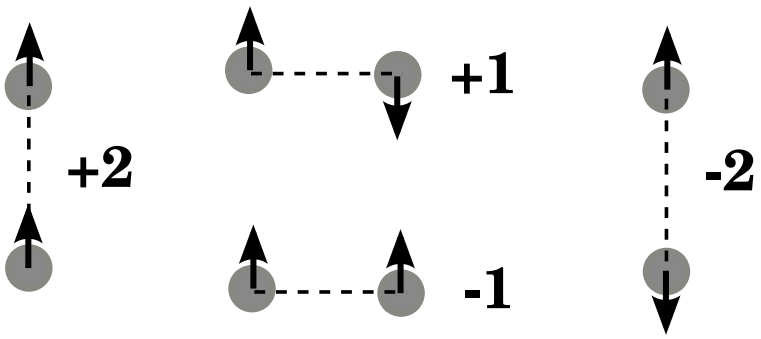

Figure 2.2: Value of the tensor operator $\mathbf{S}_{12}$ for some simple configurations of two particles (indicated by circles) with spin (indicated by arrows).

Here, $\mathbf{S}_{12}$ is the tensor operator as defined in (2.3), and $f_T(r)$ some function of r which, in the one-pion-exchange case, is positive for all r. This form is (aside from the isospin dependence) identical to that of a dipole-dipole interaction encountered in electrostatics [51]. An interaction of this form was originally proposed by Rarita and Schwinger [52] to explain the non-zero electric quadrupole moment of the deuteron [53]. The value of $\mathbf{S}_{12}$ for some simple illustrative cases are shown in Figure 2.2.

We wish to know the effect that an interaction of this type will have on nuclear structure. Consider two nucleons orbiting a nucleus, in orbits a and b, with quantum numbers (n_a, ℓ_a, j_a) and (n_b, ℓ_b, j_b). For (relative) simplicity, we consider only the monopole (i.e. angle-averaged) component of the tensor force, which is defined as

$$\bar{V}^T_{ab} = \frac{\sum\limits_{m_a m_b} \langle j_a m_a j_b m_b | V | j_a m_a j_b m_b \rangle_T}{\sum\limits_{m_a m_b} 1} = \frac{\sum\limits_J (2J+1) \langle j_a j_b | V | j_a j_b \rangle_{J,T}}{\sum\limits_J (2J+1)}. \tag{2.6}$$

By averaging over all projections m (or, equivalently, all J couplings), the monopole term gives a measure of the average effect that the nucleons in orbit a have on the nucleons in orbit b.

For a given ℓ, an orbit may have one of two values for j: $j_> = \ell + \frac{1}{2}$ and $j_< = \ell - \frac{1}{2}$.

It is stated here without proof (although a motivation is given in appendix B) that the tensor monopole is in general attractive for $\bar{V}_{j_<,j_>}$ and $\bar{V}_{j_>,j_<}$, and repulsive for $\bar{V}_{j_<,j_<}$ and $\bar{V}_{j_>,j_>}$.

This behavior of the tensor force plays an important role for the evolution of shell structure away from stability. We may consider, for example, the evolution of the splitting between the proton $d_{5/2}$ and $d_{3/2}$ orbits from $N = 20$ to $N = 28$, where, to a first approximation, neutrons are added to the $f_{7/2}$ orbital (see Figure 1.2). The tensor force monopole is repulsive between the neutron $f_{7/2}$ and the proton $d_{5/2}$ ($j_>j_>$), while it is attractive between the neutron $f_{7/2}$ and proton $d_{3/2}$ ($j_>j_<$). Table 2.1 lists some monopole terms from the SDPF-MU effective interaction to illustrate this. We would then expect that going from $N = 20$ to $N = 28$ (adding neutrons to the neutron $f_{7/2}$), the gap between the proton $d_{5/2}$ and $d_{3/2}$ should become smaller, as indicated in Figure 2.3. Likewise, beginning at ^{48}Ca (with 20 protons and 28 neutrons) and removing protons from the $d_{3/2}$ orbital will cause the energy of the neutron $f_{7/2}$ orbital to increase. The energy of the neutron $1p_{3/2}$ orbital will also increase in this case, but the effect will be reduced because the $1p_{3/2}$ orbit has a node in the radial wave function, reducing the radial overlap. Thus, going from ^{48}Ca to ^{44}S, the tensor force should cause a reduction of the $N = 28$ gap, in good agreement with experimental findings such as those described in §1.2.

One may further show that (see appendix B)

$$(2j_< + 1)\bar{V}^T_{j_<,j'} + (2j_> + 1)\bar{V}^T_{j_>,j'} = 0 \tag{2.7}$$

for either $T = 0$ or $T = 1$, which indicates that if both $j_<$ and $j_>$ orbits are filled, there is no net effect of the tensor force This may be numerically verified with the monopoles from

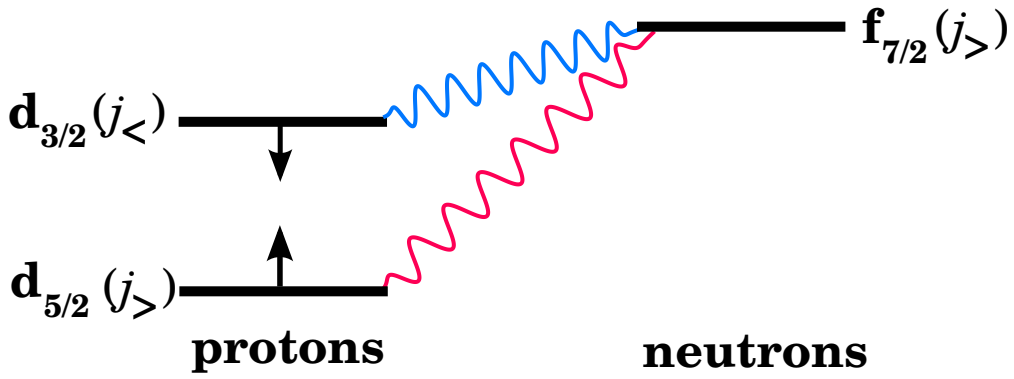

Figure 2.3: Schematic representation of the effect of the tensor force when adding neutrons to the $f_{7/2}$ orbital. The monopole component of the tensor force is attractive between the neutron $f_{7/2}$ and proton $d_{3/2}$ (indicated with the blue wavy line), while it is repulsive between the neutron $f_{7/2}$ and proton $d_{5/2}$ (indicated with the red wavy line). This results in the reduction of the spin-orbit splitting in the proton d orbitals.

Table 2.1: The monopole components of the SDPF-MU interaction between two nucleons in orbits a and b, coupled to total isospin T, broken down into central, spin-orbit, and tensor components. Energies are in MeV. Some terms have been repeated for easier comparison.

T	a	b	$V_{a,b}$ (central)	$V_{a,b}$ (spin-orbit)	$V_{a,b}$ (tensor)
0	$f_{7/2}$	$d_{5/2}$	-2.21412	-0.01714	0.20831
	$f_{7/2}$	$d_{3/2}$	-2.09208	-0.00640	-0.31247
1	$f_{7/2}$	$d_{5/2}$	-0.10499	-0.04497	0.06944
	$f_{7/2}$	$d_{3/2}$	-0.10499	-0.06868	-0.10416
0	$d_{3/2}$	$f_{7/2}$	-2.09208	-0.00640	-0.31247
	$d_{3/2}$	$p_{3/2}$	-1.46457	0.03143	-0.06835
1	$d_{3/2}$	$f_{7/2}$	-0.10499	-0.06868	-0.10416
	$d_{3/2}$	$p_{3/2}$	0.10713	0.09216	-0.02278

Table 2.1; for example, taking $j' = f_{7/2}$ and $j_<, j_> = d_{3/2}, d_{5/2}$, we have

$$4 \times (-0.31247) + 6 \times (0.20831) \approx 0.$$

The effect of the tensor force is consequently greatest when one of the spin-orbit partners is filled and the other is empty. In the case of the silicon isotopes studied in this work, the proton $d_{5/2}$ orbit is approximately filled, while the proton $d_{3/2}$ is approximately empty, and the neutron $f_{7/2}$ is being filled while the $f_{5/2}$ remains empty. Therefore, the tensor force should play an important role, in terms of comparison to the calcium isotopes, in which the proton $d_{3/2}$ is also filled, as well as evolution along the isotopic chain.

2.2 Solving the many-body problem

Once an interaction between nucleons has been obtained, the task remains to calculate observable properties of nuclei containing multiple nucleons. This consists principally of finding the eigenstates and eigenvalues of the Hamiltonian, as well as expectation values of other operators.

2.2.1 Many-body states

An A-body fermionic wave function $\Phi(\vec{r}_1, \vec{r}_2, \ldots, \vec{r}_A)$ may be described by a product of one-body wave functions $\phi_i(\vec{r}_i)$ that obey Fermi-Dirac statistics, which requires that the entire wave function must be antisymmetric with respect to the exchange of any two particles. For

a two-particle wave function, this is satisfied by

$$\Phi(\vec{r}_1, \vec{r}_2) = \frac{1}{\sqrt{2}} \left(\phi_1(\vec{r}_1)\phi_2(\vec{r}_2) - \phi_1(\vec{r}_2)\phi_2(\vec{r}_1) \right). \tag{2.8}$$

In general, for A particles, this is achieved by using a *Slater determinant*:

$$\Phi(\vec{r}_1, \vec{r}_2, \ldots, \vec{r}_A) = \frac{1}{\sqrt{A!}} \det \begin{bmatrix} \phi_1(\vec{r}_1) & \phi_2(\vec{r}_1) & \ldots & \phi_A(\vec{r}_1) \\ \phi_1(\vec{r}_2) & \phi_2(\vec{r}_2) & \ldots & \phi_A(\vec{r}_2) \\ \vdots & \vdots & \ddots & \vdots \\ \phi_1(\vec{r}_A) & \phi_2(\vec{r}_A) & \ldots & \phi_A(\vec{r}_A) \end{bmatrix} \tag{2.9}$$

Equivalently, one may use the language of second quantization [54], where the many-body wave function is represented by a *Fock state*, which is the result of creation operators $a^\dagger$ applied to the vacuum:

$$\left| \Phi^A \right\rangle = \frac{1}{\sqrt{A!}} \, a_A^\dagger \ldots a_2^\dagger a_1^\dagger \left| 0 \right\rangle \tag{2.10}$$

Here, the antisymmetrization is accounted for by the anticommutation of the creation and annihilation operators.

$$\left\{ a_i, a_j^\dagger \right\} = \delta_{ij}, \qquad \left\{ a_i, a_j \right\} = 0 = \left\{ a_i^\dagger, a_j^\dagger \right\} \tag{2.11}$$

A Fock state may be labeled simply by the index of its orbits: $|ij\rangle \equiv a_i^\dagger a_j^\dagger |0\rangle$. The Fock state and the Slater determinant represent the same object, and sometimes the labels are used interchangibly when speaking in the abstract. The actual eigenstate of the Hamiltonian for an A-body system is in general some linear combination of A-body Slater determinants.

2.2.2 Hartree-Fock

The lowest-energy single Slater determinant may be found variationally, using the *Hartree-Fock* or self-consistent mean-field method [54]. The main idea is to treat each nucleon as moving independently in a mean field generated by all the other nucleons. One starts with an ansatz for the ground state, in which the nucleons occupy orbits obeying the Pauli principle. These orbits are then used to generate a mean field potential, and the one-body Schrödinger equation is solved for each nucleon. These new orbits generate a new mean field, and the procedure is iterated until the change in wave functions from one iteration to the next are within some numerical tolerance.

The Hartree-Fock method is often used with phenomenological interactions, such as the Skyrme interaction which parameterizes the nuclear interaction with various terms, including density dependence [17]. Skyrme-Hartree-Fock calculations do a good job of reproducing bulk trends and properties such as binding energies and root-mean-squared (rms) radii for closed-shell nuclei, but they are unable to capture detailed structure because they neglect many-body correlations beyond the mean field. Additionally, as it is variational, the Hartree-Fock method is not well-suited to calculating excited states of nuclei. In this work, Skyrme Hartree-Fock calculations are used in the generation of optical potentials and form factors for the knockout reaction described in §2.3.4.

2.2.3 The shell model (configuration interaction)

Another technique is to solve for the ground state and excited states by expressing the interaction as a matrix in some basis (usually constructed from Slater determinants)

$$H_{ij} = \langle \Phi_i | \hat{K} + \hat{V} | \Phi_j \rangle \tag{2.12}$$

and diagonalizing. (Here, $\hat{K}$ is the kinetic energy and $\hat{V}$ is the interaction between nucleons). The resulting eigenstates are then a linear combination of slater determinants:

$$\big|\Psi_j\big\rangle = \sum_i c_{ij} |\Phi_i\rangle. \tag{2.13}$$

With an infinite basis[1] and a realistic interaction, this would be an exact method. However, to make the calculation tractable, the interaction is generally limited to two-body terms and the basis is truncated.

The eigenstates of the 3-dimensional harmonic oscillator potential provide an attractive basis for shell model calculations because the relative and center-of-mass motion may be separated analytically. This is useful because the interaction between nucleons depends only on the relative coordinates. Additionally, the oscillator wave functions are a reasonable first approximation to well-bound orbits[2]. The eigenstates are labeled by the radial quantum number n, the orbital angular momentum ℓ, the total angular momentum $j = \ell \pm \frac{1}{2}$ and projection m_j. They have an energy $(N + \frac{3}{2})\hbar\omega$ where $N = 2n + \ell$ [56], and ω is the oscillator

[1] The non-relativistic approximation, implicitly or explicitly, makes a high-momentum cutoff and so the basis is in fact finite, albeit large [55].

[2] It should be noted that wave functions in the oscillator basis die off asymptotically as e^{-ar^2}, while the actual wave function should go as e^{-ar}.

frequency of the potential. The difference between the harmonic oscillator potential $\hat{V}_{HO}$ and the nuclear interaction $\hat{V}_N$ is treated as a perturbation

$$\hat{H} = \hat{H}_{HO} + \hat{V}_N - \hat{V}_{HO} \equiv \hat{H}_{HO} + \hat{V}. \tag{2.14}$$

The harmonic oscillator term $\hat{H}_{HO} = \hat{K}_{HO} + \hat{V}_{HO}$ is diagonal in the oscillator basis, so we may replace it with its eigenvalues (omitting the constant $\frac{3}{2}\hbar\omega$): $\langle j|\hat{H}_{HO}|i\rangle = N_i\hbar\omega\delta_{ij}$. Neglecting 3-body and higher parts of the nuclear interaction, the potential is given in terms of *two body matrix elements* (TBME) $\langle k\ell|\hat{V}|ij\rangle$. The nuclear potential conserves total angular momentum and isospin (although isospin is only an approximate symmetry), so we may specify the TBME as $\langle ab|\hat{V}|cd\rangle_{JT}$, indicating that nucleons in orbits a and b are coupled to total angular momentum J and isospin T (and likewise for c and d).

As was mentioned earlier, in order to make the calculation tractable it is necessary to truncate the infinite oscillator basis. For light systems ($A \lesssim 12$), it is possible to cut off at high N, usually of the order of 12-14, and extrapolate to $N \to \infty$. This method is called the *no-core shell model* (NCSM), to distinguish it from the standard shell-model approach used for heavier systems for which the NCSM is computationally infeasible. In the standard shell model, in addition to truncating at high N, the active Hilbert space, or *model space* is also truncated at low N, essentially freezing a core of nucleons into a single Slater determinant[3]. A good choice for the core is a closed-shell or "doubly magic" nucleus, such as ^{16}O or ^{40}Ca, as excitations out of these cores are suppressed by the large shell gaps. The remaining orbits are collectively called the *valence space*. In this case, we may sum the one-body and

[3]Sometimes, truncations are made within a single oscillator shell if the inclusion of the full shell is intractable.

two-body matrix elements over the core orbits to obtain a zero-body term

$$E_0 = \sum_a \langle a|\hat{H}_{HO}|a\rangle + \frac{1}{2}\sum_{a,b\in\text{core}} \langle ab|\hat{V}|ab\rangle \tag{2.15}$$

and additional one-body terms

$$\delta\epsilon_a = \sum_{b\in\text{core}} \langle ab|\hat{V}|ab\rangle, \tag{2.16}$$

which result in the *single-particle energy* (SPE) of state a: $\epsilon_a = N_a\hbar\omega + \delta\epsilon_a$. Neglecting three-body and higher-body forces, the interaction is then specified by the TBME and single-particle energies (as well as the zero-body E_0 term, which, like the constant $\frac{3}{2}\hbar\omega$ oscillator term, is unimportant for calculating excited-state spectra).

2.2.4 Effective interactions for shell-model calculations

The interaction used in a shell-model calculation should ideally be derived from the interaction between free nucleons, obtained, for example, in nucleon-nucleon scattering experiments. Nucleon-nucleon potentials have been developed [5, 4, 57, 58] which can reproduce nucleon-nucleon (NN) scattering data up to a few hundred MeV. In principle, all that remains is to evaluate one of these potentials in the chosen basis and diagonalize. However, this method will produce accurate results only if contributions from configurations outside the model space are small, and this is not necessarily the case.

Two potentials which have been derived from NN scattering are plotted in Figure 2.4 for the $^1S_0$ channel[4]. The most striking feature of this figure is the very repulsive potential at

[4]This spectroscopic notation indicates two nucleons in a spin singlet, with relative orbital angular momentum $\ell = 0$ and total angular momentum $J = 0$

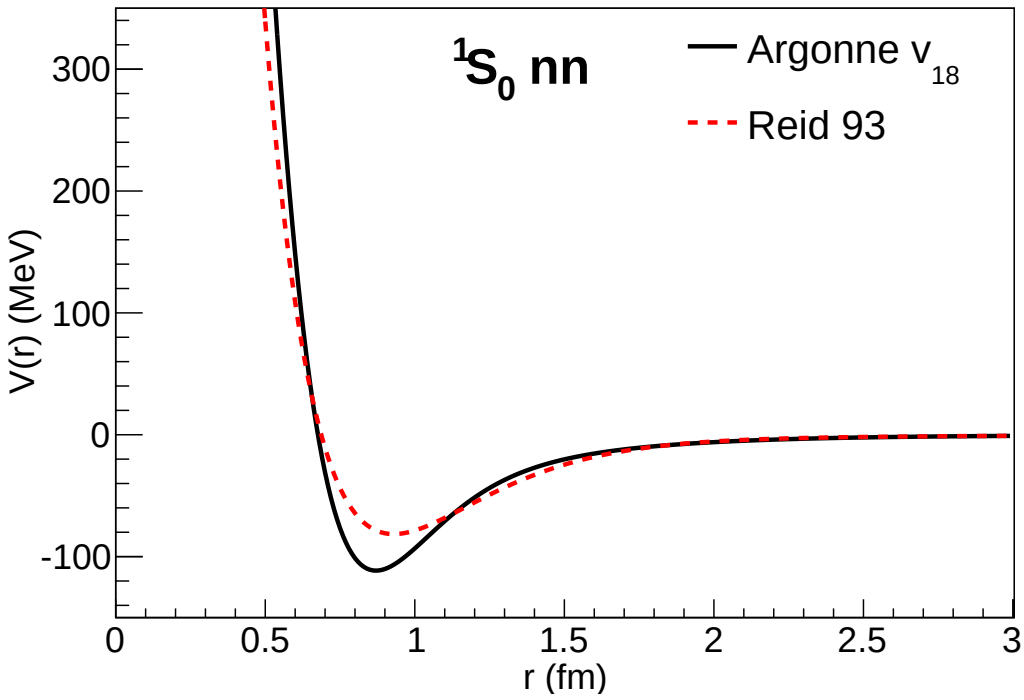

Figure 2.4: The $^1S_0$ channel of two phenomenological nucleon-nucleon potentials [4, 5] which reproduce NN scattering data.

short distances, often referred to as a *hard core*. This leads to *short-range correlations*, due to the fact that no two nucleons should be in the same place. These short-range correlations disrupt the picture of independent single-particle orbits in a mean field, and the result is that the true eigenvectors $|\Psi\rangle$ contain contributions from many different configurations $|\Phi_i\rangle$, including those outside the model space, and thus the results of calculations using bare NN interactions within a truncated model space do not accurately reproduce the data.

There are two main strategies which are used (in concert) to mitigate this problem. One is to develop NN potentials which have a softer core, but still reproduce scattering data at low energy. Historically, this was done with the Brueckner G-matrix formalism [59]. More recently, the V_{lowk} [60] and similarity renormalization group (SRG) methods [61, 62] have been developed to do this. The second strategy is to generate effective interactions for a

given model space which take into account the excluded configurations. This can be done with many-body perturbation theory (MBPT) [63] or, very recently, within the in-medium SRG (IM-SRG) [64, 65] and coupled cluster formalisms [66]. In all cases, approximations and truncations must be made, and the results are still not exact.

An alternative approach is to abandon the direct connection to the underlying NN interactions and instead fit to existing data, treating the TBME (or alternatively Talmi integrals) as free parameters [67]. The gold standard of this approach is the USD effective interaction [68], which can reproduce known energy levels in $1s0d$ shell nuclei with a root-mean-squared deviation of less than 200 keV, better than any microscopically-based interaction has been able to achieve. This approach requires a large amount of existing data, and its accuracy beyond the fitted region quickly deteriorates, making it less reliable for extrapolating into unknown regions of the nuclear chart. Often, what is done is to start with the microscopic approach, and then to phenomenologically adjust the TBME to better reproduce existing data. This is the approach adopted for both of the shell model effective interactions employed in this work.

2.2.5 Effective operators for γ decay

Once the eigenvalue problem has been solved, yielding energies and wave functions, other observables may be calculated using those wave functions. Here, I concentrate on the calculation of γ decay rates. The rate for a γ transition from an initial state with spin parity J_i^π to a final state with J_f^π is given by the *reduced transition probability* $B(\sigma\lambda; J_i^\pi \to J_f^\pi)$ multiplied by a phase-space factor which depends on the parity and multipolarity of the

emitted photon (see appendix B). The reduced transition probability is defined as

$$B(\sigma\lambda; J_i^\pi \to J_f^\pi) = \frac{\left|\left\langle J_f \middle\| \mathcal{M}_\lambda^\sigma \middle\| J_i \right\rangle\right|^2}{2J_i + 1} \tag{2.17}$$

where σ can indicate either electric or magnetic transition, λ indicates the multipolarity of the transition, $\mathcal{M}_\lambda^\sigma$ is the appropriate multipole operator, and the double bar indicates a reduced matrix element.

The free-space operators for an electric transition are [17]

$$\mathcal{M}_\lambda^E = \sum_i r_i^\lambda Y^{(\lambda)}(\hat{r}_i) e_i, \tag{2.18}$$

and the free space operators for a magnetic transition are

$$\mathcal{M}_\lambda^M = \sum_i \left[\frac{2g_i^\ell}{2\lambda + 1} \vec{\ell}_i + g_i^s \vec{s}_i \right] \vec{\nabla} \left[r^\lambda Y^{(\lambda)} \right], \tag{2.19}$$

where i sums over all nucleons. The quantities e_i in (2.18) are the charges of each nucleon, which in free space are $e_\pi = 1$ for the proton and $e_\nu = 0$ for the neutron. The quantities g^ℓ and g^s in (2.19) are the spin and orbital g factors, respectively, with free-space values $g_\pi^\ell = 1$, $g_\pi^s = 5.586$ for the proton and $g_\nu^\ell = 0$, $g_\nu^s = -3.826$ for the neutron.

When evaluating these operators between shell-model wave functions, one must keep in mind that the shell-model calculation was performed with truncations which cut out some degrees of freedom. Just as an effective Hamiltonian is required to obtain accurate energies in the truncated space, so too is an effective transition operator required to obtain accurate electromagnetic observables. Formally, there should be a unitary transformation $\mathcal{M}_{\text{eff}} = U\mathcal{M}U^\dagger$, where U is the same transformation that was used to obtain the effective

Hamiltonian. However, it is often the case (e.g. with phenomenological Hamiltonians) that U is unknown. In that case, the electromagnetic operator must also be phenomenologically adjusted, typically using the parameters e_i or g_i^ℓ and g_i^s.

The most common application of this is to $E2$ transitions, in which protons and neutrons are given an *effective charge*, typically $e_\pi = 1.5$, $e_\nu = 0.5$ [21]. The fact that the neutrons acquire a charge can be made not quite so alarming by considering the case of a single neutron orbiting a closed-shell doubly-magic core. As the neutron moves, it attracts the nucleons in the core, producing an instantaneous non-spherical charge distribution that follows the motion of the neutron. One can account for this approximately by assuming the core remains spherical and associating an effective charge with the neutron. Various terms used to describe this phenomenon include saying that the neutron has induced a *core polarization*, or that the neutron is a *dressed quasiparticle* [69]. This prescription has in fact been shown to reasonably represent the effective $E2$ operator in cases in which the unitary transformation is known [70].

Likewise, corrections to the $M1$ operator must be made to account for the model space truncation. It is further expected that corrections should be made for meson exchange currents, delta isobar excitations, relativistic effects, and processes beyond the impulse approximation which are not included in the shell model calculation [71, 72]. Regardless of relative importance of each of these effects, it is clear that the $M1$ operator used in shell model calculations should differ from the free one. In addition to effective g^ℓ and g^s factors, another term is sometimes added [71], proportional to the tensor product $\left[\sigma Y^{(2)}\right]^{(1)}$ to handle cases in which the ℓ and s operators cannot connect the initial and final state, such as a nucleon transitioning from the $1s_{1/2}$ orbit to the $0d_{3/2}$ orbit (see, for example [73]).

2.3 Probing single-particle states with knockout reactions

Direct reactions which involve the addition or removal of a single nucleon provide a useful experimental probe of the single-particle structure of nuclei [21]. Historically, electron-induced proton knockout, or $(e, e'p)$, experiments were used (and still are) to identify single-particle-like states in stable nuclei. Two drawbacks to $(e, e'p)$ experiments are that (i) they are only able to probe proton orbits, and (ii) they can currently only be performed for a nuclide which is long-lived enough to allow the production of a target. Knockout reactions on a hadronic target at intermediate energies solve both of these problems [74, 75]. In a knockout reaction, the nuclide of interest is the projectile and the target is most often beryllium or carbon. A single nucleon is removed from the A-body projectile in a reaction with the target, and the remaining $A-1$-body residue is detected. Since the target is hadronic, either a proton or a neutron may be removed. Further, since the nuclide of interest is the projectile, the often-difficult process of target fabrication is not required and so short-lived nuclides may be studied in experiments using exotic beams. In this section, I describe the formalism used in the description of these knockout reactions at energies on the order of 100 MeV per nucleon, based on developments in [74, 76, 12].

2.3.1 Factorization of the cross section

We consider a knockout reaction with some associated transition operator $\mathcal{O}^{ko}_{\alpha}$ such that the reaction amplitude $\mathcal{A}^{fi}_{\alpha}$ for removing a nucleon with quantum numbers $\alpha = (n, \ell, s, j, m, t_z)$

from an initial state $\left|\Psi_i^A\right\rangle$ and populating a final state $\left|\Psi_f^{A-1}\right\rangle$ in the residue is given by

$$\mathcal{A}_\alpha^{fi} = \left\langle \Psi_f^{A-1} \middle| \mathcal{O}_\alpha^{ko} \middle| \Psi_i^A \right\rangle. \tag{2.20}$$

This operator also should depend on the target nucleus and the incident beam energy. The reaction cross section is given by $\sigma_\alpha^{fi} = \left|\mathcal{A}_\alpha^{fi}\right|^2$. If the reaction is fast compared to the internal motion of the nucleus, then we can make the *sudden approximation* and the knockout operator becomes proportional to the annihilation operator a_α [5].

$$\mathcal{A}_\alpha^{fi} \Rightarrow \mathcal{C}_\alpha^{fi} \left\langle \Psi_f^{A-1} \middle| a_\alpha \middle| \Psi_i^A \right\rangle, \tag{2.21}$$

where $\mathcal{C}_\alpha^{fi}$ is a complex number. In most experiments, the polarizations of the incoming and outgoing particles are not measured, and so the cross section is obtained by summing over final projections and averaging over initial projections. We use k to denote all the quantum numbers α, except for m (by angular momentum conservation, $m = M_i - M_f$), and obtain

$$\sigma_k^{fi} = \frac{1}{2J_i + 1} \sum_{M_i M_f} \left|\mathcal{C}_k^{fi}\right|^2 \left| \left\langle \Psi_f^{A-1} \middle| a_{k,m} \middle| \Psi_i^A \right\rangle \right|^2. \tag{2.22}$$

We now approximate $\mathcal{C}_k^{fi}$ by taking its average value over M_i, M_f. This approximation, essentially the assumption of a spherical projectile, is exact if either J_i or J_f are zero, as is the case for the projectiles studied in this work. The remaining sum is evaluated using the

[5] Technically, a_α is not a tensor operator and we should instead use $\tilde{a}_{k,m} = (-1)^{j+m} a_{k,-m}$ [17]. For clarity, we neglect this additional notation. In any rate, this quantity is squared in the cross section, so the sign is irrelevant.

Wigner-Eckart theorem, yielding

$$\begin{aligned}\sigma_k^{fi} &= \left|\mathcal{C}_k^{\overline{fi}}\right|^2 \frac{1}{2J_i+1}\left|\left\langle \Psi_f^{A-1}\middle\| a_k \middle\| \Psi_i^A\right\rangle\right|^2 \\ &= \sigma_k^{\mathrm{sp}} S_k^{fi}.\end{aligned} \tag{2.23}$$

The term $\sigma_k^{\mathrm{sp}} = \left|\mathcal{C}_k^{\overline{fi}}\right|^2$ is called the *single-particle cross section*, and from (2.21) we see that it is the cross section if we assume $\left|\Psi_i^A\right\rangle = a_k^\dagger \left|\Psi_f^{A-1}\right\rangle$. The term S_k^{fi} is called the *spectroscopic factor* and only depends on the structure of the final and initial states. Often, the spectroscopic factor is calculated in the isospin formalism, yielding $S_k^{fi}(T)$ [17]. This quantity is related to the above S_k^{fi} by an isospin Clebsch-Gordan coefficient, and so the spectroscopic factor in the proton-neutron formalism is often written as $C^2 S_k^{fi}(T)$ or even simply C^2S, with implied dependence on the final and initial states. A small center-of-mass correction should be added, which for spectroscopic factors calculated in a harmonic oscillator basis takes the form [77]

$$C^2S \to \left(\frac{A}{A-1}\right)^N C^2S, \tag{2.24}$$

where $N = 2n + \ell$ is the principle quantum number of the oscillator shell.

We are interested in the nuclear structure which is contained in the spectroscopic factor. The extent to which we may compare this quantity with experimentally measured cross sections, is determined by the extent to which we can reliably calculate the single-particle cross section.

I will note here that the spectroscopic factors themselves are not experimental observables [78]. One may change the spectroscopic factor while simultaneously changing the single-

particle cross section in order to produce the exact same observable quantity, i.e. the cross section. However, if we keep in mind that the spectroscopic factors are *scheme-dependent*, we may still obtain insight into the structure within that scheme. Further, it may be the case that this scheme dependence is relatively weak among sensible formulations of the reaction theory. The remainder of this chapter is concerned with the calculation of the single-particle cross section and momentum distribution.

2.3.2 The eikonal approximation

The single-particle cross section $\sigma_k^{\rm sp}$ of (2.23) is calculated with a Glauber (eikonal) model [79], assuming the impulse approximation described in §2.3.1 and treating the core as a spectator – that is, internal reconfigurations of the core during the reaction are neglected.

The wave function of a projectile nucleus can be separated into relative and center-of-mass components

$$\Psi(\vec{r}_1, \vec{r}_2, \ldots, \vec{r}_A) = \psi_{CM}(\vec{R}_{CM}) \otimes \psi_{\rm rel}(\vec{r}_1, \vec{r}_2, \ldots, \vec{r}_A). \tag{2.25}$$

The relative part is the subject of the nuclear structure calculations of §2.2. The center-of-mass motion is characterized by the total momentum of the system $\vec{k}$. In free space, the center-of-mass contribution to the wave function may be approximated by a plane wave with wave vector $\vec{k}$:

$$\psi_{CM}(\vec{r}) = e^{i\vec{k}\cdot\vec{r}}. \tag{2.26}$$

In the vicinity of the target, this plane wave will be distorted by an optical potential $U(r)$, which we take to be local and constant in time, i.e. we neglect target recoil and breakup. For a high-energy projectile, where the rate of change in the reduced Compton wavelength $\lambda\!\!\!^{-} = k^{-1}$ is small $\left|\frac{d\lambda\!\!\!^{-}}{dr}\right| \ll 1$, we can make a WKB approximation [80] and express the wave

number k as a slowly-varying function of position:

$$\begin{aligned} k(r) &= \sqrt{(E - U(r))^2 - m^2} \\ &\approx k_\infty - \frac{k_\infty U(r)}{2E_k}, \end{aligned} \tag{2.27}$$

where E is the total energy at $r \to \infty$, $E_k = E - m$ is the kinetic energy, and $k_\infty = \sqrt{E^2 - m^2}$. For the second line I have taken $U(r) \ll E_k \ll m$, which is reasonable for the values $U(r) \lesssim 50$ MeV [21], $E_k \sim 100$ MeV/u, $m \sim 1$ GeV/u.

If we assume that the optical potential can be approximated by a Woods-Saxon shape, with depth U_0 and diffuseness a_0, we can estimate $\frac{dU}{dr} \leq \frac{U_0}{4a_0}$ and

$$\frac{d\lambda\!\!\!^{-}}{dr} \lesssim \frac{\lambda\!\!\!^{-}_\infty}{(1 - \frac{U}{2E_k})^2} \frac{1}{2E_k} \frac{U_0}{4a_0}. \tag{2.28}$$

Using typical values of $U_0 = 50$ MeV and a_0=0.7 fm, with a beam energy of 100 MeV/u, this amounts to $k_\infty \gg 30$ MeV for a single nucleon. At 100 MeV/u, $k_\infty \sim 400$ MeV, so the WKB approximation is reasonable.

With the approximation (2.27), and assuming an azimuthally symmetric potential, the center-of-mass wave function in (2.25) becomes

$$\psi_{CM}(R) = e^{ik_\infty z} e^{i\chi(b,z)}, \tag{2.29}$$

where the *eikonal phase* $\chi(b, z)$ is defined as

$$\chi(b, z) = -\frac{k_\infty}{2E_k} \int_{-\infty}^{z} U(b, z) dz. \tag{2.30}$$

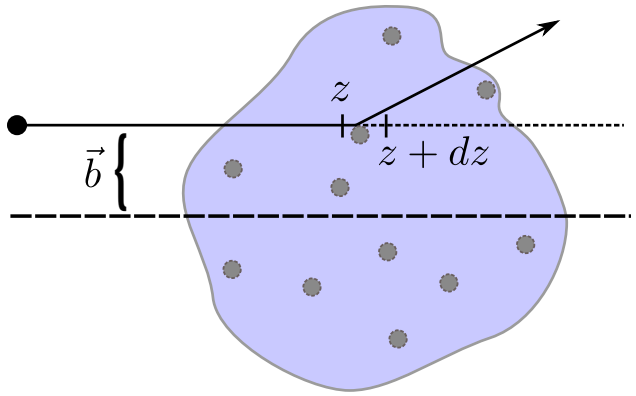

Figure 2.5: Schematic depicting a projectile nucleon scattering off of a single target nucleon.

With this we identify the elastic S-matrix (not to be confused with the spectroscopic factor of the previous section) in the eikonal limit:

$$\mathcal{S}(b) = e^{i\chi(b,+\infty)}. \tag{2.31}$$

For a real potential, $|\mathcal{S}(b)|^2 = 1$ and integrating over all impact parameters gives the far-field angular distribution for elastic scattering (see for example [81]). For a complex potential, $|\mathcal{S}(b)|^2$ may be less than 1, representing the loss of flux to other channels, such as nucleon transfer, inelastic excitation, or breakup.

2.3.3 Generating the optical potential

It is desirable to be able to generate the optical potential $U(r)$ for an arbitrary core-target-valence combination. In this section, I make a heuristic derivation of the potential which reproduces the first-order result from a more rigorous consideration [82]. First, as sketched in Figure 2.5, we consider a projectile nucleon incident on a nucleus, which is treated as a collection of scattering centers (i.e. other nucleons) with density ρ_t. The probability $dP(z)$ that the nucleon with impact parameter $\vec{b} = (b, \phi)$ will interact and scatter within a

infinitesimal path length between z and $z + dz$ is given by the probability $(1 - P(z))$ that it has not scattered up until z, multiplied by the nucleon-nucleon scattering cross section σ_{NN}, times the areal density of scattering centers $\rho_t(\vec{b}, z)dz$:

$$dP(\vec{b}, z) = \Big(1 - P(\vec{b}, z)\Big)\, \sigma_{NN} \rho_t(\vec{b}, z) dz. \tag{2.32}$$

Assuming $P(z = -\infty) = 0$, we integrate (2.32) to get

$$1 - P(\vec{b}, z) = \exp\left[-\sigma_{NN} \int_{-\infty}^{z} \rho_t(\vec{b}, z) dz\right]. \tag{2.33}$$

The quantity $1 - P(\vec{b}, z)$, the probability for the nucleon to survive up to z, may be identified as the modulus squared of the elastic S-matrix $\left|\mathcal{S}(\vec{b}, z)\right|^2$. Consulting (2.31), the imaginary part of the eikonal phase is then

$$\mathrm{Im}\{\chi(\vec{b})\} = \frac{1}{2}\sigma_{NN} \int_{-\infty}^{\infty} dz \rho_t(\vec{b}, z), \tag{2.34}$$

which suggests a corresponding imaginary part of the nucleon-nucleus optical potential

$$\mathrm{Im}\{U(\vec{b}, z)\} = \frac{-E_k \sigma_{NN}}{k_\infty} \rho_t(\vec{b}, z). \tag{2.35}$$

This may be extended to nucleus-nucleus scattering by integrating this potential over the projectile nucleon density ρ_p, yielding the imaginary part of the folded nucleus-nucleus optical potential:

$$\mathrm{Im}\{U(\vec{b}, z)\} = \frac{-E_k \sigma_{NN}}{k_\infty} \int d^3 r \rho_t(\vec{r}) \rho_p(\vec{r} - \vec{R}(\vec{b}, z)) \tag{2.36}$$

where $\vec{R}(\vec{b}, z)$ is the center-to-center separation of the target and projectile. This result is identical to the first-order optical potential obtained in multiple-scattering theory [82], often referred to as the $t\rho\rho$ approximation.

For the systems considered in this work, the real part of the optical potential has a relatively small effect on the resulting cross section, and we parameterize it following Ray [83] as $U_{NN} = (i - \alpha)\mathrm{Im}\{U_{NN}\}$, where $\alpha_{pn} = 1.0$ and $\alpha_{pp} = \alpha_{nn} = 1.87$ have been extracted from fits to nucleon-nucleus reaction cross section data. We also add a term to approximate the finite range of the nucleon-nucleon interaction with a Gaussian (this also has a small effect the cross section) and the full optical potential becomes:

$$U_{NN}(b,z) = (i-\alpha)\frac{-ik_\infty \sigma_{rNN}}{2E_\infty}\int d^3r_p d^3r_t \rho_t(\vec{r_t})\rho_p(\vec{r_p})\exp\left[-\frac{(\vec{r_t}-\vec{r_p}-\vec{R}(b,z))^2}{\gamma^2}\right]. \tag{2.37}$$

We take $\gamma_{np} = \gamma_{nn} = \gamma_{pp} = 0.5$ fm, as in [84].

2.3.4 Densities and form factors

The next ingredient is to calculate the target and core densities (the valence density is a delta function, since nucleons are treated as point particles). We calculate the core density using Skyrme Hartree-Fock, which is described in §2.2.2. An example is shown for ^{35}Si in Figure 2.6a, calculated using the Skx Skyrme parameter set [85]. For the ^{9}Be target, we assume a Gaussian density with rms radius 2.36 fm for all calculations, for consistency with previous studies. Using instead the results of a quantum Monte Carlo calculation [86] or Hartree-Fock results in a change in the relative importance in the stripping and diffraction mechanisms at the order of 5-10%, but the overall single-particle cross sections only change on the order of 1-2%.

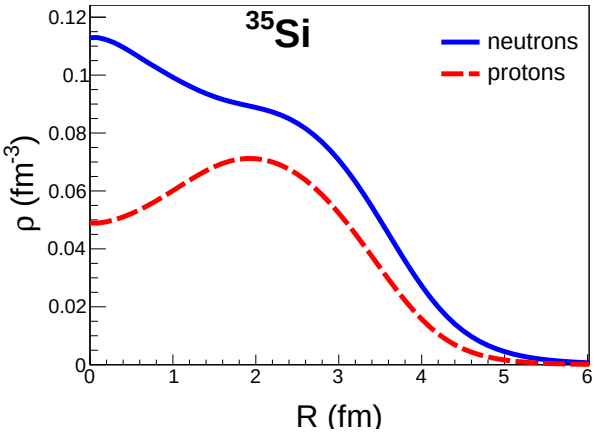

(a) core density

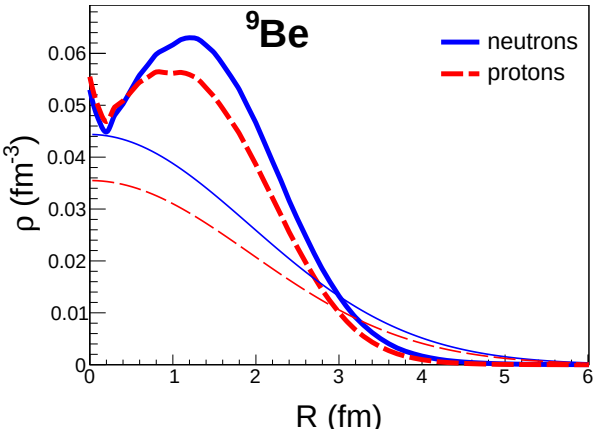

(b) target density

Figure 2.6: Calculated proton and neutron densities for (a) a ^{35}Si core, calculated with Skyrme Hartree-Fock, and (b) a ^{9}Be target, from quantum Monte Carlo calculations. The oscillations at small R for the QMC calculation are statistical. The thin lines show the Gaussian densities used for the target in this work.

Finally, we need the core-valence two-body wave function, or *form factor* $\phi(r)$. It was shown in [12] that the calculated cross section depends strongly on the rms (root-mean-squared) radius of the two-body wave function, and so it is important to have a consistent way to determine this component of the calculation. The adopted method, proposed in [12], utilizes the so-called *well-depth* prescription. The wave function is take to be the solution to the Schrödinger equation for a particle in a real Woods-Saxon potential of the form

$$V(r) = -V_0 f_{\rm ws}(r) + (\ell \cdot s)\ V_{LS} \frac{d}{dr} f_{\rm ws}(r) \tag{2.38}$$

$$f_{\rm ws}(r) = \frac{1}{1 + e^{(r-r_0)/a_0}}. \tag{2.39}$$

It then remains to choose the parameters V_0, V_{LS}, r_0, a_0. It was shown in [12] that the resulting cross section is relatively insensitive to the diffuseness a_0, so this is fixed at 0.7 fm. For the same reason, the spin-orbit depth V_{LS} is fixed to 6 MeV. We are left with two parameters, the depth V_0 and radius r_0, which are fixed in a two-step procedure. We

first adjust both parameters to simultaneously reproduce the binding energy and rms radius of the single-particle orbit obtained with a Skyrme Hartree-Fock calculation. Then, as the asymptotic form of the wave function must be an exponential with the decay constant determined by the binding energy, we adjust V_0 with r_0 held fixed to match the experimental binding energy $E_f - E_i$. The results of this procedure for neutron orbits in ^{36}Si are shown in Figure 2.7. Note that for the fully-occupied orbits $1s_{1/2}$, $0d_{3/2}$, shown in 2.7a and 2.7b, the Woods-Saxon potential is similar to optical potentials used in this mass region [21]. For the partially occupied $f_{7/2}$ orbit (Figure 2.7c), and especially for the weakly-occupied $p_{3/2}$ orbit (Figure 2.7d), which lies above the Fermi surface in the Hartree-Fock calculation, the depth of the potential is significantly greater. This reflects the fact that, for these orbits, correlations beyond the mean field play a significant role in the binding, and therefore an unrealistic mean field is required to reproduce the experimental binding energy. The proper treatment of the form factor for such orbits is an old problem which, as yet, has no satisfactory solution [87, 88, 89].

As a measure of the impact of this issue on the resulting cross sections, we consider the effect of using different prescriptions. Instead of adjusting the depth of the potential, V_0, to reproduce the experimental binding energy, we adjust either the radius parameter r_0 (referred to here as the ΔR prescription) or the spin-orbit depth V_{LS} (SO prescription). The results of these calculations are given in Table 2.2, for the $f_{7/2}$ and $p_{3/2}$ neutron orbits in ^{36}Si. Noting that the $p_{3/2}$ orbit requires an unnaturally large well depth to reproduce the Hartree-Fock calculation, we also perform the calculations starting with the more typical parameters V_0=55 MeV, r_0=1.2 fm, and V_{LS}=6.0 MeV, and adjust one of the parameters to reproduce the experimental binding energy. These calculations are indicated in Table 2.2 with a primed label.

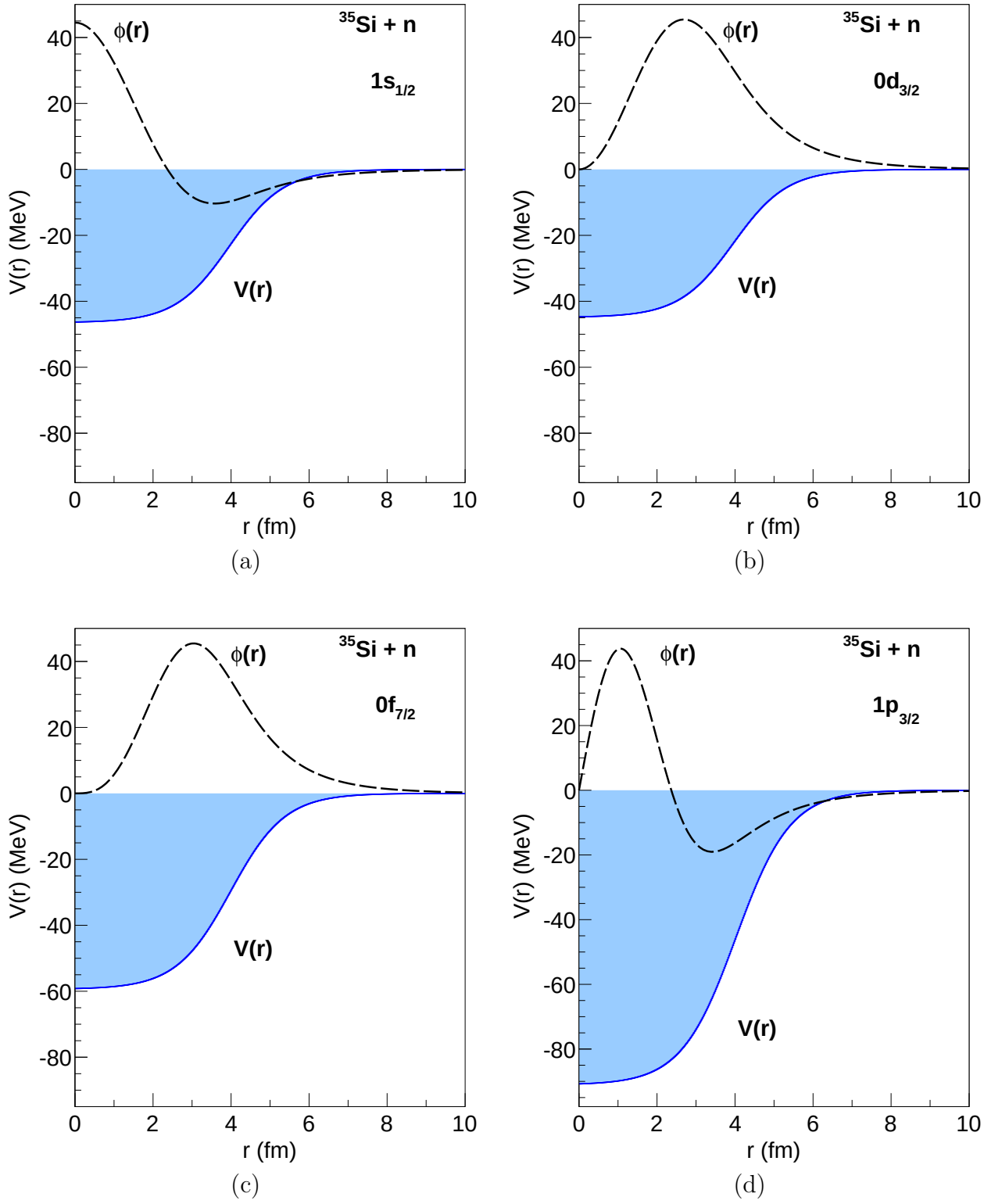

Figure 2.7: Core-valence wave functions (dashed lines) for neutron orbits near the Fermi surface in ^{36}Si, calculated with the well-depth prescription, shown with their corresponding Woods-Saxon potentials (filled blue curves).

Table 2.2: Results for the two-body core-valence wave function for ^{35}Si+n, using several prescriptions for determining the Woods-Saxon parameters: Hartree-Fock (HF), well-depth (WD), changing the radius (ΔR), and changing the spin-orbit depth (SO). Primed prescription labels indicate a starting point of V_0=55, r_0=1.2, and V_{LS}=6.0, instead of the Hartree-Fock result. Energies are in MeV, radii are in fm, and cross sections are in mb.

orbit	prescription	V_0	r_0	V_{LS}	BE	$< r_{rel}^2 >^{1/2}$	σ_{sp}
$f_{7/2}$	HF	54.2	1.191	6.0	3.348	4.06	19.4
	WD	59.4	1.191	6.0	6.129	3.87	15.5
	ΔR	54.2	1.256	6.0	6.129	4.02	17.9
	SO	54.2	1.191	12.6	6.129	3.94	16.5
$p_{3/2}$	HF	73.9	0.943	6.0	1.023	5.45	61.5
	WD	92.1	0.943	6.0	7.029	3.81	17.7
	ΔR	73.9	1.093	6.0	7.029	4.02	22.2
	SO	73.9	0.943	63.0	7.029	3.87	18.9
	WD$'$	64.2	1.200	6.0	7.029	4.18	26.0
	$\Delta R'$	55.0	1.331	6.0	7.029	4.37	31.2
	SO$'$	55.0	1.200	52.3	7.029	4.24	28.0

The results for the $f_{7/2}$ orbit, which is below the Fermi surface in the Hartree-Fock calculation, are only weakly sensitive to the method of perturbing the potential. The $p_{3/2}$ results, on the other hand, show a variation of greater than 50%. This indicates that the calculations of the absolute cross sections for removal from an orbit above the Fermi surface have a substantial uncertainty, owing to there not being a clear reason to believe one of these prescriptions more than another. For consistency in comparing with other work, we choose the well-depth prescription, constrained by the Hartree-Fock calculation. The hope is that while the absolute value of the calculated single-particle cross sections may have a large uncertainty for these orbits, we may still obtain insight from the evolution of the cross section along the isotopic chain. As can be seen in Figure 2.8c, the shift in the cross section between the well-depth procedure and the ΔR procedure remains constant within approximately 20% between ^{34}Si and ^{42}Si, and within approximately 10% for the isotopes studied in this work.

Obviously, these weakly occupied orbits have a relatively small impact on the inclusive cross sections. For example, the removal a neutron from any of the $1p_{3/2}$, $1p_{1/2}$, or $0f_{5/2}$ orbits of ^{36}Si is predicted to contribute a combined total of less than 5% of the inclusive cross section to bound states. It should be noted that these weakly occupied orbitals also carry a large uncertainty in the shell-model spectroscopic factor. One might be tempted to consider if this effect could contribute to the observed systematic reduction of knockout cross sections relative the theoretical predictions [12]. However, aside from the fact that this only becomes important when the spectroscopic factor is small, the behavior is qualitatively in the wrong direction: the deficient species should be deeply bound and the different prescriptions should have a relatively small impact on the radius whereas experimentally the cross section for the deficient species is strongly quenched.

2.3.5 Reaction mechanisms and cross sections

Following [74], the cross section is divided into two reaction mechanisms. The first – and more important in the removal of well-bound nucleons – is the so-called stripping mechanism. In a stripping reaction, illustrated in Figure 2.9a, the valence nucleon is absorbed by the imaginary part of the optical potential (with probability 1-$|\mathcal{S}_v|^2$), while the core survives (with probability $|\mathcal{S}_c|^2$). The cross section for this process is given by

$$\sigma_{\rm str} = \frac{1}{2J+1}\sum_m \int d^2b \left\langle \phi_0^m \left| |\mathcal{S}_c|^2 \left(1 - |\mathcal{S}_v|^2\right)\right| \phi_0^m \right\rangle , \tag{2.40}$$

where J is the projectile angular momentum, b is the core-target impact parameter, ϕ_0^m is the core-valence form factor of §2.3.4, and $\mathcal{S}_c$ and $\mathcal{S}_v$ are evaluated at their respective positions.

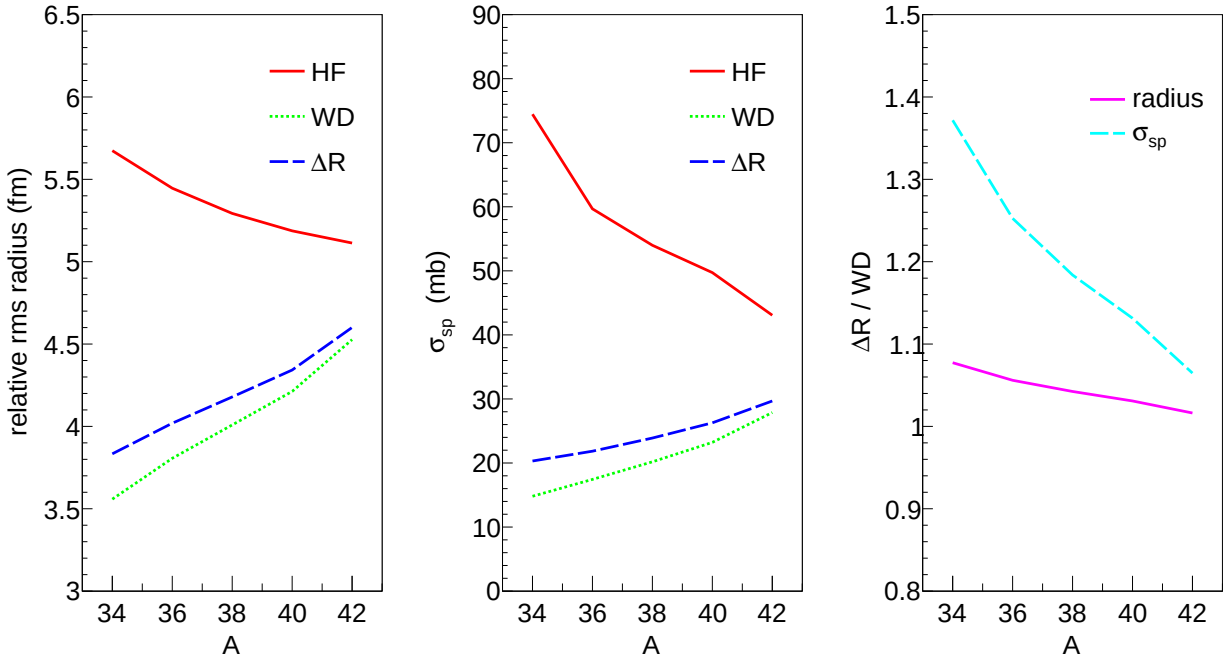

Figure 2.8: Results of three different prescriptions for obtaining the two-body wave function (see text for details) for the $1p_{3/2}$ orbit in silicon isotopes $^{34-42}$Si. (a) Rms relative radii (b) single particle cross sections (c) the ratio between results for the well-depth prescription (WD) and the potential radius prescription (ΔR).

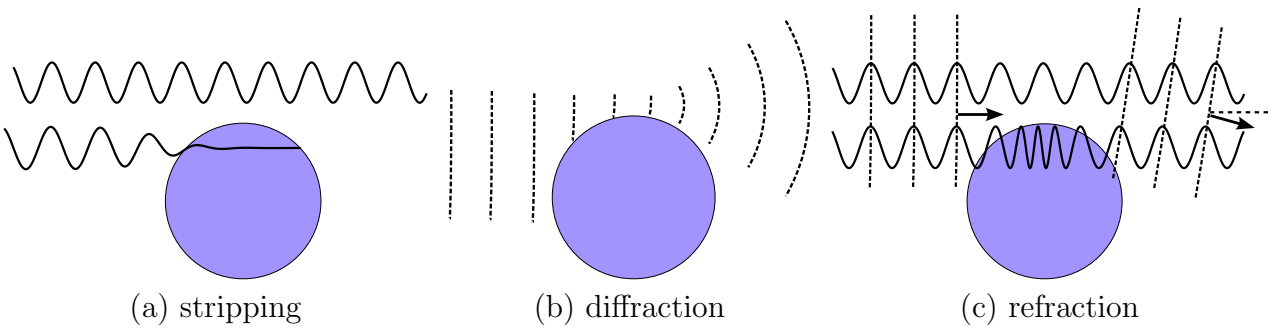

Figure 2.9: Illustrations of the three reaction mechanisms which contribute to the knockout cross section.

The second mechanism is actually composed of two processes: diffraction due to the absorptive imaginary part of the potential, shown in Figure 2.9b, and refraction due to the real part of the potential, shown in Figure 2.9c. These mechanisms add coherently and are both contained in the expression

$$\sigma_{\text{diff}} = \frac{1}{2J+1} \sum_{mm'} \int d^2b \int d^3k \left| \left\langle \phi_{\vec{k}}^{m'} \left| \mathcal{S}_c \mathcal{S}_v \right| \phi_0^m \right\rangle \right|^2 . \tag{2.41}$$

This gives the probability that in the outgoing channel, due to the presence of the potential, the core and valence are in a state with relative momentum $\vec{k}$ between them, i.e. they have been excited into a continuum state. In practice, rather than integrating over all relative momentum states we use a closure relation [90].

$$\sum_{m'} \int d^3k \left| \phi_{\vec{k}}^{m'} \right\rangle \left\langle \phi_{\vec{k}}^{m'} \right| = 1 - \sum_{m'i} \left| \phi_i^{m'} \right\rangle \left\langle \phi_i^{m'} \right| \tag{2.42}$$

where i labels bound states. Inserting this into (2.41) gives

$$\sigma_{\text{diff}} = \frac{1}{2J+1} \sum_{mm'} \int d^2b \left(\left\langle \phi_0^m \left| |\mathcal{S}_c \mathcal{S}_v|^2 \right| \phi_0^m \right\rangle - \sum_i \left| \left\langle \phi_i^{m'} \left| \mathcal{S}_c \mathcal{S}_v \right| \phi_0^m \right\rangle \right|^2 \right) . \tag{2.43}$$

In this form, the cross section is given by the probability that both the core and target survive, minus the probability that they end up in a bound final state. A further approximation is made that the ground state is the only bound final state or, more generally, that $\left\langle \phi_i^{m'} \left| \mathcal{S}_c \mathcal{S}_v \right| \phi_0^m \right\rangle \approx 0$ for $i \neq 0$, which is often a reasonable assumption [76].

The two reaction mechanisms are in principle distinguishable; diffraction leaves the target in its ground state, while stripping excites the target to another state (unbound in the case of ^{9}Be). This means that they add incoherently (there is no interference) and we may assign

the single-particle cross section to be

$$\sigma_{\rm ko} = \sigma_{\rm str} + \sigma_{\rm diff}. \tag{2.44}$$

2.3.6 Momentum distributions

When the valence nucleon is removed, the knockout residue recoils with some momentum k. The probability for a particular k is given by the momentum-space core-valence wave function, which is just the Fourier transform of the position-space wave function. Note, however, that the reaction is surface-peaked, and so the valence nucleon is not removed from all parts of the position-space wave function with equal probability. We must instead weight each point in position space by the knockout probability at that point. The momentum in the transverse direction (perpendicular to the incoming beam direction) is complicated by Coulomb effects, so we instead consider the longitudinal (parallel) momentum distribution. For the case of a stripping reaction, this is given by [74]

$$\frac{d\sigma_{\rm str}}{dk_z^c} = \frac{1}{2J+1}\sum_m \int d^2b_v \left(1-|S_v|^2\right) \int d^2\rho\, |S_c|^2 \left| \int dz\ \frac{e^{-ik_z^c z}}{2\pi}\phi(\rho,z)\right|^2, \tag{2.45}$$

where b_v is the impact parameter of the valence nucleon, $(\vec{\rho}, z)$ is the vector between the core and valence nucleon, and the integration is over all space.

It is observed that the distributions for diffraction, which is also surface-peaked, have a nearly identical shape [91]. The result of applying (2.45) to neutron orbits near the Fermi surface in ^{36}Si is shown in Figure 2.10. These calculated distributions may then be compared with experimental distributions to infer the orbital angular momentum ℓ of the removed nucleon. This procedure is analogous to the angular distributions used in classical

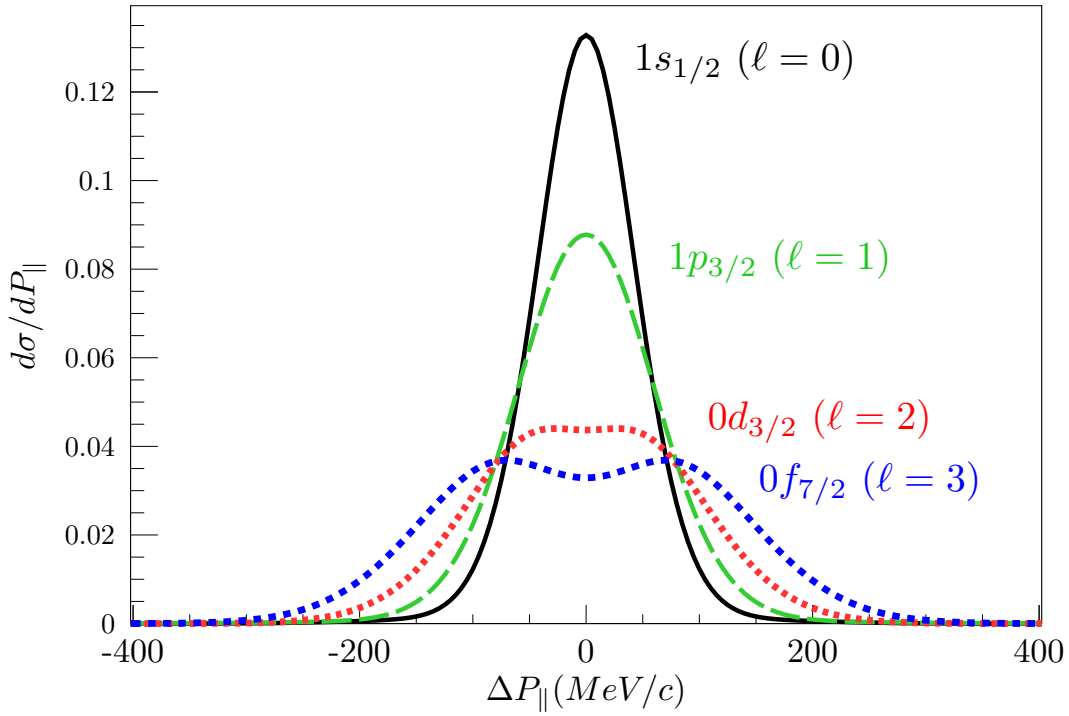

Figure 2.10: Momentum distributions calculated according to equation (2.45) for neutron removal from orbitals near the Fermi surface in ^{36}Si.

light-ion transfer reactions to infer the ℓ of the transferred nucleon [90].

Chapter 3

Experimental method and analysis

If your experiment needs statistics, you ought to have done a better experiment.
(E. Rutherford)

For the current experiment, three different secondary beams (^{36}Si, ^{38}Si, ^{40}Si) were delivered by the Coupled Cyclotron Facility and impinged upon a metallic beryllium target at the target position of the S800 spectrograph [92]. For each of these secondary beams, the rigidity of the S800 was centered on both one-neutron and one-proton knockout residues, as well as inelastically scattered beam particles. De-excitation γ rays were detected in the GRETINA array of high-purity germanium detectors [93], surrounding the target position. These systems will be detailed in the following sections.

3.1 Radioactive beam production

The silicon isotopes ^{36,38,40}Si are unstable to β decay, all having mean lifetimes of less than 1 second [94, 95, 96]. The production of beams of these nuclides was achieved by in-flight fragmentation of a stable beam of ^{48}Ca. The process begins with a block of metallic ^{48}Ca which is heated in an oven to produce a vapor. These neutral atoms are then ionized via electron cyclotron resonance (ECR), in which electrons – confined by a magnetic field and driven by a radio-frequency (RF) electric field – collide with the atoms and ionize them. The singly or double ionized atoms are injected into the K500 cyclotron (see the schematic

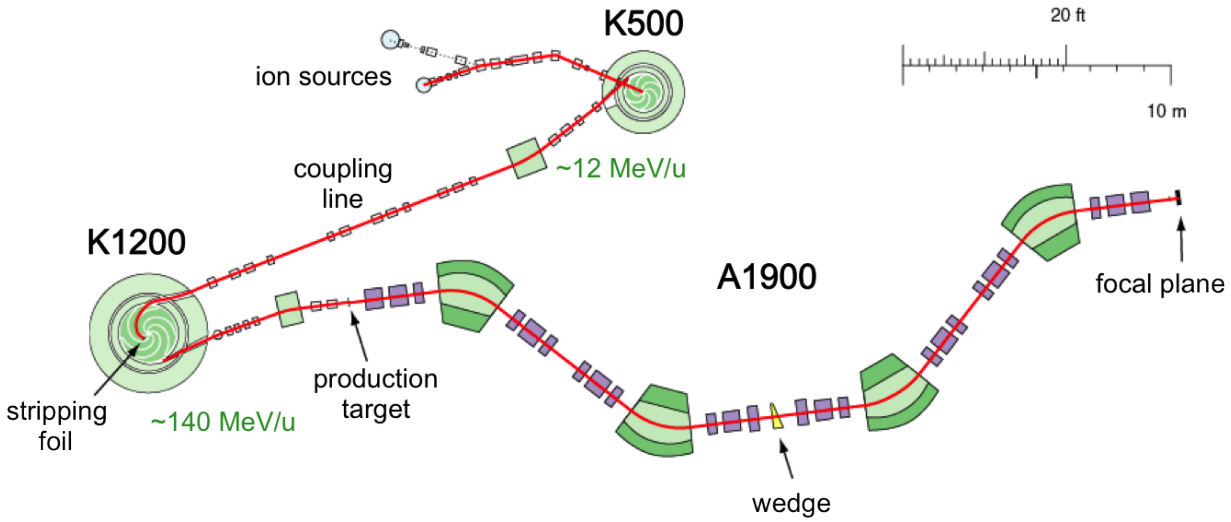

Figure 3.1: A schematic of the beam production at the Coupled Cyclotron Facility.

in Figure 3.1).

A particle with charge q, mass m, and momentum p moving in a uniform magnetic field B will trace out a circle of radius ρ at frequency ω_c given by

$$\rho = \frac{p}{qB} \quad , \qquad \omega_c = \frac{qB}{\gamma m}, \tag{3.1}$$

where γ is the relativistic factor (see appendix B). A cyclotron confines a charged particle with a uniform magnetic field and accelerates it with an RF electric field tuned to the cyclotron frequency ω_c. As the particle's momentum increases, so does its radius of orbit, according to (3.1), until it is extracted at the outer edge of the cyclotron.

Ions are accelerated up to approximately 15% of the speed of light in the K500 cyclotron and then extracted and transported to the K1200 cyclotron[1] where they are accelerated further. Note that, according to (3.1), the momentum of a particle leaving a cyclotron is $p = qB\rho$, so we may increase the final energy by increasing the charge of the particle,

[1]The K500 and K1200 cyclotrons are so named because they can accelerate a proton up to 500 MeV and 1200 MeV, respectively.

increasing the strength of the magnetic field, or increasing the size of the cyclotron. The size and magnetic field of the cyclotron are not easily increased, but we may increase the charge q by further ionizing the particle. A carbon stripper foil is placed in the center of the K1200 cyclotron to do this (in the case of ^{48}Ca, the beam becomes fully ionized), and the primary beam leaves the K1200 at approximately 50% of the speed of light.

The beam is then impinged on a thick beryllium target, producing a cocktail of secondary beam particles by fragmentation. The secondary beam of interest is selected from the rest of the fragmentation products by the so-called $B\rho - \Delta E - B\rho$ method using the A1900 fragment separator [97].

The quantity $B\rho = \frac{p}{q}$ is called the magnetic rigidity, and is useful for particle separation, as it depends on the (presumably) fixed radius of curvature of a beam line element and the adjustable magnetic field at that element. Fragmentation reactions at this energy approximately conserve energy (and momentum) per nucleon, and so – assuming the fragmentation products are fully-stripped, which is generally the case for light and medium-mass nuclei – selecting on $\frac{p}{q}$ is equivalent to selecting on $\frac{A}{Z}$. This selection is achieved with slits which only allow ions with a small range of radii of curvature ρ to pass. Next the beam is passed through an aluminum foil (called a wedge[2]) which causes the beam to lose energy from collisions with atomic electrons. The energy loss of a charged particle in matter due to collisions with electrons is given by the Bethe formula [98]

$$-\frac{dE}{dx} = \frac{4\pi e^4 n_e Z^2}{m_e \beta^2}\left[\log\left(\frac{2m_e\gamma^2\beta^2}{I}\right) - \beta^2\right], \tag{3.2}$$

where e is the electron charge, n_e is the target electron density, Z is the atomic number of

[2]The "wedge" is actually a flat piece of aluminum which is bent so as to achieve the desired effective thickness as a function of transverse position.

the projectile, m_e is the electron mass, β is the projectile velocity, γ is the relativistic factor, and I is the ionization potential of the target material. Assuming a constant beam velocity β, the energy loss for a given degrader material depends only on Z, and the outgoing beam is left with a momentum $p(Z)$ which depends on the atomic number. By passing the beam through another $B\rho$ filter, a particular A,Z combination may be selected and delivered to the experiment. For more details on radioactive beam production, see [99].

3.2 The S800 spectrograph

The beam delivered from the A1900 was then impinged on a thinner ^{9}Be reaction target located at the target position of the S800 spectrograph (see the schematic in Figure 3.2), and this is where the reactions of interest took place. Projectile-like reaction residues leaving the target were bent by the two dipole magnets of the S800 and were detected in the focal plane. The focal plane, shown in Figure 3.3, consists of two cathode-readout drift counters (CRDCs) to detect the trajectory of the particle, a gas-filled ionization chamber to measure energy loss for particle identification, and a scintillator used to trigger the system. Two additional scintillators, located at the extended focal plane (XFP) of the A1900 and at the object (OBJ) position of the S800 analysis line are used for time-of-flight (TOF) information. These detector systems and their analysis are discussed in the following sections.

3.2.1 Particle trajectories

The S800 focal plane uses two CRDCs to measure the trajectory of the reaction residue. The CRDCs are gas-filled position-sensitive detectors separated by approximately 1 m. Knowledge of the particle's coordinates (x, y) at both of the CRDCs determines the position

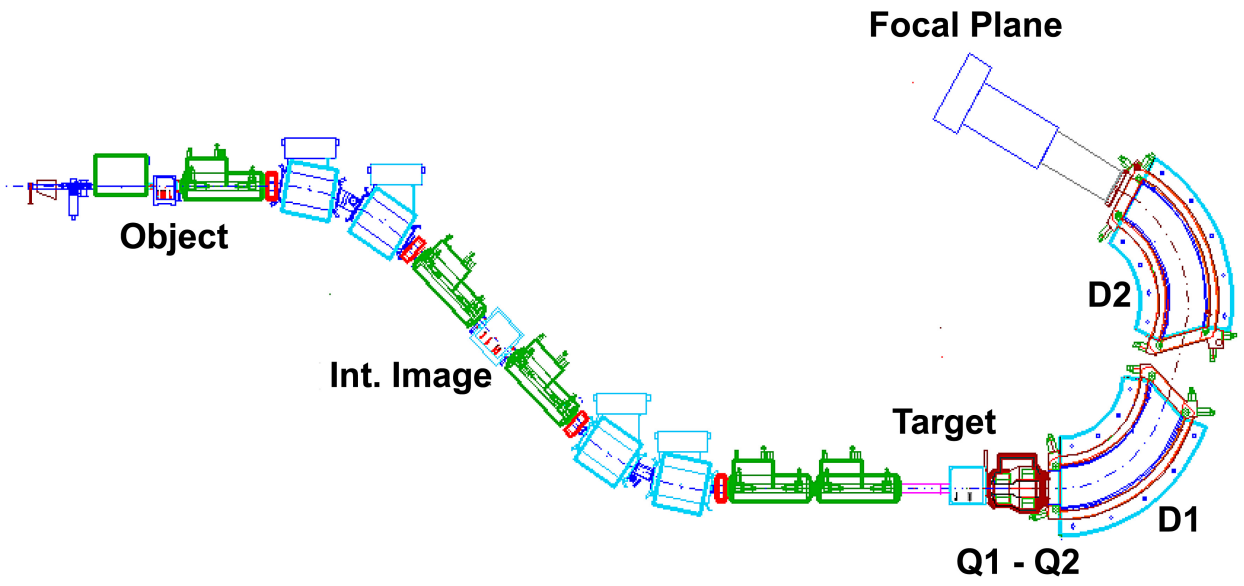

Figure 3.2: A schematic of the S800 spectrograph. The secondary beam enters from the left side and reacts at the target position. The reaction residues are detected in the focal plane.

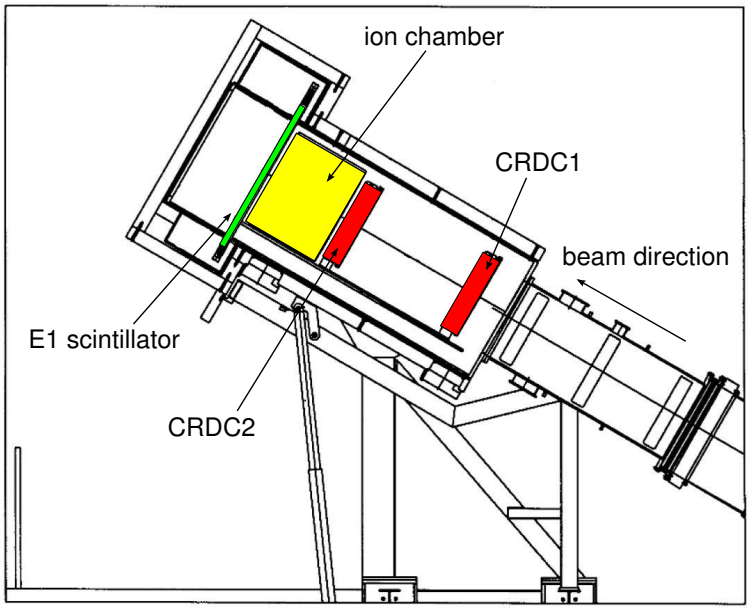

Figure 3.3: A schematic of the S800 focal plane. Taken from [6], modified from [7]. The CRDCs are separated by about one meter.

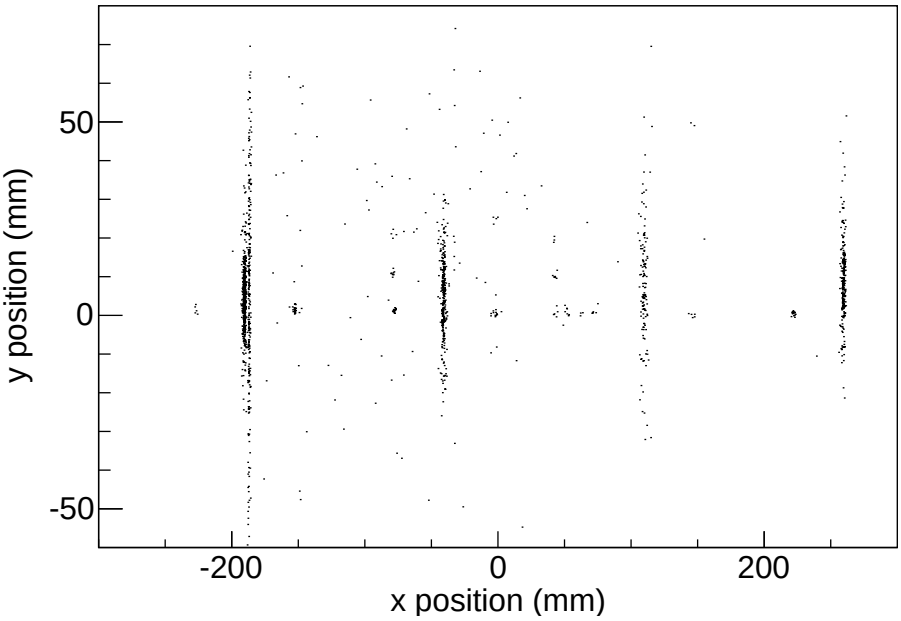

Figure 3.4: Calibrated CRDC1 x and y positions for a mask run. The calibration is performed using the known locations of the slits and pinholes in the mask.

(xfp, yfp) and angle (afp, bfp) at the focal plane. Here, afp is the angle in the dispersive (x) direction, and bfp is the angle in the non-dispersive (y) direction. The angle and energy at the target position can be obtained by the use of an inverse map which describes the trajectory of a charged-particle passing through the magnetic field of the S800. The CRDC x position is obtained by the cathode segment which collects the most charge following ionization of the fill gas, and requires trivial calibration. The y position is obtained by the drift time of that charge, and is calibrated with a mask which has holes at known positions. An example of one such mask calibration is shown in Figure 3.4.

An inverse-map generated with COSY Infinity [100] allows the conversion of the focal-plane parameters (xfp, yfp, afp, bfp) to the target parameters (dta, yta, ata, bta) – the x position at the target is assumed to be zero. The parameter dta is the difference between the energy of the particle and the energy of a particle that would arrive at the center of the focal

plane. The direction of the incoming beam may not perfectly coincide with the $\hat{z}$ direction in the S800 coordinates, so a correction is applied to *ata* and *bta* such that the distributions are centered at zero. With the four target parameters and the rigidity $B\rho$ of the S800, we may calculate the energy-momentum 4-vector of the outgoing particle (see appendix B).

3.2.2 Time-of flight

Particles which arrive in the focal plane of the S800 have been selected for rigidity $B\rho = \frac{p}{q}$, and so for a given q, the mass M of the fragment is inversely proportional to its velocity, and thus proportional to its time of flight, assuming a fixed path length. The experimental setup consists of three timing scintillators, the XFP scintillator at the end of the A1900, the OBJ scintillator at the object position of the S800 analysis line, and the E1 scintillator at the back of the S800 focal plane, which is used to trigger the readout of the S800 detector systems. This setup yields two time differences, which we take relative to the E1 scintillator. The difference between the XFP time and the OBJ time is proportional to the mass of the incoming particle, while the OBJ-E1 time difference is sensitive to the mass of the outgoing particle. The flight path through the S800 depends on the angle and momentum of the particle, so the OBJ time of flight must be corrected for these quantities, yielding a corrected time of flight OBJC. In practice, this correlation is corrected by removing the linear dependence of OBJ on the x position and angle at the focal plane of the S800.

$$\text{OBJC} = \text{OBJ} + C_1 \times xfp + C_2 \times afp \tag{3.3}$$

This correction is demonstrated in Figure 3.5.

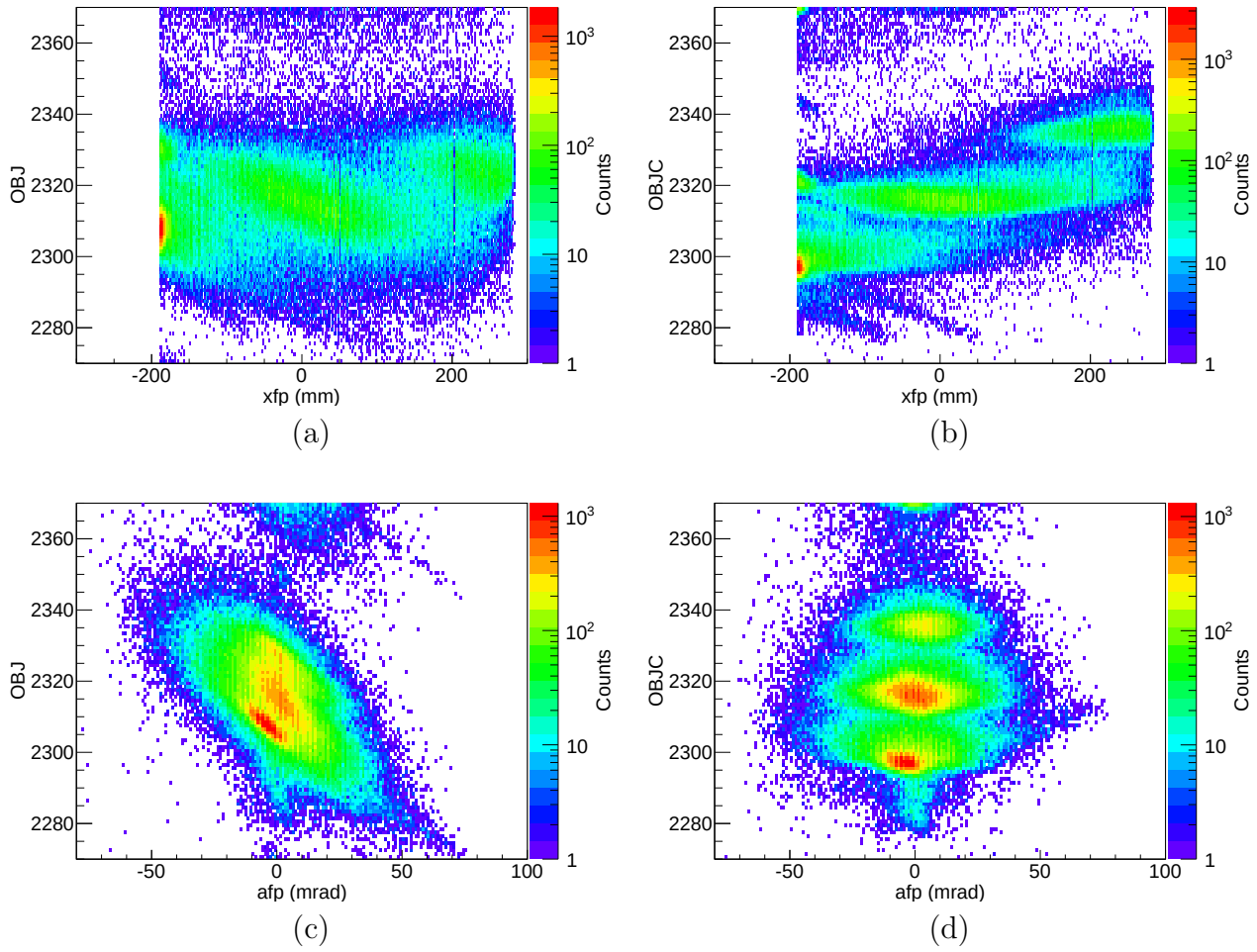

Figure 3.5: (a) Time of flight parameter OBJ vs x position in the focal plane of the S800 for the 1n knockout setting from ^{38}Si. (b) Corrected time of flight parameter OBJC vs x. (c) OBJ vs angle afp in the dispersive direction, and (d) OBJC vs afp.

3.2.3 Energy loss and particle-identification

As discussed in §3.1, the energy loss through matter is given by (3.2) and depends quadratically on the atomic number Z_p of the projectile. For two different nuclides in a beam, the only parameters which are different are Z_p and β. Assuming β is very similar for similar mass projectiles, we may discriminate Z_p by the energy deposited in the ionization chamber. The energy loss through the ionization chamber also depends on the path length of the projectile, and so the energy loss is usually corrected for the position x in the focal plane of the S800. However, in the current experiment with $Z \sim 14$, this correction is unnecessary to obtain clear separation in Z. Combining the Z discrimination with mass discrimination from time-of-flight, we can obtain a particle identification (PID) plot. The particle identification plots used for the current work are shown in Figure 3.6.

Some additional gates were used in the case of ^{35}Si and ^{37}Si. In ^{35}Si, there is a significant contamination from scattered unreacted beam which makes separation of ^{35}Si more difficult (see Figure 3.7a). This scattered beam originates in a source close to the focal plane and so its x position and angle in the focal plane are strongly correlated, as can be seen in Figure 3.7b. These structures in the x vs angle plot are gated out (see Figure 3.7d), yielding a cleaner separation, shown in Figure 3.7c. Similar cuts are made for ^{37}Si, requiring $x > -190$ in the focal plane to cut out some of the unreacted beam, and $afp - 0.18xfp < 50$ to remove scattered beam particles. These cuts result in a change of less than 1% in the total counts inside the PID gate, but they allow a clearer separation, as demonstrated in Figure 3.7.

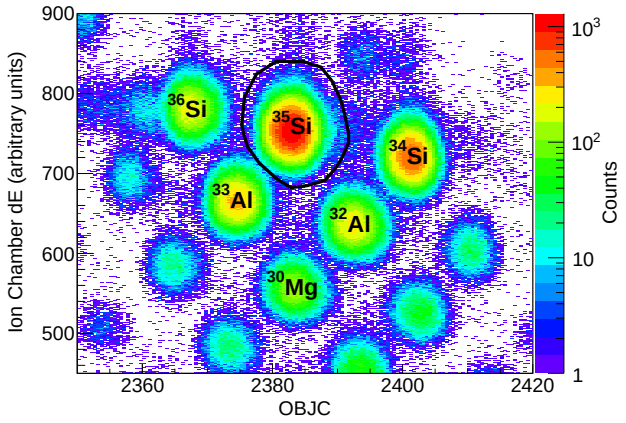

(a) ^{36}Si one neutron knockout setting.

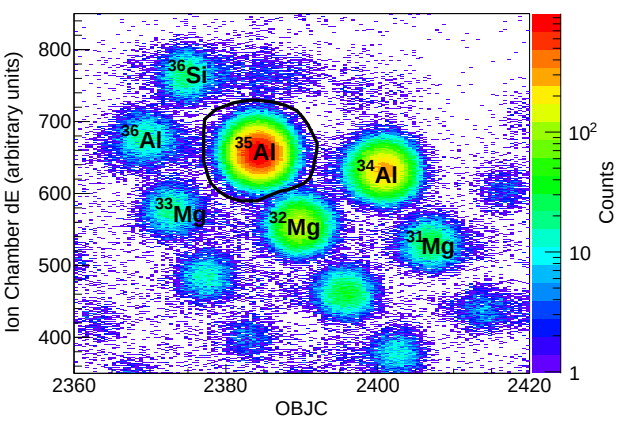

(b) ^{36}Si one proton knockout setting.

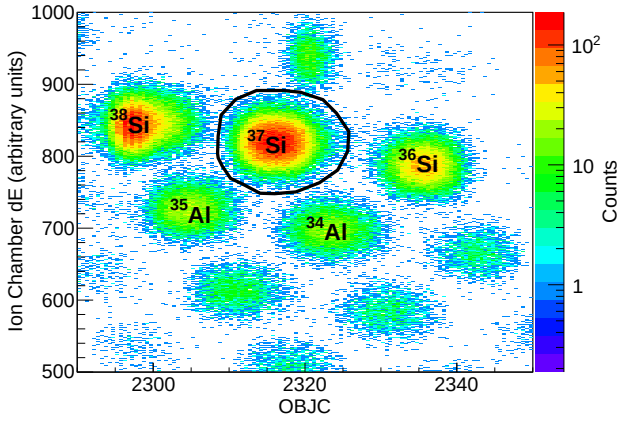

(c) ^{38}Si one neutron knockout setting.

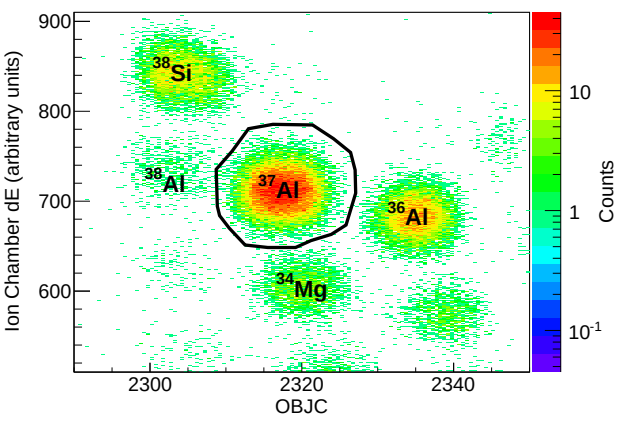

(d) ^{38}Si one proton knockout setting.

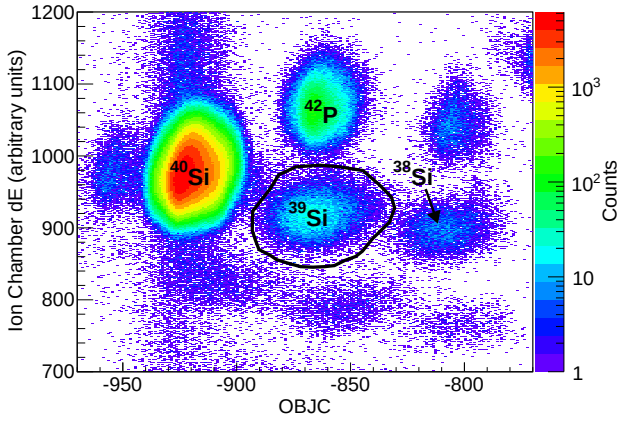

(e) ^{40}Si one neutron knockout setting.

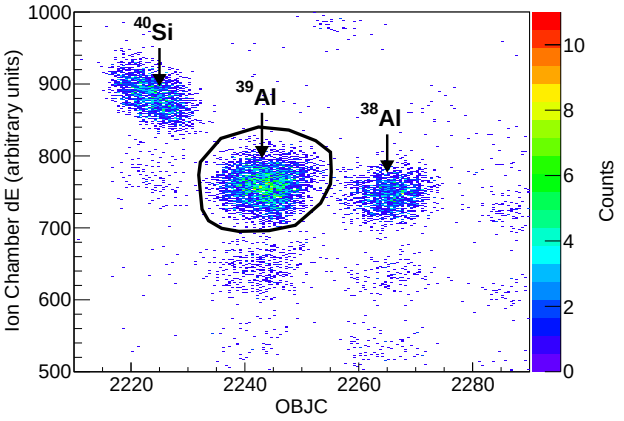

(f) ^{40}Si one proton knockout setting.

Figure 3.6: Particle identification plots for each setting, with the gate on the knockout residue.

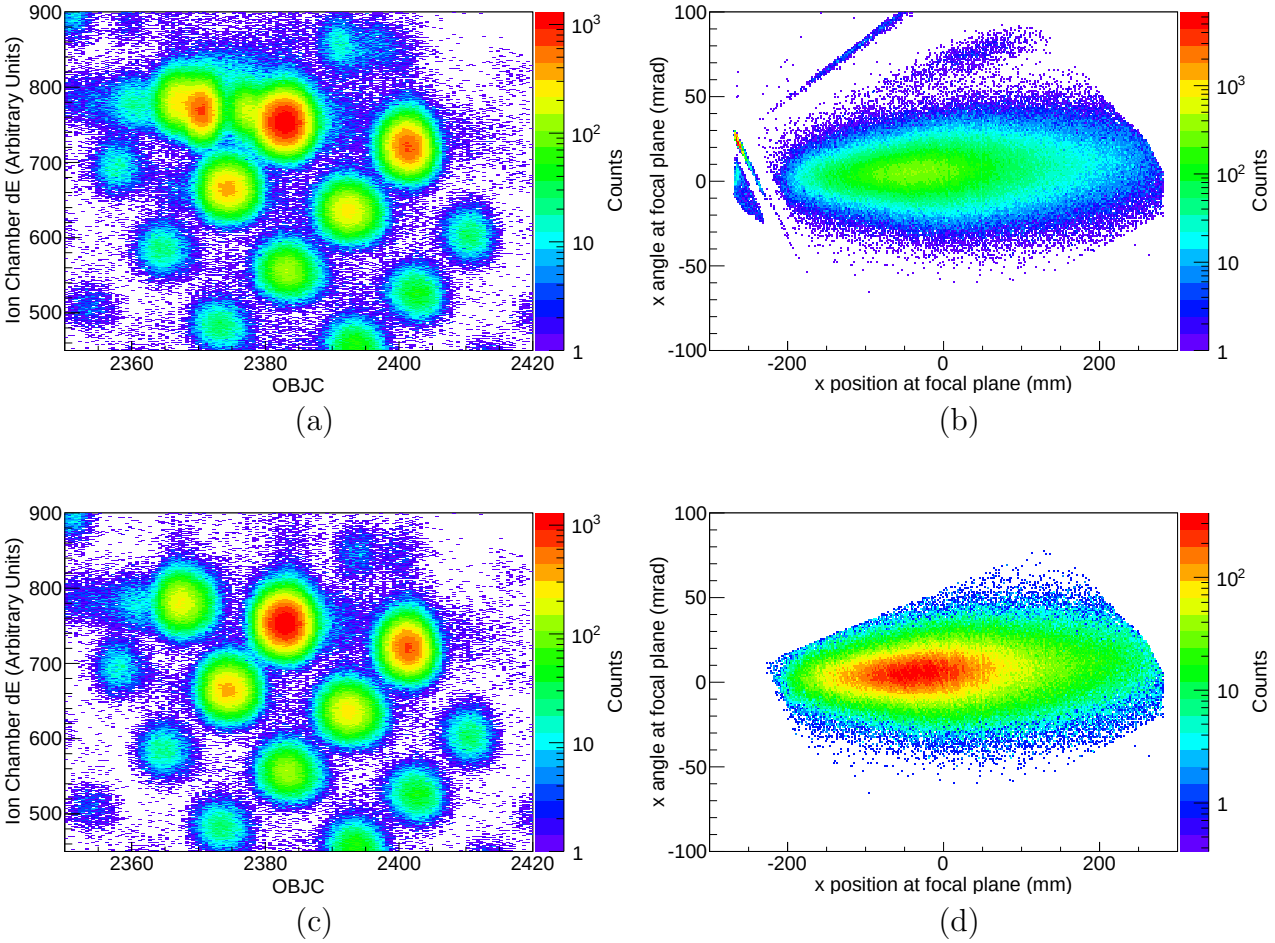

Figure 3.7: Additional gates used to improve particle identification for ^{35}Si. (a) The PID gated on incoming ^{36}Si shows poor separation between ^{35}Si (the strongest blob) and ^{36}Si, lying to the left. (b) Dispersive angle in the focal plane vs dispersive position in the focal plane gated on the ^{35}Si PID blob, showing structures due to scattering of unreacted beam. (c) PID resulting from cuts applied to (b) producing a much cleaner separation. (d) The result of those cuts in angle vs position, again gated on the ^{35}Si blob.

(a) (b)

Figure 3.8: The retracted northern (a) and southern (b) hemispheres of the GRETINA array. When the array is in use, the two hemispheres are joined and the detectors surround the target position. Images courtesy of S. Noji.

3.3 The GRETINA array

Prompt γ-rays were detected in the Gamma Ray Energy Tracking In-beam Nuclear Array (GRETINA) [93], which in this experiment consisted of 7 modules, each containing 4 high purity germanium (HPGe) crystals. The configuration of these modules is shown in Figure 3.9. The GRETINA array and the experimental details of γ-ray detection for this experiment are detailed in the following sections.

3.3.1 Doppler reconstruction

Prompt γ rays are emitted in flight by the projectile, which is moving at a velocity $v/c \approx 0.4$. This causes the energy of the γ rays in the lab frame to be Doppler shifted as a function of angle (see appendix B):

$$E_{LAB} = \frac{\sqrt{1-\beta^2}}{1-\beta\cos\theta_{LAB}} E_{CM} \tag{3.4}$$

The physical quantity of interest is the energy of the transition in the rest frame of the projectile. In order to extract this from the measured energy, we must also know the velocity of the beam and the angle of the emitted γ ray with respect to the beam's trajectory. For each reaction setting, the centroid reconstruction velocity β was chosen to align the strongest peaks at forward and backward angles. The velocity was then corrected event-by-event using the (after-target) beam velocity measured by the S800 spectrograph. The angle of emission can be reconstructed if we know the origin (assumed to be the center of the target) and the point of the first interaction. In this experiment, the GRETINA array consisted of seven modules containing four HPGe crystals each. The crystals are further electronically segmented into 36 segments. In order to maximize the position resolution of the array, digital pulse-shape analysis is employed to obtain sub-segment resolution.

3.3.2 Sub-segment position resolution

When a γ ray interacts with a germanium detector – by Compton scattering, photoabsorption, or pair production – electron-hole pairs are created and drift in opposite directions under the influence of the high voltage [98]. The moving charges induce a current on the detector electrodes, and this is read out as the signal. If the charge is collected on an electrode, there will be a net current measured on the electrode. However, if the charge is collected on

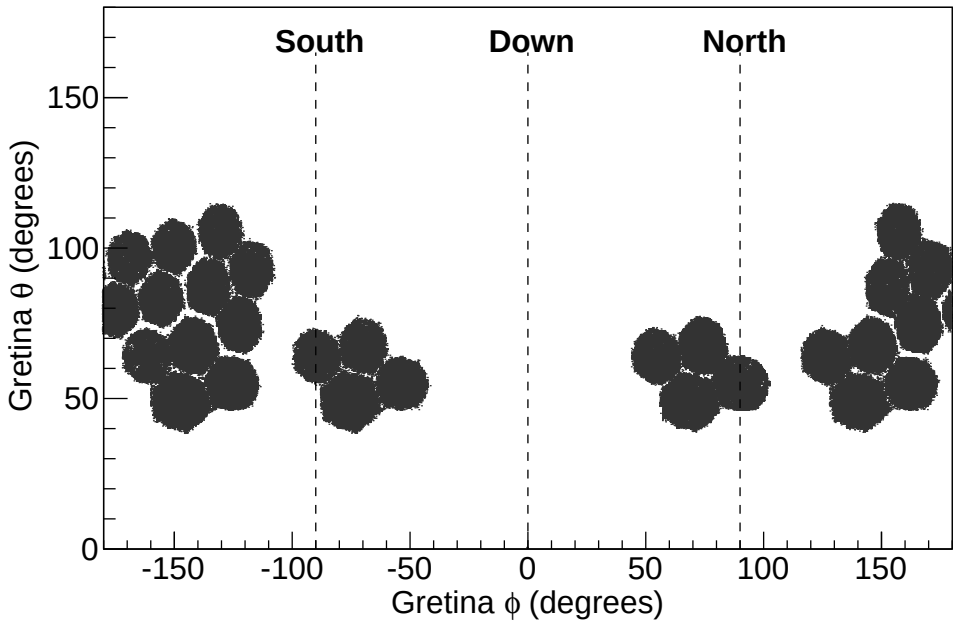

Figure 3.9: A demonstration of the angular coverage of GRETINA. Four modules were positioned in a ring at $\theta \approx 55°$, and the remaining three modules were placed at $\theta \approx 90°$.

the electrode of a nearby segment, there is no net current. The magnitude of the induced charge depends on the proximity of the electrode to the drifting charge, so by comparing the magnitude of the induced charge in two segments adjacent to a segment with net charge collection we may obtain information about the spacial origin of the charge within the segment. Simple algorithms for doing so are detailed in Appendix A, with application to the Segmented Germanium Array (SeGA) [101].

The GRETINA array employs a more sophisticated method to obtain sub-segment position resolution. Instead of the simple interpolation algorithms described in Appendix A, each event is compared to a stored basis of signals, which correspond to a mesh of single interaction points. These basis signals, unique to each interaction point, are calculated from electrostatics using the detector geometry. A χ^2 minimization procedure is used to find the best-fit interaction point. This procedure, called *decomposition*, also allows for the possibil-

ity of more than one interaction within a single segment. In the case that only one segment fires, up to three interactions are allowed to be placed in a single segment. Otherwise, only two interactions are allowed in a single segment. The output of the decomposition is a list of energies and interaction points, which are then stored with the event.

In order to obtain the emitted γ-ray energy E_{CM} of 3.4, one needs to know the angle of emission, which can be obtained from the point of first interaction, assuming that the γ ray originated from the target. One of the main features of GRETINA – and the future full 4π GRETA – is the ability to use all the interaction points provided by the decomposition algorithm to determine the most likely trajectory for the γ-ray using the Compton formula,

$$E'_\gamma = \frac{E_\gamma}{1 + E_\gamma/m(1 - \cos\theta)} \tag{3.5}$$

(see appendix B). In the current experiment, small inaccuracies in the basis signals used for decomposition, combined with the non-ideal detector geometry make this procedure challenging, and the benefits are outweighed by the added complexity in obtaining an absolute detection efficiency. For all the Doppler reconstructions in this work, it is simply assumed that the first interaction point is the one with the largest energy deposition. This is a reasonable assumption because, even if the first interaction deposits a small amount of energy, by (3.5), the scattering angle must be small as well, and so the error incurred by assuming the subsequent interaction point was the first one is relatively small.

All interaction points within a single crystal are assumed to originate from the same γ ray, which is also a reasonable assumption, considering the low γ-ray multiplicities seen in this work. For an improved peak-to-total ratio, an add-back procedure is used in which all adjacent crystals with an interaction are grouped into a cluster and assumed to originate

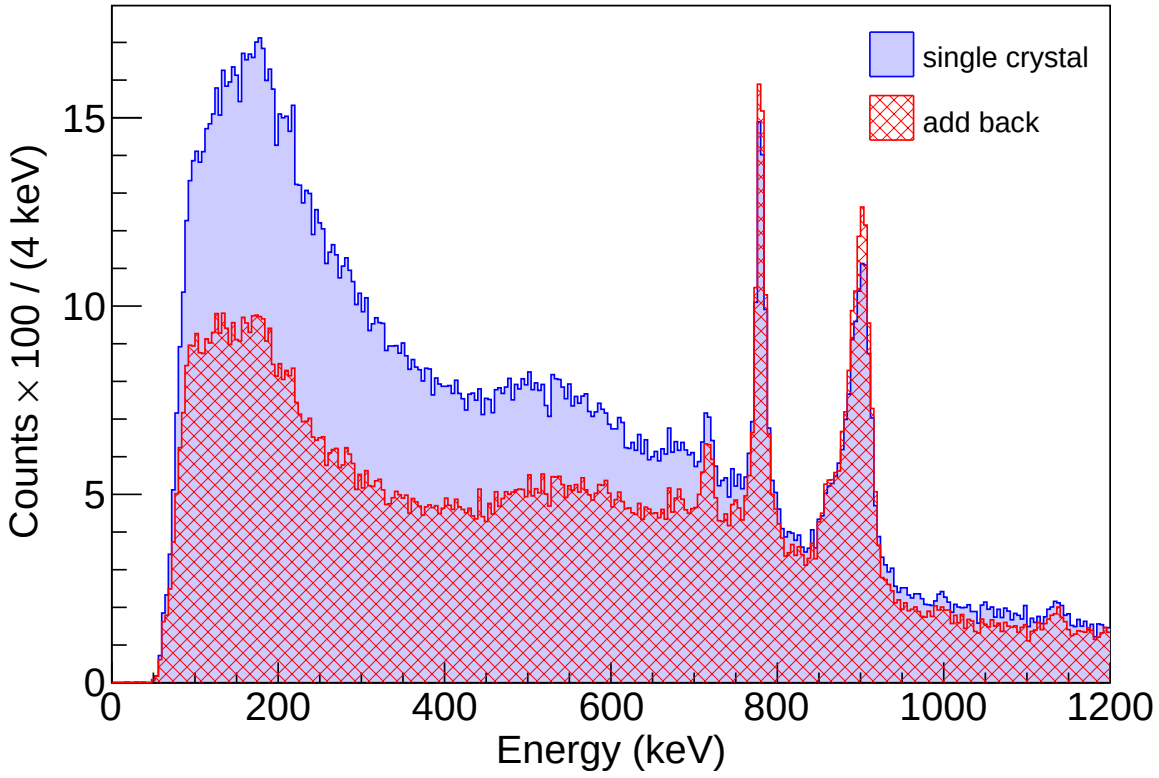

Figure 3.10: Gamma-ray energy spectra in coincidence with ^{35}Si obtained by summing all interactions within one crystal (blue filled histogram) and by the add-back procedure described in the text (red histogram).

from the same γ-ray. As an example of the difference in results obtained by the two methods, Figure 3.10 shows part of the γ-ray energy spectrum in coincidence with ^{35}Si obtained with each procedure. In this work, add-back is used for peak identification and $\gamma\gamma$ coincidences because of its superior spectral quality, while the single-crystal spectra are used to obtain the absolute yields of γ-rays because of the more accurate efficiency determination.

3.3.3 Origin of the exponential γ-ray background

Gamma-ray spectra taken in coincidence with knockout reactions at intermediate energies (approximately 100 MeV/u) inevitably exhibit a pronounced continuous background which

decays exponentially with increasing energy. The origin of this background has not been clearly established, although brief suggestions exist in the literature. A similar background is seen in other reactions at intermediate energy such as fragmentation, inelastic excitation, and Coulomb excitation [3], but not in pickup reactions (see, for example, [102]), which are particular in their minimal momentum transfer. This ubiquity is evidence that the background does not depend on the structure of the studied nucleus and so in most cases, the origin of the background is unimportant; simply fitting it with an exponential or double-exponential curve allows the extraction of the desired information. However, in the present work we encounter two peaks of interest that lie just above the γ-ray detection threshold, where the shape of the background is no longer a simple exponential. The approach taken here is to attempt to understand the origin of the background sufficiently to simulate it and extrapolate from the background at higher energy. We use three observables to illuminate the source of this background: timing information, correlation with the momentum of the detected outgoing particle, and the angular distribution of the γ rays.

Timing information on the background comes from an experiment using lanthanum bromide ($LaBr_3$) scintillator γ-ray detectors, which have superior timing resolution to high-purity germanium (HPGe) detectors. Figure 3.11, taken from [8], demonstrates that the exponential background is delayed by a few nanoseconds relative to the prompt de-excitation γ rays. Further, a gate on later times reveals the 884 keV line in ^{27}Al (not shown in Figure 3.11), indicating inelastic reactions on the aluminum beam pipe.

The relationship between the γ-ray energy and the momentum of the outgoing particle is shown in Figure 3.12. Panel (a) shows the parallel momentum distribution of outgoing ^{36}Si

[3]Coulomb excitation and inelastic scattering also have a significant contribution to the background at low energy from atomic processes.

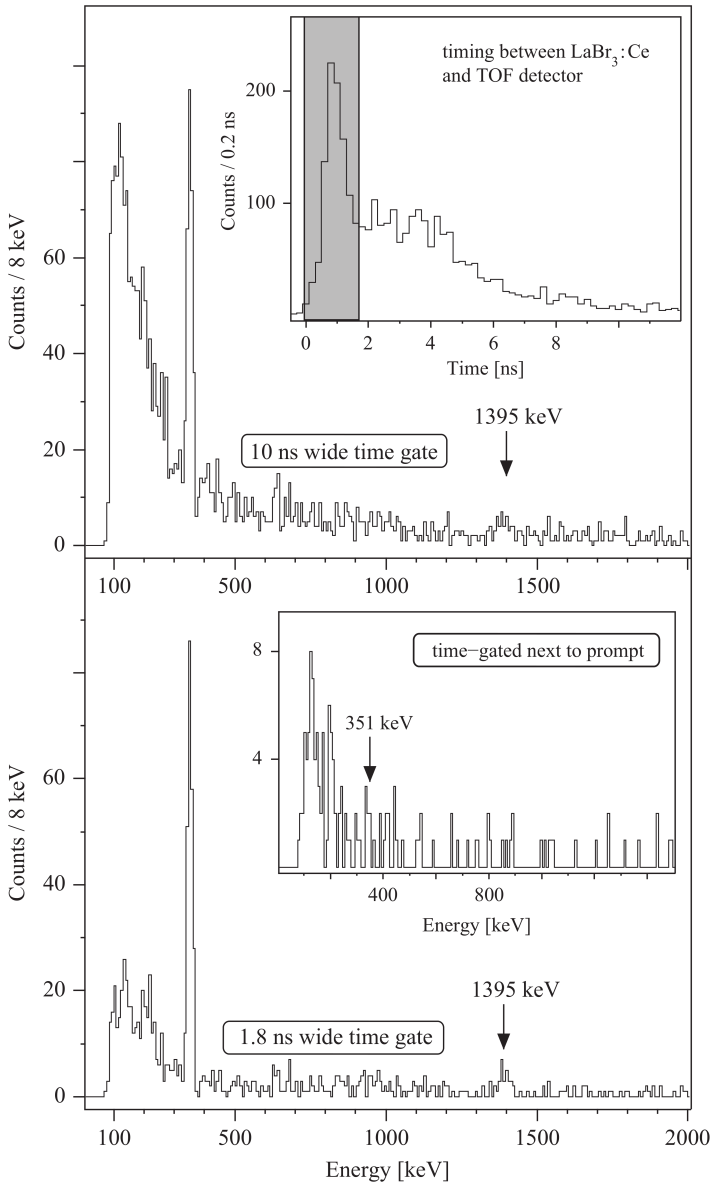

Figure 3.11: Demonstration of the time structure of the γ-ray background. The top panel shows the γ-ray spectrum in coincidence with ^{21}Ne detected with $LaBr_3$ detectors, with the time difference between the $LaBr_3$ trigger and the particle trigger shown in the inset. The bottom figure shows the γ-ray spectrum gated on the prompt peak in the timing spectrum, indicated with the gray block. Most of the exponential background is removed. The inset in the bottom figure shows the γ spectrum gated off of the prompt peak, revealing an essentially pure background spectrum. Reprinted with permission from [8].

particles, with two cuts indicated, one on the main peak and one on the low-momentum tail. Panel (b) shows the γ-ray spectra for each of the indicated cuts, normalized by the number of detected ions in each cut. It is clear that the high-energy exponential background originates from events in which a significant amount of momentum is removed from the projectile, indicating a nuclear collision with energy transfer to the target. The γ-rays associated with the main peak are much more concentrated at low energies, which indicates that they originate from atomic processes such as bremsstrahlung of scattered target electrons. The main panel, labeled (c), shows the parallel momentum distribution in coincidence with no detected γ-rays (blue hatched curve) and with γ-rays with energy above 1 MeV (solid red curve), indicating a complementary relationship to that shown in panel (b). The blue curve, with no γ-rays in coincidence, is essentially the incoming beam profile, while the red curve shows a significant tail to low energies. [4] This relationship will be used in §3.4. If the blue curve and the high-energy portion of the red curve are fit with Gaussians, the difference in their centroids corresponds to an energy loss of approximately 5 MeV.

The angular distributions of the background γ-rays are shown in Figures 3.13 (polar angle θ) and 3.14 (azimuthal angle ϕ). In obtaining these distributions, it was necessary to remove the effect of the non-trivial geometry of the GRETINA detectors.

For the polar angle distribution, the measured distribution is normalized to the distribution from a ^{226}Ra calibration source, which is assumed to be isotropic, located at the target

[4] The γ-ray detection efficiency of the GRETINA array is, of course, not 100% and so there are some counts in the blue curve which correspond to events with undetected γ-rays. As a result, one might expect a low momentum tail on the blue curve. The tail is present, but it is so overwhelmed by true no-γ events that it is invisible on a linear scale.

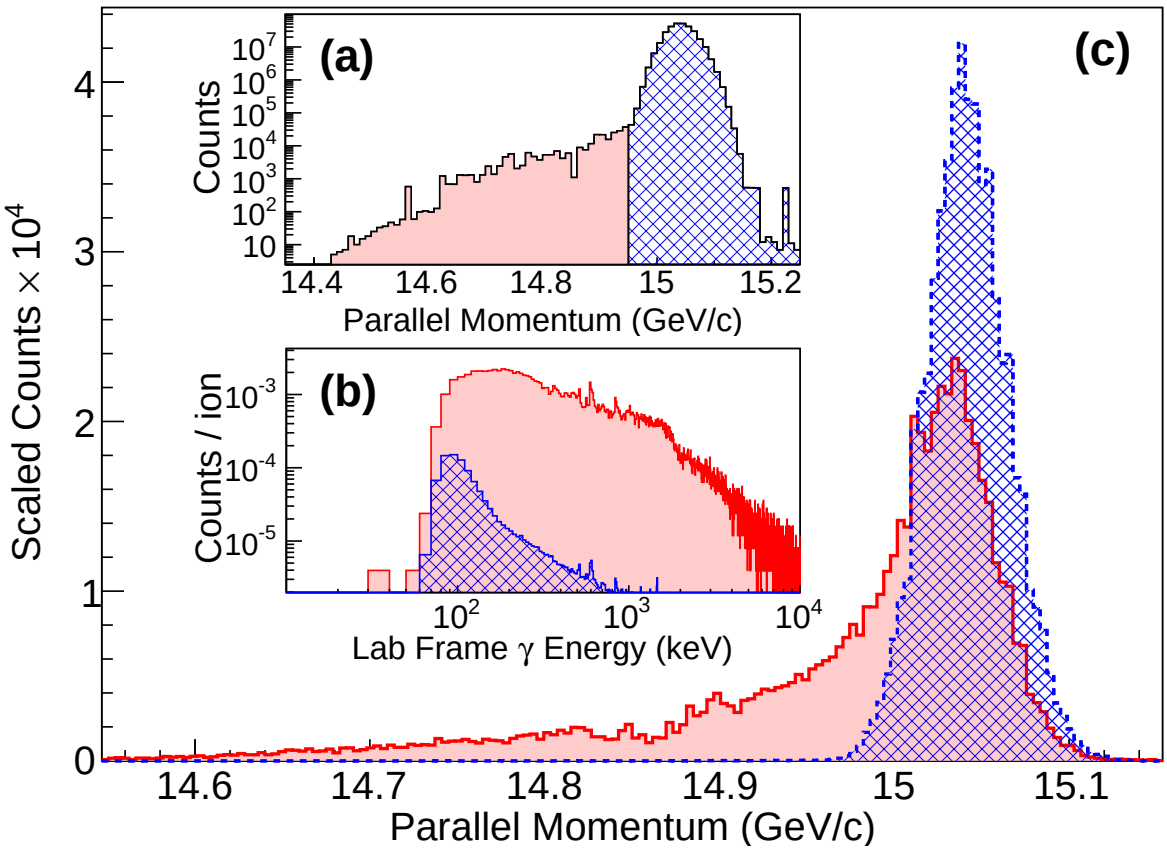

Figure 3.12: (a) Parallel momentum distribution for outgoing ^{36}Si particles, with two gates indicated. (b) The γ-ray spectrum for each of the two momentum cuts indicated in (a), normalized to γ-rays per detected ion. (c) The momentum distribution gated on no detected γ rays (blue hatches), and γ rays with energy above 1 MeV (solid red).

position. In Figure 3.13 I show the weighting function $W(\theta)$ defined by

$$dN(\theta) = \frac{1}{2} N W(\theta) \sin\theta d\theta \tag{3.6}$$

such that an isotropic distribution has $W(\theta) = 1$. The distributions for two additional calibration sources, ^{56}Co and ^{60}Co, are shown and are consistent with an isotropic distribution. Also shown is the distribution for the $2_1^+ \rightarrow 0_1^+$ transition in ^{36}Si, emitted in-flight with a velocity of $\beta \approx 0.41$ after inelastic scattering on a ^{9}Be target. A calculated curve shows the expected distribution assuming an isotropic distribution in the rest frame of the emitting ^{36}Si particle. Finally, the angular distribution for all γ-rays with energy above 1 MeV in coincidence with a detected ^{36}Si particle is shown. This distribution appears to indicate a source moving at a velocity greater than beam velocity, which is unreasonable. However, such a distribution could also be generated by a source located approximately 10 cm downstream, consistent with fragments from the target drifting down stream for a few nanoseconds before interacting with the beam pipe.

For the azimuthal distribution, the angle ϕ is taken relative to the scattering plane of the reaction, obtained with the S800. Due to the non-uniform angular coverage by GRETINA, and the non-uniform distribution of beam angles *ata* and *bta*, there could be some artificial correlation in the angle of the detected γ-ray and the angle of the scattered particle. For example, the GRETINA detectors are more concentrated along the y direction (see Figure 3.9), and if there were significantly more spread in the incoming *bta* (angle in the y direction) relative to *ata*, then even totally unrelated events would show a preference for the γ ray to be detected in the scattering plane. To remove this, a baseline correlation $I_{\text{random}}(\Delta\phi)$ was generated by constructing a distribution of ϕ in which the γ and scattered particle

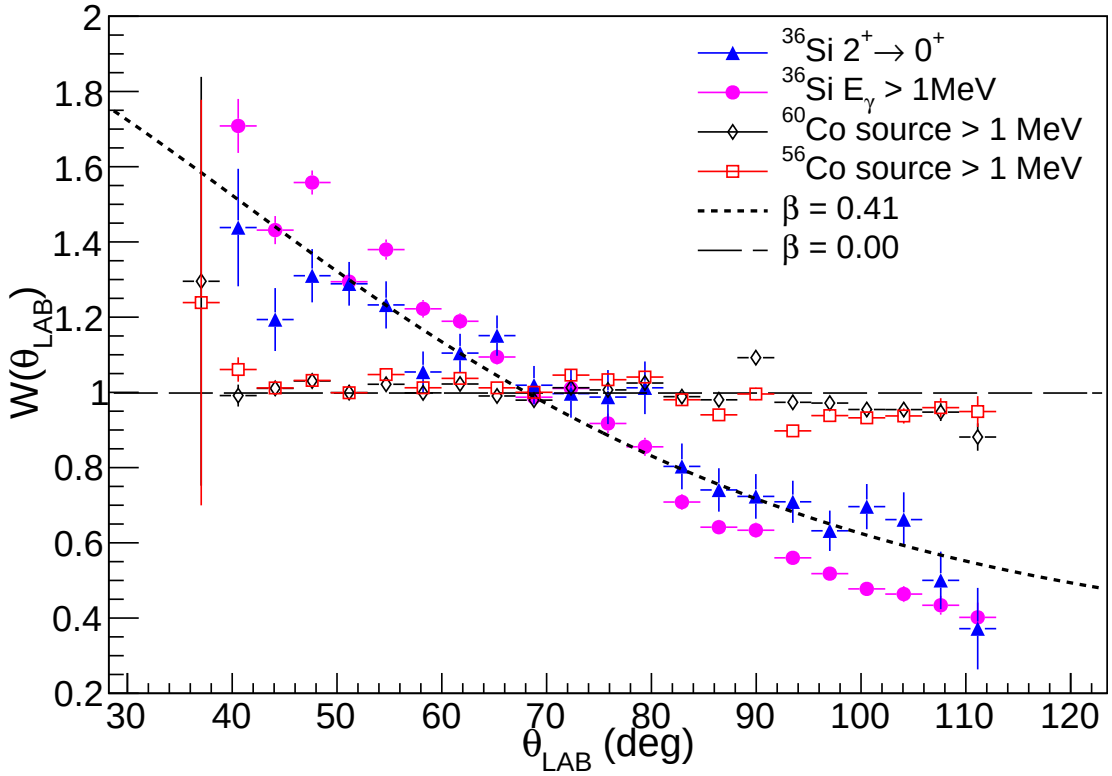

Figure 3.13: Polar angle distribution, normalized to a ^{226}Ra source measurement, for the $2^+ \rightarrow 0^+$ transition in ^{36}Si (blue triangles), the exponential γ-ray background above 1 MeV (magenta circles), and two other source measurements (black diamonds and red squares) as a consistency check. The long-dashed line indicates an isotropic distribution in the lab frame, and the short-dashed line indicates an isotropic distribution in a frame moving with beam velocity. The error bars are statistical only.

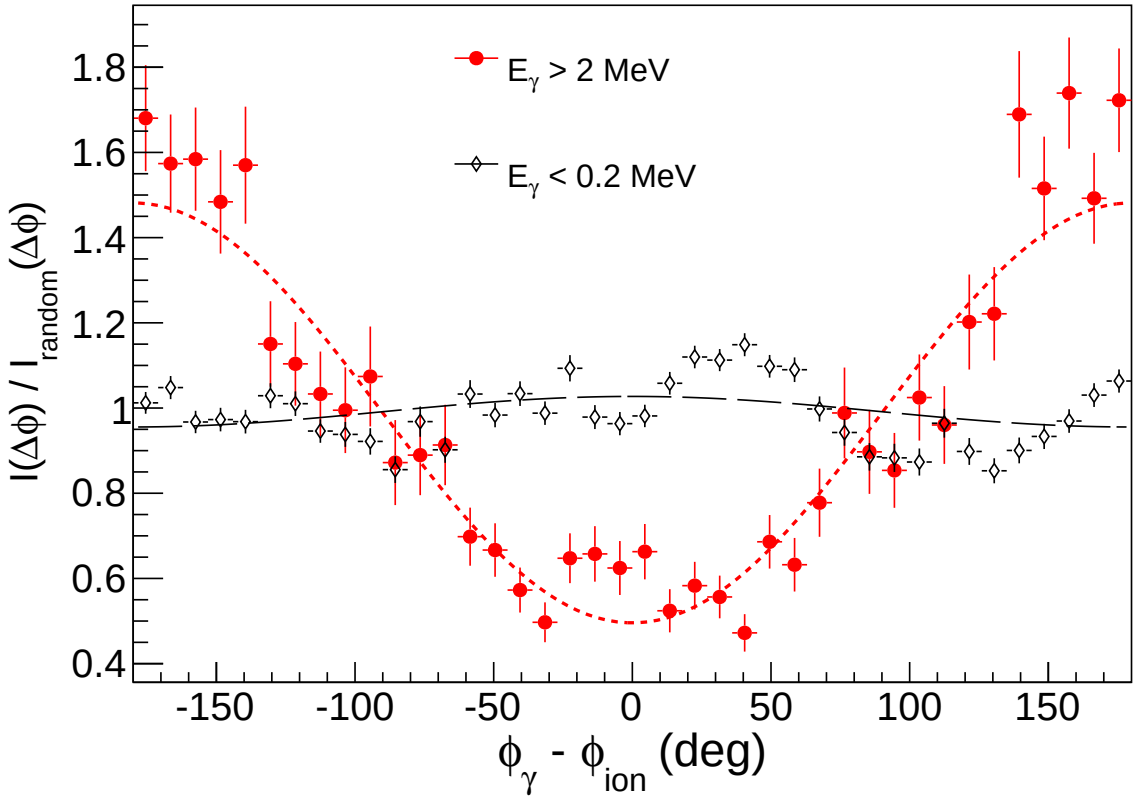

Figure 3.14: Distribution of the azimuthal angle ϕ between the direction of the scattered beam and the direction of the detected γ ray. The red circles show the distribution for γ rays with energy greater than 2 MeV, while the black diamonds show the distribution for low-energy γ rays from atomic processes, which should be uncorrelated with the beam direction. The dashed and dotted lines show fits with the two lowest-order even Legendre polynomials.

are taken from separate (uncorrelated) events. The actual distribution $I(\Delta\phi)$ was then divided by the random distribution to remove artificial correlations. Figure 3.14 shows the resulting distribution for two cuts in the γ-ray energy spectrum in coincidence with outgoing ^{36}Si. The low-energy cut $E_\gamma < 0.2$ MeV selects primarily photons originating in electronic bremsstrahlung, which should have no significant correlation with the scattering angle of the outgoing particle, and indeed the distribution is flat. The high-energy cut $E_\gamma > 2$ MeV selects the background of interest. A clear anti-correlation is evident, indicating that the γ-rays are preferentially detected in the direction of the recoiling target.

Taken together, this evidence strongly suggests that the exponential γ-ray background is produced by a collision with the target, which breaks up into nucleons and light ions. These particles then interact with the aluminum beam pipe to produce the observed γ rays, either by bremsstrahlung or by statistical γ cascades from highly excited states. In experiments with a liquid hydrogen target [103, 104], the beam-correlated background may be reproduced by the γ spectrum obtained with an empty target, scaled by the number of detected particles. This suggests that protons (and, we may infer, light ions) play a small role in the production of this background and that neutrons are the primary culprit [5]. Indeed, (n, n') induced γ-rays from germanium and aluminum confirm that neutrons are produced in abundance in these reactions. Finally, we may also understand that the more delicate pickup reactions are much less likely to occur in violent collisions which produce neutrons, and hence the absence of this background in those reactions (see, for example, [102, 105, 106]).

3.3.4 GRETINA simulations

The response of the GRETINA array was modeled using the GEANT4 simulation package [107]. The simulation includes the fully segmented detectors with crysostats and two mounting hemispheres, as well as the aluminum beam pipe and the target material. The behavior of the photons was modeled including Compton scattering, Rayleigh scattering, pair production, and the photoelectric effect. For in-beam simulations, the incoming beam characteristics were matched to data from an unreacted setting, while the reaction is modeled in a single step which produces the reaction residue in an excited state. A new momentum direction is selected, based on parameters which reproduce the measured outgoing momentum

[5] This is, of course, still speculative. A more definitive statement would require the measurement of charged particles after neutron knockout or inelastic scattering.

distribution, and the ion proceeds until it decays based on the lifetime of the excited state. The ion then continues until it has left the target, at which point its trajectory is recorded in S800 format. The energy and position of all interactions in GRETINA are associated with that event, and the simulated data may be passed through analysis identical to that applied to the experimental data.

One additional layer of complexity is the fact that GRETINA obtains the interaction points through a fairly complicated decomposition process, which has some associated error. Further, multiple interactions within a single segment are very difficult for the decomposition algorithm to distinguish. To treat this, all interactions in the same segment within a "packing radius", taken to be 8 mm, are combined into a single interaction with an energy equal to the sum of the individual energies and a position given by the energy-weighted average position. Each interaction point is then shifted in a random direction to generate the effective position resolution of 2 mm (root-mean-squared) in x, y, and z.

The simulated γ-rays fall into three categories: prompt in-flight γ's, neutron-induced lab-frame γ's, and the continuous exponential background described in §3.3.3. In principle, γ's from atomic processes should also be included, but this is found to contribute negligibly to the γ-ray spectrum for any reaction in which the outgoing fragment is different from the incoming beam. This may be understood by considering the relative likelihood of various processes: In the unreacted setting, the vast majority of outgoing particles will not have undergone a nuclear reaction in the target, and so no nuclear γ-rays are produced. There is, however, a small probability for producing and detecting a photon from an atomic process, and this small probability competes with the small probability of a nuclear reaction which produces a γ ray. In the reacted setting, by definition all outgoing particles have undergone a nuclear reaction, and the probability of producing a γ-ray is relatively large, while the

probability of producing a photon in atomic processes remains small.

Neutron-induced lines in germanium have a characteristic high-energy tail which comes from the recoil energy of the excited germanium nucleus [98]. This was modeled by, instead of generating γ rays with exactly the transition energy, selecting them from a distribution of energies which reproduces the observed peak shape.

The background described in §3.3.3 is generated by selecting γ-ray energies from a Maxwell-Boltzmann distribution

$$P(E) = E^k e^{-E/E_0} \tag{3.7}$$

and emitting these isotropically in the rest frame. The parameter E_0 is taken to be 2 MeV, to reproduce the observed high-energy behavior of the background, and we take $k = 0.2$. As this background is understood to be due to neutrons (and possibly light ions) from the fragmented target interacting with the aluminum beam pipe, the origin of the γ rays is taken to be a point on the beam pipe with z position selected from a Gaussian distribution centered 10 cm downstream of the target.

At this point, all components of the simulated γ-ray spectrum have a fixed shape, and the only remaining variables are their overall scaling factors. These scaling factors are obtained by fitting to the experimental spectrum using the MINUIT fitting package [108] included in the ROOT analysis framework [109]. To better constrain the lab-frame peaks, the spectra are fit simultaneously in the lab and Doppler-reconstructed frame. For low statistics data, it was found that a log-likelihood fit assuming Poisson-distributed errors produced a less biased fit than the default χ^2 fit, consistent with findings in [110]. However, the χ^2 fit was found to be significantly less sensitive to the initial parameter values. As a result, a two-step fit was

performed: first a χ^2 fit to get reasonable initial parameters, followed by a log-likelihood fit. The intensities of the γ-rays are then obtained by multiplying the fit parameters by the number of γ-rays simulated.

3.3.5 Energy and efficiency calibrations

Energy and efficiency calibrations for GRETINA were performed before and after the experiment using radioactive sources. The energy calibration was set at the beginning of the experiment for each segment and crystal, and the decomposition algorithm output calibrated energies. As any uncertainty in these energies is small compared to the uncertainties due to the Doppler reconstruction, no further energy calibration was performed[6].

All absolute γ-ray intensities from in-beam data were extracted by fitting with simulated peaks and comparing to the absolute number of γ-rays generated in the simulation. It is therefore critical to confirm that the simulation accurately reproduces the efficiency of GRETINA.

The absolute efficiency was obtained by D. Weisshaar [111] by first starting with a multichannel analyzer (MCA) with a calibrated dead time estimation connected to a single crystal of GRETINA. A spectrum was taken of a ^{152}Eu source with a known activity of 53.7(7) kBq, and integrated to get the total number of counts within a fixed energy range spanning most of the strong lines in ^{152}Eu. Next, the same crystal was run connected to the GRETINA data acquisition system (DAQ) in free running mode (that is, self-triggering with no external validation), and the same count rate was confirmed. The crystal was then connected to the S800 DAQ to generate an external trigger. The same count rate was again confirmed.

[6]As described in [93], there is an additional adjustment made to correct for differential nonlinearities in the digitizer modules. No further treatment was made for the current experiment.

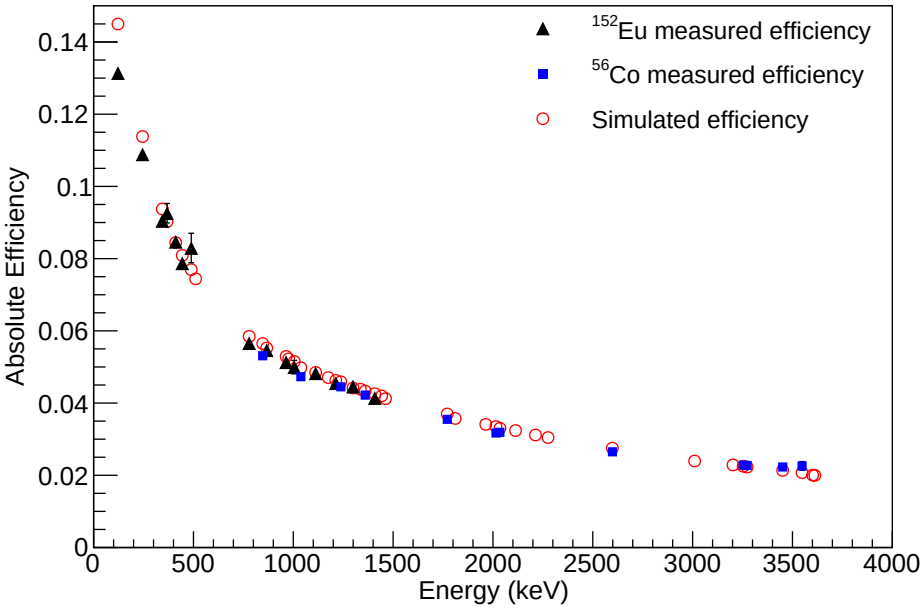

Figure 3.15: Simulated γ ray detection efficiency compared to efficiency measured with two sources. Note the discrepancy at low energy.

Finally, all detectors were connected and the full GRETINA efficiency was obtained for each prominent line from ^{152}Eu, with branching ratios taken from the IAEA [112].

This efficiency was independently confirmed by using a ^{60}Co source which emits two coincident γ rays, at 1173 and 1332 keV. A lanthanum bromide (LaBr) detector was placed near the array and used as the trigger. For events in which a 1332 keV γ ray was seen in the LaBr detector, exactly one γ ray of energy 1173 keV was emitted and the efficiency was extracted by measuring the observed counts in the 1173 keV peak. The same procedure was followed for a ^{88}Y source, which has two coincident lines at 898 keV and 1836 keV. The efficiencies of these measurements were consistent with the efficiency curve obtained with the ^{152}Eu source.

For calibration at higher energy, a ^{56}Co source was used, although its activity was not well known. Its intensity was therefore scaled to match the efficiency of the ^{152}Eu source in the

range 1.0-1.5 MeV. The resulting efficiency curve is shown in Figure 3.15. A corresponding simulated efficiency curve was generated by integrating the full-energy peaks in simulated spectra and dividing by the number of γ rays emitted in the simulation. This curve is also shown in Figure 3.15. The agreement is excellent above 500 keV, but the simulation overpredicts the efficiency at lower energies, particularly below 200 keV. Tests indicated that this discrepancy could not be due to inaccuracies in the simulation's treatment of γ-ray absorption at low energies, and the addition of absorptive material was limited by the known detector geometry. Another potential source of the discrepancy is an inefficiency in the decomposition procedure at these energies. Low-energy γ rays produce weak signals in the segments of GRETINA, which may not reach the threshold, causing an event without any segment information, which will fail in the decomposition. Even if the segment does trigger, the weak pulse will be relatively noisy and difficult for the decomposition algorithm to handle, leading to poor fit results. In both cases, and possibly others, these events may not make it through the data stream to be recorded. This additional inefficiency was accounted for by adding a modulating function into the simulation which throws away a small fraction of low energy events. The resulting efficiency curve, shown in Figure 3.16, reproduces the measured efficiency across the measured range, from 100 keV to 3.5 MeV.

3.3.6 Extracting lifetimes from peak shapes

If an excited state produced in the reaction target has a lifetime in the range of $\sim$1 ps to $\sim$10 ns, then the excited nucleus will travel some distance through the target, losing energy according to (3.2), before decaying. The γ decay will occur at a slower velocity and greater z position than that assumed in the Doppler reconstruction, resulting in a low-energy tail on the peak, according to (3.4). The low-energy tail becomes more pronounced for longer

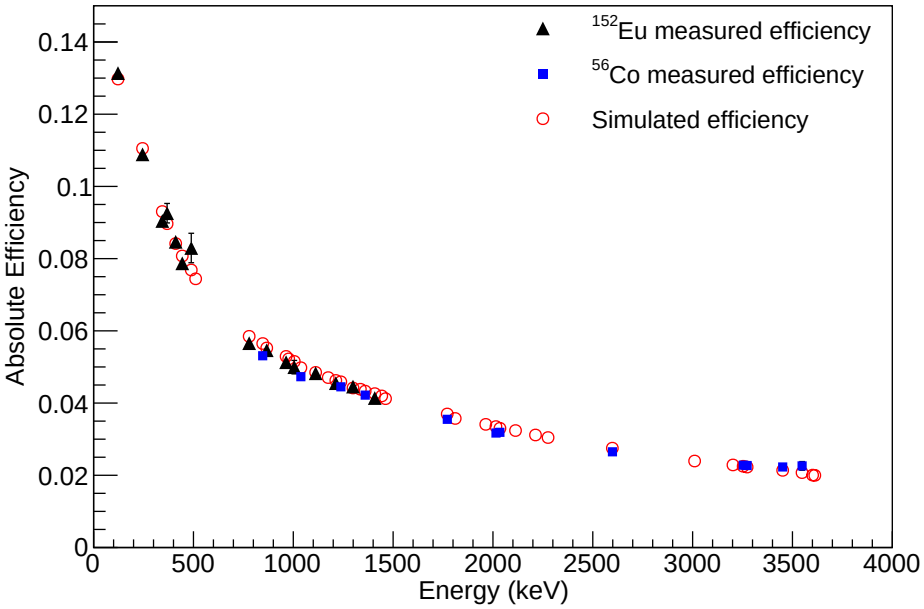

Figure 3.16: Simulated γ ray detection efficiency, with correction for losses at low energy, compared to efficiency measured with two sources. The simulation now reproduces the measured efficiency from 100 keV to 3.5 MeV.

lifetimes, and so if the lifetime of the state is unknown, it may be extracted by the γ-ray line shape. This is achieved in this work by simulating the entire process of excitation of the nucleus, the traveling of the excited nucleus according to its lifetime, followed by the γ decay and detection. By simulating this process with many different assumed lifetimes, one may extract the lifetime as the one which produces the best fit to the experimental line shape. A maximum likelihood fit is performed and the best-fit likelihood $\mathcal{L}$ for each simulated lifetime (actually, the negative logarithm of the likelihood $L \equiv -\log \mathcal{L}$) is recorded. Near the maximum overall likelihood (minimum negative log likelihood), the dependence of the likelihood on the lifetime may be parameterized by a quadratic function of the lifetime. In fact, because the relative change in the line shape for a given change in lifetime is greater at shorter lifetimes, the dependence is parameterized as quadratic function of the logarithm of

the lifetime.

$$L(\tau) = C\left[\log(\tau/\tau_0)\right]^2 + L_0 \tag{3.8}$$

The extracted lifetime is taken to be τ_0, and the uncertainty $\Delta\tau$ is estimated by [113] $L(\tau \pm \Delta\tau) = L_0 + \frac{1}{2} + \delta$ where δ is the rms deviation for the quadratic fit to $L(\tau)$.

As the excited nucleus moves in the z direction, the geometric efficiency for γ-ray detection changes, resulting in a dependence of the extracted peak intensity on the assumed lifetime. To estimate the contribution of the lifetime effect to the uncertainty in the peak intensity, the best-fit peak intensity is also recorded for each simulated lifetime. The intensities associated with $\tau \pm \Delta\tau$ are taken to represent this uncertainty.

The effect of the lifetime on the γ peak line shape is dependent on the position of the detector. Detectors at backward angles ($\sim 90^\circ$) have a much less pronounced tail, while detectors at intermediate angles are "shadowed" by the forward-most detectors, leading to a reduced efficiency for longer lifetimes. In order to maximize sensitivity, the peak is simultaneously fit for forward, backward and intermediate angles. The results of fits to lifetime-broadened peaks are shown in §4.2.1, §4.2.3, and §4.2.5.

3.4 Asymmetric momentum distributions

The sensitivity of knockout reactions to the orbital angular momentum ℓ of the removed nucleon (see §2.3.6) provides an essential tool in identifying the orbit from which the nucleon was removed and, for a 0^+ projectile, identifying the J^π of the state populated in the knockout residue. Extracting ℓ from the parallel momentum distribution of the residue is dependent on a theoretical prediction that can reproduce the data to sufficient precision to differentiate between the possible values of ℓ. Often in knockout experiments, an asymmetric

momentum distribution with a tail to the low-momentum side is seen [114, 115, 116, 117, 118], whereas the results of the eikonal calculation (2.45) are by construction symmetric. This is because in the eikonal formalism, the target is modeled as a static potential, and so no target recoil or breakup is included in the calculation. By energy and momentum conservation, any energy transferred to the target should result in a lowering of the parallel momentum of the residue, and so it is assumed that the low-momentum tail is due to the recoil and inelastic excitation of the target. Indeed, proper treatment of energy and momentum conservation, using a coupled-channels formalism, reproduces the low momentum tails convincingly for light, loosely-bound projectiles [76]. However, the knockout reaction for these processes proceeds predominantly through diffraction (see §2.3.5), in which the target is left in its ground state and the reaction is relatively simple to treat with coupled-channels. For stripping reactions, where the target is left in an excited state, the coupled-channels calculation requires a proper treatment of the target breakup.

Treating this theoretically is a tricky task, as ^{9}Be is only bound by 1.7 MeV, with no bound excited states. No existing theory can describe accurately how ^{9}Be will break up in a knockout reaction. As the stripping mechanism dominates for the cases studied here, we therefore turn to the possibility of empirically obtaining the effects of the target breakup, which we can then use to improve the eikonal description of the momentum distribution.

In order to isolate the effect of the target breakup from that due to the recoil from the removed nucleon, we investigate events in which the outgoing nucleus is the same as the incoming projectile. As we saw in §3.3.3 there is a clear correlation between the γ spectrum and the momentum distribution for such events, namely that high-energy γ rays accompany the more violent collisions. However, the requirement that the projectile survives constrains these events to be peripheral. These are exactly the collisions we wish to select, because

knockout reactions are surface-peaked, owing to the requirement that the core survive.

It is to be expected then that – to some level of approximation – the momentum distribution for knockout should be given by the distribution for these surface-peaked inelastically scattered events, folded with the additional kick from the knockout, given by the eikonal calculation. Indeed, as shown in Figure 3.17, including the core-target interaction through the inelastic scattering data clearly improves the agreement with the measured distributions.

In more detail, we denote the measured inelastic momentum distribution $F_{inel}(p)$, where p is in the lab frame. In the knockout reaction, we approximately conserve momentum per nucleon, so this distribution should be scaled by $(A-1)/A$. For the measurements of ^{36}Si and ^{38}Si, a different target thickness was used for the knockout and inelastic scattering experiments. The extra energy loss in the thicker target was estimated by the difference in centroid momenta between the inelastic scattering run (with no gate on γ-rays) and the unreacted beam particles in the knockout setting:

$$\Delta_{tgt} = \langle P \rangle_{unreacted} - \langle P \rangle_{inel} \,. \tag{3.9}$$

Further, the mass A and mass $(A-1)$ systems have different energy loss through the target, particularly for proton knockout. This difference in outgoing momentum is estimated by the parameter δp, which is the difference in outgoing momenta after the full target thickness for the mass A and mass $A-1$ systems, estimated with LISE++ [119]. The reaction takes place at any depth in the target with approximately equal probability, so the effect of the different energy loss is handled with Heaviside functions

$$h(p, \delta p) = |\Theta(p - \delta p) - \Theta(p)| \,. \tag{3.10}$$

We therefore obtain a corrected inelastic distribution

$$\mathcal{F}(p) = F_{inel}\left(\frac{A}{A-1}p - \Delta_{tgt}\right) * h(p, \delta p) \tag{3.11}$$

where $*$ indicates a convolution. The distribution $\mathcal{F}(p)$ accounts for all effects which are not due to the recoil of the removed nucleon.

The recoil is handled by the eikonal calculation, which produces a distribution $G_{eik}(p_{cm})$ in the center of mass frame, corresponding to the curves shown in Figure 2.10. The final theoretical curve $\mathcal{K}(p)$ which corresponds to the red curves in Figure 3.17 is obtained by

$$\mathcal{K}(p) = \mathcal{F}(p) * G_{eik}(p/\gamma) \tag{3.12}$$

where we have divided by the relativistic factor γ in the eikonal distribution to account for the broadening from the Lorentz boost to the lab frame. The blue curves in Figure 3.17 are obtained by replacing the inelastic scattering distribution with the unreacted distribution $F_{inel}(p) \rightarrow F_{unreacted}(p)$ in (3.11) and by taking $\Delta_{tgt} = 0$.

The amplitude of the distribution $\mathcal{K}(p)$ is then scaled so that its integral is equal to the total number of particles in the experimental momentum distribution, leaving no free parameters for fitting. This procedure is used for all theoretical momentum distribution curves shown in this work.

I note here that for momentum distributions for populating the ground state, as shown in Figure 3.17(a) and (c), the distribution is obtained by the subtraction of momentum distributions for all feeding transitions (scaled for γ detection efficiency) from the total momentum distribution.

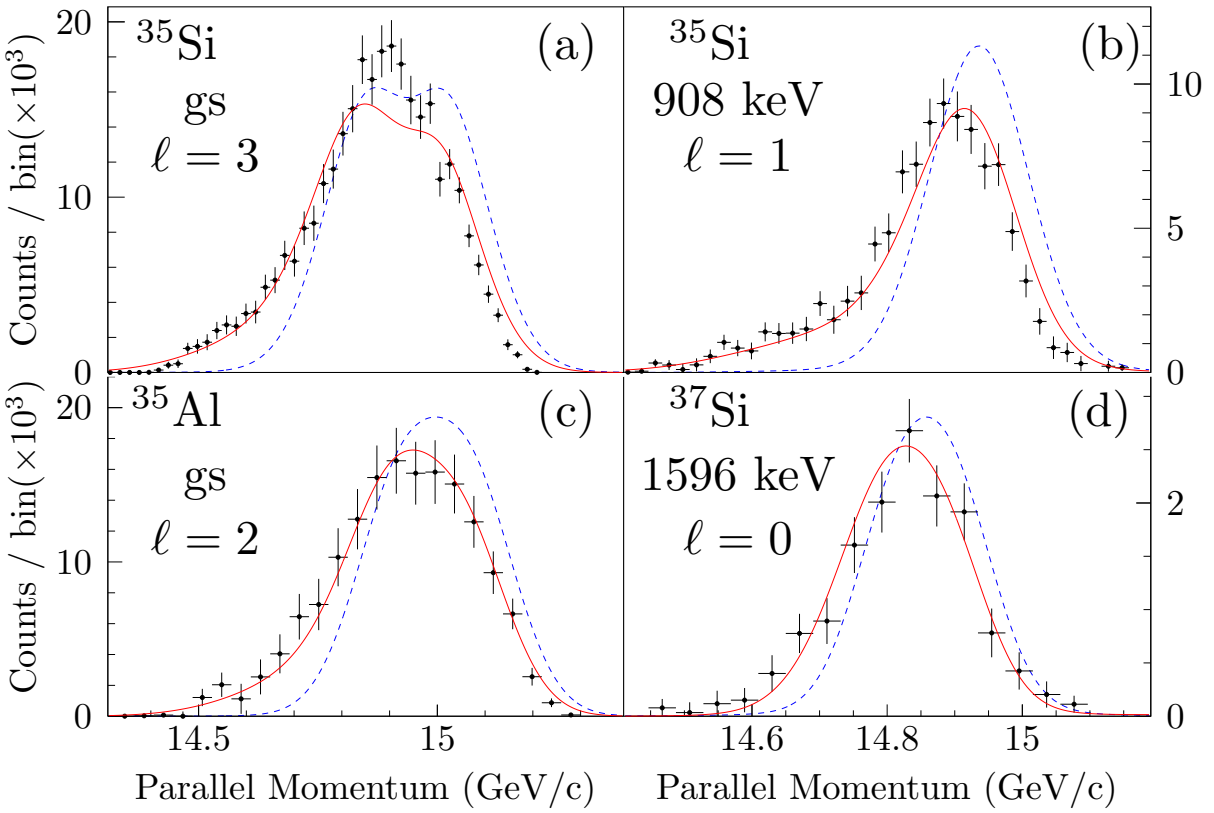

Figure 3.17: Experimental momentum distributions to specific final states, compared to eikonal model predictions folded with the incoming momentum distribution (blue dashed lines), or folded with the distribution obtained from the inelastic setting (solid red curves, see text for details).

The finding that this relatively straightforward folding procedure is so successful at reproducing the measured distributions suggests that the tails observed in the knockout reaction are primarily due to the core-target interaction, and that higher-order effects are suppressed. Further investigation of this method, using different projectiles and targets, would help to confirm this suspicion.

Chapter 4

Results and interpretation

> *There are two possible outcomes: if the result confirms the hypothesis, then you've made a measurement. If the result is contrary to the hypothesis, then you've made a discovery.* (E. Fermi)

The desired observables from this experiment are partial knockout cross sections to individual final states. This requires the knowledge of the available final states, which in the case of most of the knockout residues in this experiment are not previously known. Therefore, I must first establish level schemes for the six knockout residues studied. These levels are constructed with the aid of γ spectra, $\gamma\gamma$ coincidence spectra, momentum distributions, and comparison with shell model calculations. I begin in §4.1 by outlining the shell model calculations used here, before giving the extracted level schemes in §4.2. I then proceed with experimental knockout cross sections in §4.3, and a discussion in §4.4.

4.1 Shell model calculations

Shell model calculations in this work are carried out in the $1s0d1p0f$ model space, with the restriction that protons are kept in the *sd* shell, and we limit neutrons to 1p-1h excitations across the $N = 20$ shell gap, in order to allow for intruder parity states (i.e. those with parity different from that of the independent particle model ground state). This model space is illustrated in Figure 4.1. Allowing cross-shell excitations introduces an admixture

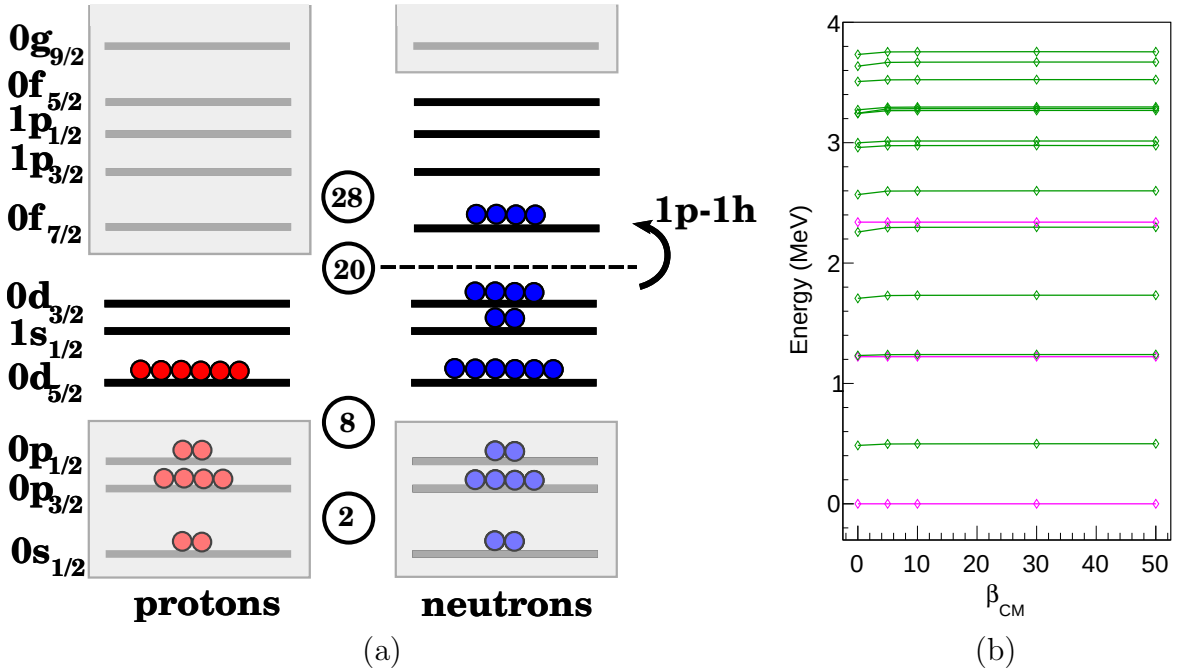

(a) (b)

Figure 4.1: (a) The *sdpf* model space used in shell model calculations. The gray boxes indicate excluded orbits. (b) The dependence of the calculated energy spectra on the center-mass-parameter β_{CM} (see text) for ^{35}Si using the SDPF-MU interaction. The green and magenta lines indicate positive and negative parity states, respectively.

of spurious center-of-mass excitations, which are removed by adding a large positive center-of-mass term to the Hamiltonian [120].

$$H' = H + \beta_{CM} H_{CM} \tag{4.1}$$

Strictly speaking, as pointed out in [121] and elsewhere, this prescription is only applicable in cases where all possible $1\hbar\omega$ excitations are included in the calculation. For the present model space, this would require including proton $0p \rightarrow 0d1s$ and $0d1s \rightarrow 0f1p$ excitations, as well as neutron $0f1p \rightarrow 0g1d2s$ excitations, in addition to the neutron $0d1s \rightarrow 0f1p$ excitations considered in these calculations. However, (4.1) is approximately valid so long as the other $1\hbar\omega$ excitations contribute a negligible amount to the low-lying intruder states, which is a reasonable assumption for the nuclides studied here.

The effect of this change may be seen by performing a calculation with a range of values for β_{CM}. If the spurious components are removed, changing β_{CM} should not change the resulting low-lying energies. Such a calculation is shown in Figure 4.1, demonstrating that above $\beta_{CM} \approx 30$, the spurious components have been removed. For all calculations in this work, we take $\beta_{CM} = 50$.

For comparison, we use two different phenomenological interactions developed specifically for this model space: SDPF-U [122] and SDPF-MU [42]. SDPF-U consists of the USD [123] interaction for the *sd* shell matrix elements and a modification of the KB interaction [124] for the *fp* shell matrix elements. The *sd*-*fp* cross-shell matrix elements, which are the least constrained by existing data, are taken from the Kahana-Lee-Scott G-matrix interaction [125]. The cross-shell interaction is then altered by adjusting monopole terms in order to better reproduce experimental data. Finally, the SDPF-U interaction is split into two

interactions, one for $Z \leq 14$ and one for $Z > 14$, with the difference being that for $Z \leq 14$ a schematic pairing interaction is subtracted from the fp part of the interaction. This is justified with the claim that proton excitations into the fp shell – which are excluded from the model space – should be accounted for by renormalizing the fp shell interaction. Excitations from the proton $d_{5/2}$ orbit (the last filled orbit for $Z \leq 14$) should be suppressed relative to excitations from the $s_{1/2}$ and $d_{3/2}$ orbits, due to the larger gap in single-particle energies, and thus the corresponding renormalization should be less.

SDPF-MU also uses the USD interaction for the sd part, although with a small change to the $\bar{V}_{d_{5/2}d_{3/2}}$ monopole. The fp matrix elements are a mixture of the GXPF1B interaction and the same modified KB interaction used in SDPF-U. The cross-shell terms are based on the V_{MU} potential, which is a schematic type potential consisting of a single-range Gaussian central interaction and a tensor interaction taken from $\pi + \rho$ meson exchange. The central interaction is adjusted to reproduce the monopole behavior of other phenomenological shell model interactions. To this is added a two-body spin-orbit component taken from the M3Y [126] interaction. There is no adjustment made for $Z \leq 14$.

We may visually compare the interactions by plotting their two-body matrix elements against one another, shown in Figure 4.2. As might be expected, the cross-shell matrix elements – least constrained by data – have the largest deviation.

Reduced matrix elements for γ decays $B(M1)$ and $B(E2)$ are also calculated using the results of the shell model calculations with effective operators (see §2.2.5). The effective $M1$ operator is constructed using $g_s = 0.75 g_s^{\text{free}}$, $g_\ell^\pi = 1.1$, and $g_\ell^\nu = 0.1$ [127], with no tensor correction. The effective $E2$ operator is constructed using effective charges $e_\pi = 1.35$ and $e_\nu = 0.35$ [42].

In §4.4, the effect of the tensor component of the interactions is investigated. This tensor

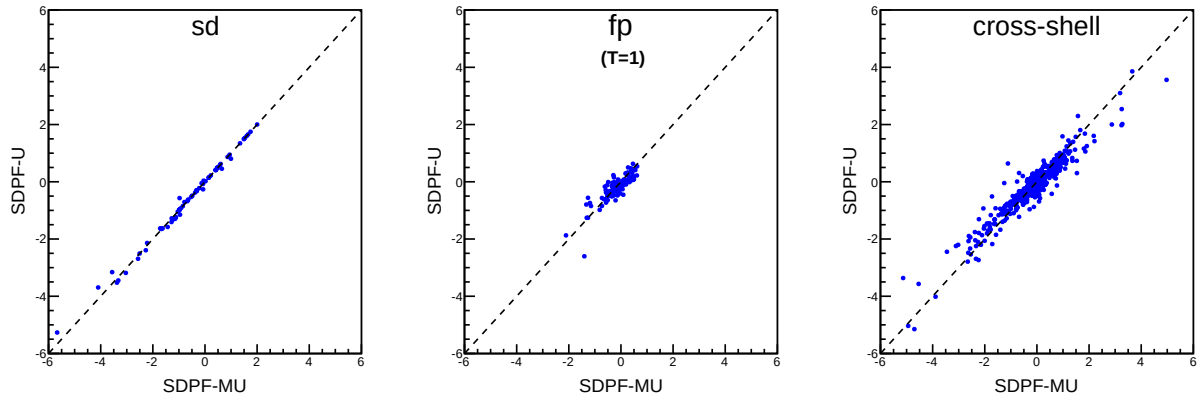

Figure 4.2: A comparison of the matrix elements of the SDPF-MU interaction vs the matrix elements of the SDPF-U interaction. If the interactions were identical, all points would lie along the diagonal lines. Only the $T = 1$ component of the fp interaction is shown, because protons are not allowed into the fp shell in these calculations.

component is extracted from an interaction via spin-tensor decomposition as described in [128], using the somewhat daunting formula:

$$\begin{aligned}\langle ab|V_k|cd\rangle_{JT} = \frac{(-1)^J(2k+1)}{\sqrt{(1+\delta_{ab})(1+\delta cd)}} \sum_{\substack{LL'\\SS'}} \begin{bmatrix} \ell_a & s_a & j_a \\ \ell_b & s_b & j_b \\ L & S & J \end{bmatrix} \begin{bmatrix} \ell_c & s_c & j_c \\ \ell_d & s_d & j_d \\ L' & S' & J \end{bmatrix} \begin{Bmatrix} L & S & J \\ S' & L' & k \end{Bmatrix} \\ \times \sum_{J'} (-1)^{J'}(2J'+1) \begin{Bmatrix} L & S & J' \\ S' & L' & k \end{Bmatrix} \\ \times \sum_{\substack{j'_a j'_b \\ j'_c j'_d}} \begin{bmatrix} \ell_a & s_a & j'_a \\ \ell_b & s_b & j'_b \\ L & S & J' \end{bmatrix} \begin{bmatrix} \ell_c & s_c & j'_c \\ \ell_d & s_d & j'_d \\ L' & S' & J' \end{bmatrix} \sqrt{(1+\delta_{a'b'})(1+\delta_{c'd'})} \langle a'b'|V|c'd'\rangle_{J'T}\end{aligned} \tag{4.2}$$

where k indicates the spin-tensor rank, the square brackets indicate a normalized 9-j symbol [17], and the curly braces indicate a 6-j symbol, and $|cd\rangle$ is shorthand for $|\ell_c s_c j_c \ell_d s_d j_d\rangle$.

4.2 Level schemes for the knockout residues

Prior to this work, few states were known in the odd-A silicon isotopes, and almost nothing was known about the excited states in the odd-A aluminum isotopes. It is therefore necessary to construct a level scheme for each of the knockout residues in order to identify which final states were populated. This was achieved using γ spectra, $\gamma\gamma$ coincidences, relative intensities, and comparison to shell model calculations. Spin-parity assignment of the levels is aided by the parallel momentum distribution gated on de-excitation γ rays.

In §4.2.1-4.2.6 below, I present these ingredients, as well as a proposed level scheme. For each fragment, the information is summarized in a table.

The γ ray intensities are obtained by a fit to simulation, as discussed in §3.3.4. The uncertainties in the intensities are due to uncertainty in the fit (as given by the fit routine), statistical ($\sqrt{N}$) uncertainty in the peak area, uncertainty in the correspondence between simulated and actual γ detection efficiencies, and uncertainty in the lifetime of long-lived ($\tau \sim 1$ ns) states. The efficiency uncertainty is estimated to be 5%, except at low energies (below 300 keV), where the need for a correction factor suggests a greater uncertainty, estimated to be 10%. The uncertainty due to extracted lifetimes is assigned based on the negative log likelihood minimization of the lifetime fit, as demonstrated in Figures 4.4, 4.14, and 4.19.

4.2.1 ^{35}Si

A previous β decay measurement [129] found three excited states in ^{35}Si: a $3/2^-$ state at 910 keV, a $3/2^+$ state at 974 keV, and a $5/2^+$ state at 2168 keV. The 974 keV state decays predominately by a 64 keV γ-ray transition with a life time of τ=8.5(9) ns – too

long to be observed in-flight in the current experiment – and so its population could not be detected here. The ground state was assumed to be $7/2^-$, from systematics and comparison with shell model calculations, consistent with the long lifetime for the $3/2^+$ state. A recent (d, p) reaction study [9] found an additional state at 2044(7) keV, and assigned it to have spin-parity $1/2^-$.

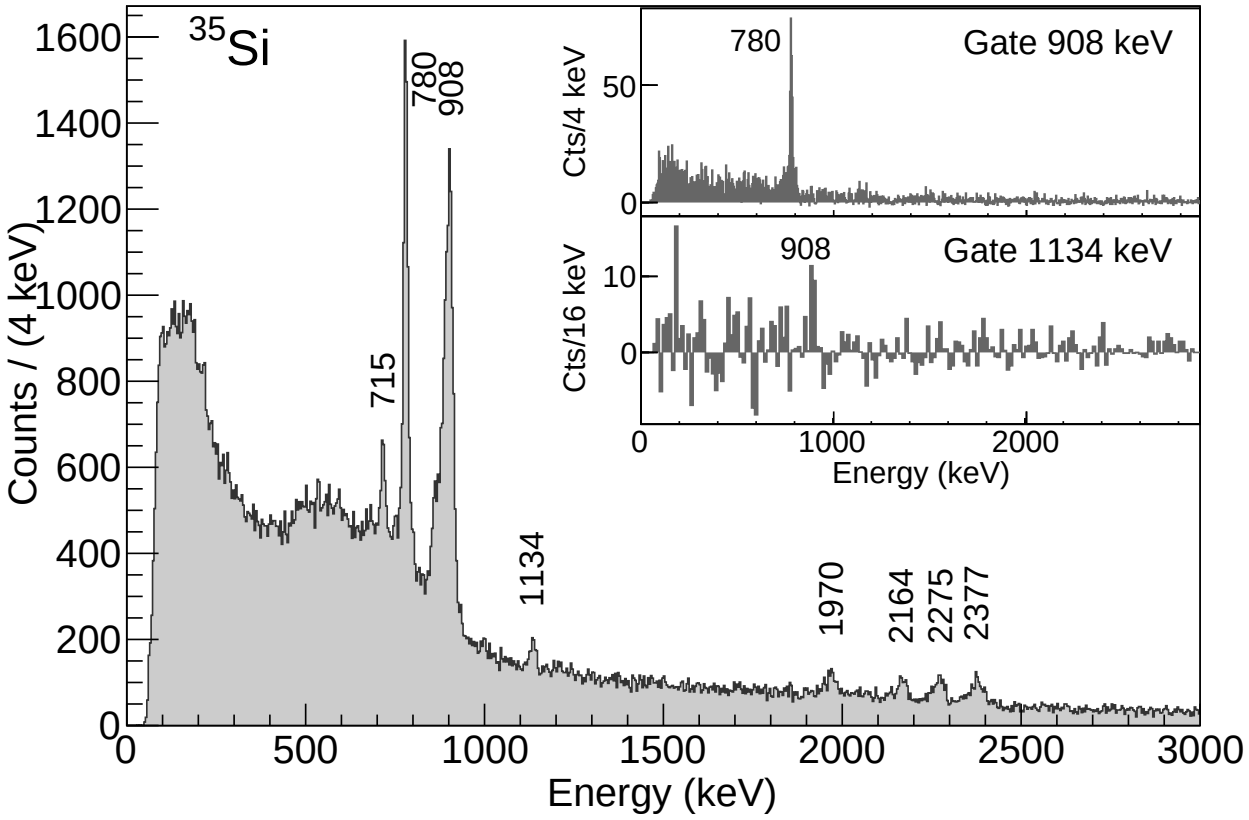

Figure 4.3: Doppler-reconstructed γ-ray spectrum detected in coincidence with ^{35}Si. The 908 keV transition is broadened by a lifetime effect. The inset figures show background-subtracted $\gamma\gamma$ coincidence spectra gated on the 908 and 1134 keV transitions. The Doppler reconstruction was performed with a velocity $v/c = 0.426$.

The γ-ray spectrum in coincidence with outgoing ^{35}Si ions in the current experiment is shown in Figure 4.3. Two strong peaks at 780 and 908 keV are observed. The latter peak, which we associate with the 910 keV transition from β decay is broadened, presumably due to a lifetime effect. The lifetime extracted from a maximum likelihood test of simulated

line shapes is τ=80(20) ps (see Figure 4.4). This corresponds to $B(E2; 3/2^- \rightarrow 7/2^-) = 17^{+4}_{-5}\ e^2\text{fm}^4$ (see appendix B), which compares well with the shell model value of 14 and 16 $e^2\text{fm}^4$ calculated with SDPF-U and SDPF-MU, respectively.

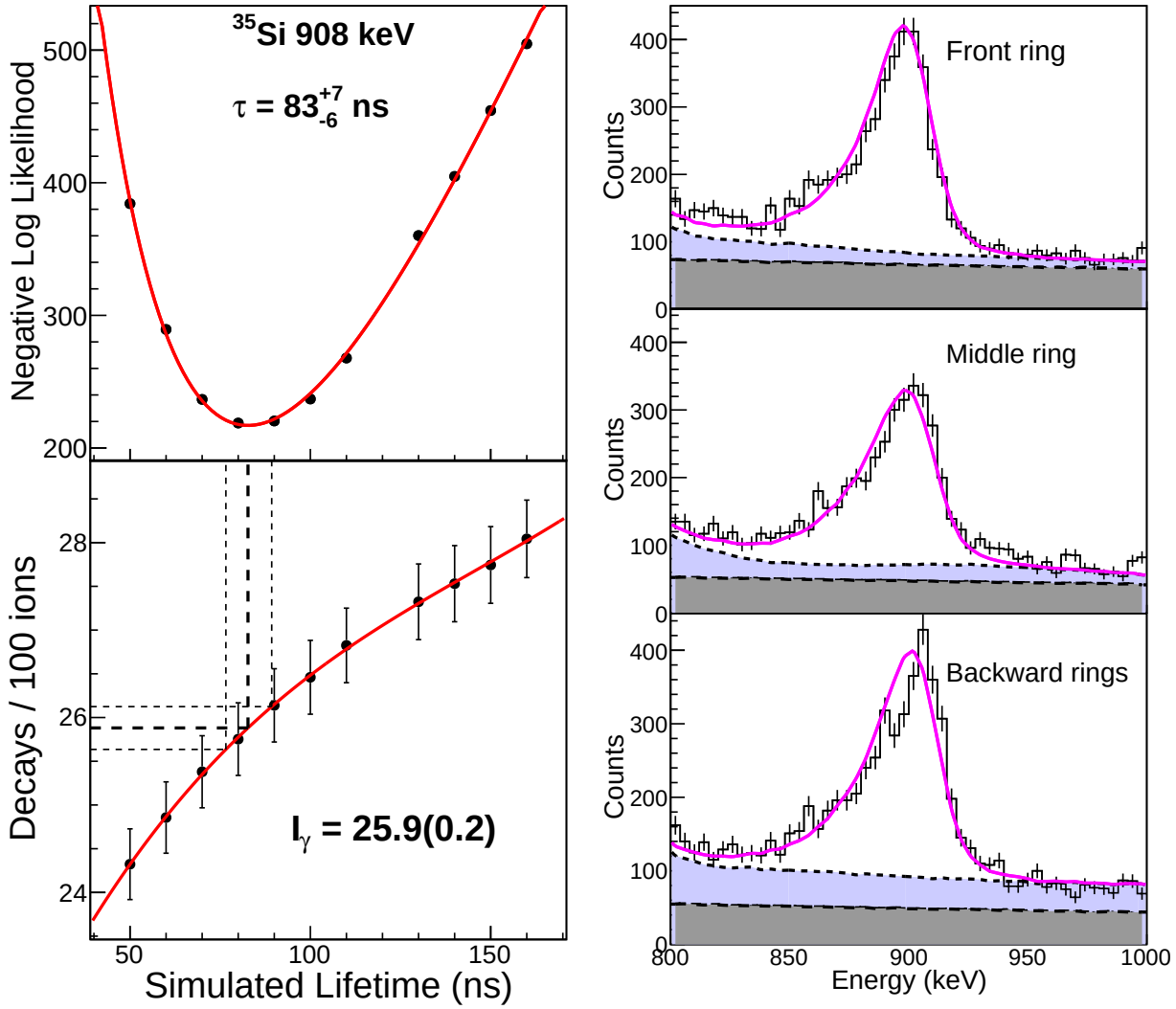

Figure 4.4: Maximum likelihood fit of the lifetime of the state decaying by a 908 keV γ ray in ^{35}Si. The upper-left panel shows the negative log likelihood as a function of simulated lifetime, while the lower-left panel demonstrates the effect of the lifetime uncertainty on the extracted γ-ray intensity. The uncertainties shown in the figure are statistical only. In the right panels, the magenta lines show the simulation with the best fit lifetime for three different rings of GRETINA. The exponential background discussed in §3.3.3 is shown filled in dark gray, and the lighter blue-filled curve shows the additional background due to higher-energy transitions.

The 780 keV transition is clearly seen in the inset to Figure 4.3 to be in coincidence with

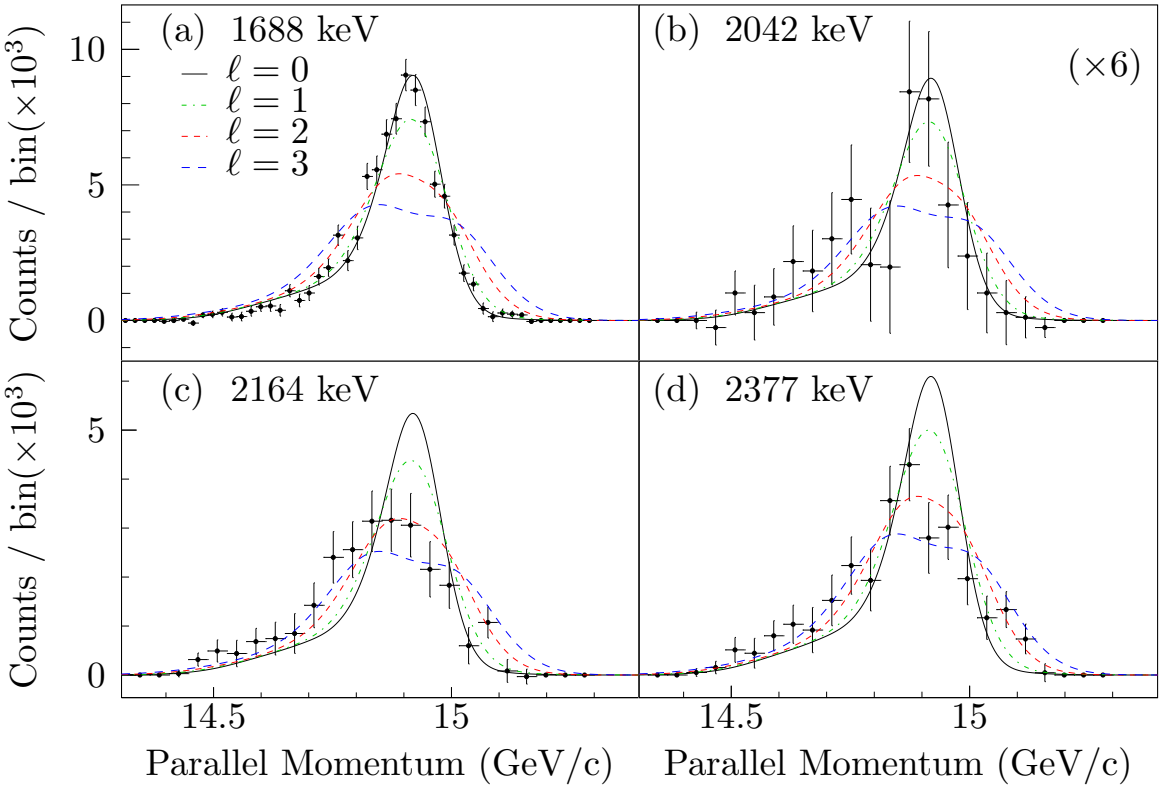

Figure 4.5: Parallel momentum distributions for the population of levels at 1688, 2042, 2164, and 2377 keV in ^{35}Si by neutron knockout from ^{36}Si.

the 908 keV line, depopulating a state at 1688 keV. From the parallel momentum distribution in coincidence with the 780 keV peak, we assign ℓ=0,1 for the removed nucleon. In this knockout reaction, we expect to strongly populate hole states with J^π=$7/2^-, 3/2^+, 1/2^+$ and so we assign this state to be $1/2^+$. While we do not observe the 974 keV $3/2^+ \rightarrow 7/2^-$ transition observed in β decay due to its lifetime, a line at 715 keV is visible, which could connect the 1688 keV and 974 keV states.

The relatively weak transition at 1134 keV likely corresponds to the unplaced 1130 keV transition seen in [129] and the 1134(6) keV transition seen in [9], which was proposed to depopulate a state at 2044 keV. The lower inset of Figure 4.3 reveals a coincidence with the 908 keV transition, confirming the state at 2044 keV. The momentum distribution gated on

the 1134 keV peak suggests $\ell = 0$ or 1, consistent with the $1/2^-$ assignment.

The 2164 keV transition seen in β decay is also present in this measurement, and the coincident momentum distribution suggests $\ell = 2$ or 3, consistent with the $5/2^+$ assignment. We do not see the reported 1194 keV transition connecting that state with the 974 keV state, although the reported 30% branching ratio would put that transition at the limit of our sensitivity.

Due to the low neutron separation energy of 2.48(4) MeV [1] in ^{35}Si and the absence of any excited states below 900 keV, it is assumed that the three other transitions near 2 MeV directly populate the ground state, indicating levels at 1970, 2275, and 2377 keV. The resulting level scheme is shown in Figure 4.6, and the observed transitions are given in Table 4.1.

Table 4.1: Gamma-ray energies, efficiency-corrected intensities, and coincidences for ^{35}Si.

E_γ [keV]	Yield/100 ions	Coincident γ rays	Level [keV]
715(4)	1.9(2)		1688(5)
780(4)	13(1)	908	1688(5)
908(4)	25(2)	780	908(4)
1134(5)	1.5(2)	908	2042(6)
1970(6)	1.4(2)		1970(6)
2164(6)	1.4(2)		2164(6)
2275(6)	2.0(3)		2275(6)
2377(7)	2.5(3)		2377(7)
3611(8)	1.0(2)		3611(8)

Surprisingly, Figure 4.7 shows that we observe one transition at 3611 keV, which must depopulate a state that is unbound to neutron emission by at least 1.1 MeV. Gamma decays which compete with *proton* emission are seen occasionally, as the proton decay may be hindered by the Coulomb barrier (see, for example, [130]). However, γ decays which compete with *neutron* emission are far less common. In general, a strong angular momentum barrier $\ell \geq 4$ is required to hinder the neutron decay, but it is unlikely that an $\ell \geq 4$ state is

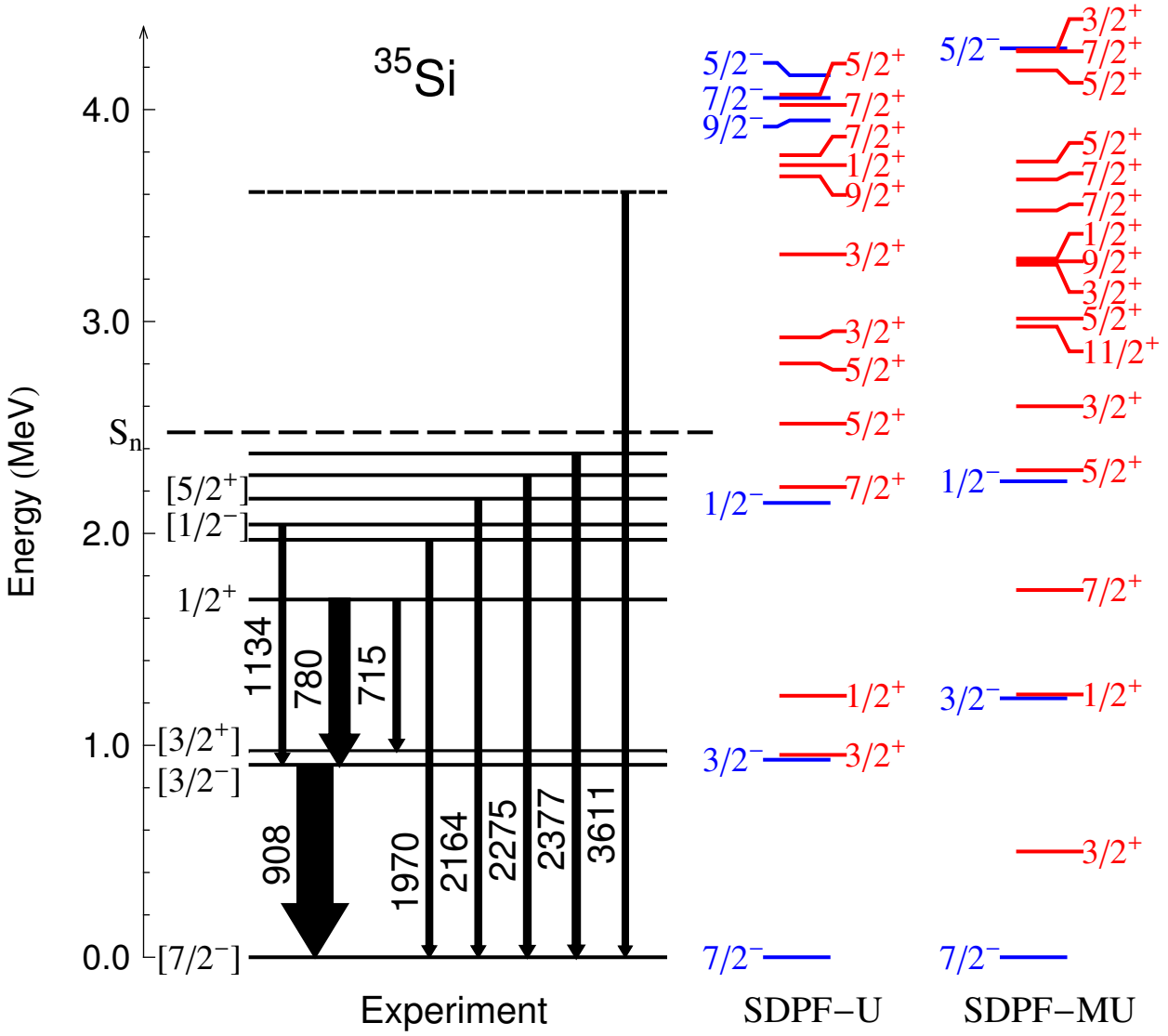

Figure 4.6: Proposed level scheme for ^{35}Si from this work compared with shell-model calculations (see text for details). The widths of the arrows are proportional to the efficiency-corrected γ-ray intensity.

populated directly in a knockout reaction, due to the expected very low occupation of the neutron $g_{9/2}$ and higher orbitals.

One possible explanation for this situation is the combination of a low neutron separation energy in the ^{35}Si parent nucleus (2.48 MeV) and a doubly-magic ^{34}Si daughter nucleus with a high first excited state (2.719 MeV [10]). While a 3.6 MeV state in ^{35}Si is unbound to

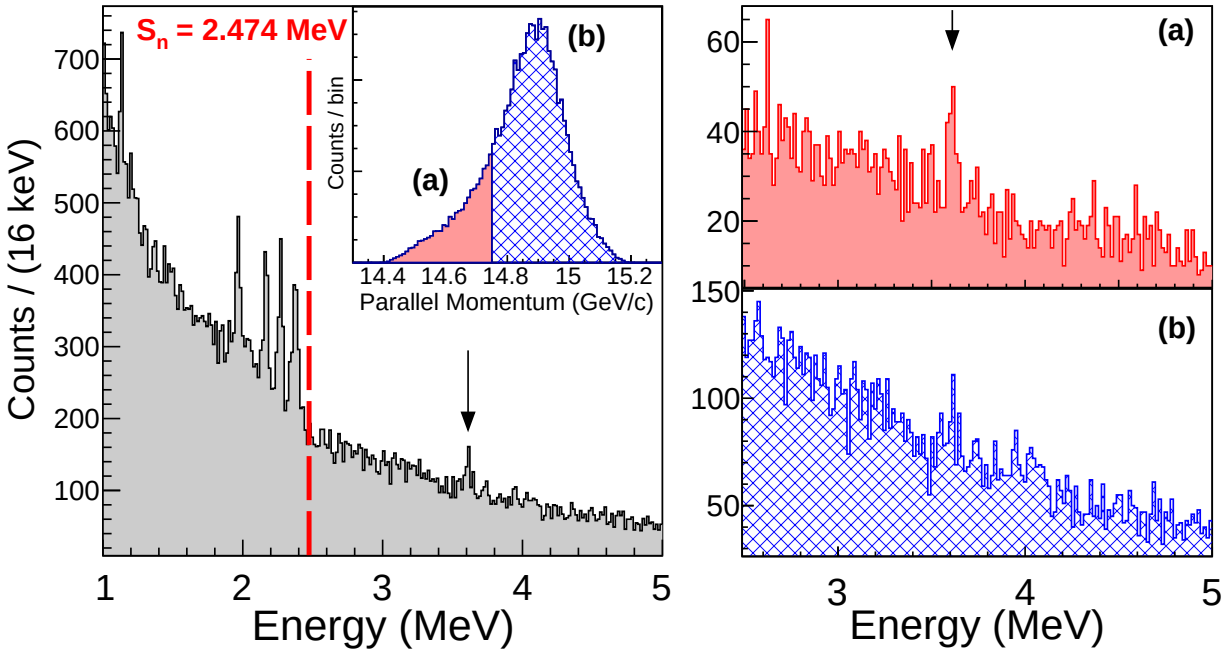

Figure 4.7: The left panel shows the 3611 keV gamma ray peak (indicated with an arrow) detected in coincidence with ^{35}Si, with an inset showing the gates used on the outgoing parallel momentum distribution. The right panel shows the γ spectra gated on the main peak in the momentum distribution (blue hatches) and the low-momentum tail (solid red). The 3611 keV peak appears to be associated with the tail of the distribution.

neutron emission, the ground state of ^{34}Si is the only energetically allowed final state, and so spectroscopic overlaps may significantly hinder the decay. The SDPF-MU (SDPF-U) shell model calculations, combined with eikonal reaction theory, predict knockout to a $5/2^+_3$ state at 3.76 (4.07) MeV with a cross section of 16.8 (13.3) mb. This $5/2^+_3$ state would necessarily contain a neutron hole in the *sd* shell, and could only decay by the emission of a $d_{5/2}$ neutron, resulting in a 2p-2h configuration dominated by two holes in the deeply-bound neutron $d_{5/2}$ orbit. Such a configuration should have a small overlap with the ground state in ^{34}Si – which has a large contribution of 0p-0h configurations [10] – leading to a significantly hindered neutron decay. The γ decay, on the other hand, would be a fast $5/2^+ \rightarrow 7/2^-$ $E1$ decay, and could potentially compete with the neutron emission. Comparing the calculated and measured cross sections, based on the intensity of the 3611 keV γ-ray (see Table 4.7),

the γ branching ratio would be on the order of 5-10%.

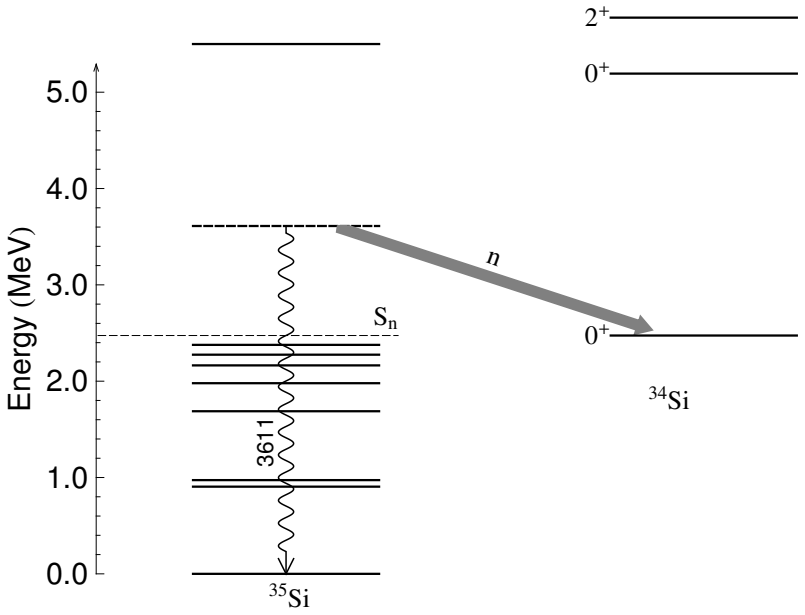

Figure 4.8: Schematic showing the competition between γ decay and neutron emission for the 3611 keV state in ^{35}Si. The ^{35}Si level scheme includes a resonance at 5.5 MeV observed in [9]. The ^{34}Si level scheme includes the recently-proposed first excited 0^+ state [10]. The ground state of ^{34}Si appears to be the only final state for which neutron emission is energetically favorable.

A second explanation could be that this state is weakly populated in a more complicated multi-step reaction pathway. To estimate the yield from such a higher-order removal mechanism, we assume a two-step reaction in which the incident ^{36}Si is first excited to its first 2^+ state, and a neutron is then removed. Such a process is plausible given the (overlapping) surface localization of the two reaction mechanisms. The joint probability for this two-step reaction as a function of the projectile's impact parameter, b, is computed from the deduced impact parameter dependences of the cross sections (reaction probabilities) $\mathrm{d}\sigma/\mathrm{d}b$, for the $0^+ \rightarrow 2^+$ inelastic excitation and the neutron removal from the 2^+_1 state. The former is deduced from a conventional inelastic scattering calculation made using the direct reactions code FRESCO [131] and the latter is extracted from the eikonal model calculation of the

single-particle cross section. The resulting joint probability, integrated over impact parameters, is then multiplied by the SDPF-MU shell-model spectroscopic factor for knockout to the candidate 3611 keV final states of ^{35}Si.

With our assumption of neutron knockout from the ^{36}Si(2_1^+) state, the most likely candidates for the 3611 keV state, based on the shell model spectroscopic factors and knockout cross sections, are the $7/2_1^+$ and $5/2_2^+$ states, see Figure 4.6. Based on the two-step model above, the estimated two-step cross sections are 0.29 and 0.21 mb, respectively. Essentially identical results are obtained if, instead, one assumes the probability of projectile excitation to the 2_1^+ state to be the ratio of the total inelastic and elastic cross sections, with the latter computed from the eikonal model S-matrix for ^{36}Si + ^{9}Be scattering using the methodology discussed here. These two-step estimates are of the same order as the experimental 3611 keV state cross section of 0.8(2) mb. We note that in both shell model calculations the first of these states lies below the neutron threshold and the second lies above, with energies near 3 MeV. So, if either candidate is the 3611 keV state, these energies suggest a significant discrepancy between the shell model and experiment.

The $7/2_1^+$ state would need to decay to the ^{34}Si ground state by an $\ell = 4$ neutron emission, whose spectroscopic factor would be very small, although it cannot be calculated in the shell model, as the $g_{7/2}$ orbit is well outside the model space. The $5/2_2^+$ state would decay by $\ell = 2$ neutron emission and, as described above for the directly-populated $5/2^+$ state, would be hindered. In both cases the γ decay to the $7/2^-$ ground state would be $E1$ and could compete with the hindered neutron decay.

An additional piece of information is given by the momentum distribution associated with the population of this state. The statistics are insufficient to obtain a background-subtracted momentum distribution for the 3611 keV γ-ray line, as was done for the states in

Figure 4.5. However, when the γ-ray spectrum is gated on high- and low-momentum regions of the outgoing momentum distribution, as shown in the right panel of Figure 4.7, it is clear that the 3611 keV line results predominantly from events with residue momenta in the tail of the momentum distribution. As was discussed in §3.3.3 and §3.4, the low-momentum tail is associated with more inelastic reactions, which would be consistent with a multi-step process. However, the direct knockout of a more deeply-bound $d_{5/2}$ neutron could potentially also produce a distribution with a significant tail.

Clearly, if the $7/2^+_1$ and $5/2^+_2$ states could be identified independently and their energies found to be different from 3.6 MeV, then these observations would favor the direct process.

4.2.2 ^{35}Al

The nuclide ^{35}Al was previously studied by Coulomb excitation, yielding one transition at 1020(8) keV [132]. The ground state is assumed to be $5/2^+$ from shell model calculations and systematics, and so the spin of the Coulomb-excited state could be anything from 1/2 to 9/2.

In this work we observe many transitions and coincidences, shown in Figure 4.9 and tabulated in Table 4.2. The two strongest transitions, at 802 and 1003 keV, are not in coincidence and are assumed to feed the ground state. Transitions at 859, 968, and 2237 keV are clearly seen to be in coincidence with the 1005 keV transition, shown in the inset of Figure 4.9, and we place them depopulating levels at 1864, 1972, and 3243 keV, respectively. Transitions at 1064, 1174, and 2440 keV each differ from the previously mentioned transitions by approximately 200 keV, and although a coincidence is not observed we tentatively assign these transitions to connect the levels at 1862, 1972 and 3243 keV to the level at 802 keV. The transition at 1932 keV is in coincidence with the 802 keV transition, as shown in the

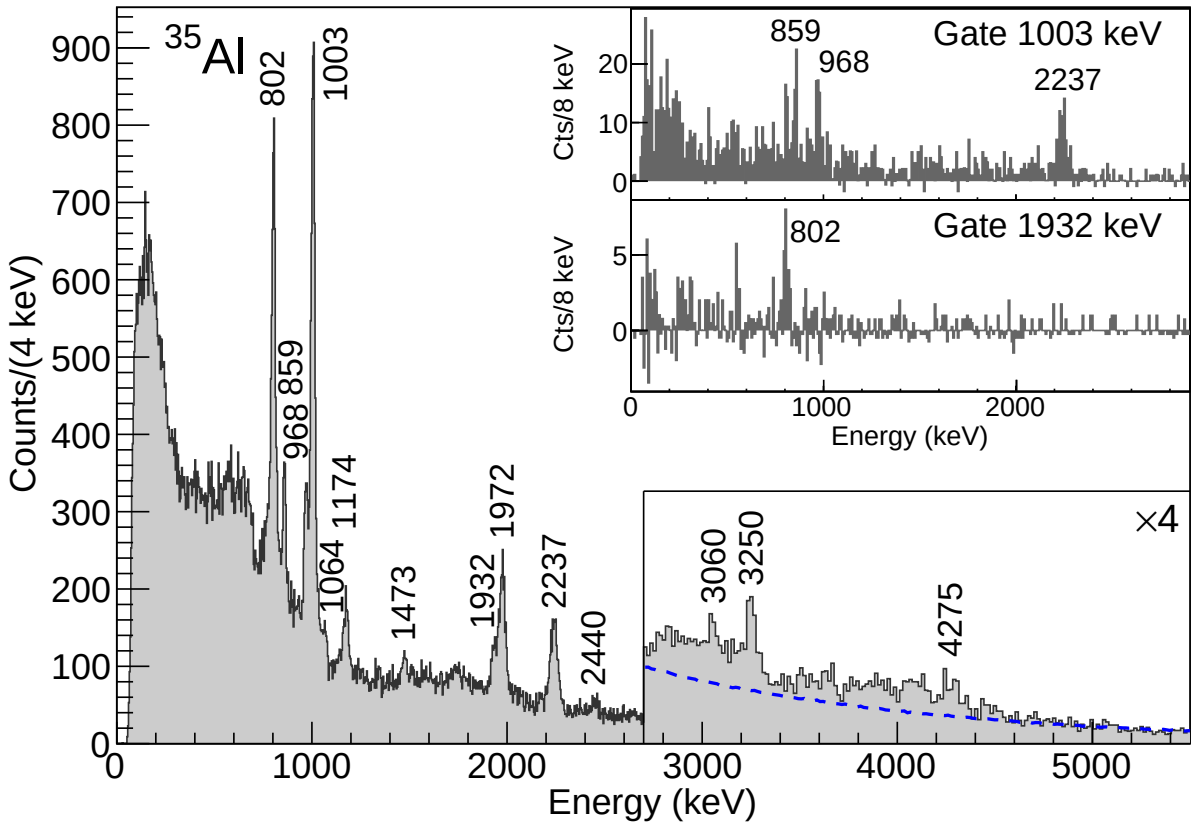

Figure 4.9: Doppler-reconstructed γ-ray spectrum detected in coincidence with ^{35}Al. The section of the spectrum in the box labeled $\times 4$ has been rebinned by a factor 4. The blue dashed line shows the fitted background, suggesting a peak at 4275 keV. The inset in the upper-right shows background-subtracted $\gamma\gamma$ coincidence matrices gated on the 1003 and 2237 keV transitions. The Doppler reconstruction was performed with a velocity $v/c = 0.424$

lower inset of Figure 4.9, and it is placed depopulating a state at 2734 keV. The transition at 1972 keV is not observed to have any coincident transitions, and we place it connecting the level at 1972 keV to the ground state. Likewise, we place the transition at 3250 keV connecting the level at 3243 keV to the ground state. The neutron separation energy for ^{35}Al is 5244(92) keV [1], so the transition at 4275 keV, shown in Figure 4.12 above an exponential background, could populate the ground state or one of the lowest two excited states. In the absence of any observed coincidences, we tentatively place the 4275 keV transition feeding the ground state.

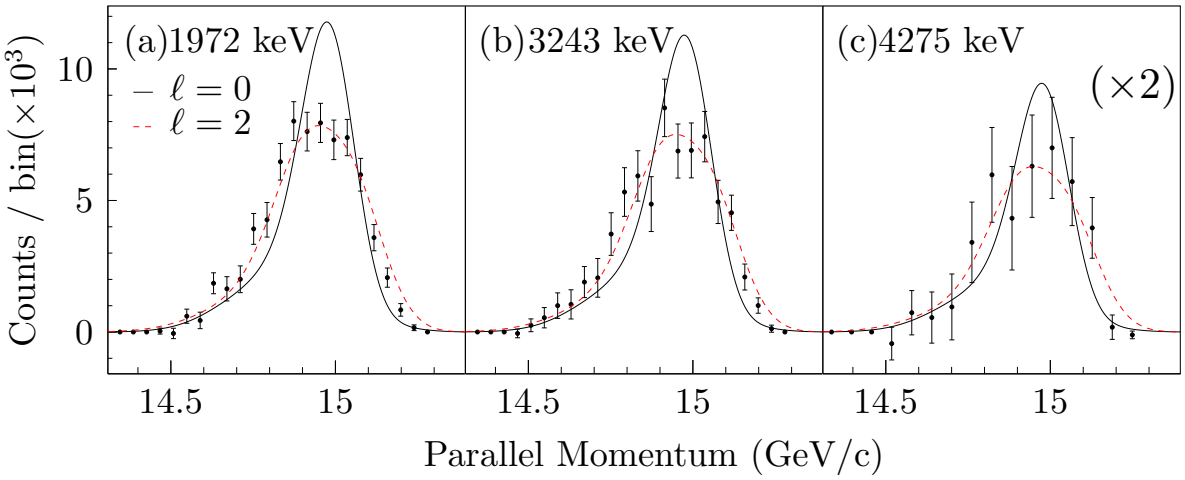

Figure 4.10: Parallel momentum distributions for the population of levels at 1972, 3243, and 4275 keV in ^{35}Al by proton knockout from ^{36}Si.

Momentum distributions in coincidence with decays from the proposed levels at 1972, 3243, and 4275 keV are shown in Figure 4.10, and the momentum distribution for the population of the ground state is shown in Figure 3.17(c). All of these distributions are consistent with the removal of an $\ell = 2$ proton.

Table 4.2: Gamma-ray energies, efficiency-corrected intensities, and coincidences for ^{35}Al. Levels marked with an asterisk are tentative.

E_γ [keV]	Yield/100 ions	Coincident γ rays	Level [keV]
802(4)	10(1)	1923	802(4)
859(4)	3.6(3)	1003	1864(5)
968(4)	4.4(3)	1003	1972(4)
1003(4)	19(1)	859, 968, 2237	1003(4)
1064(4)	0.8(2)		1864(5)
1174(5)	2.8(3)		1972(4)
1473(5)	1.1(2)		
1932(6)	2.5(3)	802	2734(7)
1972(6)	7.5(5)		1972(4)
2237(6)	7.8(6)	1003	3243(5)
2440(7)	1.4(2)		3243(5)
3060(8)	1.6(4)		
3250(8)	3.3(4)		3243(5)
4275(9)	3(1)		4275(9)*

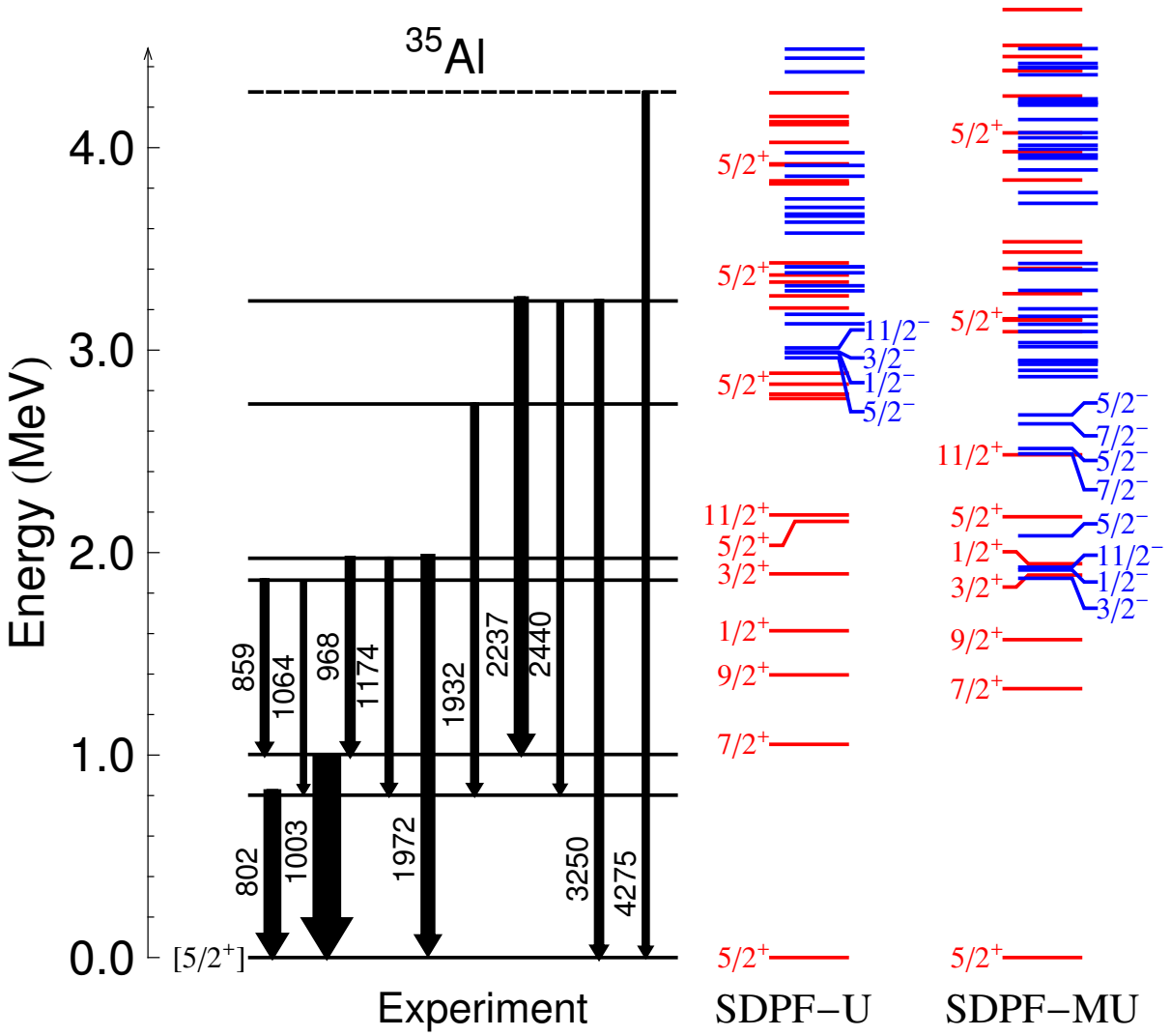

Figure 4.11: Proposed level scheme for ^{35}Al from this work compared with shell-model calculations (see text for details). The width of the arrows is proportional to the efficiency-corrected γ-ray intensity.

4.2.3 ^{37}Si

The structure of ^{37}Si has been previously studied by Coulomb excitation [132], in which the authors tentatively proposed a level at 1437(27) keV, and also by the β decay of ^{37}Al [133], in which levels at 68, 156, 717, and 1270 keV were proposed. The authors mention in [132] that the 1437 keV level is uncertain and could be due to a stripping reaction, rather than inelastic scattering. As no transition near 1437 is seen in the present work or the β decay,

and the $2_1^+ \rightarrow 0_1^+$ transition in ^{36}Si lies at 1408 keV [134], we do not include this level in the ^{37}Si level scheme. The levels from β decay at 717 and 1270 keV were tentatively assigned to $3/2^+$ and $5/2^+$, respectively, based on $\log(ft)$ values.

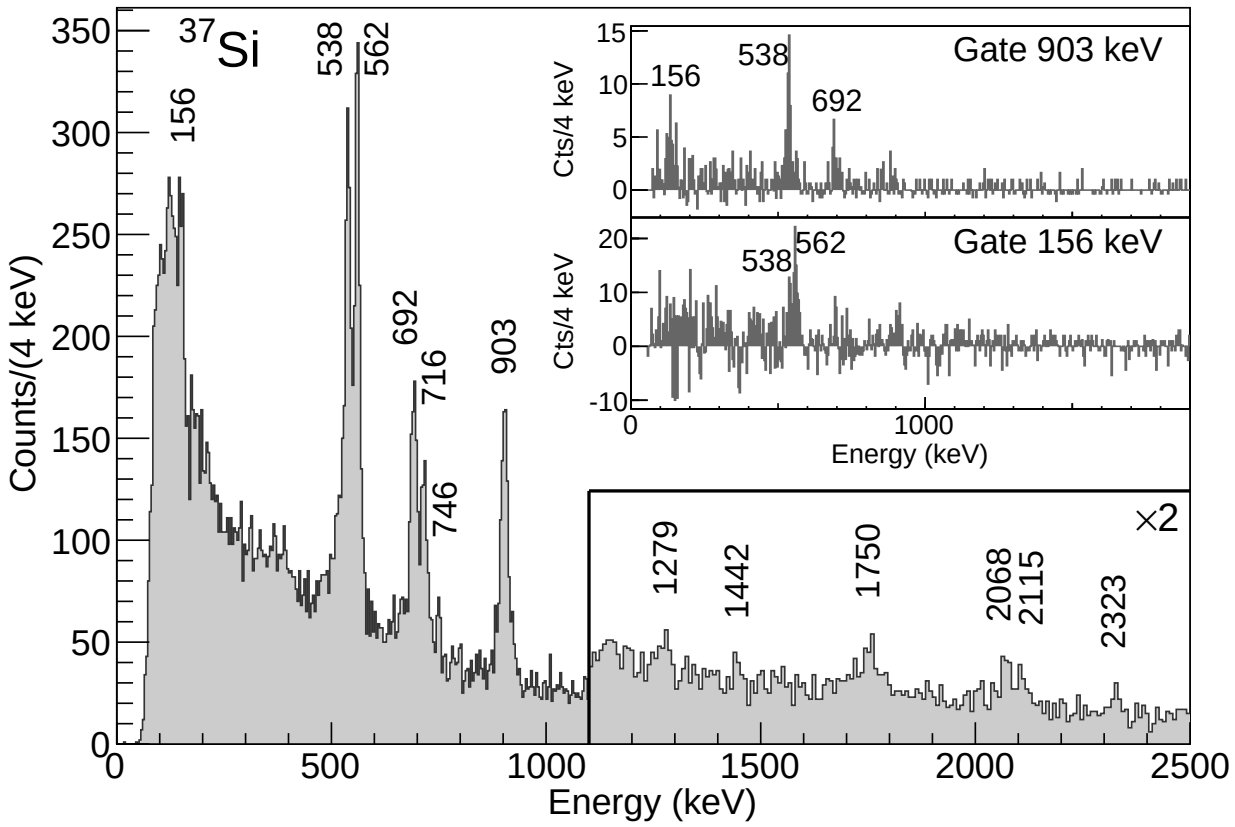

Figure 4.12: Doppler-reconstructed γ-ray spectrum detected in coincidence with ^{37}Si. The section of the spectrum in the box labeled $\times 2$ has been rebinned and scaled by a factor of 2. The inset shows the background-subtracted $\gamma\gamma$ coincidence matrix gated on the peaks at 156 and 903 keV. The Doppler reconstruction was performed with a velocity $v/c = 0.403$.

Unlike in ^{35}Si, where the $7/2^-$ ground state is well separated from the first excited states, the shell model predicts low-lying $3/2^-$ and $5/2^-$ states, which correspond primarily to seniority $v = 3$ $(f_{7/2})^3$ configurations, with the $5/2^-$ predicted to be the ground state. This suggests that, whatever the spin-parity of the ground state, the other two low-lying states may be isomers. Additionally, these states allow the $3/2^+$ intruder state to decay by a fast $E1$, making the population of the $3/2^+$ state detectable.

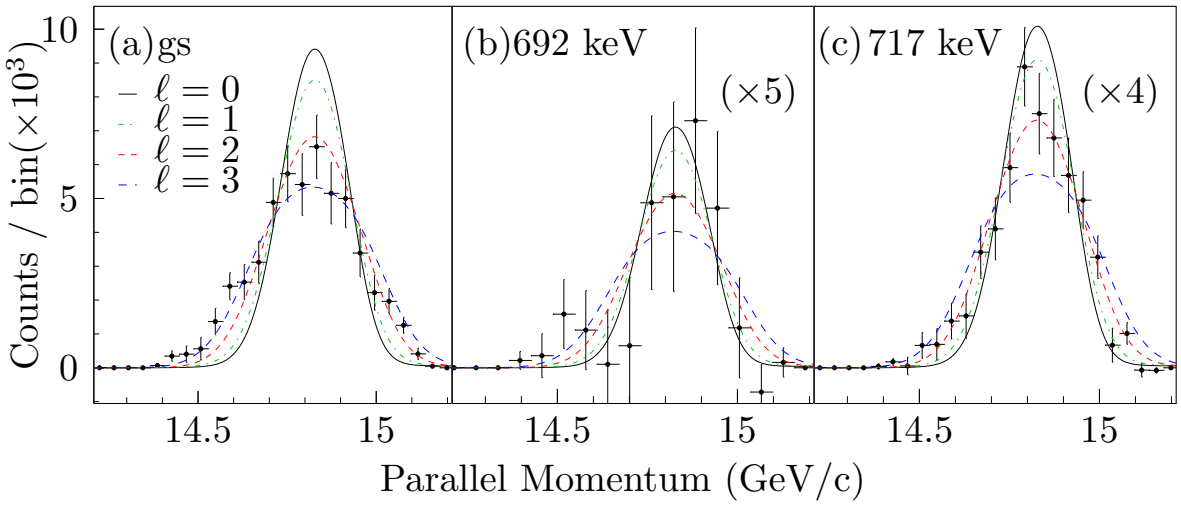

Figure 4.13: Parallel momentum distributions for the population of the ground state and excited states at 692 and 717 keV in ^{37}Si by neutron knockout from ^{38}Si. Note that the ground state distribution includes both the $5/2^-_1$ and $7/2^-_1$ states.

The γ-ray spectrum for the current measurement is shown in Figure 4.12. We observe transitions at 562 and 716 keV, consistent with the β decay findings. The parallel momentum distribution in coincidence with a decay from the 716 keV level (Figure 4.13(c)) suggests a removal of an ℓ=2 neutron, consistent with the $3/2^+$ assignment. The transition at 156 keV is also seen, although it is broadened by a lifetime effect. From simulation, we estimate the lifetime of the 156 keV state to be τ=4.4(10) ns. Assuming a pure M1 transition, this corresponds to $B(M1; 3/2^-_1 \rightarrow 5/2^-_1) = 3.4^{+1.0}_{-0.7} \times 10^{-3}\ \mu^2_N$, which may be compared with shell model values of 1×10^{-3} and $1.5 \times 10^{-2}\ \mu^2_N$ for SDPF-U and SDPF-MU, respectively.

In addition, we observe two new transitions at 538 and 692 keV, which are also separated by approximately 156 keV. We place these transitions depopulating a state at 692 keV. From the parallel momentum distribution shown in Figure 4.13(b) and comparison to shell model calculations, we assign this level to be $3/2^-$. We observe that this $3/2^-$ level is nearly degenerate with the lowest $3/2^+$ level, as in ^{35}Si and as predicted by SDPF-MU. In the calculations, the lowest-lying $3/2^-_1$ state is generated primarily by a neutron $(f_{7/2})^3$

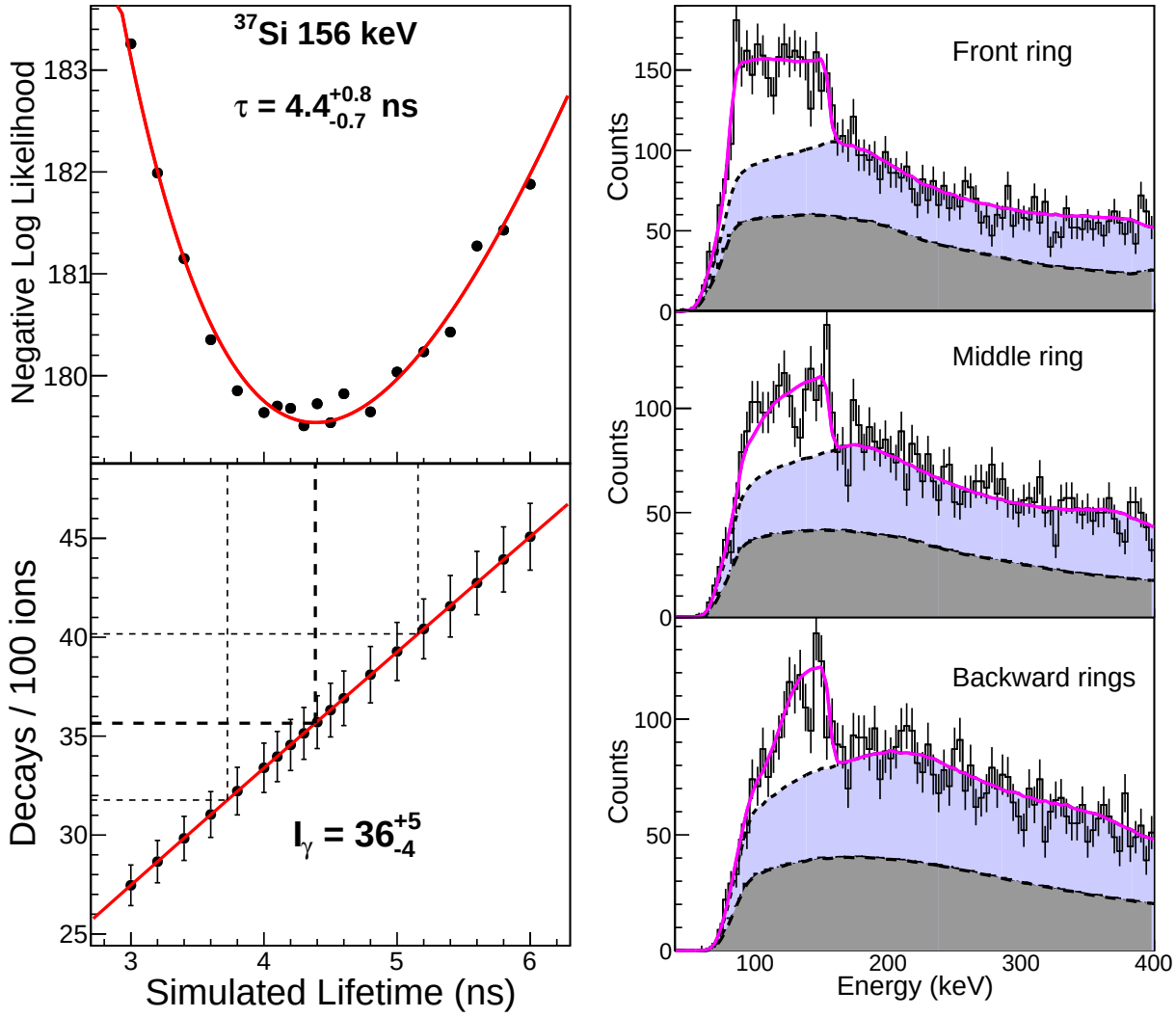

Figure 4.14: Maximum likelihood fit of the lifetime of the state decaying by a 156 keV γ ray in ^{37}Si. The upper-left panel shows the negative log likelihood as a function of simulated lifetime, while the lower-left panel demonstrates the effect of the lifetime uncertainty on the extracted γ-ray intensity. The uncertainties shown in the figure are statistical only. In the right panels, the magenta lines show the simulation with the best fit lifetime for three different rings of GRETINA. The exponential background discussed in §3.3.3 is shown filled in dark gray, and the lighter blue-filled curve shows the additional background due to higher-energy transitions.

configuration, while the $3/2^-_2$ state is generated primarily by an $(f_{7/2})^2 p_{3/2}$ configuration.

A transition at 903 keV is observed to be in coincidence with the 692 and 538 keV transitions (see the inset in Figure 4.12), and it is placed connecting a level at 1596 keV to the level at 692 keV. The corresponding parallel momentum distribution in Figure 3.17(d)

suggests $\ell = 0$ or 1. Considering its strong population and comparing to the shell model and the ^{35}Si level scheme, we assign this state to be $1/2^+$.

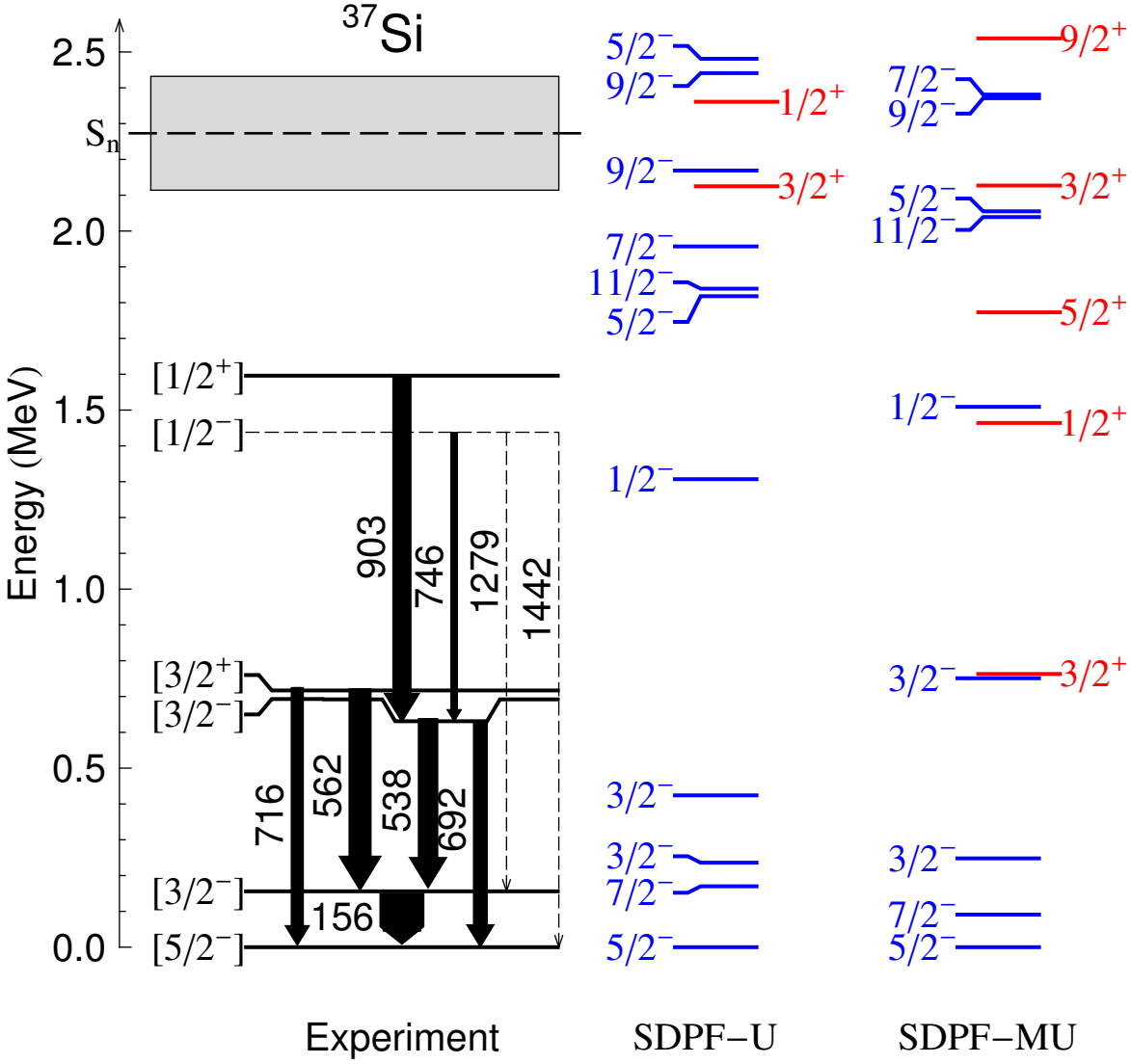

Figure 4.15: Level scheme for ^{37}Si from this work compared with shell-model calculations (see text for details). The width of the arrows is proportional to the γ-ray intensity. Fine dashed lines indicate tentative levels and transitions, while the thicker dashed line labeled S_n indicates the neutron separation energy, with the gray shaded area indicating the uncertainty.

A possible transition at 1279 keV could be associated with the $5/2^+$ level from β decay. In that work, the 1270 keV level fed the ground state and excited states at 68 and 156 keV with roughly equal branching ratios, indicating that we should see transitions at 1202 and

1115 keV, which we do not. As an alternative, we note that the difference between the 1279 and 746 keV transitions is 533 keV, which agrees within uncertainty with the energy difference between the 692 and 156 keV levels, suggesting a level at 1438 keV. Indeed, we also see a possible very weak transition at 1442 keV, which would connect this level to the ground state. This state would be a candidate for the $1/2^-_1$ level predicted in both shell model calculations in Figure 4.15, which would decay by $M1$ to both $3/2^-$ states and by $E2$ to the $5/2^-$ ground state. Decay to the $3/2^+_1$ intruder state would be hindered because the predominant single-particle configurations, $(d_{3/2})^{-1}(f_{7/2})^4$ and $(f_{7/2})^2 p_{1/2}$ cannot be connected with a one-body operator. We therefore tentatively place the $1/2^-$ state in the level scheme at 1438 keV.

Table 4.3: Gamma-ray energies, efficiency-corrected intensities, and coincidences for ^{37}Si. Levels and transitions marked with an asterisk are tentative.

E_γ [keV]	Yield/100 ions	Coincident γ rays	Level [keV]
156(3)	40(5)	538, 562	156(3)
538(4)	11(1)	156, 903	693(4)
562(4)	13(1)	156	717(4)
692(4)	6.6(9)	903	693(4)
716(4)	5.3(8)		717(4)
746(4)	0.8(6)		1438(6)*
903(4)	10(1)	538, 692	1596(5)
1279(5)*	1.4(5)		1438(6)*
1442(5)*	0.6(5)		1438(6)*
1750(6)	2.3(7)		
2068(6)	1.9(6)		
2115(6)	1.8(6)		
2323(6)*	0.8(5)		

The additional observed transitions at 1750, 2068, 2115 keV and a possible transition at 2323 keV are not placed in the level scheme, although due to the neutron separation energy at 2250(100) keV, they will very likely only feed the ground state or other members of the low-lying multiplet. The observed γ-rays are tabulated in Table 4.3 and the proposed level

scheme is shown in Figure 4.15.

4.2.4 ^{37}Al

No previous data exist on excited states of ^{37}Al. In this work, we observe a strong transition at 775 keV. This transition is seen to be coincident with the transition at 2558 keV and with itself. Since the coincidence spectrum is background-subtracted, this indicates that there is another transition with a nearly identical energy. In fact, the 775 keV peak has a shoulder at low energy, suggesting a possible second peak. A fit with two Gaussians gives a best description with peaks at 775 and 755 keV, suggesting levels at 775 and 1530 keV, as shown in Figure 4.17. The transition at 3321 keV agrees within uncertainty with the sum of 775 and 2558, and so we place that transition connecting a level at 3327 keV with the ground state. The transitions at 1255 and 1393 keV are not observed in coincidence with either peak in the doublet at 775 keV, and they are not expected to feed the state at 3327, due to the neutron separation energy at 4210(160) keV [1]. We therefore tentatively place the 1253 and 1393 keV transitions directly populating the ground state. Observed transitions at 861, 1612, and 2722 keV are not placed in the level scheme. We note that the intensities of these three unplaced transitions could account for most of the remaining population of the state at 775 keV.

4.2.5 ^{39}Si

The excited states of ^{39}Si have been studied previously by fragmentation of ^{40,41}P and ^{42,43}S [11]. Sohler *et al*. observed prominent peaks at 163(12) and 397(14) keV, as well as several other more weakly-populated transitions, and their high efficiency allowed them to establish

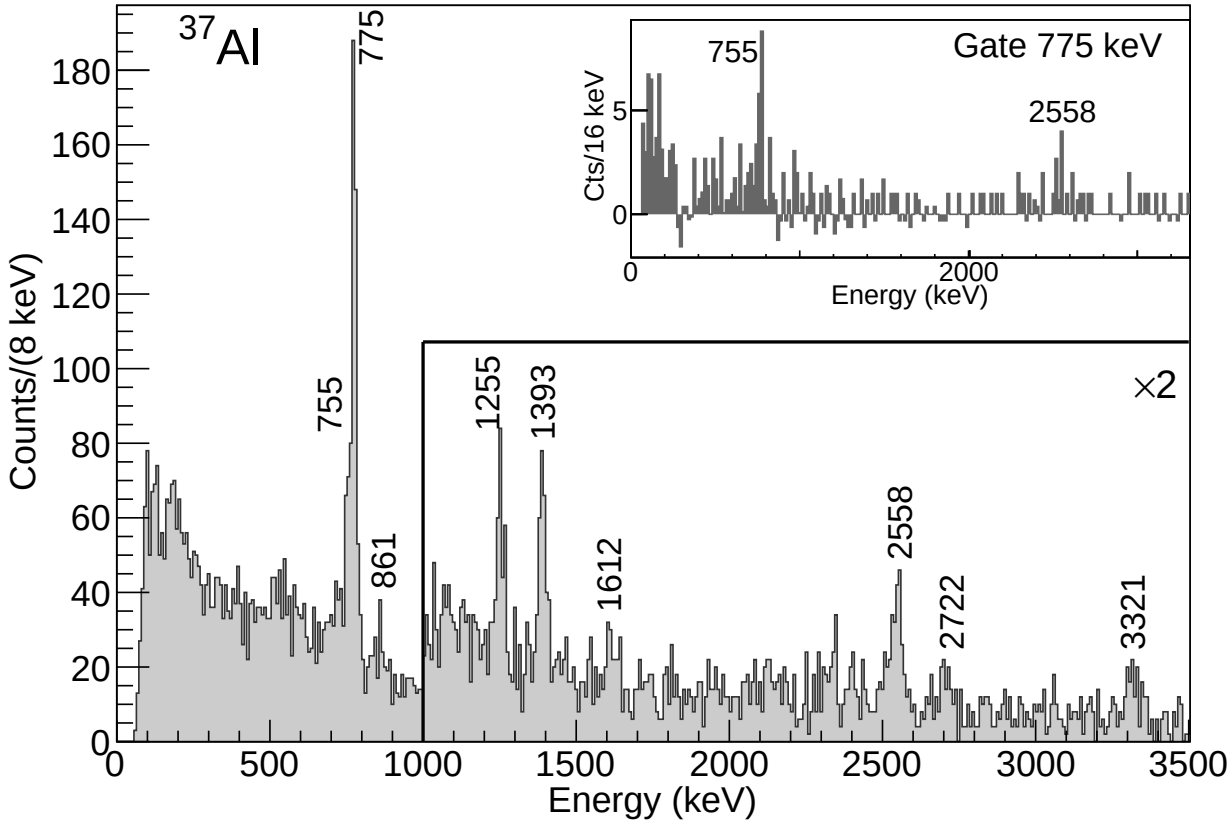

Figure 4.16: Doppler-reconstructed γ-ray spectrum detected in coincidence with ^{37}Al. The section of the spectrum in the box labeled $\times 2$ has been rebinned and scaled by a factor of 2. The inset shows the background-subtracted $\gamma\gamma$ coincidence matrix gated on the peak at 775 keV. The Doppler reconstruction was performed with a velocity $v/c = 0.400$.

Table 4.4: Gamma-ray energies, efficiency-corrected intensities, and coincidences for ^{37}Al. Levels marked with an asterisk indicate a tentative assignment.

E_γ [keV]	Yield/100 ions	Coincident γ rays	Level
755(6)	4.5(12)	775	1530(7)
775(4)	23(2)	755	775(4)
861(4)	2.6(10)		
1255(5)	7.0(13)		1255(5)*
1393(5)	6.7(13)		1393(5)*
1612(5)	3.2(11)		
2558(7)	7.3(19)	775	3327(8)
2722(7)	3.8(16)		
3321(8)	4.7(15)		3327(8)

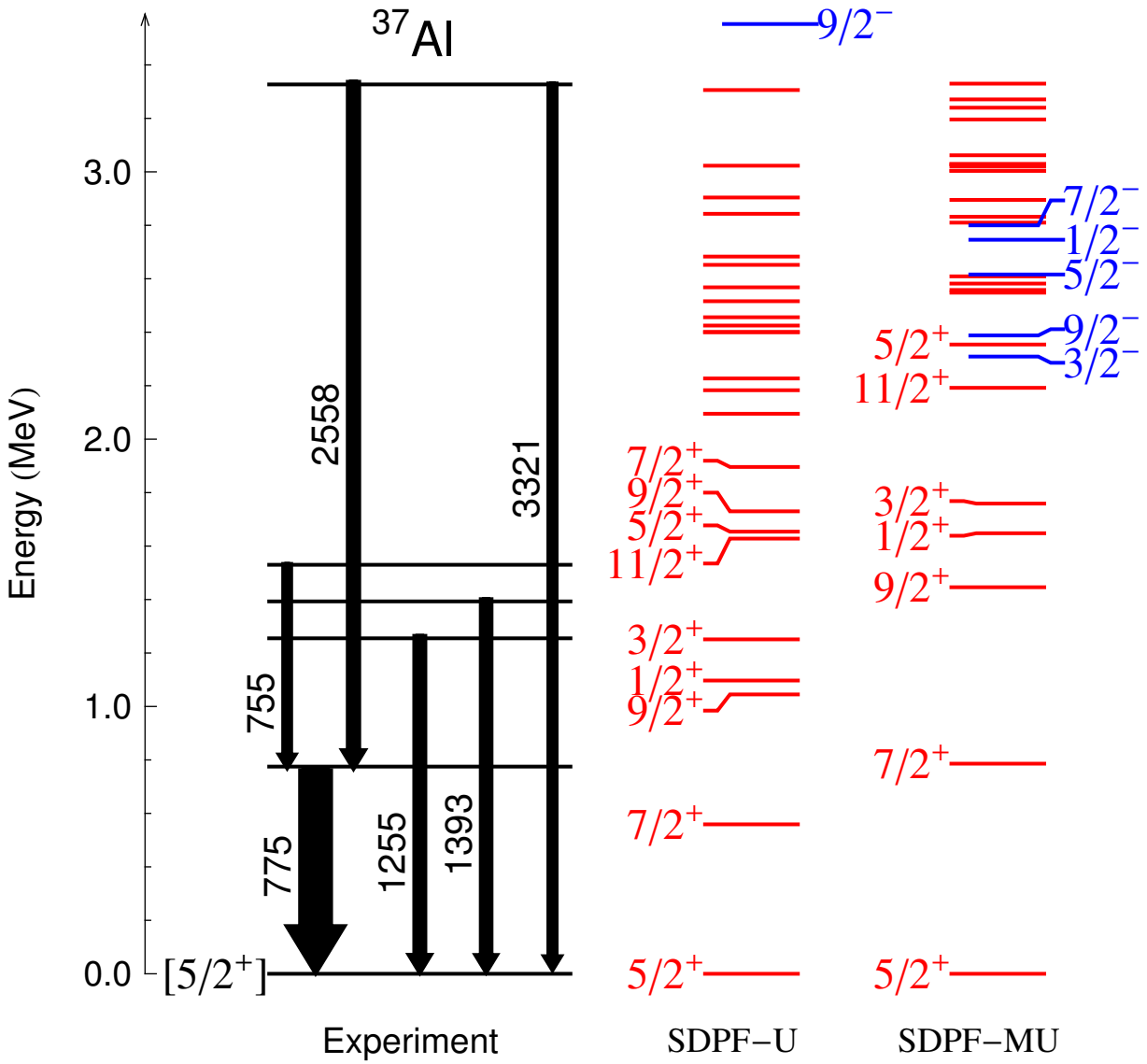

Figure 4.17: Proposed level scheme for ^{37}Al from this work compared with shell-model calculations (see text for details). The width of the arrows is proportional to the efficiency-corrected γ-ray intensity.

several $\gamma\gamma$ coincidences. As in ^{37}Si, the shell model predicts two low-lying $v = 3$ states for ^{39}Si, suggesting the presence of two isomers. As described before, these states allow the prompt decay of the $3/2^+$ intruder state.

In the present work, we observe a strong peak at 172 keV, likely broadened by a lifetime effect (see Figure 4.19). From simulation we estimate the lifetime of the 172 keV transition

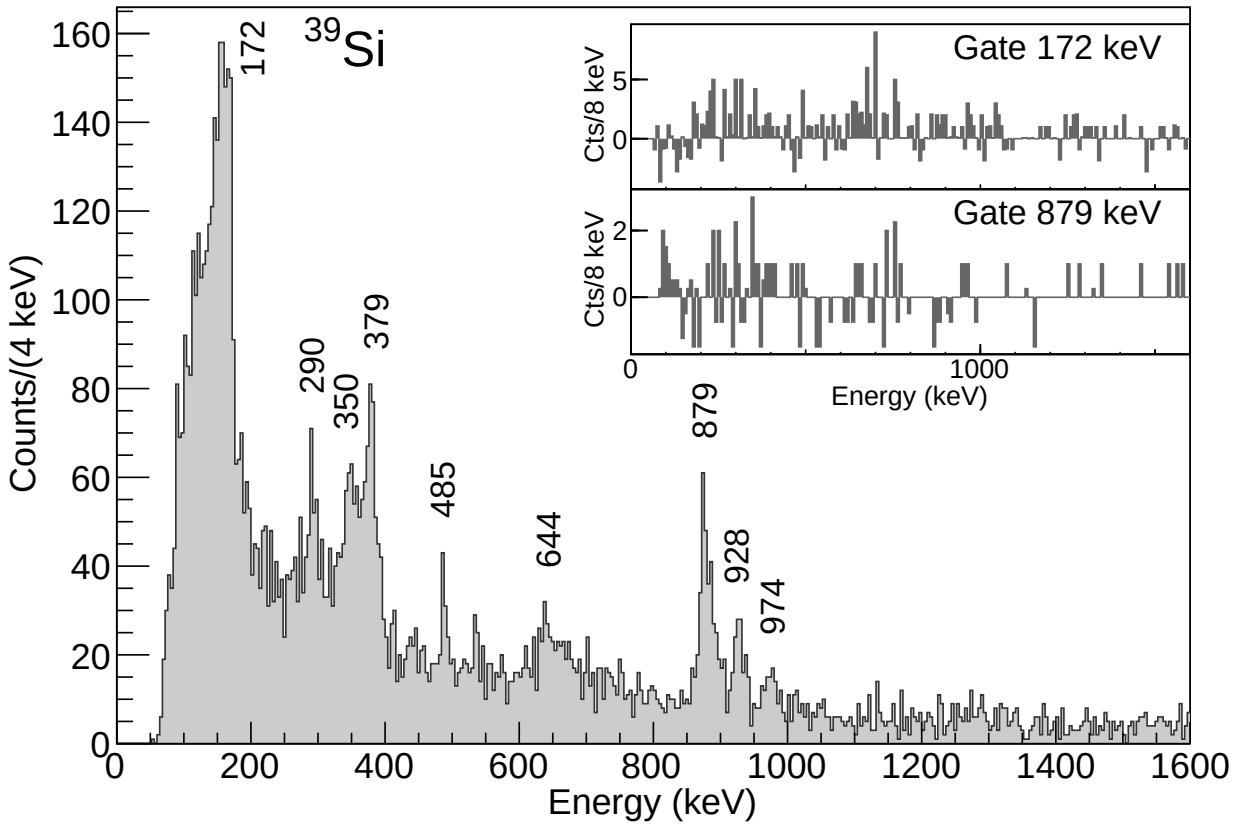

Figure 4.18: Doppler-reconstructed γ-ray spectrum detected in coincidence with ^{39}Si. The Doppler reconstruction was performed with a velocity $v/c = 0.379$. The inset shows the background-subtracted $\gamma\gamma$ coincidence matrix gated on the peaks at 172 and 879 keV, revealing no strong coincidences with either peak.

to be τ=1.4(2) ns. Assuming a pure M1 transition $7/2^- \rightarrow 5/2^-$, as discussed below, this corresponds to $B(M1; 7/2^-_1 \rightarrow 5/2^-_1) = 8(1)\times10^{-3}\ \mu_N^2$, compared to shell model predictions of 3×10^{-3} and $6 \times 10^{-3}\ \mu_N^2$ for SDPF-U and SDPF-MU, respectively.

In [11], the γ-ray spectrum resulting from proton knockout from ^{40}P was dominated by the 163 keV transition, which we associate with our 172 keV transition due to the fact that the lifetime effect – imperceptible with their energy resolution – shifts the centroid of the peak to a slightly lower energy. Using the SDPF-MU spectroscopic factors and single-particle cross sections from eikonal theory with a quenching factor R=0.4, we estimate the cross sections for one proton knockout from ^{40}P to the lowest-lying states in ^{39}Si to be $5/2^-_1$:

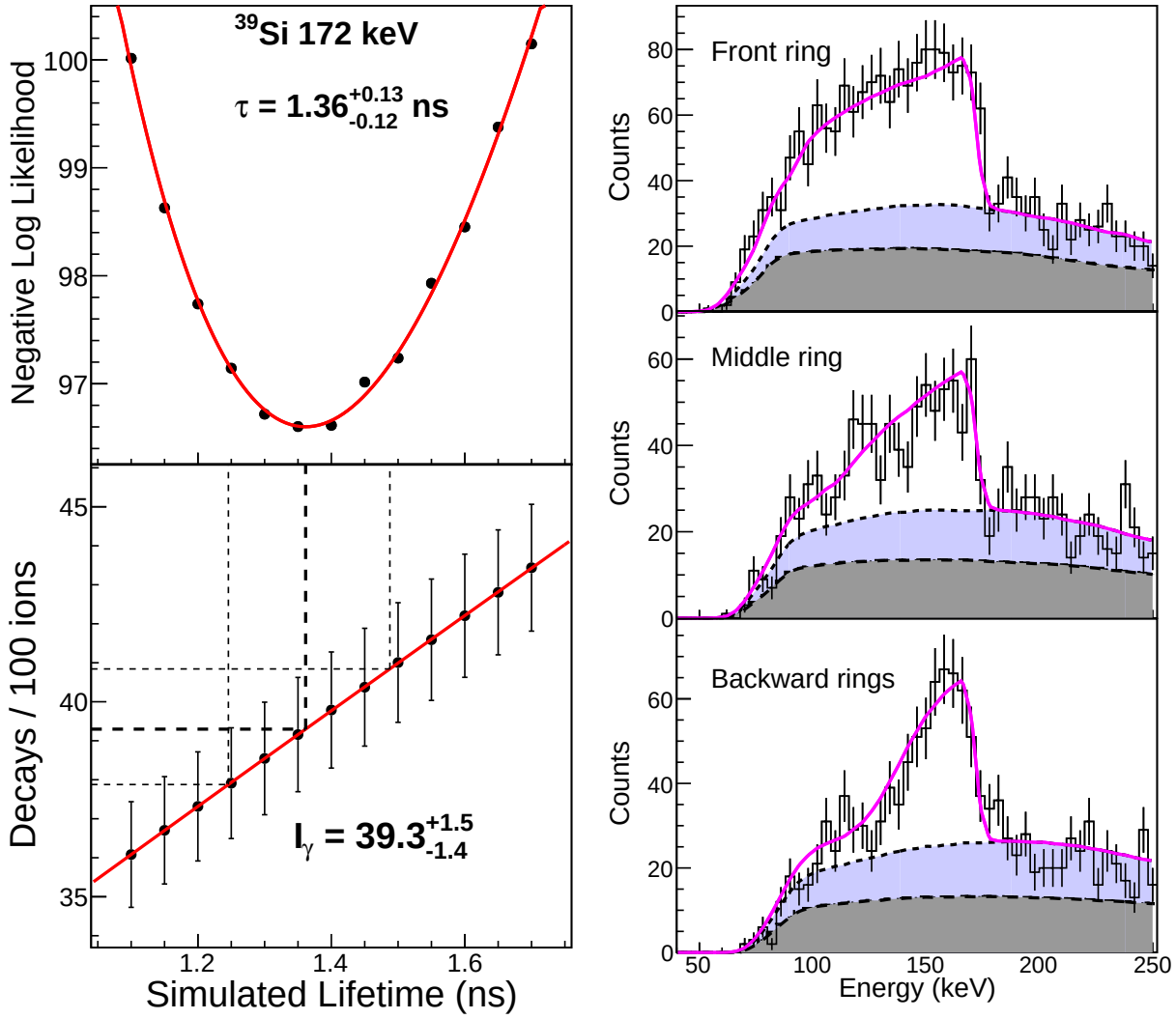

Figure 4.19: Maximum likelihood fit of the lifetime of the state decaying by a 172 keV γ ray in ^{39}Si. The upper-left panel shows the negative log likelihood as a function of simulated lifetime, while the lower-left panel demonstrates the effect of the lifetime uncertainty on the extracted γ-ray intensity. The uncertainties shown in the figure are statistical only. The right panels show the best fit for three different rings of GRETINA. The exponential background discussed in §3.3.3 is shown filled in dark gray, and the lighter blue-filled curve shows the additional background due to higher-energy transitions.

1.8 mb, $7/2^-_1$: 1.1 mb, $3/2^-_1$: 0.1 mb, $1/2^-_1$: 0.06 mb, $5/2^-_2$: 0.4 mb, $3/2^-_2$: 0.2 mb. (Here we assume a 2^- ground state, although the results are similar if we assume a 3^- ground state.) This suggests that their 163 keV transition depopulates either the $5/2^-_1$ or $7/2^-_1$. Since we also populate this transition strongly in one neutron knockout, it is most likely that this

transition depopulates the $7/2^-_1$ state. The parallel momentum distribution in coincidence with this transition shown in Figure 4.20(a) suggests $\ell = 2$ or 3 for the removed nucleon, in support of this assignment. Due to the low energy of the transition, it most likely proceeds by $E1$ or $M1$. From comparison with the shell model level schemes, the most likely candidate for the final state is $5/2^-$. The shell-model calculations also predict a low-lying $3/2^-$ state which, within the uncertainty of the calculations, could lie below the $5/2^-$, making it the ground state. If that were the case, the levels proposed here would be shifted up in energy by the gap between the $3/2^-$ and the $5/2^-$.

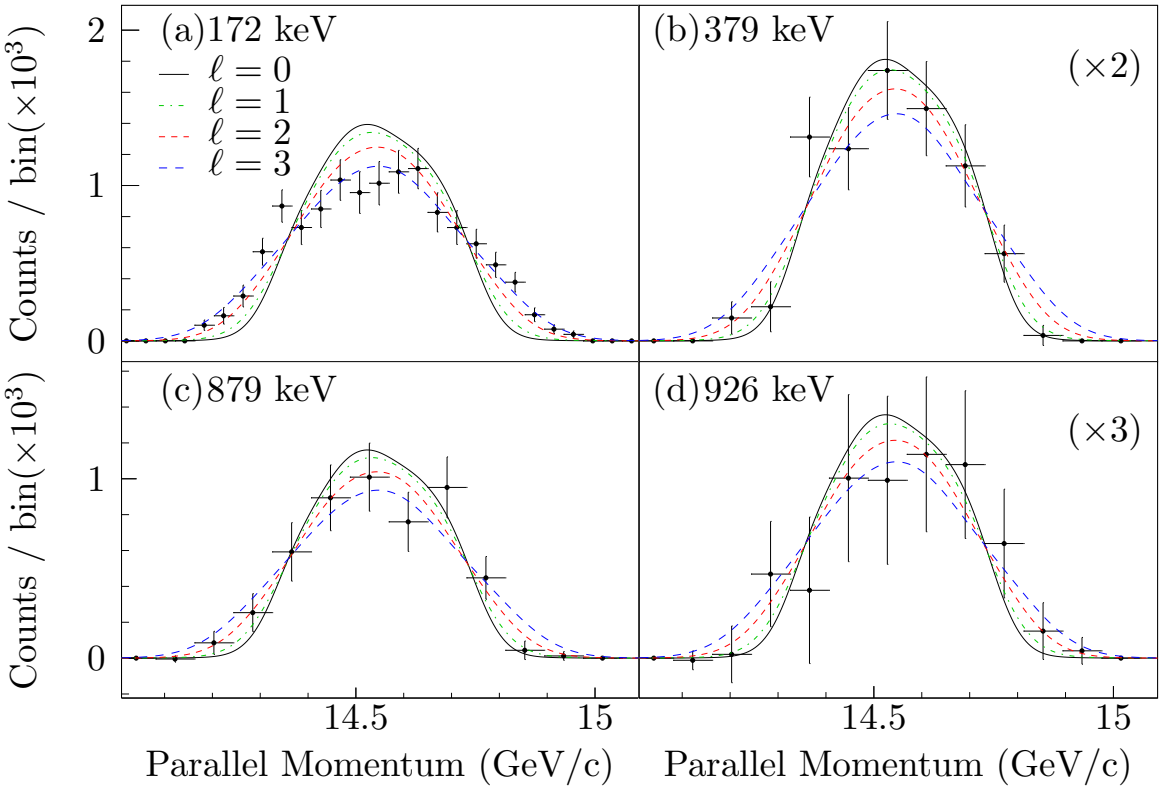

Figure 4.20: Parallel momentum distributions gated on γ-ray transitions in ^{39}Si (no feeding subtraction).

We also expect to preferentially populate $3/2^+$, $1/2^+$ and $3/2^-$ states with the knockout reaction. The next-strongest transition at 879 keV has a corresponding parallel momentum

distribution shown in Figure 4.20(c) that suggests $\ell = 2$ or 3, so we tentatively assign that transition to depopulate a $3/2^+$ level. By comparison with the shell model, the most probable final state for the decay of the $3/2^+$ state would be the $5/2^-$ ground state, as the population of the $7/2^-$ state would require a slower M2 transition, and the population of the $3/2^-$ and $1/2^-$ states would be hindered by their strong admixtures of $(f_{7/2})^4 p_{3/2}$ and $(f_{7/2})^4 p_{1/2}$, respectively. We therefore tentatively place the $3/2^+$ level at 879 keV, connecting to the $5/2^-$ ground state. The momentum distribution in Figure 4.20(b) in coincidence with the 379 keV transition suggests $\ell = 0$ or 1 but without additional information from $\gamma\gamma$ coincidences, the placement in the level scheme is unclear.

Table 4.5: Gamma-ray energies, efficiency-corrected intensities, and coincidences for ^{39}Si. Levels marked with an asterisk are tentative.

E_γ [keV]	Yield/100 ions	Coincident γ rays	Level [keV]
172(5)	36(6)		172(5)
290(3)	4(1)		
350(3)	6(2)		
379(3)	10(2)		
485(4)	2.2(8)		
644(4)	2.5(10)		
879(4)	12(2)		879(5)*
928(4)	5.3(11)		
974(4)	2.3(8)		

Additional lines at 290, 350, 485, 928, and 974 keV, as well as a broad structure around 644 keV, which likely corresponds to an unresolved multiplet, are likewise not placed in the level scheme. The inset panel in Figure 4.18 shows the $\gamma\gamma$ coincidence matrix gated on the two strongest peaks at 172 and 879 keV, revealing no clear coincidences. The most prominent structure in the 172 keV coincidence spectrum is centered around 750 keV, which does not correspond to any transition observed in singles. This supports the interpretation that these transitions depopulate states which are directly populated in the knockout reaction.

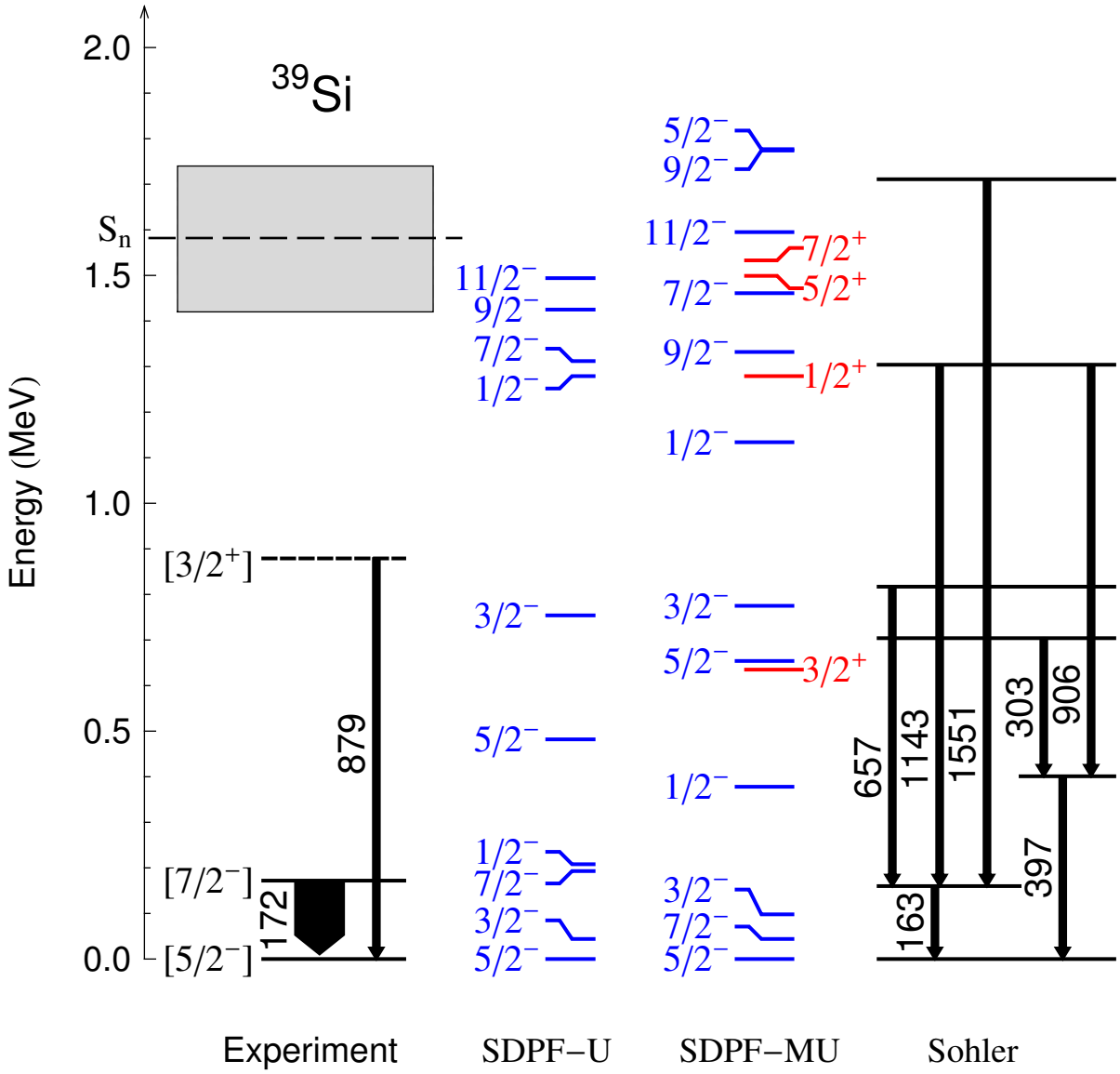

Figure 4.21: The left figure shows the proposed level scheme for ^{39}Si. The right figure is the level scheme proposed by Sohler *et al*. [11]. In the left figure, the width of the arrows in proportional to the efficiency-corrected γ-ray intensity. As described in the text, the levels could have an offset if the lowest $3/2^-$ state lies below the $5/2^-$.

4.2.6 ^{39}Al

No previous measurements of the excited states of ^{39}Al exist. In the current measurement we observe three transitions, at 764, 800, and 883 keV, and a possible peak at 995 keV. The low statistics in this setting preclude any $\gamma\gamma$ coincidence measurement. The 800 keV transition

is the most intense, and we assign it populating the ground state. The other transitions are not placed in the level scheme.

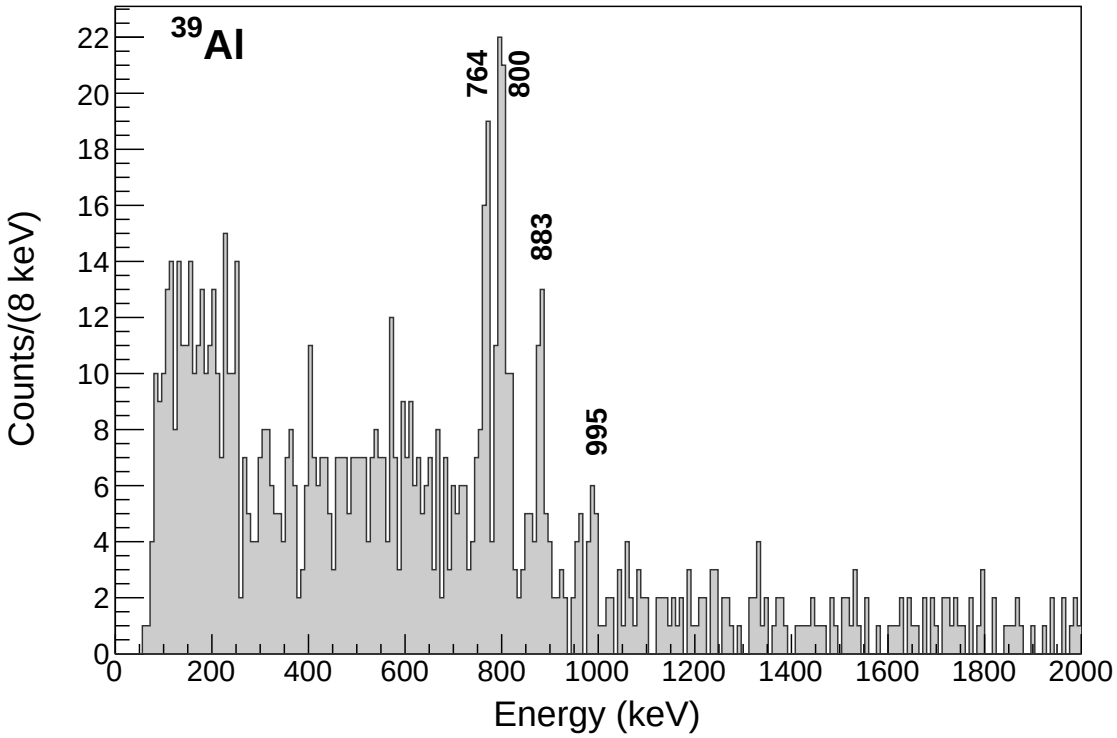

Figure 4.22: Doppler-reconstructed γ-ray spectrum detected in coincidence with ^{39}Al. The Doppler reconstruction was performed with a velocity $v/c = 0.388$.

Table 4.6: Gamma-ray energies, efficiency-corrected intensities, and coincidences for ^{39}Al.

E_γ [keV]	Yield/100 ions	Coincident γ rays	Level [keV]
764(8)	10(4)		
800(8)	12(4)		800(8)
883(8)	9(4)		
995(8)	1(2)		

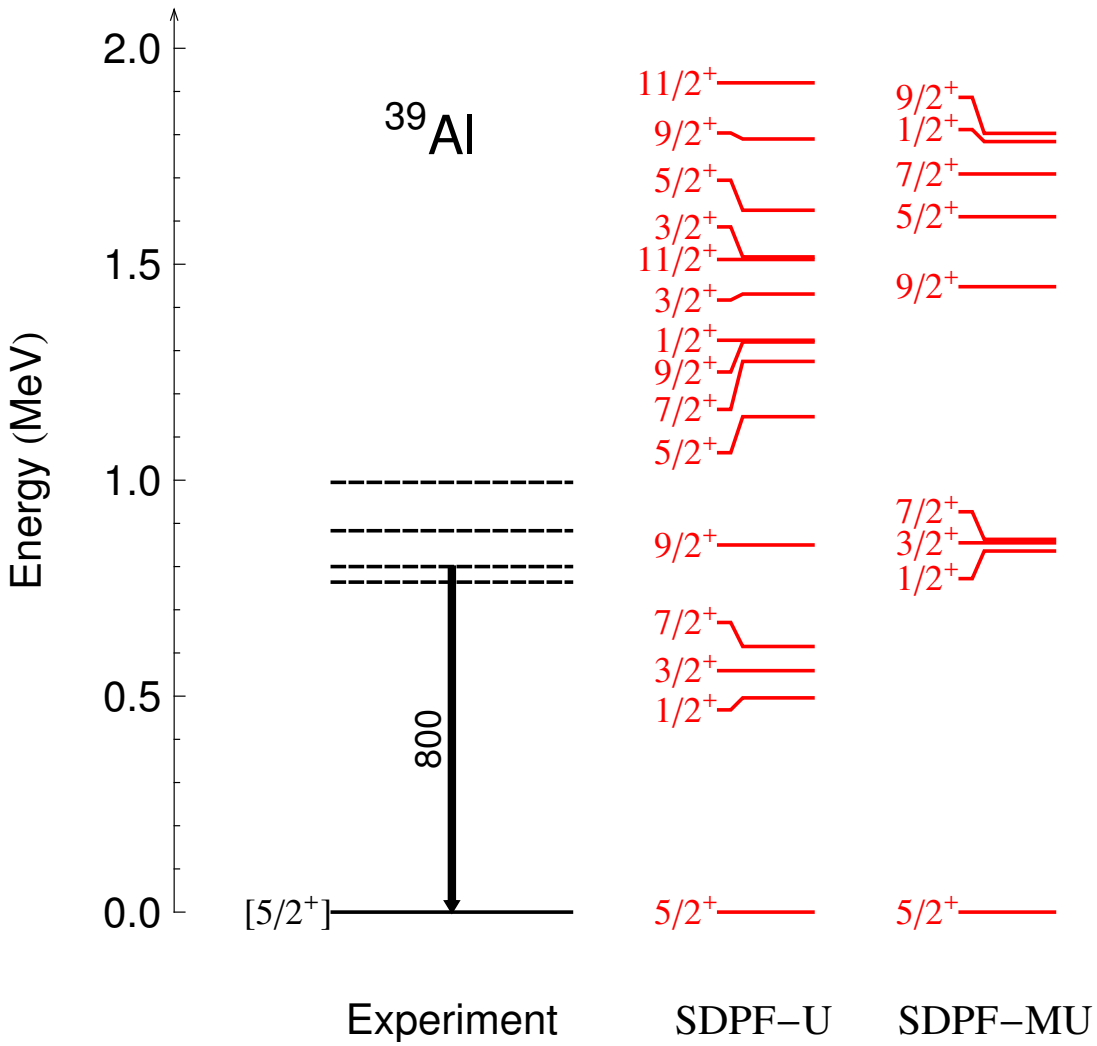

Figure 4.23: A possible level scheme for ^{39}Al, although $\gamma\gamma$ cascades cannot be ruled out due to low statistics. The center and right figures are shell-model calculations (see text for details).

4.3 Knockout cross sections

4.3.1 Inclusive cross sections to all bound states

Knockout cross sections are obtained by the equation

$$\sigma_{ko} = \frac{N_r}{N_b n_t \epsilon} \tag{4.3}$$

where N_r is the number of knockout residues detected, N_b is the number of incident beam particles, n_t is the areal target number density, and ϵ is the efficiency for detecting the knockout residues. In all knockout settings, the full momentum distribution was within the acceptance of the S800, and so I take $\epsilon = 1$ within the other uncertainties of the measurement.

The number of detected knockout residues is obtained by integrating the total number of counts within the PID gates shown in Figure 3.6. The uncertainty in this number is given by the statistical counting uncertainty $\sqrt{N_r}$ and by the systematic error due to the placement of the PID gate. The number of desired events excluded by the PID gate is estimated by fitting the gated PID distribution with at two-dimensional Gaussian and evaluating what fraction of the Gaussian lies outside the gate. In all cases, this amounts to less than 1% of the total number of counts inside the gate.

The number of incident particles was inferred by monitoring the rate of the object scintillator and scaling that rate to a calibration measurement in which the rigidity of the S800 was centered on the unreacted beam. This accounts for fluctuations in beam rate, so the main source of error in this method is fluctuations in the composition of the beam. The uncertainty due to these fluctuations is estimated by calculating the cross section for each one-hour run (shown in Figure 4.24) and taking the root-mean-squared deviation. This is the dominant source of uncertainty for the inclusive cross section measurement, and is of the order of a few millibarns.

The beryllium target used for knockout from ^{36}Si and ^{38}Si had an areal mass density of 287(3) mg/cm^2 and the target used for knockout from ^{40}Si as well as inelastic scattering for all three projectiles had a density of 376(4) mg/cm^2.

All these uncertainties are uncorrelated and so the total uncertainty in the inclusive cross

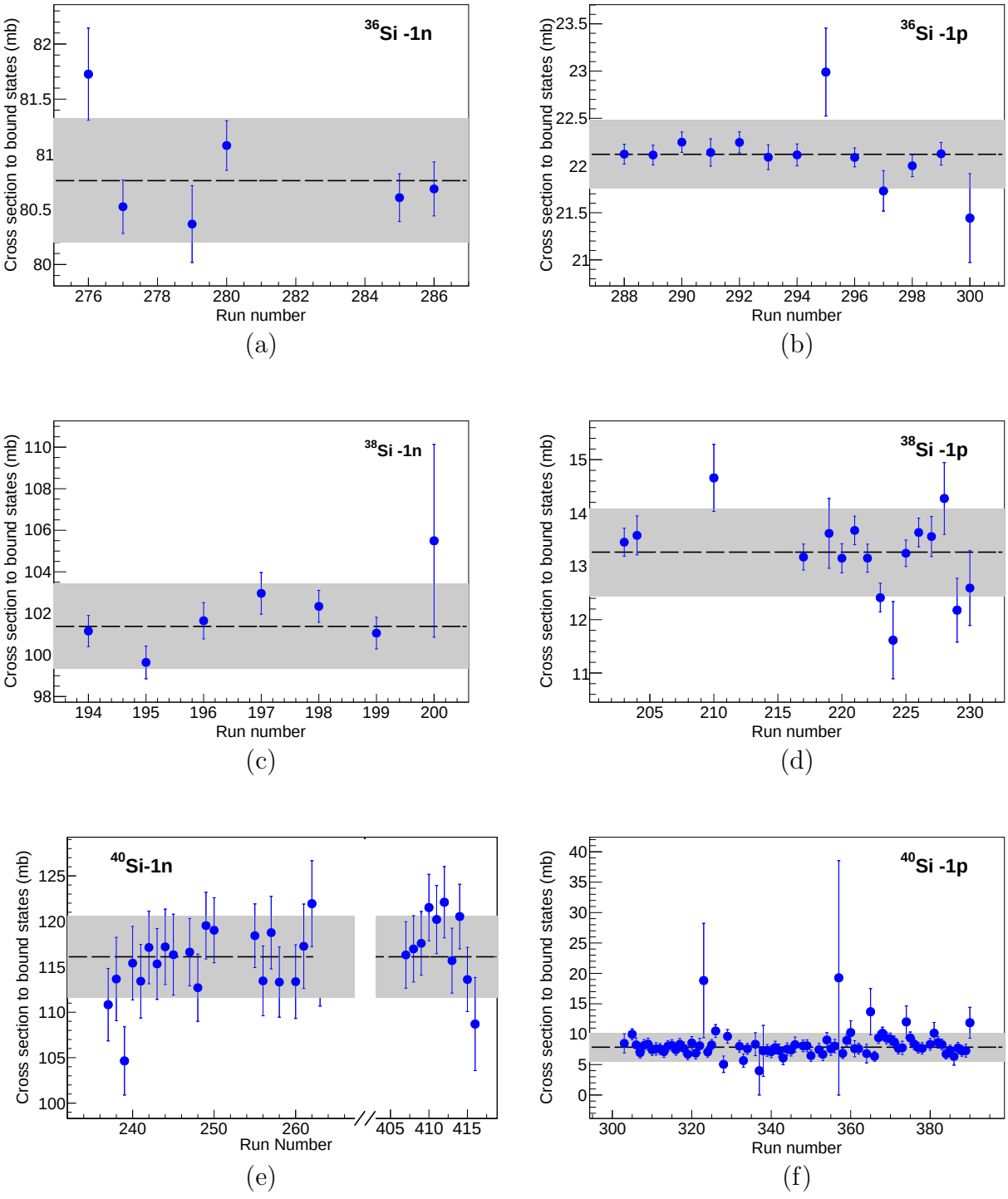

Figure 4.24: Knockout cross section to all bound states for each of the six settings, calculated on a run-by-run basis. The error bars on each point are statistical errors for counting the number of events inside the PID gate. The dashed black line shows the error-weighted mean value of all the runs, while the gray band indicates the uncertainty, which is taken from the root mean squared deviation of the points from the mean.

section Δ_{ko} is given by

$$\left(\frac{\Delta_{ko}}{\sigma_{ko}}\right)^2 = \left(\frac{\Delta_r}{N_r}\right)^2 + \left(\frac{\Delta_t}{n_t}\right)^2 + \left(\frac{\Delta_b}{N_b}\right)^2 \tag{4.4}$$

The resulting inclusive one-proton and one-neutron knockout cross sections are shown in Figure 4.25, compared to theoretical predictions using shell-model energies and spectroscopic factors. In order to account for the uncertainty in both the neutron separation energies and the shell model energies, the neutron separation energy was varied by ±500 keV to produce the error bars shown on the theoretical curves. For calculations performed with SDPF-U, the two lowest even-parity 1p-1h states were considered bound, regardless of their calculated energies. Also shown in Figure 4.25 is the theoretical cross section scaled by an empirical reduction factor $R(\Delta S) \approx 0.61 - 0.016\Delta S$, taken from a fit to the systematics in [12]. Here ΔS is defined to be the difference in separation energy between the removed species and the spectator species, e.g. for neutron knockout $\Delta S = S_n - S_p$.

One notable feature in the trend in neutron knockout cross sections is the decrease from ^{34}Si to ^{36}Si. In the shell model calculations, this is due to the fact that in ^{33}Si, which has a neutron hole in the *sd* shell, the relevant energy for a $d_{5/2}$ hole state is the $d_{3/2} - d_{5/2}$ gap, which is small enough for there to be bound $5/2^+$ states with substantial $d_{5/2}$ hole strength. At ^{35}Si, the neutron *sd* is filled and so the relevant energy becomes the $f_{7/2} - d_{5/2}$ gap, pushing $d_{5/2}$ hole states up in energy, above the low neutron separation energy in ^{35}Si. As a result, removal of a $d_{5/2}$ neutron does not substantially contribute to the cross section to bound states in ^{36}Si.

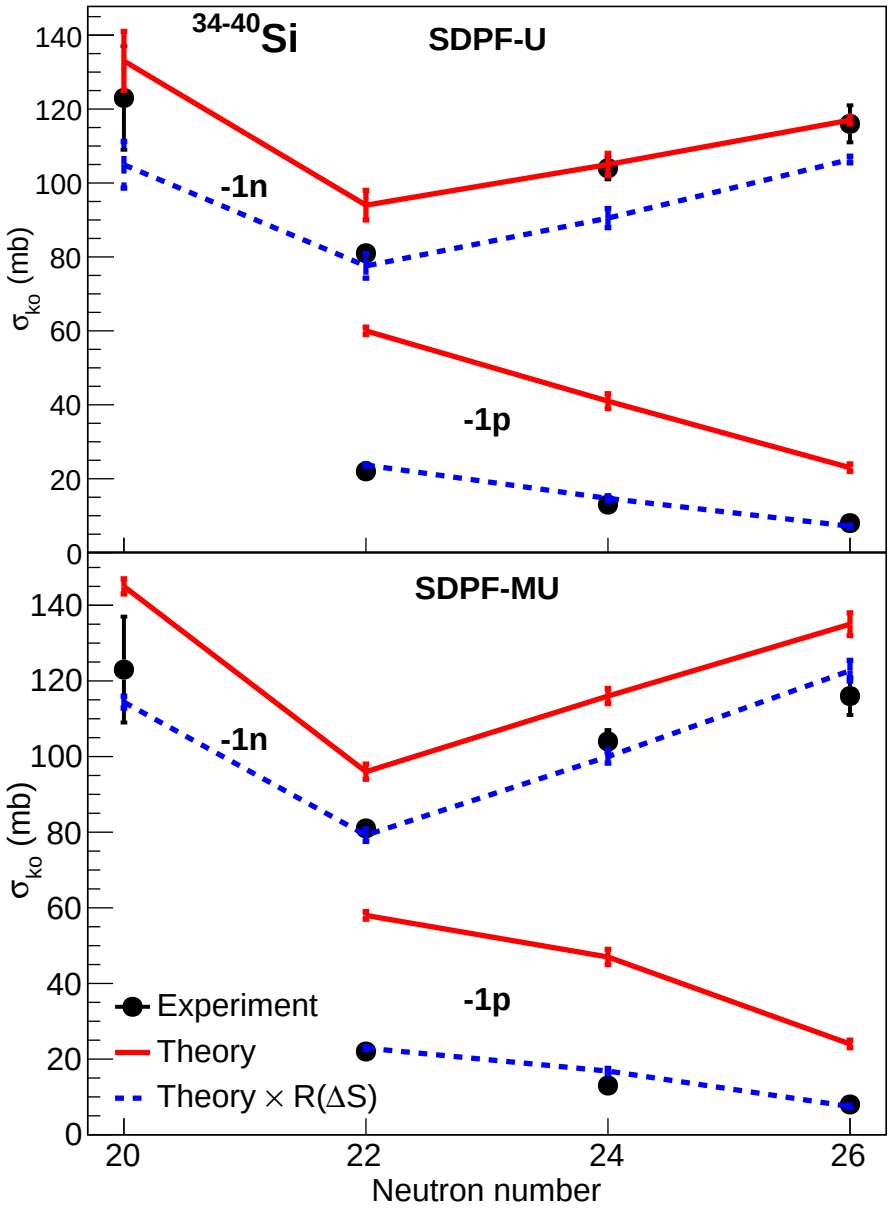

Figure 4.25: Inclusive 1n and 1p knockout cross sections from silicon isotopes to all bound states as a function of projectile neutron number, compared with theoretical prediction (solid red line) and the theoretical prediction scaled by a systematic reduction factor $R(\Delta S)$ [12]. The theoretical error bars are generated by varying the neutron separation energy by ± 500 keV. The experimental value for ^{34}Si is taken from [13]

4.3.2 Exclusive cross sections to final states

The knockout cross section to a specific final state i is given by the inclusive cross section multiplied by the probability P_i of populating that state.

$$\sigma_i = \sigma_{ko} P_i \tag{4.5}$$

This population is in turn calculated by summing the yield of all γ rays D_i that de-excite state i and subtracting the yield of all γ rays F_i that feed state i

$$P_i = \sum_{j \in D_i} Y_j - \sum_{j \in F_i} Y_j \tag{4.6}$$

The population of the ground state is taken to be the remaining strength after subtracting all populated excited states:

$$P_{gs} = 1 - \sum_i P_i \tag{4.7}$$

The uncertainty Δ in the population probability is given by

$$\left(\Delta_{P_i}\right)^2 = \sum_{j \in D_i + F_i} \left(\Delta_{Y_j}\right)^2 \tag{4.8}$$

In the case of unplaced γ transitions, the ground state cross section is taken to be the average of the maximal and minimal feeding scenarios, and the cross sections for these unplaced transitions are added in quadrature to the ground state uncertainty.

The resulting exclusive cross sections are shown in Figures 4.26-4.31, and tabulated in Table 4.7. Transitions which are not placed in the level scheme are assumed to feed the ground state for plotting purposes, in order to better demonstrate the distribution of strength.

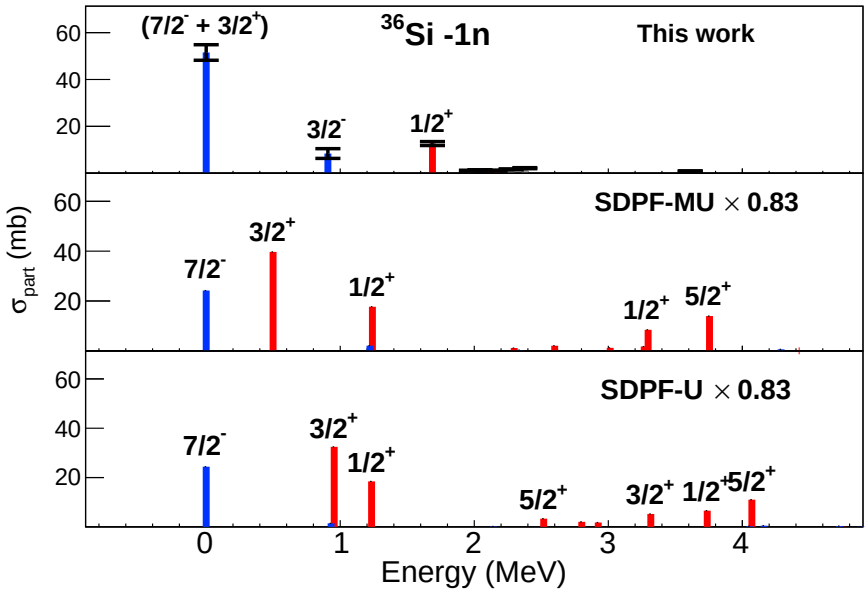

Figure 4.26: One neutron knockout cross section to final states in ^{35}Si. Experimental data is shown in the top panel, and theoretical predictions are shown in the bottom two panels.

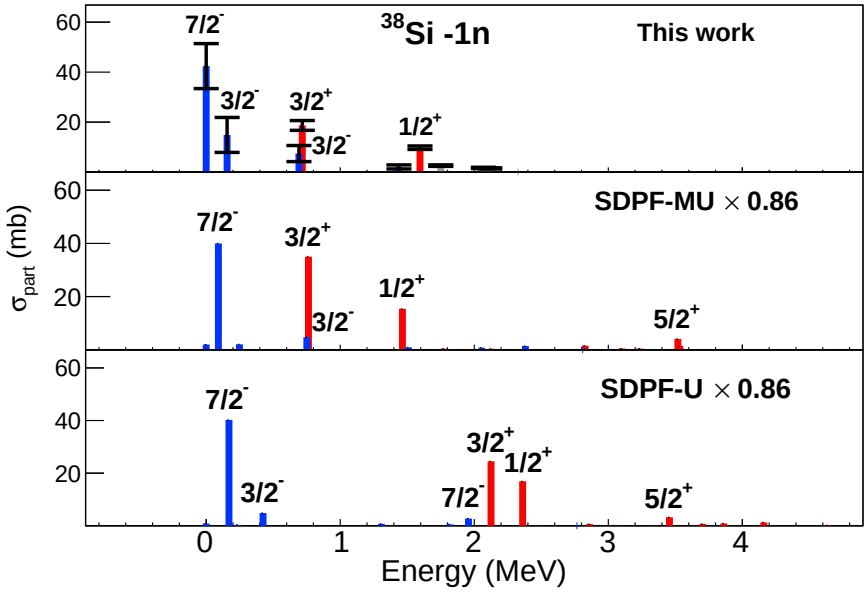

Figure 4.27: One neutron knockout cross section to final states in ^{37}Si. Experimental data is shown in the top panel, and theoretical predictions are shown in the bottom two panels.

Special care is required in evaluating partial cross sections for neutron knockout from ^{40}Si because there are so many γ transitions with are not placed in the level scheme of ^{39}Si, and which could be potential feeders. The $7/2^-_1$ state at 172 keV should be fed negligibly by

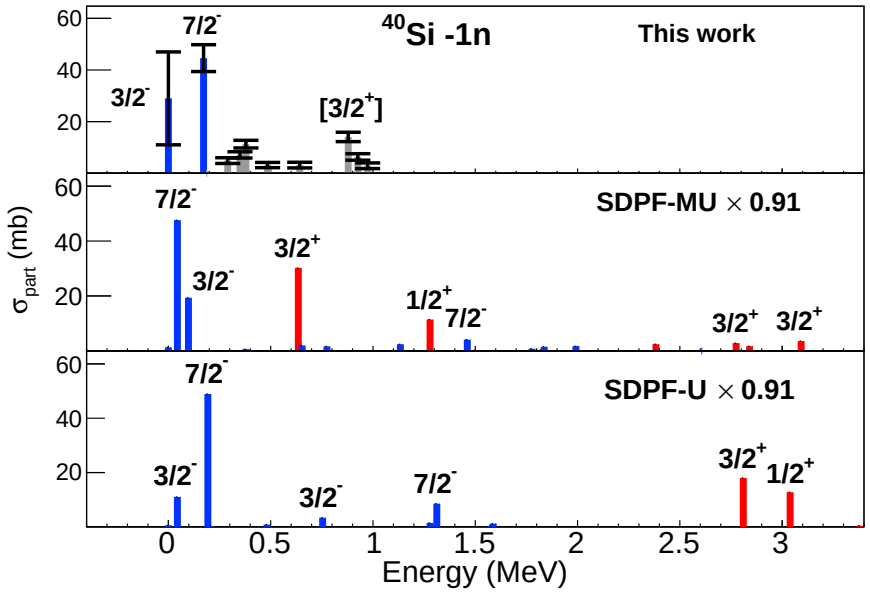

Figure 4.28: One neutron knockout cross section to final states in ^{39}Si. Experimental data is shown in the top panel, and theoretical predictions are shown in the bottom two panels.

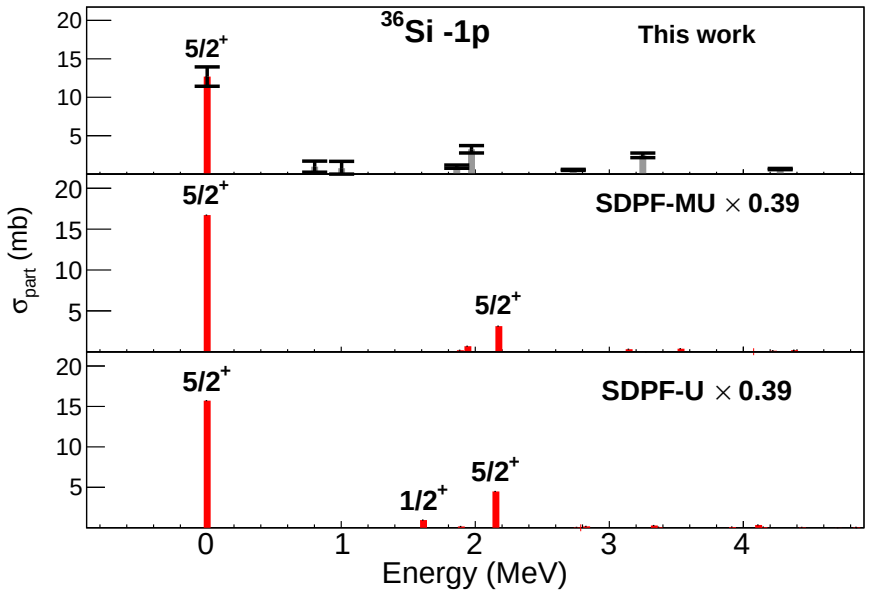

Figure 4.29: One proton knockout cross section to final states in ^{35}Al. Experimental data is shown in the top panel, and theoretical predictions are shown in the bottom two panels.

the $3/2^+$ and $1/2^+$ intruder states, due to the required $M2$ and $E3$ transitions, respectively. Low-lying $3/2^-$ states could feed the $7/2^-_1$ state by an $E2$ transition. However, the $\gamma\gamma$ coincidence spectrum gated on the 172 keV transition reveals no coincidences, and shell

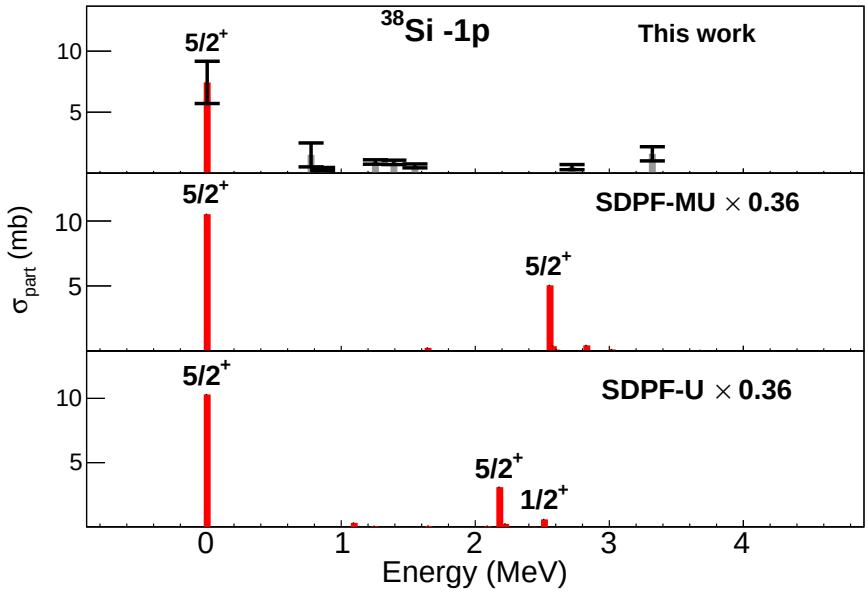

Figure 4.30: One proton knockout cross section to final states in ^{37}Al. Experimental data is shown in the top panel, and theoretical predictions are shown in the bottom two panels.

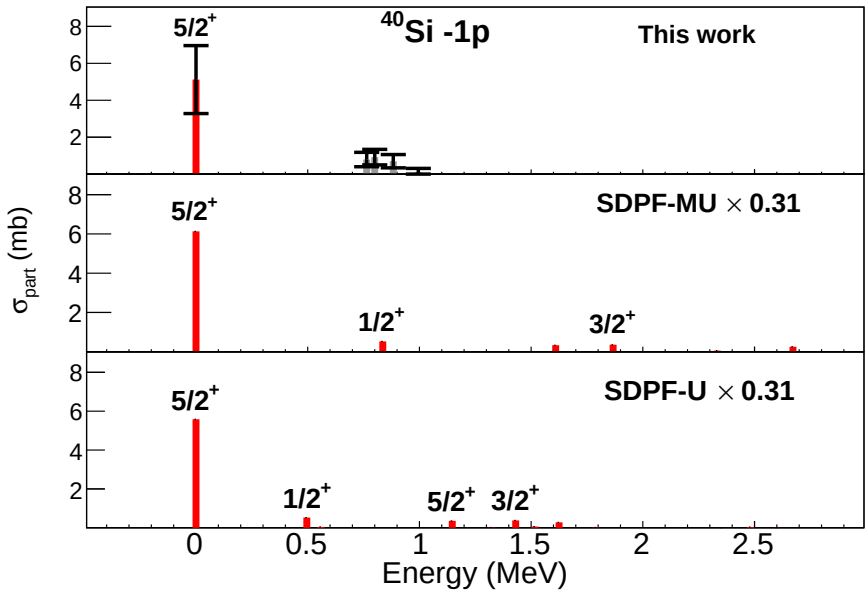

Figure 4.31: One proton knockout cross section to final states in ^{39}Al. Experimental data is shown in the top panel, and theoretical predictions are shown in the bottom two panels.

model calculations using the SDPF-MU interaction predict a ∼1% branching ratio from either of the $3/2^-$ states to the $7/2^-_1$ state. Therefore, uncertainty in the cross section to the $7/2^-_1$ state due to feeding should be small compared to the uncertainty due to extracting

the peak area.

The cross section to the $3/2^-_1$ state – which is obtained by subtraction because no de-excitation γ-rays are observed – is a more difficult case. This state should be fed by higher-lying $7/2^-$, $5/2^-$, $3/2^-$, $1/2^-$, $3/2^+$, and $1/2^+$ states and, furthermore, γ decays from these states to the $5/2^-_1$ state should also be subtracted. Clearly, a detailed knowledge of the level scheme is required to properly perform the subtraction. In the absence of such knowledge, upper and lower limits on the cross section are obtained by considering minimal and maximal feeding scenarios, constrained by requiring no direct feeding of the 172 and 879 keV transitions, and by the neutron separation energy of 1580(110) keV. The maximal feeding case is obtained by assuming all observed γ transitions directly populate the ground state (or an isomer), yielding the minimum cross section $\sigma_{3/2^-} = 19(14)$ mb. The minimal feeding case is obtained by assuming that only the 172, 350, 379, and 879 keV transitions feed the ground state or an isomer. The remaining transitions are placed depopulating higher states, with the 485 and 640 keV transitions feeding the 350 keV level, and the 664, 928, and 974 keV transitions feeding the 379 keV level. This results in the maximum cross section $\sigma_{3/2^-} = 40(9)$ mb. The cross section is taken to be the average of the maximal- and minimal-feeding results, and the uncertainty from the feeding is added in quadrature to the other uncertainties. The result is given in Table 4.7.

4.4 Discussion

The evolution of neutron single-particle strength along the silicon isotope chain may be visualized by plotting the cross sections for populating the low-lying $5/2^+$, $3/2^+$, $1/2^+$, $7/2^-$, and $3/2^-$ states, which gives an indication of the occupancy of orbits near the Fermi

Table 4.7: Total and partial knockout cross sections to bound final states for each of the knockout reactions studied.

	$\sigma_{\rm ko}$[mb]	$E_{\rm final}$[keV]	$J^\pi_{\rm final}$	$\sigma_{\rm part}$[mb]
^{36}Si$\rightarrow^{35}$Si	81(2)	0	$[7/2^-]$	52(4)[a]
		908	$[3/2^-]$	8(3)
		974	$[3/2^+]$	[b]
		1688	$1/2^+$	13(1)
		1979		1.1(2)
		2042	$[1/2^-]$	1.3(2)
		2164	$[5/2^+]$	1.1(2)
		2275		1.6(2)
		2377		2.1(2)
		3611		0.8(2)
^{38}Si$\rightarrow^{37}$Si	104(3)	?[c]	$[7/2^-]$[d]	47(9)
		156	$[3/2^-]$	9(7)
		692	$[3/2^-]$	7(3)
		717	$[3/2^+]$	19(2)
		1438	$[1/2^-]$	3(1)
		1595	$[1/2^+]$	10(1)
^{40}Si$\rightarrow^{39}$Si	116(5)	?[c]	$[3/2^-]$[d]	29(20)
		172	$[7/2^-]$	49(7)
^{36}Si$\rightarrow^{35}$Al	22(1)	0	$[5/2^+]$	13(2)
		802		1.0(7)
		1003		0.8(9)
		1862		1.0(2)
		1972		3.2(5)
		2731		0.5(1)
		3243		2.6(3)
		4275		0.5(1)
^{38}Si$\rightarrow^{37}$Al	13(1)	0	$[5/2^+]$	7(2)
		775		1.5(10)
		1253		0.9(2)
		1393		0.9(2)
		3327		1.6(6)
^{40}Si$\rightarrow^{39}$Al	8(2)	0	$[5/2^+]$	5(2)
		800		0.9(4)

[a] Includes population of the $3/2^+_1$ isomer.
[b] Not seen due to long lifetime (see text).
[c] Low lying level (energy is unknown).
[d] Includes (presumably weak) population of the $5/2^-_1$ state.

Table 4.8: Calculated spectroscopic factors to low-lying final states in ^{33,35,37,39}Si.

	interaction	$7/2^-_1$	$3/2^-_1$	$3/2^-_2$	$3/2^+_1$	$1/2^+_1$	$5/2^+_1$
^{34}Si	SDPF-U				3.48	1.38	2.42
	SDPF-MU				3.61	1.55	3.69
^{36}Si	SDPF-U	1.73	0.09		2.61	1.00	0.26
	SDPF-MU	1.71	0.13		3.07	0.96	0.09
^{38}Si	SDPF-U	2.48	0.02	0.26	2.19	0.97	0.05
	SDPF-MU	2.81	0.11	0.27	2.79	0.80	0.03
^{40}Si	SDPF-U	3.33	0.51	0.17	1.69	0.72	0.04
	SDPF-MU	3.19	0.90	0.08	2.31	0.53	0.02

surface. Figure 4.32 shows the experimental cross sections to directly populate the lowest $7/2^-$ state, and the cross section to populate the lowest two $3/2^-$ states (if they are bound), compared with theoretical predictions. The lowest two $3/2^-$ states are used because there should be mixing between the $f^x_{7/2}$ and $f^{x-1}_{7/2}p_{3/2}$ configurations in ^{37}Si and ^{39}Si. In addition to the curves predicted by the shell model calculations (shown in solid lines), results are shown for calculations in which the cross-shell (*sd*-*fp*) tensor component of the SDPF-MU interaction has been set to zero, shown in dotted lines. The results for SDPF-U with the tensor removed are similar. All theoretical curves have been scaled by a reduction factor $R(\Delta S)$, obtained from a fit to the systematics in [12].

Figure 4.33 shows the cross sections to the $5/2^+_1$, $3/2^+_1$ and $1/2^+_1$ states, corresponding to the removal of an *sd* shell neutron, compared with theoretical predictions. The cross sections for knockout from ^{34}Si are taken from a previous experiment [13]. As in Figure 4.32, the theoretical cross sections have been scaled with the systematic reduction factor. Calculated spectroscopic factors are given in Table 4.8 for reference.

A number of observations may be made regarding these plots. First, it appears that both interactions reproduce the strength to the $7/2^-_1$ state quite well. From the calculations

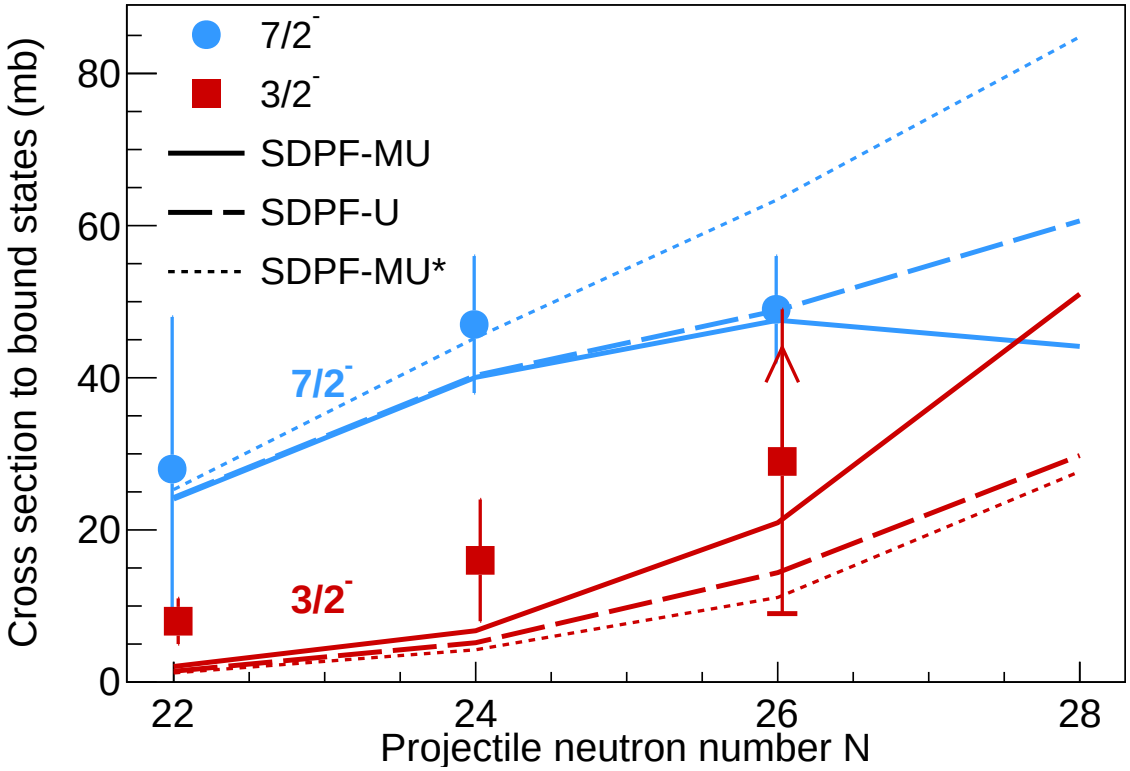

Figure 4.32: Partial cross sections for the population of a bound final state with $J^\pi = 7/2^-$ and $3/2^-$ in a one-neutron knockout reaction as a function of mass number for the silicon projectile. Theoretical predictions using the SDPF-MU (solid lines) and SDPF-U (dashed lines) effective interactions are also shown. The dotted line shows the result for the SDPF-MU interaction with the cross-shell tensor component set to zero.

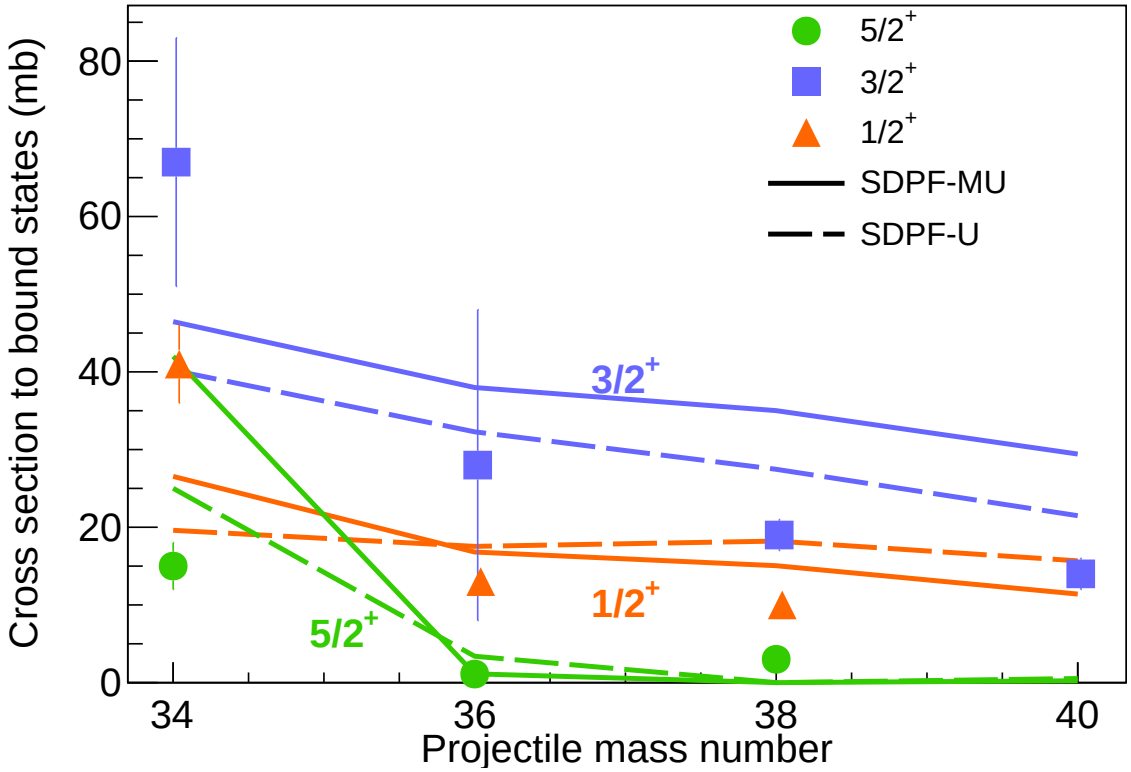

Figure 4.33: Experimental cross sections to the lowest $5/2^+$, $3/2^+$, $1/2^+$ states compared with the calculated cross sections using energies and spectroscopic factors from SDPF-MU (solid lines) and SDPF-U (dashed lines). The data for ^{34}Si are taken from [13].

it is clear that the effect of the cross-shell tensor interaction becomes important at ^{40}Si for reproducing the $7/2^-$ strength. Second, the strength to $3/2^-$ states is significantly underpredicted. These findings are consistent with findings in neutron knockout from ^{30,32}Mg [135] and from ^{33}Mg [136], as well as a ^{30}Mg(t,p)^{32}Mg study [137], all of which found evidence for an excess of $p_{3/2}$ strength relative to shell model predictions.

Turning to the positive-parity states in Figure 4.33, two features are apparent: (i) the knockout strength to positive-party states in ^{36,38,40}Si is over-predicted by the shell-model calculations, and (ii) there is a large drop in the experimental knockout strengths from ^{34}Si to ^{36}Si which is not predicted by theory. The observation (i) is perhaps not so surprising,

considering that the calculations were carried out in a model space restricted to 1p-1h neutron excitations out of the *sd* shell. For the 0^+ ground states of the even-A projectiles, this is effectively a 0p-0h truncation, which artificially increases the occupation of neutron *sd* orbitals. Additionally, the exclusion of higher np-nh excitations in the odd-A residues reduces the fragmentation of the single-particle strength to some degree. Both of these effects lead to overprediction of the knockout cross section to positive-parity states.

Observation (ii) is somewhat more surprising. The extracted spectroscopic factors for knockout to the $3/2^+_1$ and $1/2^+_1$ states in ^{33}Si are at (or above, when one includes empirical quenching [12]) their closed-shell sum-rule values of $2J + 1$. As the shell-model predictions are already restricted to 0p-0h excitations across the $N = 20$ gap for the initial and final states considered, the only way to sufficiently increase the theoretical spectroscopic factors is to freeze out proton excitations across the $Z = 14$ sub-shell gap, which is unrealistic.

Part of this discrepancy might be explained by considering effects that could lead to artificially high experimental cross sections. While ^{34}Si has good proton and neutron shell closures, there should still be some admixture of np-nh neutron excitations to the fp shell in the ground state. The removal of a neutron from the fp shell would lead predominantly to population of the lowest $7/2^-$ and $3/2^-$ states in ^{33}Si. The $7/2^-$ state is a 15 ns isomer, so it would be undetected by prompt, in-flight γ-ray spectroscopy and included in the $3/2^+$ ground state cross section. The $3/2^-$ state decays to the $1/2^+$ state by emitting a 971 keV γ-ray, which would have been difficult to distinguish from the 1010 keV γ-ray depopulating the $1/2^+$ level, due to the γ-ray energy resolution of the scintillator array used in that experiment. In this case, each population of the $3/2^-$ state would have been counted *twice* in the population of the $1/2^+$ state, and subtracted one time too many from the population of the ground state.

In a rough estimate, assuming the ground state of ^{34}Si to consist of 80% 0p-0h neutron configurations and 20% 2p-2h neutron configurations (probably an over-estimate of the 2p-2h content [138]), with equal occupation of the $0f_{7/2}$ and $1p_{3/2}$ orbits, this would correspond to a $\sim$3 mb cross section to each of the $7/2^-$ and $3/2^-$ states, with a corresponding reduction of the $1/2^+$ cross section by 6 mb. In this case, the $1/2^+$ cross section would agree with the shell model prediction within error, if the empirical quenching of [12] is neglected. Regardless, it would be enlightening to have an independent measurement of the ^{34}Si cross sections in order to ascertain the significance of the discrepancy.

Two additional observations may be made regarding the systematics of the excited state spectra in ^{35,37,39}Si. The significant cross section to a state below the 172 keV $7/2^-_1$ state in ^{39}Si, which is interpreted as a $3/2^-_1$ state, indicates that the $N = 28$ shell gap is already quite small at ^{39}Si. This is consistent with the findings in ^{27}Ne [139] and ^{29,31}Mg [135, 140], that at large proton-neutron asymmetry the energy of the $3/2^-_1$ state drops below the $7/2^-_1$ state. However, in ^{39}Si this picture is complicated because of the presence of $(f_{7/2})^5$ configurations, which can mix with single-particle excitations to the $p_{3/2}$ orbital and thwart a simple interpretation in terms of single-particle orbits. Despite this complication, it is clear that the structure of ^{39}Si does not reflect a large shell gap at $N = 28$. The significant cross section to the 156 keV $3/2^-_1$ state in ^{37}Si indicates that the reduction of the $N = 28$ gap is not abrupt, but is instead relatively smooth as a function of neutron number.

Finally, Figure 4.34 shows the $E(7/2^+_1) - E(3/2^+_1)$ and $E(7/2^-_1) - E(1/2^+_1)$ energy differences for odd silicon isotopes, which gives an indication of the $f_{7/2}$-$d_{3/2}$ and $f_{7/2}$- $s_{1/2}$ single-particle gaps. For ^{33}Si, the ground state has spin-parity $3/2^+$, and so special care must be taken for comparison with the other silicon isotopes. The $f_{7/2}$-$d_{3/2}$ gap is taken to be $E(3/2^+_1) - E(7/2^-_1)$, while the $f_{7/2}$-$s_{1/2}$ gap is taken to be the sum of the $d_{3/2}$-

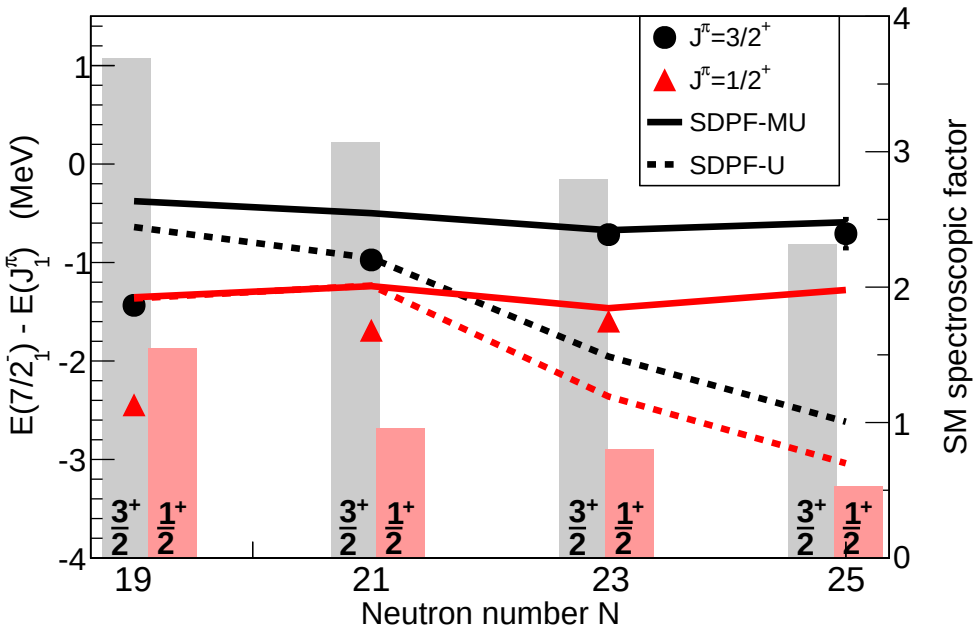

Figure 4.34: Energy difference between the J_1^π and $7/2_1^-$ levels in silicon isotopes, where $J^\pi = 3/2^+, 1/2^+$. Experimental data are indicated with points, while the shell model predictions are connected by lines. See the text for how the ^{34}Si values were obtained. The shaded bars indicate the SDPF-MU spectroscopic factors for one neutron removal (the sum rule limit is 4 for the $3/2_1^+$ state and 2 for the $1/2_1^+$ state).

Table 4.9: Comparison of $T = 1$ (neutron-neutron) monopoles for the SDPF-U and SDPF-MU interactions, evaluated for $A = 42$. The single-particle energy gaps between the $f_{7/2}$ and $d_{3/2}$ are 4.325 and 3.147 MeV for SDPF-U and SDPF-MU, respectively.

j_a	j_b	SDPF-U	SDPF-MU
$d_{3/2}$	$f_{7/2}$	-0.700	-0.278
$d_{3/2}$	$p_{3/2}$	-0.262	0.177
$s_{1/2}$	$f_{7/2}$	-0.257	-0.107
$s_{1/2}$	$p_{3/2}$	-0.875	0.202

$s_{1/2}$ and $f_{7/2}$-$d_{3/2}$ gaps, i.e. $E(3/2_1^+) - E(1/2_1^+) + E(3/2_1^+) - E(7/2_1^-)$. The evolution of these intruder-configuration energies provides a constraint on the $T = 1$ (neutron-neutron) component of the cross-shell $sd - fp$ interaction. Without knowledge of the hole states in this region, there was an ambiguity between *sd*-*fp* monopoles and fp shell single-particle energies, since both simply contribute an energy proportional to the occupation of a given orbit. For example, it is unclear how much binding for the $f_{7/2}$ orbit comes from the interaction with the ^{16}O core versus interaction with the *sd* shell neutrons. As an illustration of this point, cross-shell $T = 1$ monopole terms are given in Table 4.9 for the SDPF-U and SDPF-MU interactions. While both interactions produce similar results for non-intruder $0\hbar\omega$ states, their allocation of the $f_{7/2}$ binding between core and *sd*-shell neutrons differ significantly. The more attractive *sd*-*fp* monopoles in SDPF-U cause the neutron $d_{3/2}$ and $s_{1/2}$ orbits to be pulled down in energy as neutrons are added to the fp shell, and predict a correspondingly too-high energy for the 1p-1h $3/2_1^+$ and $1/2_1^+$ states in ^{37,39}Si.

Chapter 5

Summary and outlook

> *A scientific person will never understand why he should believe opinions only because they are written in a certain book. [Furthermore], he will never believe that the results of his own attempts are final.* (A. Einstein [141])

This work investigated the evolution of nuclear structure along the chain of exotic silicon isotopes between ^{34}Si and ^{42}Si in an attempt to understand the observed breakdown of the $N = 28$ shell closure in the vicinity of ^{42}Si. The method used for this purpose was one-proton and one-neutron knockout reactions, which provide insight into the single-particle structure of these nuclides.

In the course of this study, previously unknown states have been identified in all six reaction residues – ^{35,37,39}Si and ^{35,37,39}Al. Prior to this work, only one state in ^{35}Al was known, and none in ^{37,39}Al. An unusual γ decay from a neutron-unbound state in ^{35}Si was observed and interpreted in terms of a $d_{5/2}$ hole state or, alternatively, as the result of a two-step reaction mechanism. New spin-parity assignments were made for states in ^{35,37,39}Si, using arguments from the selectivity of the knockout reaction, comparison of the longitudinal momentum distributions to the predictions of eikonal theory, and the expected multipolarities of γ decays.

An empirical method was developed to reproduce the asymmetric longitudinal momentum distributions of the outgoing knockout residue, resulting in good agreement with nearly all measured distributions. The success of this method lends additional support to the

validity of the eikonal model for the reaction.

The measured trends in knockout cross sections are generally in good agreement with the shell model predictions, providing strong support for the interpretation of the open-shell behavior around ^{42}Si in terms of tensor-force driven evolution of single-particle structure. The one-proton knockout cross sections of §4.3.2 did not reveal any significant spectroscopic strength to orbits above the $d_{5/2}$, supporting the claim that the $Z = 14$ gap remains relatively closed. One-neutron knockout indicated spectroscopic strength to the $p_{3/2}$ orbit well above the theoretical prediction. This was interpreted in terms of excitations across both the $N = 20$ and the $N = 28$ shell gaps. Additionally, the persistence of the intruder $3/2^+$ and $1/2^+$ states was used to resolve an ambiguity in the $T = 1$ cross-shell matrix elements of shell model effective interactions developed for this region.

Experimentally, the obvious next steps in this investigation would be to (i) remeasure one-neutron knockout of ^{34}Si with improved γ-ray energy resolution in order to identify any population of intruder states, and to clarify the discrepancy in the cross sections between ^{34}Si and ^{36}Si; and (ii) measure one-neutron knockout in ^{42}Si, where the SDPF-MU shell model calculation predicts the cross section to $3/2^-$ states to become greater than that to $7/2^-$ states. In both cases, the presence of isomers would add to the experimental challenge. Additionally, one-neutron knockout from ^{37}Si and ^{39}Si could potentially provide clear ground state spin-parity assignments for these nuclei. It would be interesting as well to perform further comparisons of momentum distributions from knockout and inelastic scattering reactions with different projectile-target combinations with high statistics. This would allow a better understanding of the range of validity of the method developed in this work for reproducing the experimental momentum distributions.

From a theoretical point of view, it is clear that a proper treatment of the region studied

in this work requires the inclusion of many-particle many-hole neutron excitations across the $N = 20$ gap. Shell model calculations in such a large model space, while computationally demanding, are certainly feasible, and some calculations have already been carried out with a new interaction based on SDPF-U [142]. New experimental information, such as that in the current work, could provide guidance for effective shell model interactions in this large space, while recent developments in the derivation of *ab initio* shell model interactions [65, 66] provide hope that highly predictive interactions may be constructed without extensive prior knowledge of the spectroscopy of a given region.

APPENDICES

Appendix A

Digital pulse-shape analysis for the localization of γ-ray interaction points

When a γ-ray is emitted from a source moving at relativistic velocity, its energy is Doppler shifted as a function of its angle of emission. In fast-beam γ spectroscopy it is therefore crucial to ascertain the angle of emission in order to reconstruct the rest-frame energy. This requires knowledge of the position of the first interaction point of the γ ray with the detector. In GRETINA and the Segmented Germanium Array (SeGA), this is achieved to first order by electronic segmentation of the germanium crystals. This position resolution can be further improved by using the time structure of the electronic pulses to resolve where within a given segment the interaction took place. Here, I discuss the basic ideas of using digital pulse-shape analysis to obtain sub-segment position resolution, and give proof-of-principle demonstrations both with source data and in-beam data, building on the previous work in [143].

A.1 Principles

A charge moving in the vicinity of a grounded conductor induces an image current on that conductor, the magnitude of which is given by the weighting potential – or, equivalently, the weighting field – calculated by the Shockley-Ramo theorem [98]. The magnitude of this

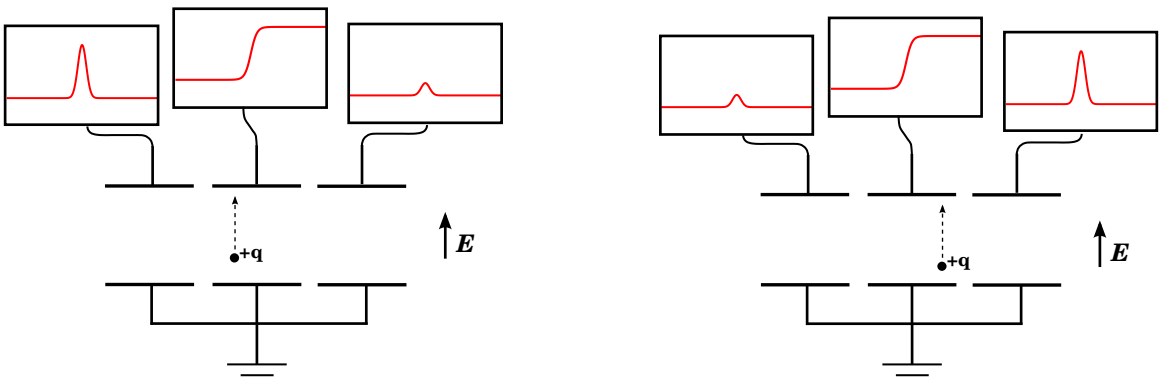

Figure A.1: An illustration of using induced charge to obtain position information. (a) If the charge is collected on the left side of the center detector, then the magnitude of the induced charge is larger in the left detector than in the right detector. (b) Vice versa.

induced current generally decreases with increasing distance between the charge and the conductor, and so measuring the induced current we may obtain information about the path of the moving charge. This is illustrated in Figure A.1 for the simple case of three parallel plate capacitors arranged side by side. We can clearly tell which "detector" collected the charge, because there is a net charge in the center detector. However, for two different positions within the center detector, we see different induced charges on the neighboring detectors. With such a configuration, we may construct the quantity

$$x = x_0 + \frac{L}{2}\frac{\mathcal{A}_R - \mathcal{A}_L}{\mathcal{A}_R + \mathcal{A}_L}, \tag{A.1}$$

where x is the position of the charge in the direction perpendicular to the field direction, L is the size of the detector in that dimension, x_0 is the x position of the center of the detector, and $\mathcal{A}_L, \mathcal{A}_R$ are the maximum amplitudes of the induced charges in the left and right detectors, respectively. It is expected that this quantity should correlate with the actual x position of the charge.

For a configuration in which there are no neighboring electrodes, such a method may not be used. Such a situation arises with both the SeGA and GRETINA detectors, which are not segmented in the radial direction. In this case, we may use the *steepest slope* algorithm. To illustrate the steepest slope algorithm, we consider the analytically solvable case of an infinitely long coaxial detector, shown in Figure A.2, with the cathode held at potential $+V_0$ and the anode grounded. Much of this discussion follows that given in chapter 12 of [98]. In a semiconductor detector, rather than a single charge, electron-hole pairs are created. For simplicity, we consider a single electron-hole pair. In this case, the electric field is $\vec{E}(r) = \frac{\beta}{r}\hat{r}$, and the potential is $V(r) = \beta \log \frac{r}{r_2}$, where $\beta \equiv \frac{V_0}{\log(r_1/r_2)}$. The weighting field and potential for the cathode are the same, with $V_0 \to 1$. For sufficiently high V_0, the charges quickly reach their maximum drift velocities, and so their positions are given by

$$r_e(t) = \begin{cases} r_0 - v_e t & t < \frac{r_0 - r_1}{v_e} \\ r_1 & \text{otherwise} \end{cases}, \qquad r_h(t) = \begin{cases} r_0 + v_h t & t < \frac{r_2 - r_0}{v_h} \\ r_2 & \text{otherwise} \end{cases} \tag{A.2}$$

since once either the electron or hole is collected, its position is $r_e(t) = r_1$ for electrons and $r_h(t) = r_2$ for holes. The charged induced on the central cathode as a function of time is then

$$Q(t) = \frac{q}{\log(r1/r2)} \log\left(\frac{r_h(t)}{r_e(t)}\right). \tag{A.3}$$

This is plotted in the top plot of Figure A.2b, for three different starting positions r_0. Notably, for each position there is a visible kink in the $Q(t)$ curve at the point where the electrons are collected on the cathode, and the times of the kinks differentiate the different starting positions. This can be seen more clearly if we look at the derivative $\frac{dQ}{dt}$, shown in the lower plot of Figure A.2b, where a discontinuity occurs at the time at which the

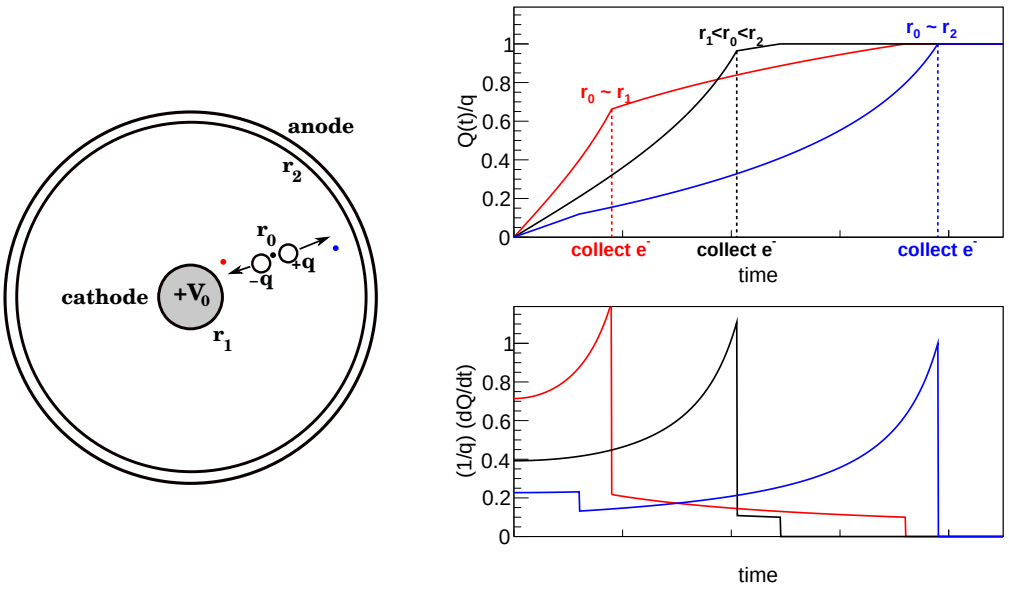

(a) (b)

Figure A.2: An illustration of using induced charge to obtain position information. (a) If the charge is collected on the left side of the center detector, then the magnitude of the induced charge is larger in the left detector than in the right detector. (b) Vice versa.

electrons are collected. In practice there are multiple charges, and these are not collected at exactly the same time, so the discontinuity becomes a steep slope. Identifying the time of the steepest slope in the current $I(t) = \frac{dQ}{dt}$ – achieved by finding the minimum of the second derivative $\frac{d^2Q}{dt^2}$ – gives the electron collection time which is strongly correlated with the original position r_0. This steepest slope method, and the linear interpolation method of (A.1) are used in the following two sections.

A.2 Sub-segment position resolution with SeGA

To test the efficacy of the above pulse-shape analysis, tests were performed using a single SeGA detector and a collimated ^{137}Cs source. A SeGA detector, as shown in Figure A.3, consists of a single cylindrical HPGe crystal electronically divided in to 32 segments consisting

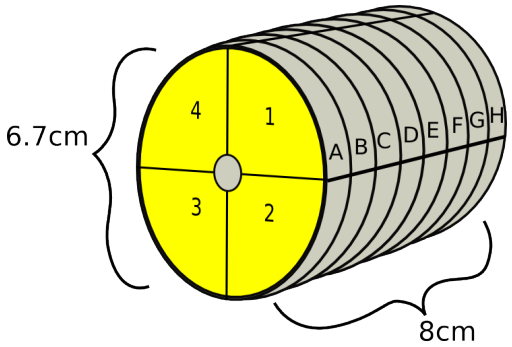

Figure A.3: A SeGA detector consists of a single HPGe crystal electronically divided into eight longitudinal slices and four azimuthal quarters, with the cathode running down the center.

of eight 1 cm slices in the longitudinal ("z") direction and four azimuthal quarters.

A scan was performed in the z direction using three steps within a single segment in order to determine if the pulse shape algorithm could distinguish between the runs. For each event in which the full energy of the 660 keV γ ray from ^{137}Cs was detected, the parameter z_n was calculated as

$$z_n = \frac{\mathcal{A}_{n+1} - \mathcal{A}_{n-1}}{\mathcal{A}_{n+1} - \mathcal{A}_{n-1}}, \tag{A.4}$$

where $\mathcal{A}_{n-1}$ is the amplitude of the induced charge in the neighboring segment. The results are shown in Figure A.4, and demonstrate a clear sensitivity to the source position, indicating that using pulse shape analysis can effectively double the segmentation in the longitudinal direction.

The scanning table used for the longitudinal direction scans was not designed for the SeGA detectors, and so scans in the radial and azimuthal directions were not feasible due to the detector geometry. Instead, a rough test was performed by pointing the collimated source in the longitudinal direction of the detector along two different axes, one near the center, and one near the outer edge, as shown in Figure A.5. The two positions also lay at different azimuthal angles, allowing a simultaneous check of the linear interpolation algorithm for the

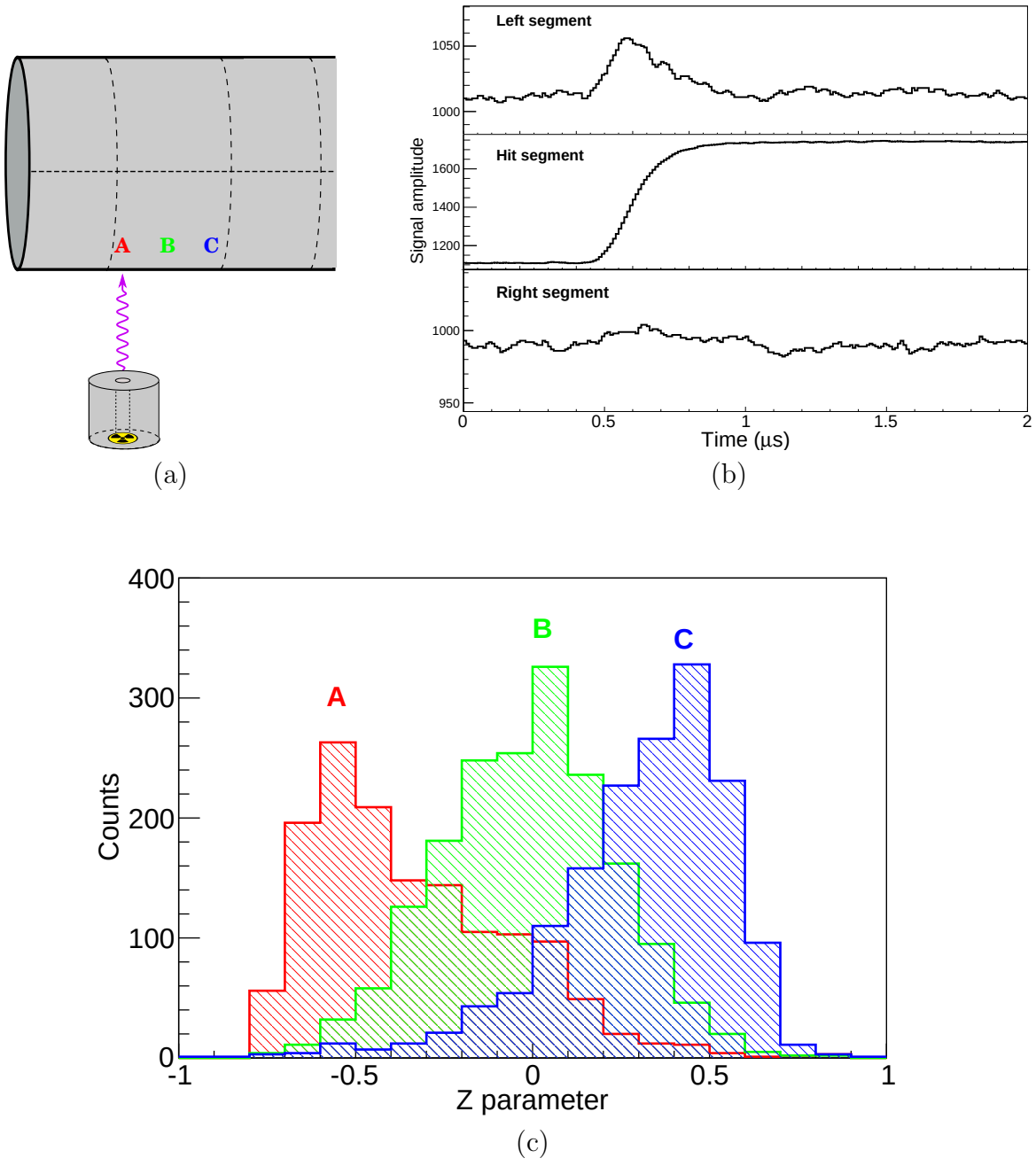

(a) (b) (c)

Figure A.4: (a) An illustration of the measurement taken, with three different positions (indicated A, B, C) for the collimated ^{137}Cs source, each aligned to illuminate a different region of the same segment. (b) An example of the recorded signals in the segment with a net energy deposited and two neighboring segments for an event with the source at position A. (c) The resulting histograms of the linear interpolation z parameter for each position, demonstrating subsegment resolution.

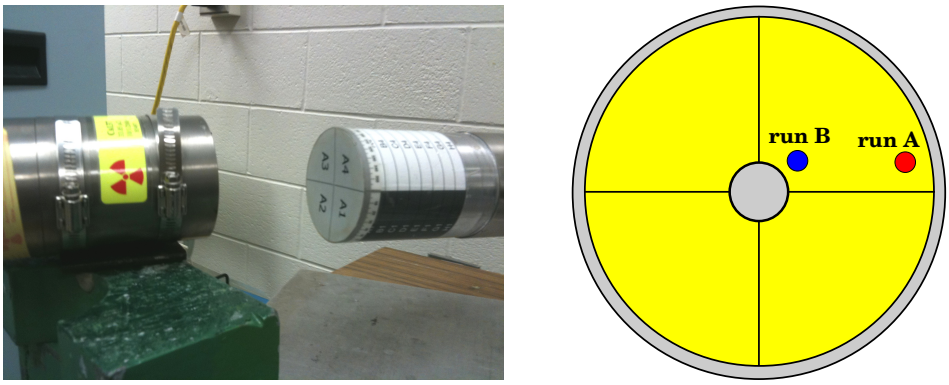

(a) (b)

Figure A.5: (a) Setup for the rough radial position measurement. (b) The two alignments used.

azimuthal direction.

For the implementation of the steepest slope algorithm, we need to perform numerical derivatives on the digitized signal. For the first derivative at the i^{th} time bin, we could take a simple difference, for example

$$\dot{Q}_i = Q_{i+1} - Q_i. \tag{A.5}$$

However, this will amplify the high-frequency noise in the signal and lead to inaccuracies in the second derivative. Instead we integrate over a small window of width w and differentiate over a larger time step d to obtain the low-frequency part of the signal

$$\dot{Q}_i = \sum_{j=-w}^{w} Q_{i+d+j} - Q_{i-d+i}. \tag{A.6}$$

Note that the derivative in (A.6) should in principle contain a factor $\frac{1}{wd}$, but since in the end we are only interested in finding the minimum of the second derivative, this normalization is irrelevant. If we take the parameters w and d to be too large, then we will wash out the signal and lose sensitivity. As shown in Figure A.6, the parameters $d = 3$, $w = 1$ are

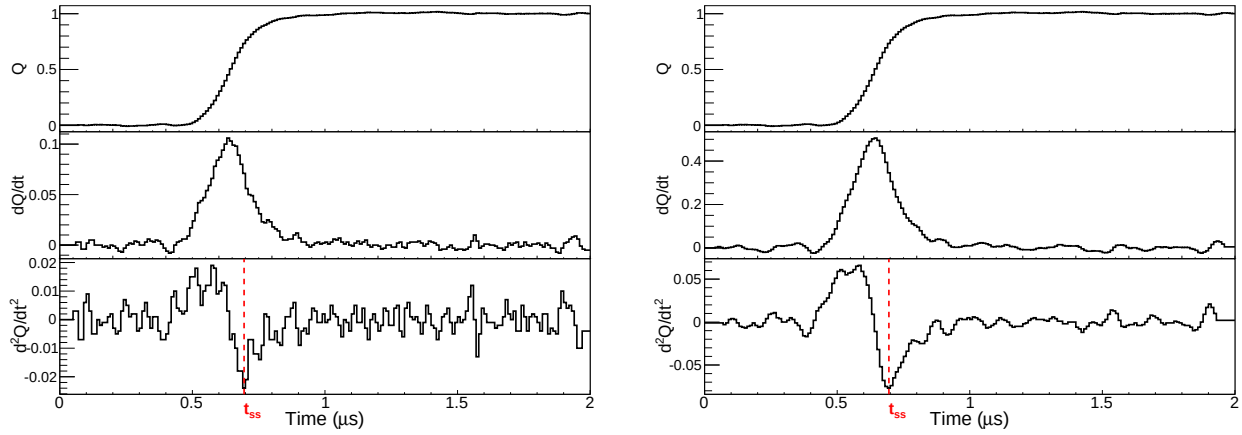

Figure A.6: An example of the steepest slope algorithm for a single trace, showing the measured signal, a numerical derivative of that signal, and a numerical second derivative, yielding the steepest slope time t_{ss}. In (a), the parameters $d = 1$, w=0 are used, while in (b) the parameters $d = 3$, $w = 1$ are used.

sufficient to remove the high-frequency noise.

The second derivative is obtained by applying (A.6) a second time

$$\ddot{Q}_i = \sum_{j=-w}^{w} \sum_{k=-w}^{w} Q_{i+2d+j+k} + Q_{i-2d+j+k} - 2Q_{i+j+k}. \tag{A.7}$$

Since the parameters j and k only appear in the combination $j+k$, we may reduce the double sum to a single sum by properly counting the ways j and k can sum to a given number m

$$\ddot{Q}_i = \sum_{m=-2w}^{2w} (2w + 1 - |m|) \left(Q_{i+2d+m} + Q_{i-2d+m} - 2Q_{i+m}\right). \tag{A.8}$$

Applying (A.8) to the traces obtained in the radial position measurements and finding the minimum of the second derivative yields the histogram shown in Figure A.7.a. The azimuthal position is obtained in an analogous way to the longitudinal position, using (A.4) where the neighboring segments are now the adjacent quarters, yielding an azimuthal parameter ϕ_n,

which is plotted in Figure A.7.b. Clearly, both parameters are sensitive to the interaction position within the segment. Taking the azimuthal position to be

$$\phi = \phi_0 + \frac{\pi}{4}\phi_n, \tag{A.9}$$

where ϕ_0 is the azimuthal angle of the center of the segment and taking the radial position to be

$$r = r_{min} + \left(\frac{r_{max} - r_{min}}{t_{max} - t_{min}}\right) t_{ss}, \tag{A.10}$$

where r_{min} and r_{max} are the inner and outer radii of the crystal and t_{min}, t_{max} are parameters taken to be 0.6 μs and 0.8 μs, respectively, we obtain the distribution of interaction points shown in Figure A.7.c. It is therefore clear from the source measurements that digital pulse-shape analysis is capable of improving the position resolution of SeGA by at least a factor of two in each dimension. In Figure A.5, some points are localized outside of the detector, reflecting the simplicity of the algorithm. This data was taken from the front-most slice of the SeGA detector, which has a more complicated geometry than the inner slices, due to the fact that the central contact ends partway through the slice. Charge deposited in the front slice may therefore have a path length which is longer than the nominal distance between the inner and outer electrodes. In practice, a more sophisticated algorithm should be used for the front slice, or at the very least all events placed outside the crystal should be moved to the edge of the crystal.

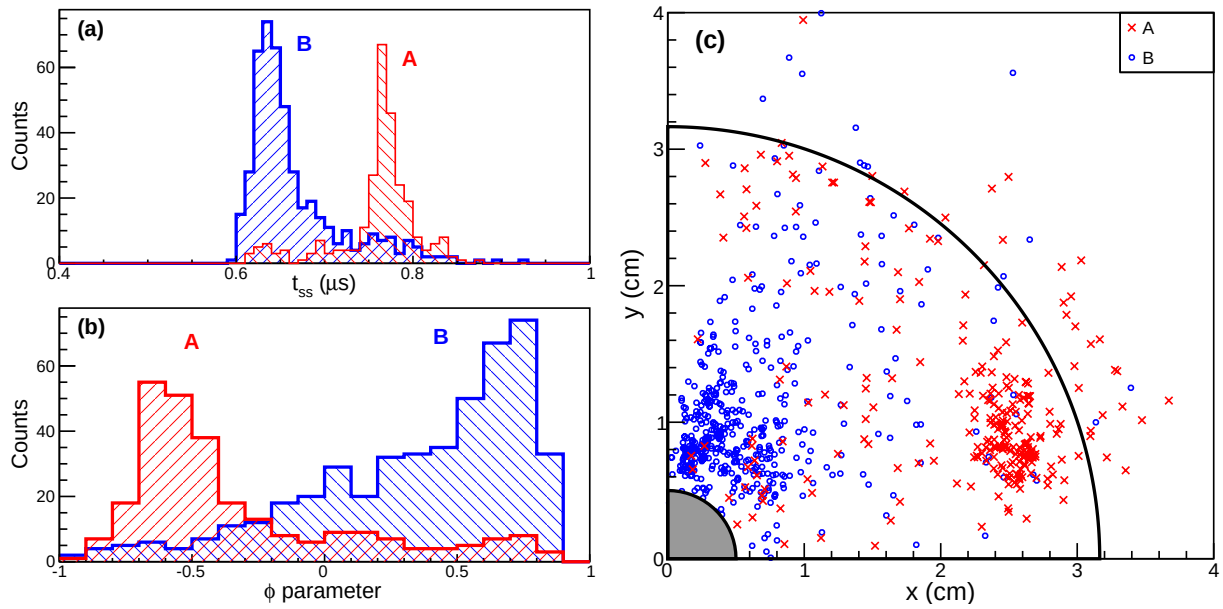

Figure A.7: The results of the rough radial position measurement showing (a) the steepest slope parameter for each run (b) the azimuthal interpolation parameter for each run and (c) the combined (r, ϕ) coordinates predicted by the pulse shape analysis. The black curves indicate the geometry of the germanium crystal.

A.3 Application to in-beam data with SeGA

As a proof of principle of the application of the sub-segment position resolution to in-beam data, the above methods were applied to experimental data from NSCL experiment e07023, which studied the structure of ^{16}C. The experiment used a plunger setup to measure the lifetime of the 2_1^+ state in ^{16}C, populated by a one neutron knockout from ^{17}C on a 500 mg/cm^2 beryllium target. However, for this proof-of-principle, the target-only runs (no plunger degraders) were used, to obtain the optimal beam energy resolution and isolate the contribution of the γ-ray interaction point determination to the γ-ray energy resolution.

The results are shown in Figure A.8, comparing the γ-ray energy resolution obtained with the standard segmentation and that obtained with the sub-segment positions. There is an improvement in the resolution from a full width at half maximum (FWHM) of 1.24% to 0.92%. This marginal improvement is due to the fact that the classic SeGA configuration was

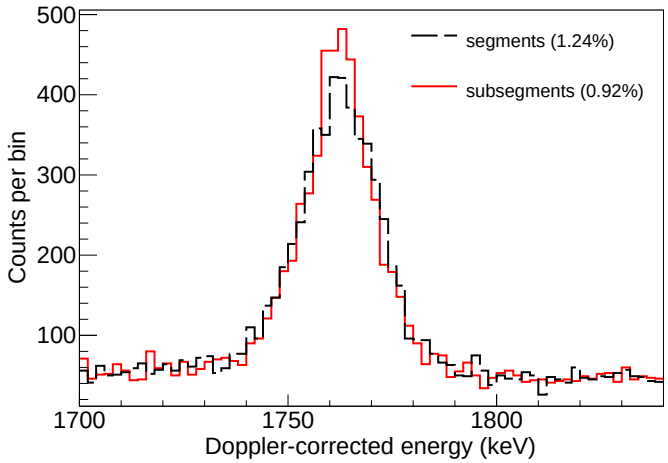

Figure A.8: The Doppler-reconstructed γ peak corresponding to the $2_1^+ \rightarrow 0_1^+$ transition in ^{16}C, at a beam velocity of β=0.36. The dashed black line shows the peak obtained with the electronic segmentation of SeGA (FWHM = 1.24%), while the solid red line shows the peak obtained with subsegment resolution from digital signal processing (FWHM=0.92%).

used for this experiment. In this configuration, the detectors are positioned approximately 30 cm from the target and the uncertainty in the angle of the emitted γ-ray due to the uncertainty in the position of the interaction point within a given segment is relatively small, and so the corresponding contribution to the resolution is small. It is hoped that for the barrel configuration, in which the detectors are positioned closer to the target for higher solid angle coverage, the improvement will be more substantial.

Appendix B

Derivations of formulas

B.1 Allowed J values for a rotational nucleus

Consider a deformed nucleus rotating about the $\hat{z}$ axis (which is *not* the symmetry axis of the deformation). We may take the symmetry axis to instantaneously be $\hat{x}$. Due to the symmetry of the intrinsic shape, a rotation about the $\hat{z}$ axis by an angle π is equivalent to a parity transformation $\vec{r} \to -\vec{r}$:

$$\mathcal{R}_z(\pi)|\Psi\rangle = P|\Psi\rangle \tag{B.1}$$

where $\mathcal{R}_n(\theta)$ is the operator for rotation about the $\hat{n}$ axis by an angle θ. Angular momentum is the generator of rotations, and we may write the rotation operator as $\mathcal{R}_n(\theta) = e^{-i\theta\vec{J}\cdot\hat{n}}$. So we have

$$e^{-i\pi J_z}|\Psi\rangle = P|\Psi\rangle \tag{B.2}$$

For a positive-parity state $P|\Psi\rangle = |\Psi\rangle$, this means even-parity states are restricted to even values of J_z, while odd-parity states are restricted to odd values of J_z. In all even-even nuclei, the ground state has spin-parity 0^+, which requires $J = J_z$ for rotational states, since there is no other angular momentum to couple to, and we have $J^\pi = 0^+, 2^+, 4^+ \ldots$

The energy of these states is taken in analogy to the classical picture where the energy

of an object with moment of inertia $\mathcal{I}$ rotating at an angular frequency ω

$$E_{rot} = \frac{1}{2}\mathcal{I}\omega^2 = \frac{J^2}{2\mathcal{I}}, \tag{B.3}$$

where $J = \mathcal{I}\omega$ is the angular momentum. Moving from the classical world to the quantum world, the quantity J^2 is replaced by the operator $\hat{J}^2$, with eigenvalues $\hbar^2 J(J+1)$. Thus the energy for a quantum mechanical rotor is given by

$$E_{rot} = \frac{\hbar^2 J(J+1)}{2\mathcal{I}}. \tag{B.4}$$

B.2 Reduced matrix elements for γ decays

In classical electrodynamics, the power radiated by an oscillating multipole distribution with multipole rank λ, z-projection μ, and frequency ω, is given by [37, 17]

$$P(\sigma\lambda\mu) = \frac{8\pi}{[(2\lambda+1)!!]^2}\left(\frac{\lambda+1}{\lambda}\right)\omega^{(2\lambda+2)}\left|M^{\sigma}_{\lambda\mu}\right|^2. \tag{B.5}$$

Where σ indicates either an electric or magnetic multipole and $M^{\sigma}_{\lambda\mu}$ is the amplitude of the oscillation.

We may obtain the quantum mechanical version of this equation by interpreting the power as the number of photons of energy ω emitted per second, and replacing $M^{\sigma}_{\lambda\mu}$ with the expectation value of the multipole operator $\mathcal{M}^{\sigma}_{\lambda\mu}$ between an initial state $|J_i M_i\rangle$ and final state $\left|J_f M_f\right\rangle$. The number of photons per second is then given by $P(\sigma\lambda)/\omega$

$$\Gamma(\sigma\lambda\mu) = \frac{8\pi}{[(2\lambda+1)!!]^2}\left(\frac{\lambda+1}{\lambda}\right)\omega^{(2\lambda+1)}\left|\left\langle J_f M_f\middle|\mathcal{M}^{\sigma}_{\lambda\mu}\middle|J_i M_i\right\rangle\right|^2. \tag{B.6}$$

The total rate is obtained by averaging over initial projections M_i and summing over final projections μ, M_f

$$\Gamma(\sigma\lambda) = \frac{8\pi}{[(2\lambda+1)!!]^2}\left(\frac{\lambda+1}{\lambda}\right)\omega^{(2\lambda+1)}B(\sigma\lambda; J_i \to J_f), \tag{B.7}$$

where the *reduced transition probability* $B(\sigma\lambda; J_i \to J_f)$ contains all the information on the structure of the initial and final states and is defined as

$$B(\sigma\lambda; J_i \to J_f) = \frac{\left|\left\langle J_f \middle\| \mathcal{M}(\sigma\lambda) \middle\| J_i \right\rangle\right|^2}{(2J_i+1)}. \tag{B.8}$$

The mean lifetime of a transition is related to the transition rate by $\tau = 1/\Gamma$. This means that measuring the lifetime of a transition is equivalent to measuring the reduced transition probability, assuming one knows the energy and multipolarity of the transition. In the case that more than one mode of decay is possible, the total decay rate is the sum of the individual decay rates. The partial lifetime $\tau_p(\sigma\lambda; i \to f)$ is defined for convenience as the inverse of the decay rate for a particular decay channel. Note however, that the actual time dependence is governed solely by the total lifetime τ, which is the reciprocal of the total decay rate.

The three most frequently used cases of (B.8), substituting $\omega = E_\gamma$, are:

$$B(E1) = \frac{0.62885}{E_\gamma^3 \tau_p} e^2\mathrm{fm}^2\mathrm{MeV}^3\mathrm{fs} \tag{B.9}$$

$$B(M1) = \frac{56.871}{E_\gamma^3 \tau_p}\ \mu_N^2\mathrm{MeV}^2\mathrm{fs} \tag{B.10}$$

$$B(E2) = \frac{816.20}{E_\gamma^5 \tau_p} e^2\mathrm{fm}^4\mathrm{MeV}^5\mathrm{ps}, \tag{B.11}$$

where $\mu_N = \frac{e}{2m_p}$ is the Bohr magneton.

B.3 Relativistic formulas

B.3.1 Doppler shift

A photon is detected with energy E^L in the lab frame at some angle θ^L. We know that the photon was emitted by a particle moving with velocity β in the $\hat{z}$ direction. We know that the energy-momentum 4-vector for a photon $P^\mu = (E, \vec{p})$, noting that the photon is massless so $E = |\vec{p}|$. To find the energy E_{CM} of the photon in the projectile-photon center-of-mass frame we use a Lorentz-transformation

$$\begin{aligned} E_{CM} &= \gamma \left(E_{LAB} - \beta p_{zLAB} \right) \\ &= \gamma \left(E_{LAB} - \beta E_{LAB} \cos\theta_{LAB} \right) \\ &= \gamma \left(1 - \beta \cos\theta_{LAB} \right) E_{LAB}, \end{aligned} \tag{B.12}$$

where γ is the relativistic factor $1/\sqrt{1-\beta^2}$.

B.3.2 Compton formula

Consider a photon with 4-momentum $K = (\omega, \vec{k})$ scattering of an electron at rest, with 4-momentum $P = (E, \vec{p})$, resulting in final momenta K', P', where the photon has been scattered to an angle θ. We are interested in what the final energy ω' will be. From conservation of energy and momentum $K - K' = P' - P$. Squaring both sides and evaluating

in the lab frame gives

$$-2\omega\omega' + 2\vec{k}\cdot\vec{k}' = 2m^2 - 2mE'$$

$$\omega\omega'(1-\cos\theta) = -m^2 + m(m+E)$$

$$\omega'\left[m + \omega(1-\cos\theta)\right] = m\omega$$

where I have used $\vec{k}\cdot\vec{k}' = \omega\omega'\cos\theta$, $E' = E + m$, and $E = \omega - \omega'$. Solving for ω' results in the Compton formula:

$$\omega' = \frac{\omega}{1 + \omega/m(1-\cos\theta)}. \tag{B.13}$$

B.3.3 Cyclotron frequency for a relativistic particle

I follow here the derivation given in [144]. A particle with charge q moving with velocity β in the $\hat{y}$ direction, traversing a magnetic field B in the $\hat{z}$ direction experiences a Lorentz force

$$\vec{F} = \frac{d\vec{p}}{dt} = qB\beta\hat{x}. \tag{B.14}$$

This force is perpendicular to the particle's motion and so, for an infinitesimal time interval dt, does not alter the magnitude of β, only its direction. The direction is shifted by an angle

$$d\theta = \frac{dp}{p} = \frac{qB\beta dt}{p}. \tag{B.15}$$

The particle has traversed a path length $ds = \beta dt$. In the next infinitesimal time step dt, the force is again perpendicular to the motion, and again there is no change in the magnitude of β. The particle then traces out a circle with radius $\rho = \frac{ds}{d\theta}$, and substituting into (B.15)

we have

$$B\rho = \frac{p}{q}, \tag{B.16}$$

which is identical to the non-relativistic result. The frequency of the orbit, called the cyclotron frequency, is given by

$$\omega_c = \frac{\beta}{\rho} = \frac{\beta qB}{p} = \frac{qB}{\gamma m}. \tag{B.17}$$

B.3.4 Energy and momentum from the inverse map

Given the rigidity $B\rho$ of the S800 and the parameters dta, yta, ata, bta, and we wish to extract the more physically relevant 4-vector P^μ. First we convert $B\rho = \frac{P}{q}$ into the useful quantity $\gamma\beta$:

$$\gamma\beta = \frac{P}{M} = \frac{B\rho Ze}{M} \approx \frac{Z}{A} \cdot \frac{B\rho}{3.10715 \text{ Tm}}. \tag{B.18}$$

For the last term, I have made the approximation $M \approx A \times 931.502$ MeV. The relativistic parameter γ_0 corresponding to the rigidity setting of the S800 is given by

$$\gamma_0 = \sqrt{1 + (\gamma_0\beta_0)^2} = \sqrt{1 + \left(\frac{B\rho Ze}{M}\right)^2}. \tag{B.19}$$

The parameter dta is defined as the difference between the kinetic energy of the outgoing particle $(E - M)$ and the kinetic energy $(E_0 - M)$ corresponding to the rigidity setting of the S800, expressed as a fraction of the central kinetic energy

$$dta = \frac{E - E_0}{E_0 - M} = \frac{\gamma - \gamma_0}{\gamma_0 - 1}. \tag{B.20}$$

Therefore,

$$\gamma = \gamma_0 + (\gamma_0 - 1)dta \tag{B.21}$$

and

$$E_{kin} = [\gamma_0 + (\gamma_0 - 1)dta - 1]\, M. \tag{B.22}$$

The magnitude of the momentum may be obtained, using $\left|\vec{P}\right| = \gamma\beta M = \sqrt{\gamma^2 - 1}M$, and $\gamma^2 \approx \gamma_0^2 + 2 \times dta \times \gamma_0(\gamma_0 - 1)$:

$$\begin{aligned} \frac{P}{P_0} &= \sqrt{\frac{\gamma^2 - 1}{\gamma_0^2 - 1}} \\ &\approx 1 + dta\frac{\gamma_0}{\gamma_0 + 1} \end{aligned} \tag{B.23}$$

Finally, the direction of the momentum vector is given by

$$\hat{P} = \Big(\sin\theta\cos\phi, \quad \sin\theta\sin\phi, \quad \cos\theta\Big) \tag{B.24}$$

where

$$\sin\theta = \sqrt{\sin^2 ata + \sin^2 bta} \tag{B.25}$$

$$\tan\phi = \frac{\sin bta}{\sin ata} \tag{B.26}$$

B.4 The tensor force

B.4.1 Representations for the tensor operator S_{12}

A rank-1 tensor is equivalent to a vector. For a vector $\vec{a} = (a_x, a_y, a_z)$, the components of a rank-1 tensor are

$$\begin{aligned} a_+ &= -\frac{1}{\sqrt{2}}(a_x + ia_y) \\ a_- &= \frac{1}{\sqrt{2}}(a_x - ia_y) \\ a_0 &= a_z. \end{aligned} \tag{B.27}$$

The scalar product of two rank-1 tensors is given by

$$(a \cdot b) = -a_+ b_- - a_- b_+ + a_0 b_0. \tag{B.28}$$

Two rank-1 tensors may be combined to form a rank-2 tensor

$$T^{(2)}_\mu = \left[a^{(1)} \otimes b^{(1)}\right]^{(2)} = \sum_{\mu_1,\mu_2} \langle 1\mu_1, 1\mu_2 | 2\mu \rangle a_{\mu 1} b_{\mu 2}. \tag{B.29}$$

The components of T are then given by

$$\begin{aligned} T^{(2)}_{\pm 2} &= a_\pm b_\pm \\ T^{(2)}_{\pm 1} &= \frac{1}{\sqrt{2}}(a_\pm b_0 + a_0 b_\pm) \\ T^{(2)}_0 &= \frac{1}{\sqrt{6}}(a_+ b_- + a_- b_+ + 2a_0 b_0). \end{aligned} \tag{B.30}$$

The scalar product of two rank-two tensors is given by

$$\begin{aligned} T^{(2)} \cdot U^{(2)} &= \sqrt{5} \sum_{\mu_1} \langle 1\mu_1, 1-\mu_1 | 00 \rangle T^{(2)}_{\mu_1} U^{(2)}_{-\mu_1} \\ &= T^{(2)}_{-2} U^{(2)}_{2} - T^{(2)}_{-1} U^{(2)}_{1} + T^{(2)}_{0} U^{(2)}_{0} - T^{(2)}_{1} U^{(2)}_{-1} + T^{(2)}_{2} U^{(2)}_{-2}. \end{aligned} \tag{B.31}$$

This may be written in terms of the constituent rank-1 tensors by inserting (B.30) into (B.31)

$$\begin{aligned} T^{(2)}(a,b) \cdot U^{(2)}(c,d) = \; & (a_- b_-)(c_+ d_+) \\ & -\frac{1}{2}(a_- b_0 + a_0 b_-)(c_+ d_0 + c_0 d_+) \\ & +\frac{1}{6}(a_+ b_- + a_- b_+ + 2a_0 b_0)(c_+ d_- + c_- d_+ + 2c_0 d_0) \\ & -\frac{1}{2}(a_+ b_0 + a_0 b_+)(c_- d_0 + c_0 d_-) \\ & +(a_+ b_+)(c_- d_-). \end{aligned} \tag{B.32}$$

With some reshuffling of terms, this becomes

$$\begin{aligned} T^{(2)}(a,b) \cdot U^{(2)}(c,d) = \; & \frac{1}{2}(-a_+ c_- - a_- c_+ + a_0 c_0)(-b_+ d_- - b_- d_+ + b_0 d_0) \\ & +\frac{1}{2}(-a_+ d_- - a_- d_+ + a_0 d_0)(-b_+ c_- - b_- c_+ + b_0 c_0) \\ & -\frac{1}{3}(-a_+ b_- - a_- b_+ + a_0 b_0)(-c_+ d_- - c_- d_+ + c_0 d_0). \end{aligned} \tag{B.33}$$

Comparing this form with (B.28), this may be rewritten as

$$T^{(2)}(a,b) \cdot U^{(2)}(c,d) = \frac{1}{2}(a \cdot c)(b \cdot d) + \frac{1}{2}(a \cdot d)(b \cdot c) - \frac{1}{3}(a \cdot b)(c \cdot d). \tag{B.34}$$

The normalized rank-2 spherical harmonic is given by

$$Y^{(2)} = \sqrt{\frac{15}{8\pi}}\,[\hat{r},\hat{r}]^{(2)}\,. \tag{B.35}$$

Inserting this into (B.34) and using $\hat{r}\cdot\hat{r}=1$, we obtain a relation for the tensor product of $Y^{(2)}$ with a rank-2 tensor constructed from the spin operators:

$$[\sigma_1,\sigma_2]^{(2)}\cdot Y^{(2)} = \sqrt{\frac{15}{8\pi}}\left\{(\sigma_1\cdot\hat{r})(\sigma_2\cdot\hat{r}) - \frac{1}{3}(\sigma_1\cdot\sigma_2)\right\}. \tag{B.36}$$

B.4.2 The tensor force in the jj coupling scheme

The tensor force involves both the orbital and spin degrees of freedom and is most easily dealt with in the LS coupling scheme. However, because the shell model is often treated in the jj coupling scheme, it is convenient to have an idea of how the tensor force behaves in that scheme. As a preface, we note that the direct term vanishes in the monopole term [31], leaving only the exchange term, so the isospin dependence is simply given by $(\tau_1\cdot\tau_2)(-1)^T$, which is negative for both $T=0$ and $T=1$. Therefore, if the remaining part of the tensor operator (the spin-coordinate part) produces a positive monopole, then the interaction will be attractive; otherwise the interaction is repulsive.

The greatest impediment to an intuitive understanding of the tensor force in the jj scheme is that the orbital part of the operator $Y^{(2)}$ acts on the *relative* coordinates of the two particles, while the shell-model orbits are in the lab frame. We may transform between lab frame and relative/center-of-mass coordinates by

$$|n_1\ell_1 n_2\ell_2, LM\rangle = \sum_{N\Lambda n\lambda} \langle N\Lambda n\lambda, L|n_1\ell_1 n_2\ell_2, L\rangle |N\Lambda n\lambda, LM\rangle. \tag{B.37}$$

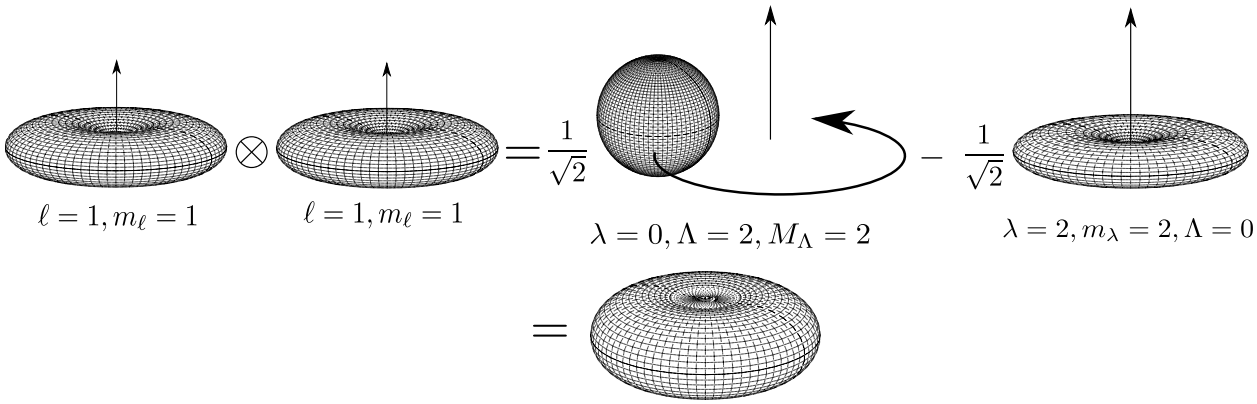

Figure B.1: Decomposition of two $\ell = 1$ orbits in lab frame coordinates into relative and center-of-mass coordinates. For each component, $\left|Y^\ell_m(\theta,\phi)\right|^2$ is shown. On the right side of the equation, the shapes represent the relative wave function, while the center-of-mass motion is indicated by a curved arrow. The straight arrows indicate the semi-classical direction of the angular momentum vector.

In a harmonic oscillator basis, the coefficients $\langle N\Lambda n\lambda, L|n_1\ell_1 n_1\ell_2, L\rangle$ – called *Moshinsky brackets* – have an analytic, although somewhat intimidating, formula [145], which will not be presented here.

For some special cases, the results of the transformation may be understood somewhat intuitively, and I consider here the simplest non-trivial pair made from the $0p$-shell orbits. For the $j_>, j'_>$ interaction (that is, $0p_{3/2}, 0p_{3/2}$), consider first the case $m_j = j$, $m'_j = j'$ in the uncoupled basis, which implies $m_s = m'_s = +\frac{1}{2}$ and $m_\ell = \ell$, $m'_\ell = \ell'$. These maximally-projected orbits will both lie predominantly in the x-y plane, and so their relative separation will be greater in the x and y directions than in the z direction, leading to an oblate shape for the relative wave function.

Indeed, we have $\langle 0200, 2|0101, 2\rangle = \frac{1}{\sqrt{2}}$ and $\langle 0002, 2|0101, 2\rangle = -\frac{1}{\sqrt{2}}$. This is displayed in Figure B.1, which shows the decomposition graphically. The wave function consists of a mixture of two cases: (i) two particles with relative angular momentum $\lambda = 2$ and center-of-mass angular momentum $\Lambda = 0$, and (ii) $\lambda = 0$ and $\Lambda = 2$. The average shape is, as

expected, oblate, and combining with both spin projections being +1, this leads to essentially the configuration labeled "-1" in Figure 2.2, producing a repulsive interaction.

If the spin of one of the particles were to be flipped, this would result in predominantly a $j_>, j_<$ pair. The shape of the relative wave function would be the same, but now the situation would be more like the configuration labeled "+1" in Figure 2.2. Combining this with the isospin dependence, this gives an attractive interaction. For other projections m'_ℓ, the situation becomes more complicated. However, the property holds that the $j_>, j_>$ and $j_<, j_<$ pairs are repulsive and the $j_>, j_<$ pairs are attractive.

B.4.3 Sum rule for the tensor force monopole

I prove here the relation

$$(2j_< + 1)\bar{V}_{j_<,j'} + (2j_> + 1)\bar{V}_{j_>,j'} = 0 \tag{B.38}$$

for the monopole component of the tensor force where $j' \neq j_<$ and $j' \neq j_>$. Beginning with the definition of the monopole (2.6)

$$\bar{V}_{j,j'} = \frac{\sum_{mm'} \langle jmj'm' | V | jmj'm' \rangle}{(2j+1)(2j'+1)} \tag{B.39}$$

we sum over all possible j for a given ℓ, which amounts to two possibilities: $j_>$ and $j_<$. We may therefore write

$$(2j'+1)\left[(2j_>+1)\bar{V}_{j_>,j'} + (2j_<+1)\bar{V}_{j_<,j'}\right] = \sum_{jm}\sum_{m'} \langle jmj'm' | V | jmj'm' \rangle \tag{B.40}$$

The sum over jm may be converted into a sum over $m_\ell m_s$, leaving

$$(2j'+1)\left[(2j_>+1)\bar{V}_{j_>,j'}+(2j_<+1)\bar{V}_{j_<,j'}\right]=\sum_{m_\ell m_s}\sum_{m'}\left\langle \ell m_\ell s m_s j' m'\middle| V\middle|\ell m_\ell s m_s j' m'\right\rangle \tag{B.41}$$

For a given m_ℓ and m', taking $m_s \to -m_s$ is equivalent to taking $\mathbf{S}_{12} \to -\mathbf{S}_{12}$, as my be seen from 2.3. Summing over $m_s = \pm\frac{1}{2}$ then gives zero. The entire sum on the right side of (B.41) becomes zero, and since $(2j'+1) \neq 0$, this proves (B.38). Note that if $n, \ell = n', \ell'$ then some of the m_s projections in (B.41) will be Pauli blocked and (B.38) will not hold exactly.

B.4.4 Explicit calculation of tensor monopole terms

Here we explicitly calculate a few terms to demonstrate some properties of the tensor monopole. In order to evaluate the matrix element of an operator which is the scalar product of commuting tensor operators of rank k, $Y^{(k)}$ and $X^{(k)}$, which operate on the L and S coordinates, respectively, we use

$$\left\langle LSJ\middle|Y^{(k)}\cdot X^{(k)}\middle|L'S'J'\right\rangle=\delta_{JJ'}(-1)^{S+J+L'}\begin{Bmatrix}L & S & J\\ S' & L' & k\end{Bmatrix}\left\langle L\middle\|Y^{(k)}\middle\|L'\right\rangle\left\langle S\middle\|X^{(k)}\middle\|S'\right\rangle. \tag{B.42}$$

In order to transform from the jj coupling scheme to the LS coupling scheme, we use

$$|\ell_a s_a j_a, \ell_b s_b j_b, J\rangle=\sum_{L,S}\begin{bmatrix}\ell_a & s_a & j_a\\ \ell_b & s_b & j_b\\ L & S & J\end{bmatrix}|\ell_a\ell_b L, s_a s_b S, J\rangle. \tag{B.43}$$

To convert from lab coordinates to relative and center-of-mass coordinates, we use Talmi-Moshinsky brackets [146]

$$|n_a\ell_a n_b\ell_b L\rangle = \sum_{N\Lambda n\lambda} \langle n_a\ell_a n_b\ell_b L|N\Lambda n\lambda\rangle |N\Lambda n\lambda L\rangle. \tag{B.44}$$

To evaluate the matrix element in relative and center-of-mass coordinates, we use

$$\begin{aligned}\left\langle n\lambda N\Lambda L\middle\| Y^{(k)} f(r)\middle\| n'\lambda' N\Lambda L'\right\rangle = (-1)^{\lambda+\Lambda+L'}\sqrt{(2L+1)(2L'+1)}\begin{Bmatrix} L & \lambda & \Lambda \\ \lambda' & L' & k\end{Bmatrix} \\ \times \left\langle \lambda\middle\| Y^{(k)}\middle\|\lambda'\right\rangle \langle n\lambda[|f(r)|]n'\lambda'\rangle.\end{aligned} \tag{B.45}$$

The strange bracket on the last term indicates an integration over the radial coordinates only, which may be evaluated with Talmi integrals [147]:

$$\langle n\lambda[|f(r)|]n'\lambda'\rangle = \sum_p B(n,\lambda,n',\lambda',p) I_p, \tag{B.46}$$

where

$$I_p = \frac{2}{\Gamma(p+\frac{3}{2})}\int_0^\infty r^{2p} e^{-r^2} f(r) r^2 dr. \tag{B.47}$$

When evaluating the reduced matrix element of a rank-2 harmonic oscillator, we use

$$\left\langle \lambda\middle\| Y^{(2)}\middle\|\lambda'\right\rangle = \sqrt{\frac{5}{4\pi}}\sqrt{2\lambda+1}\langle \lambda 020|\lambda' 0\rangle. \tag{B.48}$$

Combining all of this, we have for the tensor force $V_t = X^{(2)}\cdot Y^{(2)} f(r)$, with $X^{(2)}$ acting

on the spins and $Y^{(2)}$ acting on the relative coordinates:

$$\langle ab|V_t|cd\rangle_J = \sum_p \mathcal{C}_{Jp}^{abcd} I_p \tag{B.49}$$

with the coefficient $\mathcal{C}_{Jp}^{abcd}$ defined as

$$\begin{aligned}\mathcal{C}_{Jp}^{abcd} =& \sum_{LL'} (-1)^{S+J+L'} \begin{bmatrix} \ell_a & s_a & j_a \\ \ell_b & s_b & j_b \\ L & S & J \end{bmatrix} \begin{bmatrix} \ell_c & s_c & j_c \\ \ell_d & s_d & j_d \\ L' & S & J \end{bmatrix} \begin{Bmatrix} L & S & J \\ S & L' & k \end{Bmatrix} \\ &\times \sum_{n\lambda N\Lambda\lambda'} \langle n_a \ell_a n_b \ell_b L | N\Lambda n\lambda \rangle \big\langle n_c \ell_c n_d \ell_d L' \big| N\Lambda n'\lambda' \big\rangle \\ &\times (-1)^{\lambda+\Lambda+L'} \sqrt{(2L+1)(2L'+1)} \begin{Bmatrix} L & \lambda & \Lambda \\ \lambda' & L' & k \end{Bmatrix} \\ &\times \sqrt{2\lambda+1} \big\langle \lambda 0 k 0 \big| \lambda' 0 \big\rangle B(n,\lambda,n',\lambda',p)\end{aligned} \tag{B.50}$$

Here $k = 2$, $S = 1$ and I have absorbed the positive constants $\left\langle S \middle\| X^{(2)} \middle\| S \right\rangle$ and $\sqrt{\frac{5}{4\pi}}$ into $f(r)$. The monopole component may be written as

$$\overline{V}_{ab} = \sum_p I_p \frac{\sum_J \left(\mathcal{D}_{Jp}^{ab} + \mathcal{E}_{Jp}^{ab} \right)}{\sum_J (2J+1)} \tag{B.51}$$

where the direct and exchange terms

$$\mathcal{D}_{Jp}^{ab} \equiv \frac{(2J+1)}{1+\delta_{ab}} \mathcal{C}_{Jp}^{abab}, \quad \text{and} \quad \mathcal{E}_{Jp}^{ab} \equiv \frac{(2J+1)(-1)^{ja+jb-J-T}}{1+\delta_{ab}} \mathcal{C}_{Jp}^{abba} \tag{B.52}$$

have been defined for convenience.

The results of (B.50) are given for a few cases in Table B.1. It is clear that, regardless of the form of the radial dependence $f(r)$, the direct term vanishes in the monopole and that (B.38) holds for $j \neq j'$. We may further see that if we assume a Gaussian form for the radial dependence $f(r) = e^{-ar^2}$, then the Talmi integral in (B.46) is simply $I_p = (1+a)^{-(p+3/2)}$. The tensor monopole is then attractive for $j_>, j'_<$ type configurations, while it is repulsive for $j_>, j'_>$ and $j_<, j'_<$ configurations, for all positive values of a.

Table B.1: Coefficients of the Talmi integrals I_p for the calculation of the $T = 1$ monopole term for a tensor interaction $V_t = X^{(2)} \cdot Y^{(2)} f(r)$ for the given orbits.

a	b	p	J	$\mathcal{D}^{ab}_{Jp}$	$\mathcal{E}^{ab}_{Jp}$	$\sum_J \mathcal{D}^{ab}_{Jp}$	$\sum_J \mathcal{E}^{ab}_{Jp}$
$0d_{3/2}$	$0p_{1/2}$	1	1	0.0218	0.1030		
		1	2	-0.0131	0.0113	-0.0000	0.3651
		2	1	0.0355	-0.0862		
		2	2	-0.0213	-0.0213	-0.0000	-0.3651
		3	1	0.0178	0.0178		
		3	2	-0.0107	-0.0107	0.0000	0.0000
$0d_{3/2}$	$0p_{3/2}$	0	3	0.0000	-0.0000	0.0000	0.0000
		1	0	-0.3165	-0.1947		
		1	1	0.1684	-0.0101		
		1	2	-0.0633	-0.0536		
		1	3	0.0183	0.0183	0.0000	-0.3651
		2	0	0.3956	0.2130		
		2	1	-0.2698	0.1075		
		2	2	0.0791	-0.0304		
		2	3	0.0026	-0.0026	-0.0000	0.3651
		3	0	-0.2130	-0.2130		
		3	1	0.0568	0.0568		
		3	2	-0.0426	-0.0426		
		3	3	0.0365	0.0365	-0.0000	0.0000
$0p_{3/2}$	$0p_{1/2}$	1	1	-0.0051	-0.0862		
		1	2	0.0030	0.0030	-0.0000	-0.2434
		2	1	-0.0761	0.0761		
		2	2	0.0456	-0.0456	0.0000	-0.0000
$0p_{3/2}$	$0p_{3/2}$	1	0	0.0304	0.0304		
		1	1	-0.0203	0.0203		
		1	2	0.0061	0.0061		
		1	3	0.0000	-0.0000	0.0000	0.1217
		2	0	0.0000	0.0000		
		2	1	0.0304	-0.0304		
		2	2	0.0000	0.0000		
		2	3	-0.0130	0.0130	-0.0000	0.0000

Appendix C

Parameters used in knockout reaction calculations

Tabulated below are the parameters used in the eikonal model reaction calculations. $J^{\pi}_{i,f}$ and $E_{i,f}$ are the spin-parities and excited state energies of the initial (projectile) and final (residue) states. The orbit of the removed nucleon is indicated by ψ_{α}. V_0 and R_0 give the depth and radius parameters for the Woods-Saxon potential used in the core-valence two-body wave function, or form factor. In all cases, a fixed diffuseness parameter $a = 0.7$ fm and spin-orbit depth $V_{LS} = 6.0$ MeV are used. The effective separation energy to each final state is given by $S^{fi}_{n,p} = S_{n,p} + E_f - E_i$, where $S_{n,p}$ is the neutron or proton ground-state to ground-state separation energy from Table C.1. The resulting relative wave function rms radius is given in the column marked r_{rms}. The target density is approximated as a Gaussian with rms radius 2.36 fm, and the incident beam energies were taken to be 73.4 [13], 97.7, 86.0, and 79.0 MeV/u for ^{34}Si,^{36}Si,^{38}Si and ^{40}Si, respectively. The calculated stripping and diffraction cross sections, and their sum are indicated by σ_{str}, σ_{diff}, and $\sigma^{\rm sp}_{\alpha}$, respectively. The shell-model spectroscopic factor is labeled C^2S, and the resulting theoretical cross section (including the $[A/(A-1)]^N$ center-of-mass correction, see equation (1) in the text) is labeled σ^{fi}_{α}. Table C.2 gives the results of the calculation of the two-step process for ^{36}Si described in section IV.A of the text. Parameters and cross sections

for neutron knockout from ^{34}Si using the SDPF-MU and SDPF-U interactions are given in Tables C.3 and C.4. Parameters and cross sections for neutron and proton knockout with each interaction are given in Tables C.5-C.8 (^{36}Si), Tables C.9-C.12 (^{38}Si), and Tables C.13-C.16 (^{40}Si). All energies are in MeV, lengths are in fm, and cross sections are in mb.

Table C.1: One-neutron and one-proton separation energies, in MeV, from [1].

	S_n	S_p
^{33}Si	4.508(08)	
^{34}Si	7.514(14)	18.780(80)
^{35}Si	2.470(40)	
^{36}Si	6.100(80)	19.460(100)
^{37}Si	2.270(110)	
^{38}Si	5.650(110)	21.270(140)
^{39}Si	1.580(110)	
^{40}Si	4.960(250)	22.860(550)
^{35}Al	5.220(100)	
^{37}Al	4.210(160)	
^{39}Al	3.290(560)	

Table C.2: Calculated cross sections for a two-step ^{36}Si(0^+) $\rightarrow$ ^{36}Si(2^+) $\rightarrow$^{35}Si(J^π) process. Energies and spectroscopic factors are from shell model calculations with the SDPF-MU interaction. $\sigma^{\rm sp}_{2step}$ is the cross section for excitation to ^{36}Si(2^+), followed by a neutron knockout, assuming a normalized neutron single-particle state. The last column gives the summed cross section for a given final state in ^{35}Si. Only final states which could decay via an $E1$ transition to the $7/2^-$ ground state of ^{35}Si are shown.

^{35}Si(J^π)	E_f [MeV]	orbit	$\sigma^{\rm sp}_{2step}$ (mb)	C^2S	$\sum\sigma_{2step}$
$7/2^+_1$	1.733	$d_{5/2}$	0.26	0.0086	
		$d_{3/2}$	0.22	1.2997	0.29
$5/2^+_2$	3.015	$d_{5/2}$	0.26	0.0063	
		$d_{3/2}$	0.23	0.0006	
		$s_{1/2}$	0.36	0.5820	0.21
$9/2^+_2$	4.447	$d_{5/2}$	0.26	0.0531	0.01

Table C.3: Parameters used in the calculation and the resulting theoretical cross sections σ_α^{fi} for neutron knockout from ^{34}Si using level energies and spectroscopic factors from the SDPF-MU interaction. The beam energy is 73.4 MeV/u on a ^{9}Be target.

J_i^π	E_i	J_f^π	E_f	ψ_α	V_0	R_0	r_{rms}	σ_{str}	σ_{diff}	$\sigma_\alpha^{\rm sp}$	C^2S	σ_α^{fi}
0^+	0.000	$3/2^+$	0.000	$0d_{3/2}$	45.706	1.267	3.692	11.65	3.72	15.37	3.609	58.90
0^+	0.000	$1/2^+$	0.976	$1s_{1/2}$	49.446	1.181	3.783	15.01	5.50	20.51	1.546	33.65
0^+	0.000	$5/2^+$	3.934	$0d_{5/2}$	46.257	1.255	3.623	10.52	3.05	13.58	3.694	53.24
0^+	0.000	$3/2^+$	4.944	$0d_{3/2}$	53.087	1.267	3.475	8.96	2.48	11.45	0.066	0.81

Table C.4: Parameters used in the calculation and the resulting theoretical cross sections σ_α^{fi} for neutron knockout from ^{34}Si using level energies and spectroscopic factors from the SDPF-U interaction. The beam energy is 73.4 MeV/u on a ^{9}Be target.

J_i^π	E_i	J_f^π	E_f	ψ_α	V_0	R_0	r_{rms}	σ_{str}	σ_{diff}	$\sigma_\alpha^{\rm sp}$	C^2S	σ_α^{fi}
0^+	0.000	$3/2^+$	0.000	$0d_{3/2}$	45.706	1.267	3.692	11.65	3.72	15.37	3.478	56.76
0^+	0.000	$1/2^+$	0.725	$1s_{1/2}$	48.992	1.181	3.805	15.33	5.67	21.01	1.382	30.82
0^+	0.000	$5/2^+$	3.931	$0d_{5/2}$	46.253	1.255	3.623	10.53	3.05	13.58	2.422	34.92
0^+	0.000	$3/2^+$	4.030	$0d_{3/2}$	51.758	1.267	3.507	9.34	2.64	11.98	0.152	1.93
0^+	0.000	$3/2^+$	4.312	$0d_{3/2}$	52.170	1.267	3.497	9.22	2.59	11.81	0.000	0.00
0^+	0.000	$1/2^+$	4.650	$1s_{1/2}$	55.792	1.181	3.534	11.62	3.74	15.35	0.475	7.75

Table C.5: Parameters used in the calculation and the resulting theoretical cross sections σ_α^{fi} for neutron knockout from ^{36}Si using level energies and spectroscopic factors from the SDPF-MU interaction. The beam energy is 97.7 MeV/u on a ^{9}Be target.

J_i^π	E_i	J_f^π	E_f	ψ_α	V_0	R_0	r_{rms}	σ_{str}	σ_{diff}	$\sigma_\alpha^{\rm sp}$	C^2S	σ_α^{fi}
0^+	0.000	$7/2^-$	0.000	$0f_{7/2}$	59.389	1.191	3.876	12.25	3.43	15.68	1.709	29.16
0^+	0.000	$3/2^+$	0.499	$0d_{3/2}$	44.098	1.245	3.751	11.37	3.36	14.72	3.070	47.83
0^+	0.000	$3/2^-$	1.222	$1p_{3/2}$	91.845	0.949	3.794	13.11	4.17	17.28	0.132	2.48
0^+	0.000	$1/2^+$	1.240	$1s_{1/2}$	45.642	1.188	3.929	15.61	5.45	21.06	0.957	21.31
0^+	0.000	$5/2^+$	2.298	$0d_{5/2}$	40.897	1.241	3.788	11.55	3.28	14.83	0.086	1.36
0^+	0.000	$1/2^-$	2.340	$1p_{1/2}$	100.221	0.950	3.680	11.67	3.51	15.18	0.022	0.36
0^+	0.000	$3/2^+$	2.600	$0d_{3/2}$	47.345	1.245	3.631	9.93	2.71	12.64	0.184	2.46
0^+	0.000	$5/2^+$	3.014	$0d_{5/2}$	42.048	1.241	3.749	11.08	3.07	14.15	0.096	1.44
0^+	0.000	$3/2^+$	3.268	$0d_{3/2}$	48.353	1.245	3.600	9.57	2.56	12.13	0.162	2.08
0^+	0.000	$1/2^+$	3.297	$1s_{1/2}$	49.296	1.188	3.747	13.18	4.22	17.41	0.552	10.17
0^+	0.000	$5/2^+$	3.755	$0d_{5/2}$	43.224	1.241	3.712	10.63	2.88	13.51	1.176	16.82
0^+	0.000	$5/2^-$	4.289	$0f_{5/2}$	73.551	1.224	3.620	9.32	2.27	11.59	0.057	0.72
0^+	0.000	$1/2^+$	4.420	$1s_{1/2}$	51.211	1.188	3.668	12.20	3.75	15.95	0.000	0.00

Table C.6: Parameters used in the calculation and the resulting theoretical cross sections σ_α^{fi} for neutron knockout from ^{36}Si using level energies and spectroscopic factors from the SDPF-U interaction. The beam energy is 97.7 MeV/u on a ^{9}Be target.

J_i^π	E_i	J_f^π	E_f	ψ_α	V_0	R_0	r_{rms}	σ_{str}	σ_{diff}	$\sigma_\alpha^{\mathrm{sp}}$	C^2S	σ_α^{fi}
0^+	0.000	$7/2^-$	0.000	$0f_{7/2}$	59.389	1.191	3.876	12.25	3.43	15.68	1.727	29.46
0^+	0.000	$3/2^-$	0.932	$1p_{3/2}$	91.133	0.949	3.822	13.46	4.34	17.81	0.090	1.75
0^+	0.000	$3/2^+$	0.955	$0d_{3/2}$	44.814	1.245	3.722	11.01	3.19	14.20	2.609	39.20
0^+	0.000	$1/2^+$	1.234	$1s_{1/2}$	45.631	1.188	3.930	15.62	5.46	21.08	0.998	22.25
0^+	0.000	$1/2^-$	2.144	$1p_{1/2}$	99.761	0.950	3.696	11.86	3.59	15.45	0.019	0.33
0^+	0.000	$5/2^+$	2.518	$0d_{5/2}$	41.253	1.241	3.775	11.40	3.21	14.61	0.260	4.02
0^+	0.000	$5/2^+$	2.802	$0d_{5/2}$	41.709	1.241	3.760	11.21	3.13	14.34	0.163	2.47
0^+	0.000	$3/2^+$	2.925	$0d_{3/2}$	47.837	1.245	3.616	9.75	2.63	12.39	0.163	2.14
0^+	0.000	$3/2^+$	3.317	$0d_{3/2}$	48.427	1.245	3.597	9.55	2.55	12.09	0.495	6.34
0^+	0.000	$1/2^+$	3.738	$1s_{1/2}$	50.054	1.188	3.715	12.77	4.03	16.80	0.446	7.93
0^+	0.000	$7/2^-$	4.055	$0f_{7/2}$	66.458	1.191	3.701	10.10	2.51	12.61	0.025	0.35
0^+	0.000	$5/2^+$	4.071	$0d_{5/2}$	43.720	1.241	3.697	10.46	2.81	13.26	0.950	13.33
0^+	0.000	$5/2^-$	4.162	$0f_{5/2}$	73.353	1.224	3.625	9.36	2.29	11.65	0.045	0.58
0^+	0.000	$5/2^-$	4.725	$0f_{5/2}$	74.230	1.224	3.607	9.17	2.21	11.38	0.032	0.40
0^+	0.000	$1/2^+$	4.752	$1s_{1/2}$	51.768	1.188	3.647	11.94	3.63	15.57	0.010	0.17
0^+	0.000	$7/2^-$	4.886	$0f_{7/2}$	67.852	1.191	3.673	9.77	2.38	12.16	0.012	0.16
0^+	0.000	$3/2^-$	4.929	$1p_{3/2}$	100.406	0.949	3.528	9.95	2.73	12.68	0.000	0.00

Table C.7: Parameters used in the calculation and the resulting theoretical cross sections σ_α^{fi} for proton knockout from ^{36}Si using level energies and spectroscopic factors from the SDPF-MU interaction. The beam energy is 97.7 MeV/u on a ^{9}Be target.

J_i^π	E_i	J_f^π	E_f	ψ_α	V_0	R_0	r_{rms}	σ_{str}	σ_{diff}	$\sigma_\alpha^{\mathrm{sp}}$	C^2S	σ_α^{fi}
0^+	0.000	$5/2^+$	0.000	$0d_{5/2}$	59.899	1.327	3.491	8.49	1.85	10.34	3.936	43.05
0^+	0.000	$3/2^+$	1.889	$0d_{3/2}$	65.943	1.342	3.373	7.42	1.55	8.98	0.050	0.48
0^+	0.000	$1/2^+$	1.945	$1s_{1/2}$	70.227	1.276	3.273	8.33	1.96	10.29	0.159	1.74
0^+	0.000	$5/2^+$	2.176	$0d_{5/2}$	62.798	1.327	3.448	8.06	1.71	9.77	0.780	8.07
0^+	0.000	$5/2^+$	3.148	$0d_{5/2}$	64.082	1.327	3.430	7.88	1.66	9.54	0.079	0.79
0^+	0.000	$3/2^+$	3.278	$0d_{3/2}$	67.716	1.342	3.350	7.21	1.49	8.70	0.001	0.00
0^+	0.000	$1/2^+$	3.404	$1s_{1/2}$	72.221	1.276	3.242	8.02	1.85	9.87	0.005	0.05
0^+	0.000	$3/2^+$	3.535	$0d_{3/2}$	68.042	1.342	3.346	7.17	1.47	8.65	0.103	0.94
0^+	0.000	$5/2^+$	4.073	$0d_{5/2}$	65.298	1.327	3.414	7.73	1.61	9.34	0.000	0.00
0^+	0.000	$5/2^+$	4.225	$0d_{5/2}$	65.497	1.327	3.412	7.70	1.60	9.30	0.032	0.32
0^+	0.000	$1/2^+$	4.380	$1s_{1/2}$	73.545	1.276	3.223	7.83	1.78	9.61	0.022	0.22
0^+	0.000	$3/2^+$	4.382	$0d_{3/2}$	69.117	1.342	3.333	7.05	1.44	8.49	0.055	0.49
0^+	0.000	$3/2^+$	4.869	$0d_{3/2}$	69.733	1.342	3.326	6.99	1.42	8.40	0.006	0.05
0^+	0.000	$5/2^+$	5.069	$0d_{5/2}$	66.600	1.327	3.397	7.57	1.56	9.13	0.004	0.04
0^+	0.000	$5/2^+$	5.127	$0d_{5/2}$	66.676	1.327	3.396	7.56	1.56	9.11	0.067	0.65
0^+	0.000	$3/2^+$	5.349	$0d_{3/2}$	70.340	1.342	3.319	6.92	1.40	8.32	0.005	0.05
0^+	0.000	$3/2^+$	5.548	$0d_{3/2}$	70.591	1.342	3.316	6.90	1.39	8.29	0.008	0.07
0^+	0.000	$1/2^+$	5.650	$1s_{1/2}$	75.257	1.276	3.199	7.60	1.70	9.30	0.003	0.03
0^+	0.000	$5/2^+$	5.769	$0d_{5/2}$	67.512	1.327	3.386	7.46	1.53	8.99	0.044	0.42

Table C.8: Parameters used in the calculation and the resulting theoretical cross sections σ_α^{fi} for proton knockout from ^{36}Si using level energies and spectroscopic factors from the SDPF-U interaction. The beam energy is 97.7 MeV/u on a ^{9}Be target.

J_i^π	E_i	J_f^π	E_f	ψ_α	V_0	R_0	r_{rms}	σ_{str}	σ_{diff}	$\sigma_\alpha^{\mathrm{sp}}$	C^2S	σ_α^{fi}
0^+	0.000	$5/2^+$	0.000	$0d_{5/2}$	59.899	1.327	3.491	8.49	1.85	10.34	3.699	40.46
0^+	0.000	$1/2^+$	1.614	$1s_{1/2}$	69.772	1.276	3.281	8.41	1.99	10.39	0.223	2.46
0^+	0.000	$3/2^+$	1.896	$0d_{3/2}$	65.952	1.342	3.373	7.42	1.55	8.97	0.044	0.42
0^+	0.000	$5/2^+$	2.154	$0d_{5/2}$	62.769	1.327	3.449	8.06	1.72	9.78	1.118	11.56
0^+	0.000	$3/2^+$	2.761	$0d_{3/2}$	67.057	1.342	3.359	7.29	1.51	8.80	0.015	0.14
0^+	0.000	$1/2^+$	2.783	$1s_{1/2}$	71.374	1.276	3.255	8.15	1.89	10.05	0.000	0.00
0^+	0.000	$5/2^+$	2.831	$0d_{5/2}$	63.664	1.327	3.436	7.94	1.68	9.61	0.044	0.45
0^+	0.000	$3/2^+$	3.336	$0d_{3/2}$	67.789	1.342	3.350	7.20	1.48	8.69	0.077	0.71
0^+	0.000	$5/2^+$	3.372	$0d_{5/2}$	64.377	1.327	3.426	7.84	1.65	9.49	0.020	0.20
0^+	0.000	$5/2^+$	3.919	$0d_{5/2}$	65.096	1.327	3.417	7.75	1.62	9.37	0.025	0.25
0^+	0.000	$3/2^+$	4.114	$0d_{3/2}$	68.778	1.342	3.337	7.09	1.45	8.54	0.099	0.89
0^+	0.000	$1/2^+$	4.154	$1s_{1/2}$	73.239	1.276	3.227	7.88	1.80	9.67	0.022	0.22
0^+	0.000	$3/2^+$	4.441	$0d_{3/2}$	69.192	1.342	3.332	7.04	1.44	8.48	0.015	0.13
0^+	0.000	$5/2^+$	4.709	$0d_{5/2}$	66.130	1.327	3.403	7.62	1.58	9.20	0.003	0.03
0^+	0.000	$5/2^+$	4.846	$0d_{5/2}$	66.309	1.327	3.401	7.60	1.57	9.17	0.016	0.16
0^+	0.000	$3/2^+$	4.850	$0d_{3/2}$	69.709	1.342	3.326	6.99	1.42	8.41	0.000	0.00
0^+	0.000	$5/2^+$	4.987	$0d_{5/2}$	66.493	1.327	3.399	7.58	1.56	9.14	0.062	0.60
0^+	0.000	$3/2^+$	5.142	$0d_{3/2}$	70.078	1.342	3.322	6.95	1.41	8.36	0.002	0.02
0^+	0.000	$1/2^+$	5.151	$1s_{1/2}$	74.585	1.276	3.208	7.69	1.73	9.42	0.008	0.08
0^+	0.000	$3/2^+$	5.365	$0d_{3/2}$	70.360	1.342	3.319	6.92	1.40	8.32	0.002	0.02
0^+	0.000	$1/2^+$	5.530	$1s_{1/2}$	75.095	1.276	3.201	7.62	1.71	9.33	0.002	0.01
0^+	0.000	$1/2^+$	5.682	$1s_{1/2}$	75.300	1.276	3.198	7.60	1.70	9.30	0.007	0.07

Table C.9: Parameters used in the calculation and the resulting theoretical cross sections σ_α^{fi} for neutron knockout from ^{38}Si using level energies and spectroscopic factors from the SDPF-MU interaction. The beam energy is 86.0 MeV/u on a ^{9}Be target.

J_i^π	E_i	J_f^π	E_f	ψ_α	V_0	R_0	r_{rms}	σ_{str}	σ_{diff}	$\sigma_\alpha^{\rm sp}$	C^2S	σ_α^{fi}
0^+	0.000	$5/2^-$	0.000	$0f_{5/2}$	64.812	1.212	3.833	10.68	3.15	13.83	0.150	2.25
0^+	0.000	$7/2^-$	0.091	$0f_{7/2}$	57.304	1.185	3.930	11.68	3.50	15.18	2.814	46.28
0^+	0.000	$3/2^-$	0.248	$1p_{3/2}$	83.584	0.966	3.992	14.57	5.27	19.84	0.109	2.34
0^+	0.000	$3/2^-$	0.751	$1p_{3/2}$	84.830	0.966	3.934	13.79	4.85	18.65	0.270	5.45
0^+	0.000	$3/2^+$	0.763	$0d_{3/2}$	43.657	1.224	3.766	10.45	3.27	13.73	2.793	40.45
0^+	0.000	$1/2^+$	1.464	$1s_{1/2}$	43.674	1.195	3.990	15.32	5.69	21.01	0.799	17.71
0^+	0.000	$1/2^-$	1.509	$1p_{1/2}$	91.263	0.971	3.842	12.57	4.24	16.81	0.062	1.13
0^+	0.000	$5/2^+$	1.773	$0d_{5/2}$	38.797	1.227	3.865	11.34	3.51	14.85	0.029	0.46
0^+	0.000	$5/2^-$	2.055	$0f_{5/2}$	68.165	1.212	3.738	9.53	2.62	12.15	0.067	0.88
0^+	0.000	$3/2^+$	2.127	$0d_{3/2}$	45.784	1.224	3.682	9.47	2.81	12.27	0.032	0.42
0^+	0.000	$7/2^-$	2.381	$0f_{7/2}$	61.349	1.185	3.817	10.27	2.85	13.12	0.113	1.61
0^+	0.000	$7/2^-$	2.774	$0f_{7/2}$	62.027	1.185	3.800	10.07	2.76	12.84	0.008	0.11
0^+	0.000	$5/2^-$	2.805	$0f_{5/2}$	69.363	1.212	3.708	9.19	2.48	11.66	0.000	0.00
0^+	0.000	$5/2^+$	2.827	$0d_{5/2}$	40.510	1.227	3.801	10.56	3.14	13.70	0.120	1.74
0^+	0.000	$3/2^-$	2.828	$1p_{3/2}$	89.727	0.966	3.743	11.37	3.63	15.00	0.010	0.17
0^+	0.000	$1/2^-$	3.036	$1p_{1/2}$	94.756	0.971	3.713	10.99	3.46	14.45	0.006	0.10
0^+	0.000	$3/2^+$	3.100	$0d_{3/2}$	47.270	1.224	3.631	8.90	2.55	11.44	0.043	0.52
0^+	0.000	$1/2^+$	3.237	$1s_{1/2}$	46.796	1.195	3.823	13.08	4.50	17.58	0.027	0.50
0^+	0.000	$5/2^+$	3.519	$0d_{5/2}$	41.616	1.227	3.764	10.12	2.94	13.06	0.341	4.69
0^+	0.000	$1/2^+$	3.534	$1s_{1/2}$	47.304	1.195	3.800	12.78	4.34	17.12	0.091	1.65
0^+	0.000	$1/2^-$	4.619	$1p_{1/2}$	98.212	0.971	3.605	9.76	2.89	12.65	0.001	0.01

Table C.10: Parameters used in the calculation and the resulting theoretical cross sections σ_α^{fi} for neutron knockout from ^{38}Si using level energies and spectroscopic factors from the SDPF-U interaction. The beam energy is 86.0 MeV/u on a ^{9}Be target.

J_i^π	E_i	J_f^π	E_f	ψ_α	V_0	R_0	r_{rms}	σ_{str}	σ_{diff}	$\sigma_\alpha^{\mathrm{sp}}$	C^2S	σ_α^{fi}
0^+	0.000	$5/2^-$	0.000	$0f_{5/2}$	64.812	1.212	3.833	10.68	3.15	13.83	0.065	0.98
0^+	0.000	$7/2^-$	0.170	$0f_{7/2}$	57.447	1.185	3.926	11.63	3.47	15.10	2.848	46.57
0^+	0.000	$3/2^-$	0.236	$1p_{3/2}$	83.554	0.966	3.993	14.59	5.28	19.87	0.018	0.39
0^+	0.000	$3/2^-$	0.424	$1p_{3/2}$	84.023	0.966	3.971	14.29	5.12	19.41	0.266	5.59
0^+	0.000	$1/2^-$	1.307	$1p_{1/2}$	90.787	0.971	3.862	12.82	4.37	17.19	0.050	0.93
0^+	0.000	$5/2^-$	1.818	$0f_{5/2}$	67.784	1.212	3.747	9.64	2.67	12.32	0.048	0.64
0^+	0.000	$7/2^-$	1.957	$0f_{7/2}$	60.614	1.185	3.836	10.50	2.95	13.45	0.217	3.17
0^+	0.000	$3/2^+$	2.125	$0d_{3/2}$	45.781	1.224	3.682	9.47	2.81	12.27	2.191	28.36
0^+	0.000	$1/2^+$	2.361	$1s_{1/2}$	45.274	1.195	3.899	14.08	5.02	19.10	0.968	19.50
0^+	0.000	$5/2^-$	2.481	$0f_{5/2}$	68.847	1.212	3.720	9.33	2.54	11.87	0.007	0.10
0^+	0.000	$7/2^-$	2.762	$0f_{7/2}$	62.006	1.185	3.801	10.08	2.77	12.85	0.000	0.00
0^+	0.000	$5/2^+$	2.860	$0d_{5/2}$	40.563	1.227	3.800	10.54	3.13	13.67	0.052	0.75
0^+	0.000	$3/2^-$	2.895	$1p_{3/2}$	89.880	0.966	3.738	11.31	3.60	14.91	0.002	0.03
0^+	0.000	$3/2^+$	3.045	$0d_{3/2}$	47.186	1.224	3.634	8.93	2.56	11.49	0.010	0.12
0^+	0.000	$1/2^-$	3.302	$1p_{1/2}$	95.347	0.971	3.693	10.76	3.35	14.11	0.007	0.11
0^+	0.000	$5/2^+$	3.456	$0d_{5/2}$	41.516	1.227	3.767	10.15	2.96	13.11	0.271	3.75
0^+	0.000	$3/2^+$	3.704	$0d_{3/2}$	48.180	1.224	3.603	8.58	2.41	10.99	0.070	0.81
0^+	0.000	$1/2^+$	3.862	$1s_{1/2}$	47.861	1.195	3.775	12.46	4.18	16.64	0.058	1.01
0^+	0.000	$5/2^+$	4.160	$0d_{5/2}$	42.627	1.227	3.732	9.74	2.78	12.52	0.111	1.47
0^+	0.000	$1/2^-$	4.205	$1p_{1/2}$	97.322	0.971	3.631	10.05	3.02	13.07	0.000	0.01
0^+	0.000	$1/2^+$	4.638	$1s_{1/2}$	49.162	1.195	3.720	11.78	3.84	15.62	0.011	0.19

Table C.11: Parameters used in the calculation and the resulting theoretical cross sections σ_α^{fi} for proton knockout from ^{38}Si using level energies and spectroscopic factors from the SDPF-MU interaction. The beam energy is 86.0 MeV/u on a ^{9}Be target.

J_i^π	E_i	J_f^π	E_f	ψ_α	V_0	R_0	r_{rms}	σ_{str}	σ_{diff}	$\sigma_\alpha^{\mathrm{sp}}$	C^2S	σ_α^{fi}
0^+	0.000	$5/2^+$	0.000	$0d_{5/2}$	60.568	1.334	3.514	7.59	1.73	9.31	2.704	26.57
0^+	0.000	$1/2^+$	1.648	$1s_{1/2}$	70.124	1.286	3.287	7.52	1.83	9.35	0.056	0.55
0^+	0.000	$3/2^+$	1.759	$0d_{3/2}$	66.424	1.344	3.392	6.57	1.44	8.01	0.008	0.07
0^+	0.000	$5/2^+$	2.354	$0d_{5/2}$	63.638	1.334	3.471	7.18	1.59	8.78	0.007	0.07
0^+	0.000	$5/2^+$	2.558	$0d_{5/2}$	63.902	1.334	3.467	7.15	1.58	8.73	1.381	12.72
0^+	0.000	$3/2^+$	2.582	$0d_{3/2}$	67.459	1.344	3.380	6.46	1.40	7.86	0.107	0.88
0^+	0.000	$1/2^+$	2.609	$1s_{1/2}$	71.409	1.286	3.268	7.33	1.76	9.10	0.030	0.29
0^+	0.000	$3/2^+$	2.810	$0d_{3/2}$	67.745	1.344	3.376	6.42	1.39	7.82	0.006	0.05
0^+	0.000	$1/2^+$	2.832	$1s_{1/2}$	71.707	1.286	3.264	7.29	1.75	9.04	0.102	0.98
0^+	0.000	$3/2^+$	2.985	$0d_{3/2}$	67.965	1.344	3.373	6.40	1.39	7.79	0.002	0.02
0^+	0.000	$5/2^+$	3.021	$0d_{5/2}$	64.501	1.334	3.459	7.08	1.56	8.64	0.022	0.20
0^+	0.000	$1/2^+$	3.682	$1s_{1/2}$	72.837	1.286	3.247	7.14	1.69	8.83	0.012	0.12
0^+	0.000	$3/2^+$	3.703	$0d_{3/2}$	68.863	1.344	3.363	6.31	1.36	7.67	0.000	0.00
0^+	0.000	$5/2^+$	4.033	$0d_{5/2}$	65.805	1.334	3.443	6.92	1.51	8.44	0.040	0.35
0^+	0.000	$3/2^+$	4.046	$0d_{3/2}$	69.292	1.344	3.358	6.27	1.34	7.61	0.000	0.00
0^+	0.000	$1/2^+$	4.382	$1s_{1/2}$	73.764	1.286	3.235	7.02	1.65	8.67	0.000	0.00
0^+	0.000	$3/2^+$	4.577	$0d_{3/2}$	69.954	1.344	3.350	6.20	1.32	7.53	0.001	0.00
0^+	0.000	$1/2^+$	4.990	$1s_{1/2}$	74.566	1.286	3.224	6.93	1.62	8.54	0.013	0.12
0^+	0.000	$1/2^+$	5.034	$1s_{1/2}$	74.624	1.286	3.223	6.92	1.61	8.53	0.003	0.03
0^+	0.000	$1/2^+$	5.161	$1s_{1/2}$	74.791	1.286	3.221	6.90	1.61	8.50	0.004	0.04

Table C.12: Parameters used in the calculation and the resulting theoretical cross sections σ_α^{fi} for proton knockout from ^{38}Si using level energies and spectroscopic factors from the SDPF-U interaction. The beam energy is 86.0 MeV/u on a ^{9}Be target.

J_i^π	E_i	J_f^π	E_f	ψ_α	V_0	R_0	r_{rms}	σ_{str}	σ_{diff}	$\sigma_\alpha^{\mathrm{sp}}$	C^2S	σ_α^{fi}
0^+	0.000	$5/2^+$	0.000	$0d_{5/2}$	60.568	1.334	3.514	7.59	1.73	9.31	2.632	25.86
0^+	0.000	$1/2^+$	1.097	$1s_{1/2}$	69.384	1.286	3.299	7.63	1.87	9.50	0.076	0.76
0^+	0.000	$3/2^+$	1.251	$0d_{3/2}$	65.783	1.344	3.401	6.64	1.46	8.10	0.016	0.13
0^+	0.000	$5/2^+$	1.654	$0d_{5/2}$	62.729	1.334	3.483	7.30	1.63	8.93	0.021	0.20
0^+	0.000	$1/2^+$	2.095	$1s_{1/2}$	70.723	1.286	3.278	7.43	1.80	9.23	0.015	0.15
0^+	0.000	$5/2^+$	2.183	$0d_{5/2}$	63.416	1.334	3.474	7.21	1.60	8.81	0.873	8.11
0^+	0.000	$3/2^+$	2.227	$0d_{3/2}$	67.013	1.344	3.385	6.50	1.42	7.92	0.073	0.61
0^+	0.000	$5/2^+$	2.400	$0d_{5/2}$	63.697	1.334	3.470	7.17	1.59	8.77	0.605	5.60
0^+	0.000	$3/2^+$	2.425	$0d_{3/2}$	67.262	1.344	3.382	6.48	1.41	7.89	0.006	0.05
0^+	0.000	$1/2^+$	2.516	$1s_{1/2}$	71.285	1.286	3.270	7.35	1.77	9.12	0.149	1.44
0^+	0.000	$3/2^+$	2.568	$0d_{3/2}$	67.441	1.344	3.380	6.46	1.40	7.86	0.061	0.51
0^+	0.000	$1/2^+$	3.306	$1s_{1/2}$	72.338	1.286	3.254	7.21	1.72	8.92	0.009	0.08

Table C.13: Parameters used in the calculation and the resulting theoretical cross sections σ_α^{fi} for neutron knockout from ^{40}Si using level energies and spectroscopic factors from the SDPF-MU interaction. The beam energy is 79.0 MeV/u on a ^{9}Be target.

J_i^π	E_i	J_f^π	E_f	ψ_α	V_0	R_0	r_{rms}	σ_{str}	σ_{diff}	$\sigma_\alpha^{\mathrm{sp}}$	C^2S	σ_α^{fi}
0^+	0.000	$5/2^-$	0.000	$0f_{5/2}$	62.503	1.202	3.894	10.34	3.26	13.59	0.095	1.39
0^+	0.000	$7/2^-$	0.044	$0f_{7/2}$	54.620	1.179	4.008	11.51	3.69	15.20	3.191	52.33
0^+	0.000	$3/2^-$	0.098	$1p_{3/2}$	77.319	0.981	4.150	15.64	6.18	21.81	0.903	21.26
0^+	0.000	$1/2^-$	0.378	$1p_{1/2}$	81.582	0.993	4.103	14.94	5.79	20.73	0.031	0.68
0^+	0.000	$3/2^+$	0.635	$0d_{3/2}$	42.203	1.204	3.829	10.21	3.44	13.65	2.312	33.20
0^+	0.000	$5/2^-$	0.654	$0f_{5/2}$	63.590	1.202	3.858	9.89	3.03	12.92	0.153	2.13
0^+	0.000	$3/2^-$	0.775	$1p_{3/2}$	79.001	0.981	4.058	14.36	5.45	19.81	0.084	1.79
0^+	0.000	$1/2^-$	1.134	$1p_{1/2}$	83.395	0.993	4.008	13.64	5.06	18.71	0.131	2.64
0^+	0.000	$1/2^+$	1.279	$1s_{1/2}$	40.688	1.202	4.129	16.18	6.50	22.68	0.526	12.55
0^+	0.000	$7/2^-$	1.461	$0f_{7/2}$	57.164	1.179	3.927	10.48	3.18	13.66	0.305	4.50
0^+	0.000	$5/2^+$	1.499	$0d_{5/2}$	36.684	1.216	3.952	11.32	3.78	15.10	0.016	0.26
0^+	0.000	$5/2^-$	1.777	$0f_{5/2}$	65.426	1.202	3.802	9.23	2.72	11.95	0.065	0.84
0^+	0.000	$3/2^+$	1.821	$0d_{3/2}$	44.086	1.204	3.745	9.22	2.95	12.16	0.026	0.34
0^+	0.000	$7/2^-$	1.837	$0f_{7/2}$	57.826	1.179	3.907	10.24	3.07	13.31	0.114	1.63
0^+	0.000	$3/2^-$	1.918	$1p_{3/2}$	81.727	0.981	3.930	12.65	4.52	17.18	0.001	0.01
0^+	0.000	$7/2^-$	1.992	$0f_{7/2}$	58.097	1.179	3.900	10.15	3.03	13.17	0.131	1.86
0^+	0.000	$5/2^-$	2.237	$0f_{5/2}$	66.168	1.202	3.781	8.99	2.61	11.60	0.003	0.03
0^+	0.000	$5/2^+$	2.383	$0d_{5/2}$	38.147	1.216	3.890	10.55	3.40	13.95	0.182	2.67
0^+	0.000	$3/2^-$	2.383	$1p_{3/2}$	82.801	0.981	3.885	12.08	4.22	16.30	0.011	0.20
0^+	0.000	$1/2^-$	2.605	$1p_{1/2}$	86.764	0.993	3.858	11.71	4.04	15.76	0.000	0.00
0^+	0.000	$3/2^+$	2.775	$0d_{3/2}$	45.567	1.204	3.687	8.58	2.64	11.22	0.262	3.10
0^+	0.000	$1/2^-$	2.805	$1p_{1/2}$	87.208	0.993	3.840	11.50	3.93	15.43	0.004	0.07
0^+	0.000	$5/2^+$	2.841	$0d_{5/2}$	38.893	1.216	3.861	10.20	3.23	13.43	0.132	1.87
0^+	0.000	$3/2^+$	3.093	$0d_{3/2}$	46.055	1.204	3.670	8.39	2.55	10.94	0.340	3.91
0^+	0.000	$5/2^+$	3.341	$0d_{5/2}$	39.700	1.216	3.831	9.85	3.06	12.91	0.005	0.07

Table C.14: Parameters used in the calculation and the resulting theoretical cross sections σ_α^{fi} for neutron knockout from ^{40}Si using level energies and spectroscopic factors from the SDPF-U interaction. The beam energy is 79.0 MeV/u on a ^{9}Be target.

J_i^π	E_i	J_f^π	E_f	ψ_α	V_0	R_0	r_{rms}	σ_{str}	σ_{diff}	$\sigma_\alpha^{\mathrm{sp}}$	C^2S	σ_α^{fi}
0^+	0.000	$5/2^-$	0.000	$0f_{5/2}$	62.503	1.202	3.894	10.34	3.26	13.59	0.043	0.62
0^+	0.000	$3/2^-$	0.044	$1p_{3/2}$	77.182	0.981	4.158	15.75	6.24	21.99	0.513	12.18
0^+	0.000	$7/2^-$	0.193	$0f_{7/2}$	54.892	1.179	3.999	11.39	3.63	15.02	3.328	53.93
0^+	0.000	$1/2^-$	0.208	$1p_{1/2}$	81.165	0.993	4.126	15.27	5.98	21.25	0.018	0.40
0^+	0.000	$5/2^-$	0.482	$0f_{5/2}$	63.305	1.202	3.867	10.00	3.09	13.09	0.065	0.91
0^+	0.000	$3/2^-$	0.754	$1p_{3/2}$	78.949	0.981	4.061	14.39	5.47	19.86	0.174	3.74
0^+	0.000	$1/2^-$	1.279	$1p_{1/2}$	83.736	0.993	3.991	13.42	4.94	18.36	0.085	1.68
0^+	0.000	$7/2^-$	1.312	$0f_{7/2}$	56.900	1.179	3.935	10.57	3.23	13.80	0.634	9.43
0^+	0.000	$5/2^-$	1.577	$0f_{5/2}$	65.101	1.202	3.811	9.34	2.77	12.11	0.032	0.42
0^+	0.000	$7/2^-$	1.587	$0f_{7/2}$	57.386	1.179	3.920	10.39	3.14	13.54	0.089	1.31
0^+	0.000	$3/2^-$	1.779	$1p_{3/2}$	81.402	0.981	3.944	12.83	4.62	17.46	0.001	0.02
0^+	0.000	$1/2^-$	2.764	$1p_{1/2}$	87.117	0.993	3.844	11.54	3.95	15.50	0.001	0.02
0^+	0.000	$3/2^+$	2.810	$0d_{3/2}$	45.621	1.204	3.685	8.56	2.63	11.19	1.688	19.87
0^+	0.000	$1/2^+$	3.039	$1s_{1/2}$	43.818	1.202	3.936	13.50	4.99	18.49	0.723	14.07
0^+	0.000	$5/2^+$	3.379	$0d_{5/2}$	39.761	1.216	3.829	9.82	3.05	12.87	0.037	0.50

Table C.15: Parameters used in the calculation and the resulting theoretical cross sections σ_α^{fi} for proton knockout from ^{40}Si using level energies and spectroscopic factors from the SDPF-MU interaction. The beam energy is 79.0 MeV/u on a ^{9}Be target.

J_i^π	E_i	J_f^π	E_f	ψ_α	V_0	R_0	r_{rms}	σ_{str}	σ_{diff}	$\sigma_\alpha^{\rm sp}$	C^2S	σ_α^{fi}
0^+	0.000	$5/2^+$	0.000	$0d_{5/2}$	61.131	1.339	3.538	6.83	1.60	8.43	2.450	21.73
0^+	0.000	$1/2^+$	0.836	$1s_{1/2}$	69.344	1.293	3.312	6.91	1.72	8.63	0.186	1.69
0^+	0.000	$3/2^+$	0.855	$0d_{3/2}$	65.810	1.345	3.425	5.96	1.36	7.32	0.000	0.00
0^+	0.000	$5/2^+$	1.610	$0d_{5/2}$	63.198	1.339	3.510	6.58	1.52	8.10	0.122	1.04
0^+	0.000	$1/2^+$	1.784	$1s_{1/2}$	70.592	1.293	3.294	6.74	1.66	8.41	0.003	0.02
0^+	0.000	$3/2^+$	1.867	$0d_{3/2}$	67.069	1.345	3.410	5.83	1.32	7.15	0.152	1.14
0^+	0.000	$3/2^+$	2.334	$0d_{3/2}$	67.648	1.345	3.403	5.78	1.30	7.08	0.024	0.18
0^+	0.000	$5/2^+$	2.507	$0d_{5/2}$	64.342	1.339	3.495	6.45	1.47	7.93	0.000	0.00
0^+	0.000	$5/2^+$	2.672	$0d_{5/2}$	64.552	1.339	3.492	6.43	1.47	7.89	0.096	0.80
0^+	0.000	$3/2^+$	3.070	$0d_{3/2}$	68.560	1.345	3.393	5.69	1.27	6.97	0.006	0.04
0^+	0.000	$1/2^+$	3.238	$1s_{1/2}$	72.495	1.293	3.268	6.51	1.58	8.08	0.003	0.02
0^+	0.000	$1/2^+$	3.548	$1s_{1/2}$	72.899	1.293	3.262	6.46	1.56	8.02	0.001	0.01

Table C.16: Parameters used in the calculation and the resulting theoretical cross sections σ_α^{fi} for proton knockout from ^{40}Si using level energies and spectroscopic factors from the SDPF-U interaction. The beam energy is 79.0 MeV/u on a ^{9}Be target.

J_i^π	E_i	J_f^π	E_f	ψ_α	V_0	R_0	r_{rms}	σ_{str}	σ_{diff}	$\sigma_\alpha^{\mathrm{sp}}$	C^2S	σ_α^{fi}
0^+	0.000	$5/2^+$	0.000	$0d_{5/2}$	61.131	1.339	3.538	6.83	1.60	8.43	2.231	19.79
0^+	0.000	$1/2^+$	0.496	$1s_{1/2}$	68.895	1.293	3.319	6.97	1.75	8.72	0.184	1.69
0^+	0.000	$3/2^+$	0.559	$0d_{3/2}$	65.441	1.345	3.430	6.00	1.37	7.37	0.018	0.14
0^+	0.000	$5/2^+$	1.147	$0d_{5/2}$	62.605	1.339	3.518	6.65	1.54	8.19	0.130	1.12
0^+	0.000	$1/2^+$	1.324	$1s_{1/2}$	69.987	1.293	3.303	6.82	1.69	8.52	0.005	0.05
0^+	0.000	$3/2^+$	1.431	$0d_{3/2}$	66.527	1.345	3.417	5.89	1.33	7.22	0.159	1.21
0^+	0.000	$3/2^+$	1.517	$0d_{3/2}$	66.634	1.345	3.415	5.88	1.33	7.21	0.026	0.20
0^+	0.000	$5/2^+$	1.625	$0d_{5/2}$	63.217	1.339	3.510	6.58	1.52	8.10	0.103	0.88
0^+	0.000	$5/2^+$	1.790	$0d_{5/2}$	63.428	1.339	3.507	6.55	1.51	8.06	0.006	0.05
0^+	0.000	$1/2^+$	2.353	$1s_{1/2}$	71.339	1.293	3.283	6.65	1.63	8.28	0.002	0.01
0^+	0.000	$3/2^+$	2.482	$0d_{3/2}$	67.832	1.345	3.401	5.76	1.29	7.05	0.016	0.12
0^+	0.000	$1/2^+$	2.602	$1s_{1/2}$	71.665	1.293	3.279	6.61	1.61	8.22	0.003	0.03

REFERENCES

REFERENCES

[1] M. Wang, G. Audi, A. H. Wapstra, F. G. Kondev, M. MacCormick, X. Xu, and B. Pfeiffer. The AME2012 atomic mass evaluation. *Chinese Phys. C*, 36(12):1603–2014, December 2012.

[2] Evaluated Nuclear Structure Database, http://www.nndc.bnl.gov/ensdf.

[3] S. Takeuchi, M. Matsushita, N. Aoi, P. Doornenbal, K. Li, T. Motobayashi, H. Scheit, D. Steppenbeck, H. Wang, H. Baba, D. Bazin, L. Càceres, H. L. Crawford, P. Fallon, R. Gernhäuser, J. Gibelin, S. Go, S. Grévy, C. Hinke, C. R. Hoffman, R. Hughes, E. Ideguchi, D. Jenkins, N. Kobayashi, Y. Kondo, R. Krücken, T. Le Bleis, J. Lee, G. Lee, A. Matta, S. Michimasa, T. Nakamura, S. Ota, M. Petri, T. Sako, H. Sakurai, S. Shimoura, K. Steiger, K. Takahashi, M. Takechi, Y. Togano, R. Winkler, and K. Yoneda. Well Developed Deformation in ^{42}Si. *Phys. Rev. Lett.*, 109(18):182501, November 2012.

[4] R. Wiringa, V. Stoks, and R. Schiavilla. Accurate nucleon-nucleon potential with charge-independence breaking. *Phys. Rev. C*, 51(1):38–51, January 1995.

[5] A. M. Klomp, V. Stoks, R. Klomp, C. Terheggen, and J. de Swart. Construction of high-quality NN potential models. *Phys. Rev. C*, 49(6):2950–2962, June 1994.

[6] T. R. Baugher. *Neutron-rich Chromium and Manganese Isotopes and the Role of the* $0g_{9/2}$ *and* $1d_{5/2}$ *Neutron Orbitals in the Region Below* ^{68}*Ni*. PhD thesis, Michigan State University, June 2014.

[7] J. Yurkon, D. Bazin, W. Benenson, D. J. Morrissey, B. M. Sherrill, D. Swan, and R. Swanson. Focal plane detector for the S800 high-resolution spectrometer. *Nucl. Instruments Methods Phys. Res.. A*, 422(1-3):291–295, February 1999.

[8] D. Weisshaar, M. S. Wallace, P. Adrich, D. Bazin, C. M. Campbell, J. M. Cook, S. Ettenauer, A. Gade, T. Glasmacher, S. McDaniel, A. Obertelli, A. Ratkiewicz, A. M. Rogers, K. P. Siwek, and S. R. Tornga. $LaBr_3$:Ce scintillators for in-beam gamma-ray spectroscopy with fast beams of rare isotopes. *Nucl. Instruments Methods Phys. Res.. A*, 594(1):56–60, August 2008.

[9] G. Burgunder, O. Sorlin, F. Nowacki, S. Giron, F. Hammache, M. Moukaddam, N. de Séréville, D. Beaumel, L. Càceres, E. Clément, G. Duchêne, J. P. P. Ebran,

B. Fernandez-Dominguez, F. Flavigny, S. Franchoo, J. Gibelin, A. Gillibert, S. Grévy, J. Guillot, A. Lepailleur, I. Matea, A. Matta, L. Nalpas, A. Obertelli, T. Otsuka, J. Pancin, A. Poves, R. Raabe, J. A. Scarpaci, I. Stefan, C. Stodel, T. Suzuki, J. C. C. Thomas, and V. Lapoux. Experimental Study of the Two-Body Spin-Orbit Force in Nuclei. *Phys. Rev. Lett.*, 112(4):042502, January 2014.

[10] F. Rotaru, F. Negoita, S. Grévy, J. Mrazek, S. M. Lukyanov, F. Nowacki, A. Poves, O. Sorlin, C. Borcea, R. Borcea, A. Buta, L. Cáceres, S. Calinescu, R. Chevrier, Zs. Dombrádi, J. M. Daugas, D. Lebhertz, Y. Penionzhkevich, C. Petrone, D. Sohler, M. Stanoiu, J. C. Thomas, and L. Càceres. Unveiling the Intruder Deformed 0_2^+ State in ^{34}Si. *Phys. Rev. Lett.*, 109(9):092503, August 2012.

[11] D. Sohler, S. Grévy, Zs. Dombrádi, O. Sorlin, L. Gaudefroy, B. Bastin, N. L. Achouri, J. C. Angélique, F. Azaiez, D. Baiborodin, R. Borcea, C. Bourgeois, A. Buta, A. Burger, L. Caceres, R. Chapman, J. C. Dalouzy, Z. Dlouhy, A. Drouard, Z. Elekes, S. Franchoo, S. Iacob, I. Kuti, B. Laurent, M. Lazar, X. Liang, E. Liénard, S. M. Lukyanov, J. Mrazek, L. Nalpas, F. Negoita, F. Nowacki, N.a. Orr, Yu. E. Penionzkhevitch, Zs. Podolyák, F. Pougheon, A. Poves, P. Roussel-Chomaz, M. Stanoiu, I. Stefan, and M. G. St-Laurent. Spectroscopy of ^{39,41}Si and the border of the island of inversion. *Phys. Lett. B*, 703(4):417–421, September 2011.

[12] A. Gade, P. Adrich, D. Bazin, M. D. Bowen, B. A. Brown, C. M. Campbell, J. M. Cook, T. Glasmacher, P. G. Hansen, K. Hosier, S. McDaniel, D. McGlinchery, A. Obertelli, K. P. Siwek, L. A. Riley, J. A. Tostevin, and D. Weisshaar. Reduction of spectroscopic strength: Weakly-bound and strongly-bound single-particle states studied using one-nucleon knockout reactions. *Phys. Rev. C*, 77(4):044306, April 2008.

[13] J. Enders, A. Bauer, D. Bazin, A. Bonaccorso, B. A. Brown, T. Glasmacher, P. Hansen, V. Maddalena, K. Miller, A. Navin, B. M. Sherrill, and J. A. Tostevin. Single-neutron knockout from ^{34,35}Si and ^{37}S. *Phys. Rev. C*, 65(3):034318, March 2002.

[14] E. Rutherford. The scattering of α and β particles by matter and the structure of the atom. *Philos. Mag. Ser. 6*, 21(125):669–688, May 1911.

[15] H. Geiger and E. Marsden. On a Diffuse Reflection of the α-Particles. *Proc. R. Soc. A Math. Phys. Eng. Sci.*, 82(557):495–500, July 1909.

[16] C. F. von Weizsäcker. Zur Theorie der Kernmassen. *Zeitschrift für Phys.*, 96(7-8):431–458, July 1935.

[17] B. A. Brown. *Lecture Notes in Nuclear Structure Physics*. 2010.

[18] G. Audi. The history of nuclidic masses and of their evaluation. *Int. J. Mass Spectrom.*, 251(2-3):85–94, April 2006.

[19] W. M. Elsasser. Sur le principe de Pauli dans les noyaux - III. *J. Phys. Rad.*, 5(12):635–639, December 1934.

[20] E. Gapon and D. Iwanenko. Zur Bestimmung der Isotopenzahl. *Naturwissenschaften*, 20(43):792–793, October 1932.

[21] A. Bohr and B. R. Mottleson. *Nuclear Structure*. W. A. Benjamin, Inc., New York, 1 edition, 1969.

[22] M. G. Mayer. On Closed Shells in Nuclei. II. *Phys. Rev.*, page 1969, 1949.

[23] O. Haxel, J. H. D. Jensen, and H. E. Suess. On the "magic numbers" in nuclear structure. *Phys. Rev.*, page 1766, 1949.

[24] M. G. Mayer. Nuclear Configurations in the Spin-Orbit Coupling Model. II. Theoretical Considerations. *Phys. Rev.*, 78(1):22, 1950.

[25] L. H. Thomas. I. The kinematics of an electron with an axis. *Philos. Mag. Ser. 7*, 3(13):1–22, 1927.

[26] L. Schiff. Nonlinear Meson Theory of Nuclear Forces. I. Neutral Scalar Mesons with Point-Contact Repulsion. *Phys. Rev.*, 84(1):1–9, October 1951.

[27] M. Johnson and E. Teller. Classical Field Theory of Nuclear Forces. *Phys. Rev.*, 98(3):783–787, May 1955.

[28] J. D. Walecka. A theory of highly condensed matter. *Ann. Phys. (N. Y).*, 83(2):491–529, April 1974.

[29] P. Ring. Relativistic mean field theory in finite nuclei. *Prog. Part. Nucl. Phys.*, 37:193–263, January 1996.

[30] R. J. Furnstahl, J. J. Rusnak, and B. D. Serot. The nuclear spin-orbit force in chiral effective field theories. *Nucl. Phys. A*, 632(4):607–623, March 1998.

[31] T. Otsuka, T. Suzuki, R. Fujimoto, H. Grawe, and Y. Akaishi. Evolution of Nuclear Shells due to the Tensor Force. *Phys. Rev. Lett.*, 95(23):232502, November 2005.

[32] J. Fujita and H. Miyazawa. Spin-Orbit Coupling in Heavy Nuclei. *Prog. Theor. Phys.*, 17(3):366–372, March 1957.

[33] N. Kaiser and W. Weise. Note on spin-orbit interactions in nuclei and hypernuclei. *Nucl. Phys. A*, 804(1-4):60–70, May 2008.

[34] O. Sorlin and M.-G. Porquet. Nuclear magic numbers: New features far from stability. *Prog. Part. Nucl. Phys.*, 61(2):602–673, October 2008.

[35] T. Otsuka, R. Fujimoto, Y. Utsuno, B. A. Brown, M. Honma, and T. Mizusaki. Magic Numbers in Exotic Nuclei and Spin-Isospin Properties of the NN Interaction. *Phys. Rev. Lett.*, 87(8):082502, August 2001.

[36] T. Glasmacher, B. A. Brown, M. J. Chromik, P. D. Cottle, M. Fauerbach, R.W. Ibbotson, K.W. Kemper, D.J. Morrissey, H. Scheit, D.W. Sklenicka, and M. Steiner. Collectivity in 44S. *Phys. Lett. B*, 395(3-4):163–168, March 1997.

[37] J. M. Blatt and V. F. Weisskopf. *Theoretical Nuclear Physics*. Springer-Verlag, New York, 1979.

[38] P. D. Cottle and K. W. Kemper. Persistence of the N= 28 shell closure in neutron-rich nuclei. *Phys. Rev. C*, 58(6):3761–3762, 1998.

[39] J. Fridmann, I. Wiedenhöver, A. Gade, L. T. Baby, D. Bazin, B. A. Brown, C. M. Campbell, J. M. Cook, P. D. Cottle, E. Diffenderfer, D.-C. Dinca, T. Glasmacher, P. G. Hansen, K. W. Kemper, J. L. Lecouey, W. F. Mueller, H. Olliver, E. Rodriguez-Vieitez, J. R. Terry, J. A. Tostevin, and K. Yoneda. 'Magic' nucleus ^{42}Si. *Nature*, 435(7044):922–4, June 2005.

[40] J. Fridmann, I. Wiedenhöver, A. Gade, L. T. Baby, D. Bazin, B. A. Brown, C. M. Campbell, J. M. Cook, P. D. Cottle, E. Diffenderfer, D.-C. Dinca, T. Glasmacher, P. Hansen, K. W. Kemper, J. L. Lecouey, W. F. Mueller, E. Rodriguez-Vieitez, J. R. Terry, J. A. Tostevin, K. Yoneda, and H. Zwahlen. Shell structure at N=28 near the dripline: Spectroscopy of ^{42}Si, ^{43}P, and ^{44}S. *Phys. Rev. C*, 74(3):034313, September 2006.

[41] B. Bastin, S. Grévy, D. Sohler, O. Sorlin, Zs. Dombrádi, N. L. Achouri, J. C. Angélique, F. Azaiez, D. Baiborodin, R. Borcea, C. Bourgeois, A. Buta, A. Bürger, R. Chapman, J. C. Dalouzy, Z. Dlouhy, A. Drouard, Z. Elekes, S. Franchoo, S. Iacob, B. Laurent, M. Lazar, X. Liang, E. Liénard, J. Mrazek, L. Nalpas, F. Negoita, N. Orr, Y. Penionzhkevich, Zs. Podolyák, F. Pougheon, P. Roussel-Chomaz, M. G. Saint-Laurent,

M. Stanoiu, I. Stefan, F. Nowacki, and A. Poves. Collapse of the N=28 Shell Closure in ^{42}Si. *Phys. Rev. Lett.*, 99(2):022503, July 2007.

[42] Y. Utsuno, T. Otsuka, B. A. Brown, M. Honma, T. Mizusaki, and N. Shimizu. Shape transitions in exotic Si and S isotopes and tensor-force-driven Jahn-Teller effect. *Phys. Rev. C*, 86(5):051301, November 2012.

[43] S. Weinberg. *The Quantum Theory of Fields Volume II*. Cambridge University Press, New York, 1996.

[44] D. J. Gross and F. Wilczek. Ultraviolet Behavior of Non-Abelian Gauge Theories. *Phys. Rev. Lett.*, 30(26):1343–1346, June 1973.

[45] H. Politzer. Reliable Perturbative Results for Strong Interactions? *Phys. Rev. Lett.*, 30(26):1346–1349, June 1973.

[46] K. G. Wilson. Confinement of quarks. *Phys. Rev. D*, 10(8):2445, October 1974.

[47] T. Yamazaki, K. Ishikawa, Y. Kuramashi, and A. Ukawa. Helium nuclei, deuteron, and dineutron in 2+1 flavor lattice QCD. *Phys. Rev. D*, 86(7):074514, October 2012.

[48] M. J. Savage. Nuclear Forces from Lattice Quantum Chromodynamics. *arXiv Prepr.*, page 16, September 2013.

[49] C. A. Bertulani. *Nuclear Physics in a Nutshell*. Princeton University Press, Princeton, 2007.

[50] J. Fujita and H. Miyazawa. Pion Theory of Three-Body Forces. *Prog. Theor. Phys.*, 17(3):360–365, March 1957.

[51] J. D. Jackson. *Classical Electrodynamics*. Wiley & Sons, New York, 2 edition, 1975.

[52] W. Rarita and J. Schwinger. On the Neutron-Proton Interaction. *Phys. Rev.*, 59(5):436–452, March 1941.

[53] J. Kellogg, I. Rabi, N. Ramsey, and J. Zacharias. An Electrical Quadrupole Moment of the Deuteron. *Phys. Rev.*, 55(3):318–319, February 1939.

[54] A. L. Fetter and J. D. Walecka. *QuantumTheory of Many-Particle Systems*. Dover Publications, Inc, Mineola, 2003.

[55] E. Caurier, G. Martínez-Pinedo, F. Nowacki, A. Poves, and A. P. Zuker. The shell model as a unified view of nuclear structure. *Rev. Mod. Phys.*, 77(April):427–488, 2005.

[56] D. J. Griffiths. *Introduction to Quantum Mechanics*. Pearson Prentice Hall, Upper Saddle River, NJ, 2nd edition, 2005.

[57] R. Machleidt. High-precision, charge-dependent Bonn nucleon-nucleon potential. *Phys. Rev. C*, 63(2):024001, January 2001.

[58] D. R. Entem and R. Machleidt. Accurate charge-dependent nucleon-nucleon potential at fourth order of chiral perturbation theory. *Phys. Rev. C*, 68(4):041001, October 2003.

[59] K. Brueckner. Two-Body Forces and Nuclear Saturation. III. Details of the Structure of the Nucleus. *Phys. Rev.*, 97(5):1353–1366, March 1955.

[60] S. K. Bogner, T. T. S. Kuo, and a. Schwenk. Model-independent low momentum nucleon interaction from phase shift equivalence. *Phys. Rep.*, 386(1):1–27, October 2003.

[61] S. K. Bogner, R. J. Furnstahl, and R. Perry. Similarity renormalization group for nucleon-nucleon interactions. *Phys. Rev. C*, 75(6):061001, June 2007.

[62] E. Jurgenson, P. Navrátil, and R. J. Furnstahl. Evolution of Nuclear Many-Body Forces with the Similarity Renormalization Group. *Phys. Rev. Lett.*, 103(8):082501, August 2009.

[63] M. Hjorth-Jensen, T. T. S. Kuo, and E. Osnes. Realistic effective interactions for nuclear systems. *Phys. Rep.*, 261:125–270, 1995.

[64] K. Tsukiyama, S. K. Bogner, and A. Schwenk. In-medium similarity renormalization group for open-shell nuclei. *Phys. Rev. C*, 85(6):061304, June 2012.

[65] S. K. Bogner, H. Hergert, J. D. Holt, A. Schwenk, S. Binder, A. Calci, J. Langhammer, and R. Roth. Nonperturbative shell-model interactions from the in-medium similarity renormalization group. *arXiv Prepr.*, page 6, February 2014.

[66] G. R. Jansen, J. Engel, G. Hagen, P. Navrátil, and A. Signoracci. Ab-initio coupled-cluster effective interactions for the shell model: Application to neutron-rich oxygen and carbon isotopes. *arXiv Prepr.*, February 2014.

[67] I. Talmi. Effective Interactions and Coupling Schemes in Nuclei. *Rev. Mod. Phys.*, 34(4):704–722, October 1962.

[68] B. A. Brown and W. A. Richter. New USD Hamiltonians for the sd shell. *Phys. Rev. C*, 74(3):034315, September 2006.

[69] R. D. Mattuck. *A Guide to Feynman Diagrams in the Many-Body Problem*. McGraw-Hill, New York, 2nd edition, 1976.

[70] P. Navrátil, M. Thoresen, and B. R. Barrett. Microscopic origins of effective charges in the shell model. *Phys. Rev. C*, 55(2):R573–R576, February 1997.

[71] B. A. Brown and B. H. Wildenthal. Corrections to the free-nucleon values of the single-particle matrix elements of the M1 and Gamow-Teller operators, from a comparison of shell-model predictions with sd-shell data. *Phys. Rev. C*, 28(6):2397–2413, December 1983.

[72] B. A. Brown and B. H. Wildenthal. Status of the Nuclear Shell Model. *Annu. Rev. Nucl. Part. Sci.*, 38(1):29–66, December 1988.

[73] S. R. Stroberg, A. Gade, T. R. Baugher, D. Bazin, B. A. Brown, J. M. Cook, T. Glasmacher, G. F. Grinyer, S. McDaniel, A. Ratkiewicz, and D. Weisshaar. In-beam γ-ray spectroscopy of $^{43-46}$Cl. *Phys. Rev. C*, 86(2):024321, August 2012.

[74] P. G. Hansen and J. A. Tostevin. Direct Reactions With Exotic Nuclei. *Annu. Rev. Nucl. Part. Sci.*, 53(1):219–261, December 2003.

[75] A. Gade and T. Glasmacher. In-beam nuclear spectroscopy of bound states with fast exotic ion beams. *Prog. Part. Nucl. Phys.*, 60(1):161–224, January 2008.

[76] J. A. Tostevin. Single-nucleon knockout reactions at fragmentation beam energies. *Nucl. Phys. A*, 682:320–331, 2001.

[77] A. E. L. Dieperink and T. de Forest. Center-of-mass effects in single-nucleon knock-out reactions. *Phys. Rev. C*, 10(2), 1974.

[78] A. M. Mukhamedzhanov and A. S. Kadyrov. Unitary correlation in nuclear reaction theory: Separation of nuclear reactions and spectroscopic factors. *Phys. Rev. C*, 82(5):051601, November 2010.

[79] R. J. Glauber. *Lectures in Theoretical Physics*. Interscience, New York, 1959.

[80] D. Bohm. *Quantum Theory*. Prentice-Hall, New York, 1951.

[81] J. Brooke, J. S. Al-Khalili, and J. A. Tostevin. Noneikonal calculations for few-body projectiles. *Phys. Rev. C*, 59(3):1560–1566, March 1999.

[82] M. S. Hussein, R. A. Rego, and C. A. Bertulani. Microscopic theory of the total reaction cross section and application to stable and exotic nuclei. *Phys. Rep.*, 5(5), 1991.

[83] L. Ray. Proton-nucleus total cross sections in the intermediate energy range. *Phys. Rev. C*, 20(5), 1979.

[84] J. A. Tostevin. Core excitation in halo nucleus break-up. *J. Phys. G*, 25:735, 1999.

[85] B. A. Brown. New Skyrme interaction for normal and exotic nuclei. *Phys. Rev. C*, 58(1):220–231, July 1998.

[86] S. Pieper, K. Varga, and R. Wiringa. Quantum Monte Carlo calculations of A=9,10 nuclei. *Phys. Rev. C*, 66(4):044310, October 2002.

[87] R. J. Philpott, W. T. Pinkston, and G. R. Satchler. Some studies of realistic form factors for nucleon-transfer reactions. *Nucl. Phys. A*, 9:241–289, 1968.

[88] G. R. Satchler, D. D. Armstrong, A. G. Blair, E. R. Flynn, R. J. Philpott, and W. T. Pinkston. Excitation of the $3/2^+$, 2.02-MeV State in ^{41}Ca by the (t,d) Reaction. *Phys. Rev.*, 182(4):1141, 1968.

[89] A. Moalem, J. F. A. van Hienen, and E. Kashy. Role of the RMS radius in DWBA calculations of the (p, d) reaction. *Nucl. Phys. A*, 307:277–284, 1978.

[90] I. J. Thompson and F. M. Nunes. *Nuclear Reactions for Astrophysics*. Cambridge University Press, New York, 2009.

[91] C. A. Bertulani and A. Gade. MOMDIS: a Glauber model computer code for knockout reactions. *Comput. Phys. Commun.*, 175(5):372–380, September 2006.

[92] D. Bazin, J. A. Caggiano, B. M. Sherrill, J. Yurkon, and A. Zeller. The S800 spectrograph. *Nucl. Instruments Methods Phys. Res. Sect. B Beam Interact. with Mater. Atoms*, 204:629–633, May 2003.

[93] S. Paschalis, I. Y. Lee, A. O. Macchiavelli, C. M. Campbell, M. Cromaz, S. Gros, J. Pavan, J. Qian, R. M. Clark, H. L. Crawford, D. Doering, P. Fallon, C. Lionberger, T. Loew, M. Petri, T. Stezelberger, S. Zimmermann, D.C. Radford, K. Lagergren, D. Weisshaar, R. Winkler, T. Glasmacher, J. T. Anderson, and C. W. Beausang. The performance of the Gamma-Ray Energy Tracking In-beam Nuclear Array GRETINA. *Nucl. Instruments Methods Phys. Res.. A*, 709:44–55, May 2013.

[94] J. P. Dufour, R. Moral, A. Fleury, F. Hubert, D. Jean, M. S. Pravikoff, H. Delagrange, H. Geissel, and K. H. Schmidt. Beta decay of ^{17}C, ^{19}N, ^{22}O, ^{24}F, ^{26}Ne, ^{32}Al, ^{34}Al, $^{35-36}$Si, $^{36-37-38}$P, ^{40}S. *Zeitschrift für Phys. A At. Nucl.*, 324(4):487–488, December 1986.

[95] S. Grévy, J. C. Angélique, P. Baumann, C. Borcea, A. Buta, G. Canchel, W. N. Catford, S. Courtin, J. M. Daugas, F. de Oliveira, P. Dessagne, Z. Dlouhy, A. Knipper, K.-L. Kratz, F. R. Lecolley, J. L. Lecouey, G. Lehrsenneau, M. Lewitowicz, E. Liénard, S. M. Lukyanov, F. Maréchal, C. Miehé, J. Mrazek, F. Negoita, N. A. Orr, D. Pantelica, Yu. Penionzhkevich, J. Péter, B. Pfeiffer, S. Pietri, E. Poirier, O. Sorlin, M. Stanoiu, I. Stefan, C. Stodel, and C. Timis. Beta-decay half-lives at the N=28 shell closure. *Phys. Lett. B*, 594(3-4):252–259, August 2004.

[96] G. Audi, O. Bersillon, J. Blachot, and A. H. Wapstra. The Nubase evaluation of nuclear and decay properties. *Nucl. Phys. A*, 729(1):3–128, December 2003.

[97] D. J. Morrissey, B. M. Sherrill, M. Steiner, A. Stolz, and I. Wiedenhöver. Commissioning the A1900 projectile fragment separator. *Nucl. Instruments Methods Phys. Res. Sect. B Beam Interact. with Mater. Atoms*, 204:90–96, May 2003.

[98] G. F. Knoll. *Radiation detection and measurement*. Wiley, 2000.

[99] DJ Morrissey and BM Sherrill. Radioactive Nuclear Beam Facilities Based on Projectile Fragmentation. *Philos. Trans. Math. Phys. Eng. Sci.*, 356(1744):1985–2006, 1998.

[100] M. Berz, K. Joh, J. Nolen, B. M. Sherrill, and A. F. Zeller. Reconstructive correction of aberrations in nuclear particle spectrographs. *Phys. Rev. C*, 47(2):537–544, February 1993.

[101] W. F. Mueller, J. A. Church, T. Glasmacher, D. Gutknecht, G. Hackman, P. G. Hansen, Z. Hu, K. L. Miller, and P. Quirin. Thirty-two-fold segmented germanium detectors to identify γ-rays from intermediate-energy exotic beams. *Nucl. Instruments Methods Phys. Res.. A*, 466(3):492–498, July 2001.

[102] A. Gade, P. Adrich, D. Bazin, M. D. Bowen, B. A. Brown, C. M. Campbell, J. M. Cook, T. Glasmacher, K. Hosier, S. McDaniel, D. McGlinchery, A. Obertelli, L. a. Riley, K. Siwek, J. A. Tostevin, and D. Weisshaar. Inverse-kinematics one-proton pickup with intermediate-energy beams: The ^{9}Be (^{20}Ne,^{21}Na+γ)X reaction. *Phys. Rev. C*, 76(6):061302, December 2007.

[103] C. M. Campbell. *Quadruople Collectivity Measurements in Even-Even, Neutron-Rich Silicon and Sulfur Isotopes Approaching N=28*. PhD thesis, Michigan State University, 2007.

[104] L. A. Riley. Private communication, 2014.

[105] A. Gade, J. A. Tostevin, T. R. Baugher, D. Bazin, B. A. Brown, C. M. Campbell, T. Glasmacher, G. F. Grinyer, S. McDaniel, K. Meierbachtol, A. Ratkiewicz, S. R. Stroberg, K. A. Walsh, D. Weisshaar, and R. Winkler. Inverse-kinematics one-neutron pickup with fast rare-isotope beams. *Phys. Rev. C*, 83(5):054324, May 2011.

[106] S. McDaniel, A. Gade, J. A. Tostevin, T. R. Baugher, D. Bazin, B. A. Brown, J. M. Cook, T. Glasmacher, G. F. Grinyer, A. Ratkiewicz, and D. Weisshaar. Intermediate-energy inverse-kinematics one-proton pickup reactions on neutron-deficient fp-shell nuclei. *Phys. Rev. C*, 85(1):014610, January 2012.

[107] S. Agostinelli, et al. GEANT4 – a simulation toolkit. *Nucl. Instruments Methods Phys. Res.. A*, 506(3):250–303, July 2003.

[108] F. James and M. Roos. Minuit - a system for function minimization and analysis of the parameter errors and correlations. *Comput. Phys. Commun.*, 10(6):343–367, December 1975.

[109] R. Brun and F. Rademakers. ROOT An object oriented data analysis framework. *Nucl. Instruments Methods Phys. Res.. A*, 389(1-2):81–86, April 1997.

[110] T. Hauschild and M. Jentschel. Comparison of maximum likelihood estimation and chi-square statistics applied to counting experiments. *Nucl. Instruments Methods Phys. Res.. A*, 457(1-2):384–401, January 2001.

[111] D. Weisshaar. Private communication, 2014.

[112] M.-M Bé, V. P. Chechev, R. Dersch, O. A. M. Helene, R. G. Helmer, M. Herman, S. Hlavác, A. Marcinkowski, G. L. Molnár, A. L. Nichols, E. Schönfeld, V. R. Vanin, and M. J. Woods. *Update of X Ray and Gamma Ray Decay Data Standards for*

Detector Calibration and Other Applications. International Atomic Energy Agency, Vienna, Austria, 2007.

[113] G. Cowan. *Statistical Data Analysis*. Oxford University Press, New York, 1998.

[114] A. Navin, D. Bazin, B. A. Brown, and B Davids. Spectroscopy of Radioactive Beams from Single-Nucleon Knockout Reactions: Application to the sd Shell Nuclei ^{25}Al and ^{26,27,28}P. *Phys. Rev. Lett.*, 81(23):5089–5092, 1998.

[115] A. Gade, D. Bazin, C. A. Bertulani, B. A. Brown, C. M. Campbell, J. Church, D.-C. Dinca, J. Enders, T. Glasmacher, P. G. Hansen, Z. Hu, K. W. Kemper, W. F. Mueller, H. Olliver, B. Perry, L. a. Riley, B. Roeder, B. M. Sherrill, J. R. Terry, J. A. Tostevin, and K. Yurkewicz. Knockout from ^{46}Ar: $\ell = 3$ neutron removal and deviations from eikonal theory. *Phys. Rev. C*, 71(5):051301, May 2005.

[116] K. Yurkewicz, D. Bazin, B. A. Brown, J. Enders, A. Gade, T. Glasmacher, P. G. Hansen, V. Maddalena, A. Navin, B. M. Sherrill, and J. A. Tostevin. One-neutron knockout from ^{57}Ni. *Phys. Rev. C*, 74(2):024304, August 2006.

[117] F. Flavigny, A. Obertelli, A. Bonaccorso, G. F. Grinyer, C. Louchart, L. Nalpas, and A. Signoracci. Nonsudden Limits of Heavy-Ion Induced Knockout Reactions. *Phys. Rev. Lett.*, 108(25):252501, June 2012.

[118] L. A. Riley, P. Adrich, N. Ahsan, T. R. Baugher, D. Bazin, B. A. Brown, J. M. Cook, P. D. Cottle, C. Aa. Diget, A. Gade, T. Glasmacher, K. E. Hosier, K. W. Kemper, A. Ratkiewicz, K. P. Siwek, J. A. Tostevin, A. Volya, and D. Weisshaar. γ-ray spectroscopy of one-proton knockout from ^{45}Cl. *Phys. Rev. C*, 86(4):047301, October 2012.

[119] O. B. Tarasov and D. Bazin. LISE++: Radioactive beam production with in-flight separators. *Nucl. Instruments Methods Phys. Res. Sect. B Beam Interact. with Mater. Atoms*, 266(19-20):4657–4664, October 2008.

[120] D. H. Gloeckner and R. D. Lawson. Spurious center-of-mass motion. *Phys. Lett. B*, 53(4):313–318, 1974.

[121] J. B. McGrory and B. H. Wildenthal. Further comment on spurious center-of-mass motion. *Phys. Lett. B*, 60(1):5–8, December 1975.

[122] F. Nowacki and A. Poves. New effective interaction for $0\hbar\omega$ shell-model calculations in the sd-pf valence space. *Phys. Rev. C*, 79(1):014310, January 2009.

[123] B. H. Wildenthal. Empirical strengths of spin operators in nuclei. *Prog. Part. Nucl. Phys.*, 11:5–51, January 1984.

[124] A. Poves and A. Zuker. Theoretical spectroscopy and the fp shell. *Phys. Rep.*, 70(4):235–314, 1981.

[125] S. Kahana, H. C. Lee, and C. K. Scott. Effect of Woods-Saxon Wave Functions on the Calculation of A = 18, 206, 210 Spectra with a Realistic Interaction. *Phys. Rev.*, 180(4):956–966, 1969.

[126] G. Bertsch, J. Borysowicz, H. McManus, and W. G. Love. Interactions for inelastic scattering derived from realistic potentials. *Nucl. Phys. A*, 284(3):399–419, July 1977.

[127] M. De Rydt, J. M. Daugas, F. de Oliveira Santos, L. Gaudefroy, S. Grévy, D. Kameda, V. Kumar, R. Lozeva, T. J. Mertzimekis, P. Morel, T. Nagatomo, G. Neyens, L. Perrot, O. Sorlin, C. Stödel, J. C. Thomas, N. Vermeulen, and P. Vingerhoets. g factor of the Cl 44 ground state: Probing the reduced Z= 16 and N= 28 gaps. *Phys. Rev. C*, 81(3):034308, March 2010.

[128] M. W. Kirson. Spin-Tensor Decomposition of Nuclear Effective Interactions. *Phys. Lett. B*, 47(2):110–114, 1973.

[129] S. Nummela, P. Baumann, E. Caurier, P. Dessagne, A. Jokinen, A. Knipper, G. Le Scornet, C. Miehé, F. Nowacki, M. Oinonen, Z. Radivojevic, M. Ramdhane, G. Walter, and J. Äystö. Spectroscopy of ^{34,35}Si by β decay: sd-fp shell gap and single-particle states. *Phys. Rev. C*, 63(4):044316, March 2001.

[130] A. Gade, P. Adrich, D. Bazin, M. D. Bowen, B. A. Brown, C. M. Campbell, J. M. Cook, T. Glasmacher, K. Hosier, S. McDaniel, D. McGlinchery, A. Obertelli, L. A. Riley, K. Siwek, J. A. Tostevin, and D. Weisshaar. In-beam γ-ray spectroscopy at the proton dripline: ^{23}Al. *Phys. Lett. B*, 666(3):218–221, August 2008.

[131] I. J. Thompson. Coupled reaction channels calculations in nuclear physics. *Comput. Phys. Reports*, 7(4):167–212, April 1988.

[132] R. W. Ibbotson, T. Glasmacher, P. F. Mantica, and H. Scheit. Coulomb excitation of odd-A neutron-rich π (sd) and ν (fp) shell nuclei. *Phys. Rev. C*, 59(2):642–647, 1999.

[133] K. Steiger. *Decay spectroscopy of neutron-rich nuclei around ^{37}Al.* PhD thesis, TU München, 2013.

[134] R. W. Ibbotson, T. Glasmacher, B. A. Brown, L. Chen, M. J. Chromik, P. D. Cottle, M. Fauerbach, K. W. Kemper, D. J. Morrissey, H. Scheit, and M. Thoennessen. Quadrupole Collectivity in ^{32,34,36,38}Si and the N= 20 Shell Closure. *Phys. Rev. Lett.*, 80(March):2081–2084, March 1998.

[135] J. Terry, B. A. Brown, C. Campbell, J. Cook, A. Davies, D.-C. Dinca, A. Gade, T. Glasmacher, P. Hansen, B. M. Sherrill, H. Zwahlen, D. Bazin, K. Yoneda, J. Tostevin, T. Otsuka, Y. Utsuno, and B. Pritychenko. Single-neutron knockout from intermediate energy beams of ^{30,32}Mg: Mapping the transition into the island of inversion. *Phys. Rev. C*, 77(1):014316, January 2008.

[136] R. Kanungo, C. Nociforo, A. Prochazka, Y. Utsuno, T. Aumann, D. Boutin, D. Cortina-Gil, B. Davids, M. Diakaki, F. Farinon, H. Geissel, R. Gernhäuser, J. Gerl, R. Janik, B. Jonson, B. Kindler, R. Knöbel, R. Krücken, M. Lantz, H. Lenske, Y. Litvinov, K. Mahata, P. Maierbeck, A. Musumarra, T. Nilsson, T. Otsuka, C. Perro, C. Scheidenberger, B. Sitar, P. Strmen, B. Sun, I. Szarka, I. Tanihata, H. Weick, and M. Winkler. Structure of ^{33}Mg sheds new light on the island of inversion. *Phys. Lett. B*, 685(4-5):253–257, March 2010.

[137] K. Wimmer, T. Kröll, R. Krücken, V. Bildstein, R. Gernhäuser, B. Bastin, N. Bree, J. Diriken, P. Van Duppen, M. Huyse, N. Patronis, P. Vermaelen, D. Voulot, J. Van de Walle, F. Wenander, L. M. Fraile, R. Chapman, B. Hadinia, R. Orlandi, J. F. Smith, R. Lutter, P. G. Thirolf, M. Labiche, A. Blazhev, M. Kalkühler, P. Reiter, M. Seidlitz, N. Warr, A. O. Macchiavelli, H. B. Jeppesen, E. Fiori, G. Georgiev, G. Schrieder, S. Das Gupta, G. Lo Bianco, S. Nardelli, J. Butterworth, J. Johansen, and K. Riisager. Discovery of the Shape Coexisting 0^+ State in ^{32}Mg by a Two Neutron Transfer Reaction. *Phys. Rev. Lett.*, 105(25):252501, December 2010.

[138] R. G. T. Zegers, R. Meharchand, Y. Shimbara, Sam M. Austin, D. Bazin, B. a. Brown, C. Aa. Diget, A. Gade, C. J. Guess, M. Hausmann, G. W. Hitt, M. E. Howard, M. King, D. Miller, S. Noji, A. Signoracci, K. Starosta, C. Tur, C. Vaman, P. Voss, D. Weisshaar, and J. Yurkon. ^{34}P(^{7}Li,^{7}Be+γ) Reaction at 100A MeV in Inverse Kinematics. *Phys. Rev. Lett.*, 104(21):212504, May 2010.

[139] S. M. Brown, W. N. Catford, J. S. Thomas, B. Fernández-Domínguez, N. A. Orr, M. Labiche, M. Rejmund, N. L. Achouri, H. Al Falou, N. I. Ashwood, D. Beaumel, Y. Blumenfeld, B. A. Brown, R. Chapman, M. Chartier, N. Curtis, G. de France, N. de Sereville, F. Delaunay, A. Drouart, C. Force, S. Franchoo, J. Guillot, P. Haigh, F. Hammache, V. Lapoux, R. C. Lemmon, A. Leprince, F. Maréchal, X. Mougeot, B. Mouginot, L. Nalpas, A. Navin, N. P. Patterson, B. Pietras, E. C. Pollacco, A. Ramus, J. A. Scarpaci, I. Stefan, and G. L. Wilson. Low-lying neutron fp-shell intruder states in ^{27}Ne. *Phys. Rev. C*, 85(1):011302, January 2012.

[140] H. Mach, L. M. Fraile, O. Tengblad, R. Boutami, C. Jollet, W. A. Póciennik, D. T. Yordanov, M. Stanoiu, M. J. G. Borge, P. A. Butler, J. Cederkäll, Ph. Dessagne, B. Fogelberg, H. Fynbo, P. Hoff, A. Jokinen, A. Korgul, U. Köster, W. Kurcewicz, F. Marechal, T. Motobayashi, J. Mrazek, G. Neyens, T. Nilsson, S. Pedersen, A. Poves, B. Rubio, and E. Ruchowska. New structure information on ^{30}Mg, ^{31}Mg and ^{32}Mg. *Eur. Phys. J. A*, 25(S1):105–109, July 2005.

[141] A. Calaprice. *The Ultimate Quotable Einstein*. Princeton University Press, Princeton, NJ, 2011.

[142] E. Caurier, F. Nowacki, and A. Poves. The merging of the islands of inversion at N=20 and N=28. *arXiv Prepr.*, page 10, September 2013.

[143] D.-C. Dinca. *Study of the Development of Shell Closures at N=32,34 and Approaches to Sub-Segment Interaction-Point Determination in 32-Fold Segmented High-Purity Germanium Detectors*. PhD thesis, Michigan State University, 2005.

[144] A. P. French. *Special Relativity*. W. W. Norton & Co, New York, 1968.

[145] B. Buck and A. C. Merchant. A simple expression for the general oscillator bracket. *Nucl. Phys. A*, 600(3):387–402, 1996.

[146] M Moshinsky. Transformation brackets for harmonic oscillator functions. *Nucl. Phys.*, 13:102–116, 1959.

[147] T. A. Brody and M Moshinsky. *Tables of Transformation Brackets for Nuclear Shell Model Calculations*. Gordon and Breach, New York, 1967.